frontiers | Research Topics

Smart nanomaterials for biosensing and therapy applications, volume II

Edited by
Qitong Huang, Ziqiang Xu, Miaomiao Yuan, Youbin Zheng and Zhe Wang

Published in
Frontiers in Bioengineering and Biotechnology

ISSN 1664-8714
ISBN 978-2-8325-4849-3
DOI 10.3389/978-2-8325-4849-3

About Frontiers

Frontiers is more than just an open access publisher of scholarly articles: it is a pioneering approach to the world of academia, radically improving the way scholarly research is managed. The grand vision of Frontiers is a world where all people have an equal opportunity to seek, share and generate knowledge. Frontiers provides immediate and permanent online open access to all its publications, but this alone is not enough to realize our grand goals.

Frontiers journal series

The Frontiers journal series is a multi-tier and interdisciplinary set of open-access, online journals, promising a paradigm shift from the current review, selection and dissemination processes in academic publishing. All Frontiers journals are driven by researchers for researchers; therefore, they constitute a service to the scholarly community. At the same time, the *Frontiers journal series* operates on a revolutionary invention, the tiered publishing system, initially addressing specific communities of scholars, and gradually climbing up to broader public understanding, thus serving the interests of the lay society, too.

Dedication to quality

Each Frontiers article is a landmark of the highest quality, thanks to genuinely collaborative interactions between authors and review editors, who include some of the world's best academicians. Research must be certified by peers before entering a stream of knowledge that may eventually reach the public - and shape society; therefore, Frontiers only applies the most rigorous and unbiased reviews. Frontiers revolutionizes research publishing by freely delivering the most outstanding research, evaluated with no bias from both the academic and social point of view. By applying the most advanced information technologies, Frontiers is catapulting scholarly publishing into a new generation.

What are Frontiers Research Topics?

Frontiers Research Topics are very popular trademarks of the *Frontiers journals series*: they are collections of at least ten articles, all centered on a particular subject. With their unique mix of varied contributions from Original Research to Review Articles, Frontiers Research Topics unify the most influential researchers, the latest key findings and historical advances in a hot research area.

Find out more on how to host your own Frontiers Research Topic or contribute to one as an author by contacting the Frontiers editorial office: frontiersin.org/about/contact

Smart nanomaterials for biosensing and therapy applications, volume II

Topic editors

Qitong Huang — Gannan Medical University, China
Ziqiang Xu — Hubei University, China
Miaomiao Yuan — Sun Yat-sen University, China
Youbin Zheng — University of Liverpool, United Kingdom
Zhe Wang — Jilin University, China

Citation

Huang, Q., Xu, Z., Yuan, M., Zheng, Y., Wang, Z., eds. (2024). *Smart nanomaterials for biosensing and therapy applications, volume II*. Lausanne: Frontiers Media SA. doi: 10.3389/978-2-8325-4849-3

Table of contents

frontiers | Frontiers in Bioengineering and Biotechnology

TYPE Editorial
PUBLISHED 19 April 2024
DOI 10.3389/fbioe.2024.1387969

OPEN ACCESS

EDITED AND REVIEWED BY
Gianni Ciofani,
Italian Institute of Technology (IIT), Italy

*CORRESPONDENCE
Miaomiao Yuan,
miaomiaoyuan2023@shsmu.edu.cn,
yuanmm2019@163.com
Ziqiang Xu,
ziqiang.xu@hubu.edu.cn
Youbin Zheng,
youbin.zheng@liverpool.ac.uk
Zhe Wang,
zhe_wang@jlu.edu.cn,
hqt@gmu.edu.cn
Qitong Huang,
hqtblue@163.com

RECEIVED 19 February 2024
ACCEPTED 04 April 2024
PUBLISHED 19 April 2024

CITATION
Liao J, Yuan M, Xu Z, Zheng Y, Wang Z and Huang Q (2024), Editorial: Smart nanomaterials for biosensing and therapy applications, volume II.
Front. Bioeng. Biotechnol. 12:1387969.
doi: 10.3389/fbioe.2024.1387969

Editorial: Smart nanomaterials for biosensing and therapy applications, volume II

Jing Liao[1], Miaomiao Yuan[2]*, Ziqiang Xu[3]*, Youbin Zheng[4]*, Zhe Wang[5]* and Qitong Huang[1]*

[1]Key Laboratory of Prevention and Treatment of Cardiovascular and Cerebrovascular Diseases of Ministry of Education, Key Laboratory of Tissue Engineering of Jiangxi Province, Key Laboratory of Biomedical Sensors of Ganzhou, School of Medical and Information Engineering, School of Pharmacy, Science Research Center, Gannan Medical University, Ganzhou, China, [2]Precision Research Center for Refractory Diseases in Shanghai General Hospital, Shanghai Jiao Tong University School of Medicine, Shanghai, China, [3]School of Materials Science and Engineering, Hubei University, Wuhan, China, [4]Department of Electrical Engineering and Electronics, University of Liverpool, Liverpool, United Kingdom, [5]School of Biology and Agricultural Engineering, Jilin University, Changchun, China

KEYWORDS

smart nanomaterials, biosensing, nanozyme, cancer therapies, intelligent drug-delivery system, early-diagnosis

Editorial on the Research Topic
Smart nanomaterials for biosensing and therapy applications, volume II

Early diagnosis and effective treatment of diseases are key to improving people's health levels (Yi et al., 2022; Zhang et al., 2022; Zheng et al., 2022; Yuan et al., 2023; Liu et al., 2024). However, there are still some problems in early diagnosis and efficient treatment, such as: 1) how to more sensitively measure disease markers to achieve early diagnosis of diseases, 2) how to make drugs effectively reach the lesion site and achieve efficient treatment? The effective resolution of the above problems will greatly promote the development of life sciences and medicine. Smart nanomaterials have been widely used in biomedical engineering and biotechnology due to their excellent physical, chemical, and biological properties, especially in the fields of biosensors and therapies (Huang et al., 2020; Chen et al., 2021a; Chen et al., 2021b; Huang et al., 2022; Yang et al., 2023; Luo et al., 2023; Thatte et al., 2023). Therefore, smart nanomaterials are expected to be used for early diagnosis of diseases and efficient treatment of diseases.

In order to present the most advanced research in this field, we have launched a Research Topic on "Smart Nanomaterials for Biosensing and Therapy Applications" in the "Frontiers in Bioengineering and Biotechnology". This Research Topic has been published in two Research Topic. The first Research Topic has a total of 21 articles published in this Research Topic, including one editorial article, 11 original research articles, seven review articles, and two mini review articles. The second Research Topic has 10 articles published in this Research Topic, including eight original research articles, one review article, and one mini review article. The main content of the second Research Topic includes the application of smart nanomaterials in fields such as fluorescent probes, electrochemical sensors, tumor therapy, *Parkinson's* disease treatment, and so on.

As is well known, high-performance early-diagnosis' methods are key to disease prevention (Mei et al., 2022a; Mei et al., 2022b; He et al., 2022; Liao et al., 2023; Pourmadadi et al., 2023). Fluorescent probes and electrochemical sensors have played important roles in early disease detection. Chen et al. successfully prepared a near-infrared

(NIR) fluorescent probe QSN based on a quinolone scaffold, which has strong photostability, large Stokes shift, and cell membrane targeting ability. After transplantation, human neural stem cells labeled with QSN are retained in the striatum of the mouse brain for at least 6 weeks, indicating the excellent application prospects of QSN in tracking ultra long term transplanted cells. As a member of smart nanomaterials, metal-organic frameworks/metal nanoparticles (MOFs/MNPs) have excellent chemical, physical, and biological properties, and have been widely used in electrochemical sensors. Jiang et al. reviewed the application of MOFs/MNPs-based composite materials in electrochemical sensors, providing some reference for the future development of electrochemical sensors based on MNPs/MOFs smart nanomaterials.

Currently, cancer is one of the deadliest diseases, accounting for one-sixth of global deaths, and it is an urgent health Research Topic that requires attention (Arnold et al., 2022; Song et al., 2023; Yang et al., 2023). Traditional methods for treating cancer include surgical resection, radiation therapy, and chemotherapy (CDT). However, traditional treatment methods have not been able to cure cancer well, so there is an urgent need to improve traditional methods or combine them with other methods to achieve cancer treatment. The emergence of smart nanomaterials not only promotes the development of traditional cancer methods, but also brings some new treatment technologies, such as photothermal therapy, photoacoustic therapy, photodynamic therapy (PDT), and so on, which will promote the development of cancer treatment. The second Research Topic of this Research Topic also published some latest achievements on the application of smart nanomaterials in cancer treatment.

Cisplatin (CDDP) drugs can act by interacting with DNA, leading to DNA damage and subsequent cell apoptosis, thereby achieving cancer treatment. However, the presence of intracellular PARP1 (Poly (ADP-ribose) polymerase 1) reduces the anti-cancer efficacy of CDDP by repairing DNA strands. Olaparib (OLA) enhances the accumulation of DNA damage by inhibiting its repair, effectively enhancing the sensitivity of CDDP chemotherapy and improving treatment outcomes. However, the CDDP and OLA drugs suffer from poor water solubility and limited tumor targeting ability. To overcome the above difficulties, Zhang et al. proposed the self-assembly of CDDP and OLA through hydrogen bonding to form stable and uniform nanoparticles. The modification scheme can improve the water solubility of two drugs, eliminate the need for exogenous carriers, and achieve targeted delivery to the tumor site through enhanced permeability and retention effect. These enhanced functions improve characteristics, promote cancer cell apoptosis, and minimize harmful effects on normal cells. The acidic tumor microenvironment disrupts hydrogen bonds, leading to the release of free CDDP and OLA. CDDP has the ability to induce DNA damage and initiate the process of cell apoptosis, while OLA enhances the anti-cancer sensitivity of CDDP by inhibiting PARP1 activity, thereby reducing the repair of damaged DNA and improving the efficacy of tumor treatment.

The construction of nanomedicine systems has always been a key factor affecting the effectiveness of nanomedicine in tumor treatment (Chen et al., 2022; Zhou et al., 2022; Wang et al., 2023a; Wang et al., 2023b). Zhang et al. successfully summarized the advantages and disadvantages of nanomedicine systems currently used for the treatment and diagnosis of esophageal cancer, and proposed multiple excellent suggestions for the development of nanomedicine systems in the future. Lv et al. have successfully prepared Fe@PCN-224@hyaluronic acid smart nanomaterial and used the smart nanomaterial to load sulfasalazine drug for the combined treatment of tumors with PDT and CDT (Lv et al.). This smart nanomaterial can effectively regulate mitochondria, reduce the tolerance of tumor cells to combination therapy, induce tumor cell apoptosis, and accelerate cancer treatment. Wang et al. designed a novel reactive oxygen species-sensitive polymeric prodrug micelle (Ce6@PTP/DP) with high drug-loading capacity and self-amplified drug release. The multidrug delivery system comprised three parts: a ROS-sensitive polymeric prodrug methoxyl poly (ethylene glycol)-thioketal-paclitaxel (mPEG-TK-PTX, PTP), DSPE-mPEG (DP), and a traditional photosensitizer of chlorin e6 (Ce6). The Ce6@PTP/DP prodrug micelles exhibit good colloidal stability and biocompatibility, with PTX and Ce6 loading amounts reaching 21.7% and 7.38%, respectively. Under light irradiation, ingested by tumor cells Ce6@PTP/DPmicelles can generate sufficient ROS, which can not only achieve photodynamic therapy and inhibit tumor cell proliferation, but also trigger local PTX release and methoxy polyethylene glycol by breaking down the thiol ketone bridge bond between PTX. In addition, compared to single drug loaded micelles, light triggered Ce6@PTP/DP micelles exhibit self amplifying drug release and significantly greater inhibition of HeLa cells growth. Therefore, the Ce6@PTP/DP micelles represent an alternative for realizing synergistic chemo-photodynamic therapy. Wang et al. utilized baicalin (BA) and polyethyleneimine (PEI) through condensation reaction to prepare BA-PEI nanocomposites with effective gene delivery and perfect transfection performance, including charge regulation, hydrophobic modification, and functional modification. BA-PEI nanocomposites can effectively load miR-34a, thereby constructing a new type of nanotherapy system. miR-34a can synergistically exert anti-tumor effects with BA to enhance the therapeutic effect, which provided a new method for gene therapy based on miR-34a.

In addition to being applied in cancer treatment, the application of smart nanomaterials in the treatment of other diseases has also received much attention. Li et al. constructed an antibacterial nanomaterial that combines photothermal effect and peroxidase like activity ZIF-8@PDA@PtNPs combines photothermal antibacterial and free radical antibacterial strategies to achieve efficient synergistic antibacterial activity (Li et al.). By *in-situ* polymerization, a polydopamine (PDA) layer with excellent photothermal effect was encapsulated on the surface of ZIF-8, and then platinum nanoparticles (PtNPs) with peroxidase like activity were grown on the PDA layer. The synergistic effect of the two produces efficient antibacterial activity: The obtained nano antibacterial agent not only efficiently catalyzes the generation of ROS from H_2O_2, causing damage to bacteria, but also converts the photon energy of near-infrared light into thermal energy to kill bacteria. Deng et al. have prepared a biological nanomaterial composed of Fibrinogen-Thrombin-Genipin, which can effectively repair defects in the annulus fibrosus (AF) of the scaffold in rats' model, providing a therapeutic alternative for repairing AF tears (Deng et al.). Xu et al. constructed a ternary nanoenzyme PtCuSe smart nanomaterial as a cascade catalyst for the treatment of Parkinson's disease (PD) (Xu et al.). This smart nanomaterial was used as a ROS scavenger both *in vitro* and *in*

vivo, effectively alleviating oxidative damage and inflammatory reactions in nerve cells, and significantly alleviating behavioral and pathological symptoms in PD mouse models.

The application of intelligent nanomaterials in biosensing and therapy is still of great concern. Therefore, in order to get the latest achievements in this field, the Research Topic will launch the third Research Topic, entitled "Smart Nanomaterials for Biosensing and Therapy Applications, Volume III", welcome to submit and share your latest research.

Author contributions

JL: Writing–original draft. MY: Writing–review and editing. ZX: Writing–review and editing. YZ: Writing–review and editing. ZW: Writing–review and editing. QH: Writing–review and editing.

Funding

The author(s) declare that no financial support was received for the research, authorship, and/or publication of this article.

Acknowledgments

We very much appreciate the contributions of all authors to this Research Topic and are grateful for the time and dedication of those who contributed to the peer review process.

Conflict of interest

The authors declare that the research was conducted in the absence of any commercial or financial relationships that could be construed as a potential conflict of interest.

Publisher's note

References

Arnold, M., Morgan, E., Rumgay, H., Mafra, A., Singh, D., Laversanne, M., et al. (2022). Current and future burden of breast cancer: global statistics for 2020 and 2040. *Breast* 66, 15–23. doi:10.1016/j.breast.2022.08.010

Chen, Z., Liao, T., Wan, L., Kuang, Y., Liu, C., Duan, J., et al. (2021a). Dual-stimuli responsive near-infrared emissive carbon dots/hollow mesoporous silica-based integrated theranostics platform for real-time visualized drug delivery. *Nano Research* 14 (11), 4264–4273. doi:10.1007/s12274-021-3624-4

Chen, M., Wang, Z., Zhang, Q., Wang, Z., Liu, W., Chen, M., et al. (2021b). Self-powered multifunctional sensing based on super-elastic fibers by soluble-core thermal drawing. *Nature Communications* 21 (1), 1416. doi:10.1038/s41467-021-21729-9

Chen, L., Huang, J., Li, X., Huang, M., Zeng, S., Zheng, J., et al. (2022). Progress of nanomaterials in photodynamic therapy against tumor. *Frontiers in Bioengineering and Biotechnology* 10, 920162. doi:10.3389/fbioe.2022.920162

He, C., Lin, X., Mei, Y., Luo, Y., Yang, M., Kuang, Y., et al. (2022). Recent advances in carbon dots for *in vitro*/Vivo fluorescent bioimaging: a mini-review. *Front. Chem.* 10, 905475. doi:10.3389/fchem.2022.905475

Huang, Q., Lin, X., Tong, L., and Tong, Q. -X. (2020). Graphene quantum dots/multiwalled carbon nanotubes composite-based electrochemical sensor for detecting dopamine release from living cells. *ACS Sustainable Chemistry & Engineering* 8 (3), 1644–1650. doi:10.1021/acssuschemeng.9b06623

Huang, Q., Lin, X., Chen, D., and Tong, Q. -X. (2022). Carbon Dots/α-Fe2O3-Fe3O4 nanocomposite: efficient synthesis and application as a novel electrochemical aptasensor for the ultrasensitive determination of aflatoxin B1. *Food Chemistry* 373, 131415. doi:10.1016/j.foodchem.2021.131415

Liao, C., Chen, X., Nachod, B. E., and Fu, Y. (2023). Salivary analysis: an emerging paradigm for non-invasive healthcare diagnosis and monitoring. *Interdisciplinary Medicine* 1 (3), e20230009. doi:10.1002/INMD.20230009

Liu, C., Lin, X., Liao, J., Yang, M., Jiang, M., Huang, Y., et al. (2024). Carbon dots-based dopamine sensors: recent advances and challenges. *Chinese Chemical Letters*. doi:10.1016/j.cclet.2024.109598

Luo, X., Liu, J., Sun, C., Zhang, F., Yu, W., Jiang, B., et al. (2023). Red-Emissive carbon dots combined with ferric ions for detection of total antioxidant capacity in food. *ACS Appl. Nano Mater.* 6 (15), 14332–14342. doi:10.1021/acsanm.3c02323

Mei, Y., He, C., Zeng, W., Luo, Y., Liu, C., Yang, M., et al. (2022a). Electrochemical biosensors for foodborne pathogens detection based on carbon nanomaterials: recent advances and challenges. *Food Bioprocess Technol.* 15 (3), 498–513. doi:10.1007/s11947-022-02759-7

Mei, Y., Lin, X., He, C., Zeng, W., Luo, Y., Liu, C., et al. (2022b). Recent progresses in electrochemical DNA biosensors for SARS-CoV-2 detection. *Front. Bioeng. Biotechnol.* 10, 952510. doi:10.3389/fbioe.2022.952510

Pourmadadi, M., Rahmani, E., Rajabzadeh-Khosroshahi, M., Samadi, A., Behzadmehr, R., Rahdar, A., et al. (2023). Properties and application of carbon quantum dots (CQDs) in biosensors for disease detection: a comprehensive review. *J. Drug Deliv. Sci. Technol.* 80, 104156. doi:10.1016/j.jddst.2023.104156

Song, Z., Zhao, L., Fang, W., Guo, S., Xu, A., Zhan, Z., et al. (2023). Glioma cell membrane camouflaged cinobufotalin delivery system for combinatorial orthotopic glioblastoma therapy. *Nano Res.* 16 (8), 11164–11175. doi:10.1007/s12274-023-5807-7

Thatte, A. S., Hamilton, A. G., Nachod, B. E., Mukalel, A. J., Billingsley, M. M., Palanki, R., et al. (2023). mRNA lipid nanoparticles for *ex vivo* engineering of immunosuppressive T cells for autoimmunity therapies. *Nano Lett.* 23 (22), 10179–10188. doi:10.1021/acs.nanolett.3c02573

Wang, Y., Qiao, W., Zhao, Z., Zhao, Z., and Li, M. (2023a). Preparation of two-dimensional porphyrin-based MOFs/derivatives and their potential in sensing and biomedical applications. *Interdisciplinary Medicine* 1 (3), e20230010. doi:10.1002/INMD.20230010

Wang, Y., Zhan, J., Huang, J., Wang, X., Chen, Z., Yang, Z., et al. (2023b). Dynamic responsiveness of self-assembling peptide-based nano-drug systems. *Interdisciplinary Medicine* 1 (1), e20220005. doi:10.1002/INMD.20220005

Yang, Y., Guan, S., Ou, Z., Li, W., Yan, L., Situ, B., et al. (2023). Advances in AI-based cancer cytopathology. *Interdisciplinary Medicine* 1 (3), e20230013. doi:10.1002/INMD.20230013

Yi, X., Zeng, W., Wang, C., Chen, Y., Zheng, L., Zhu, X., et al. (2022). A step-by-step multiple stimuli-responsive metal-phenolic network prodrug nanoparticles for chemotherapy. *Nano Research* 15 (2), 1205–1212. doi:10.1007/s12274-021-3626-2

Yuan, M., Chen, T., Jin, L., Zhang, P., Xie, L., Zhou, S., et al. (2023). A carrier-free supramolecular nano-twin-drug for overcoming irinotecan-resistance and enhancing efficacy against colorectal cancer. *Journal of Nanobiotechnology* 21 (1), 393. doi:10.1186/s12951-023-02157-x

Zhang, R., Zheng, Y., Liu, T., Tang, N., Mao, L., Lin, L., et al. (2022). The marriage of sealant agent between structure transformable silk fibroin and traditional Chinese medicine for faster skin repair. *Chinese Chemical Letters* 33 (3), 1599–1603. doi:10.1016/j.cclet.2021.09.018

Zheng, Y., Omar, R., Zhang, R., Tang, N., Khatib, M., Xu, Q., et al. (2022). A wearable microneedle-based extended gate transistor for real-time detection of Sodium in interstitial fluids. *Advanced Materials* 34 (10), 2108607. doi:10.1002/adma.202108607

Zhou, M., Wen, L., Wang, C., Lei, Q., Li, Y., and Yi, X. (2022). Recent advances in stimuli-sensitive amphiphilic polymer-paclitaxel prodrugs. *Frontiers in Bioengineering and Biotechnology* 10, 875034. doi:10.3389/fbioe.2022.875034

frontiers | Frontiers in Bioengineering and Biotechnology

TYPE Original Research
PUBLISHED 09 February 2023
DOI 10.3389/fbioe.2023.1139668

OPEN ACCESS

EDITED BY
Qitong Huang,
Gannan Medical University, China

REVIEWED BY
Guangxue Feng,
South China University of Technology, China
Xiaofeng Lin,
Gannan Medical University, China

*CORRESPONDENCE
Kongkai Zhu,
hkhhh.k@163.com
Leilei Shi,
shillei@mail.sysu.edu.cn
Xuemei Fu,
fxmzj2004@163.com

†These authors share first authorship

SPECIALTY SECTION
This article was submitted to Nanobiotechnology, a section of the journal Frontiers in Bioengineering and Biotechnology

RECEIVED 07 January 2023
ACCEPTED 20 January 2023
PUBLISHED 09 February 2023

CITATION
Chen J, Li D, Li H, Zhu K, Shi L and Fu X (2023), Cell membrane-targeting NIR fluorescent probes with large Stokes shifts for ultralong-term transplanted neural stem cell tracking.
Front. Bioeng. Biotechnol. 11:1139668.
doi: 10.3389/fbioe.2023.1139668

Cell membrane-targeting NIR fluorescent probes with large Stokes shifts for ultralong-term transplanted neural stem cell tracking

Jing Chen[1†], Dan Li[1†], Hongfu Li[1], Kongkai Zhu[2*], Leilei Shi[1*] and Xuemei Fu[1*]

[1]The Eighth Affiliated Hospital, Sun Yat-sen University, Shenzhen, China, [2]Advanced Medical Research Institute, Shandong University, Jinan, China

There is an emerging therapeutic strategy to transplant stem cells into diseased host tissue for various neurodegenerative diseases, owing to their self-renewal ability and pluripotency. However, the traceability of long-term transplanted cells limits the further understanding of the mechanism of the therapy. Herein, we designed and synthesized a quinoxalinone scaffold-based near-infrared (NIR) fluorescent probe named QSN, which exhibits ultra-strong photostability, large Stokes shift, and cell membrane-targeting capacity. It could be found that QSN-labeled human embryonic stem cells showed strong fluorescent emission and photostability both *in vitro* and *in vivo*. Additionally, QSN would not impair the pluripotency of embryonic stem cells, indicating that QSN did not perform cytotoxicity. Moreover, it is worth mentioning that QSN-labeled human neural stem cells held cellular retention for at least 6 weeks in the mouse brain striatum post transplantation. All these findings highlight the potential application of QSN for ultralong-term transplanted cell tracking.

KEYWORDS

NIR fluorescent probe, cell membrane-targeting, large Stokes shift, ultra-strong photostability, ultralong-term tracing

Introduction

Human stem cells are excellent sources of cell therapy due to their self-renewal ability and pluripotency (Cossu et al., 2018; Yamanaka, 2020). Therefore, the transplantation of human neural stem cells (hNSCs) brought hope for the treatment of central nervous system (CNS) diseases such as spinal cord injury, ischemic stroke, and amyotrophic lateral sclerosis (Curtis et al., 2018; Yang H. et al., 2022; Baloh et al., 2022). The ways in which hNSCs exert their therapeutic effects are mainly through proliferation, differentiation, homing, etc. (Koch et al., 2009; Zheng et al., 2017; Hayashi et al., 2020; Pluchino et al., 2020). However, due to the lengthy self-repair process of hNSCs, the detailed therapeutic mechanism of hNSCs is still unclear. It was thought that long-term and real-time tracking of transplanted hNSCs is the first step to studying the mechanism of stem cell therapy (Zhang et al., 2016; Ceto et al., 2020). Hence, developing effective tracking tools for long-term and real-time monitoring of the differentiation process of transplanted hNSCs could help us learn more about the therapeutic mechanism of stem cells.

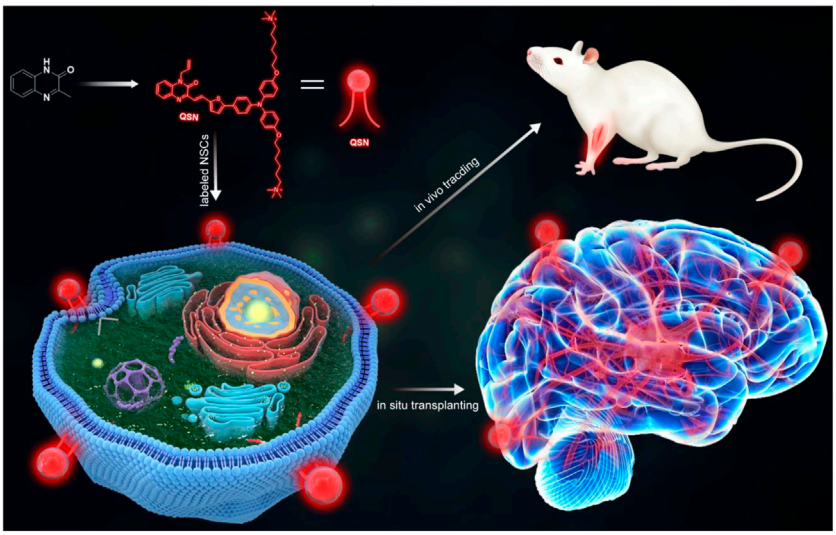

SCHEME 1
Scheme of the design and synthesis of QSN. QSN could be located in the neural stem cell membrane. Then, this membrane-targeting probe could be used for tracking the transplanted neural stem cells and ultralong-term *in vivo* imaging.

Currently, since optical imaging could perform high space-time resolution, fluorescent probe-based bioimaging has become the most popular real-time biological process imaging technique, which provides varied information for biological research (Li et al., 2013; Jeong et al., 2018; Zhao et al., 2018; Yang et al., 2020; Fang et al., 2021; Ghanim et al., 2021). Recently, there are some reports about smart nanomaterials which are applied in biosensing and therapy (Yi et al., 2022; Zheng et al., 2022; Zhu et al., 2022). Conventional fluorescent probes in the visible region always suffer from tissue scattering, autofluorescence, etc., resulting in low tissue penetration depth and spatial resolution. Compared with those probes in the visible region, the near-infrared (NIR) window (wavelength > 700 nm) could provide deeper tissue optical imaging, which could overcome these aforementioned issues (Hong et al., 2017; Chen et al., 2018; Huang et al., 2020; Lu et al., 2020). However, the weak photostability and resistance to photobleaching of small-molecule NIR fluorescent probes limit their long-term tracking ability *in vivo* (Zhang et al., 2012; Gong et al., 2016; Yang and Chen, 2020; Borlan et al., 2021). Therefore, developing near-infrared fluorescent probes with strong fluorescence emission intensity, good photostability, and resistance to photobleaching would be a potential method for the long-term tracking of stem cells *in vivo*.

The critical issue in designing an ideal NIR probe for long-term *in vivo* tracking of stem cells was the screening for a suitable chromophore scaffold. The quinoxalinone (or quinoxalin-2-one) core, characterized by pyrazin-2(1H)-one fused to the benzene ring at two adjacent carbon atoms, could exhibit strong blue light emission and photostability. Based on this scaffold, we have successfully designed a series of probes for autophagy detection, ferroptosis identification, and Parkinson's disease diagnosis (Shi et al., 2018; Zhang et al., 2020; Yang J. et al., 2022). Based on our previous work, a stem cell membrane-targeting NIR fluorescent probe with strong fluorescence emission, good photostability, and photobleaching resistance was designed for real-time and long-term tracking of stem cell differentiation *in vivo* (Scheme 1). In contrast to traditional fluorescent proteins, fluorescent probes could avoid the side effects of gene editing tools and could not induce genomic perturbations in stem cells (Tennstaedt et al., 2015; Anzalone et al., 2020; Alvarez et al., 2022).

Results and discussion

Design of QSN

First, the high-performance fluorescent probe QSN was designed and synthesized using a quinoxalinone scaffold as the core chromophore (Supplementary Scheme S1). To obtain red-to-NIR emission, good electron donors including thiophene and triphenylamine were conjugated to the quinoxalinone scaffold by which the emission of a conjugated molecular probe is expected to be greatly bathchromically shifted to the NIR region. In detail, thiophene was first covalently linked to the quinoxalinone scaffold by aldol condensation and then conjugated to triphenylamine through Suzuki–Miyaura coupling. To achieve membrane-targeting capacity, two cationic groups were further decorated on the quinoxalinone scaffold to yield QSN. The final product, QSN, was obtained with a yield of 29%, which was characterized by 1H-NMR, 13C-NMR, and mass spectra (Supplementary Figures S1, S2).

Chemistry and photophysical properties

After synthesis, the optical properties of QSN were characterized. The absorption and emission spectra of QSN in dimethyl sulfoxide/water (DMSO/H2O) = 1/99 (v/v) were measured with peaks centered at 490 and 670 nm, respectively (Figures 1A, B). The large Stokes shift (typically over 80 nm) of QSN can minimize the cross talk between the excitation source and fluorescence emission, providing us with a high signal-to-noise ratio during bioimaging. In contrast to conventional fluorescent dyes with fluorescence of aggregation caused by quenching features, aggregation-induced emission (AIE) fluorophores exhibit

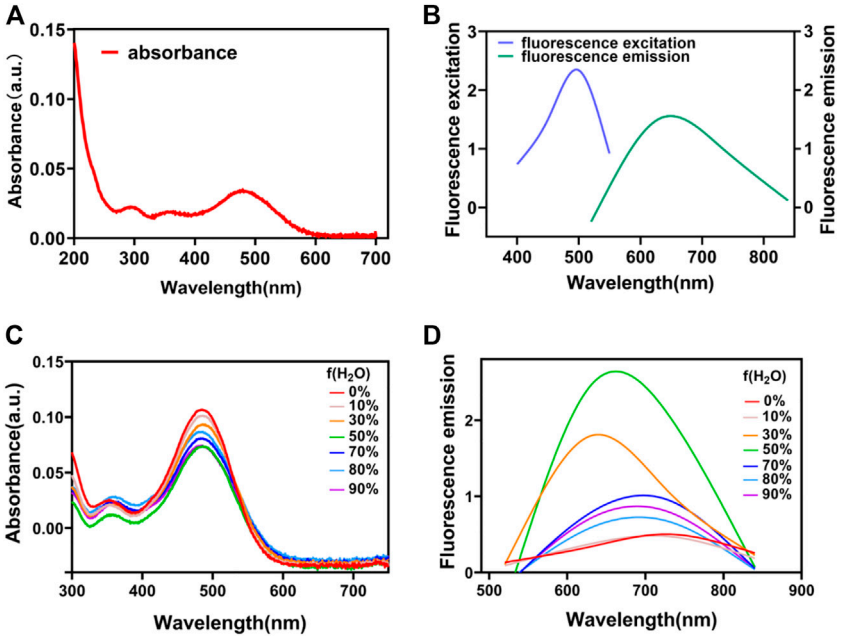

FIGURE 1
UV–vis absorption **(A)** and fluorescence spectra **(B)** of QSN. UV–vis absorption **(C)** and fluorescence spectra **(D)** of QSN in the mixed solvent with various DMSO/H_2O ratios.

bright fluorescence in the aggregated state but very weak fluorescence in a good solvent, making them an ideal "turn-on" fluorescent probe for bioanalysis. Herein, the AIE property of QSN was measured with different ratios of DMSO/H_2O mixtures. When the water content was increased, both the absorption and emission intensity of QSN were greatly increased upon aggregation formation (Figures 1C, D). Notably, the emission wavelength of QSN performed a significantly bathochromic shift from 670 to 700 nm with the increase in the water ratio (Figure 1D). In addition, the simulation result indicated that the distribution of LUMO was mainly located on the terminal triphenylamine, whereas the electron densities of LUMO and HOMO were separated, resulting in a low ΔEst value (0.1022 eV) (Supplementary Figure S3). All these phenomena indicated that QSN exhibited in an AIE-active manner with strong NIR emission in an aqueous solution, indicating that QSN could be a potential tracking tool for monitoring biological processes.

Cell viability study

With the satisfactory photophysical property of QSN in hand, the potential cytotoxicity of QSN was first evaluated using cell counting kit-8 (CCK-8). The human embryonic cell line H7 was treated with QSN at various concentrations and incubated for 24 h. It could be found that H7 viability still remained at a high value (≈89%) even after incubating with QSN at a concentration of up to 100 μM for 24 h, which means that QSN did not exhibit obvious cytotoxicity (Supplementary Figure S4A). In addition, QSN also exhibited a low cytotoxicity capacity for H7-derived NSCs (H7NSCs). These results showed that H7NSCs could maintain high cell viability up to 90% even after 15 min of incubation with 300 μM QSN (Supplementary Figure S4B). All these outcomes brought a good signal for the further biological research and application of QSN, owing to its high biocompatibility.

Cellular uptake and confocal imaging study

Then, in order to identify where QSN binds to the cells, confocal imaging-based colocalization experiments were conducted by co-staining the cells with both QSN and other organelle trackers. First, the localization of QSN in cells was investigated by co-staining with DiO, a cell membrane fluorescent probe. H7 cells were incubated with QSN (50 μM) for 15 min, followed by DiO (1:1000) for another 30 min. The red fluorescence of QSN almost completely targeted that of the DiO (green), revealing the excellent cell membrane-targeting capacity of QSN. In addition, H7 cells were incubated with QSN and other different organelle trackers such as Mito and Tublin, providing fluorescent staining of ER, lysosome, and Golgi apparatus, which were added and incubated for further 30 min or 1 h. On the contrary, QSN could barely target the other organelle trackers except the plasma membrane, indicating that QSN has a highly specific cytomembrane-dyeing ability (Figure 2). Additionally, QSN showed the same cytomembrane-staining capacity for H7NSCs as well (Supplementary Figure S5B). These results corroborated our hypothesis that QSN could perform as an excellent cell membrane-targeting fluorescent probe for bioimaging.

In vitro photostability study

Hence, for further confirming the potential of QSN to be applied as a stable imaging agent, a study on photostability of QSN was conducted by comparing the cytomembrane staining of H7 using QSN

10.3389/fbioe.2023.1139668

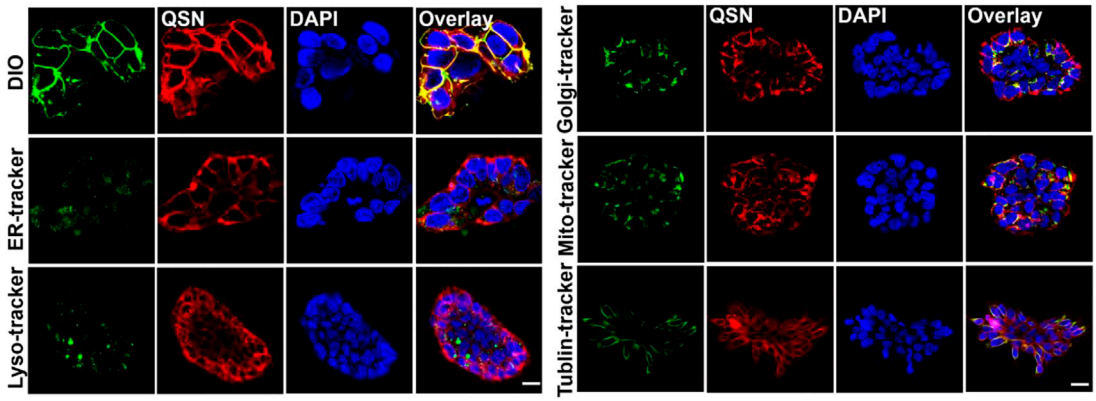

FIGURE 2
Confocal imaging of human embryonic stem cells-7 (H7) co-stained with QSN (50 μM), DiO, ER-Tracker, lysosome tracker, Golgi-Tracker, MitoTracker, and Tublin Tracker. Cells were incubated with QSN for 15 min, and different organelle trackers were added and incubated for an additional 30 min to 1 h. DIO, ER-Tracker, and MitoTracker were incubated with cells for 30 min. Lysosome tracker, Golgi-Tracker, and Tublin Tracker were incubated with cells for 1 h according to the protocols. Scale bar: 20 μm. All experiments were carried out three times independently.

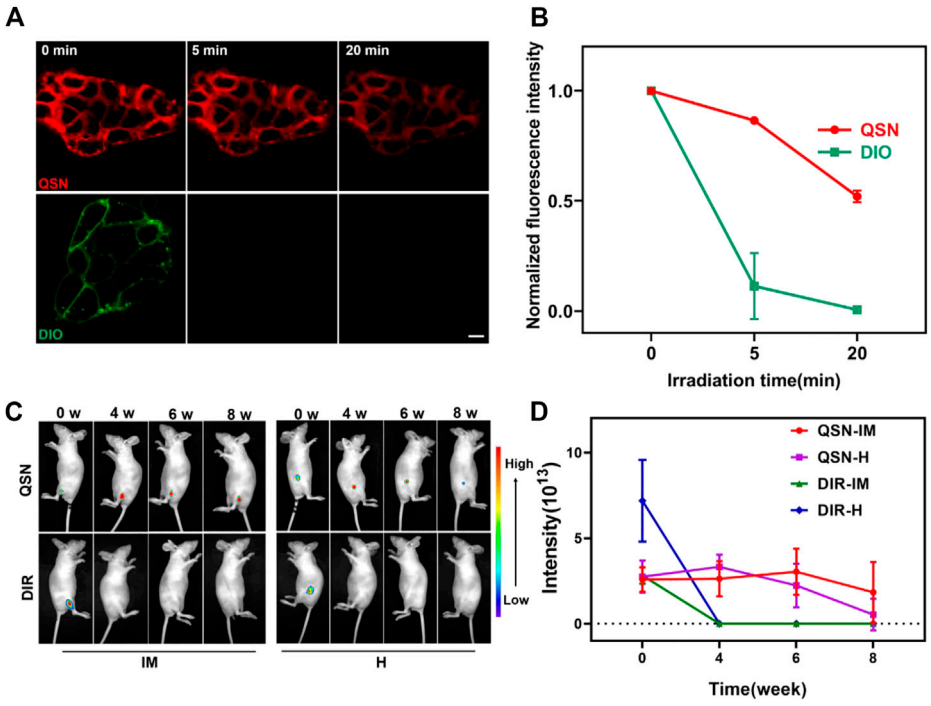

FIGURE 3
(A,B) Comparison of photostability of QSN (upper) and DiO (below) when incubating the samples with H7 and exposing to laser irradiation for 20 min, respectively. Scale bar: 10 μm. **(C,D)** Long-term *in vivo* imaging of time-dependent whole-body imaging of H7NSC-bearing nude mice (n = 3) after treatment with QSN (300 μM) and DiR (1:2500) *via* intramuscular (IM) injection and hypodermic (H) injection.

(upper) and commercially available DiO (bottom) *via* persistent laser irradiation for 20 min. The fluorescence intensity of DiO swiftly decreased and became inconsiderable after 5 min of irradiation because of photobleaching (Figures 3A, B). For the QSN probe, strong fluorescence signals could be observed with no distinct signal decay even after 20 min of irradiation. This result demonstrated that QSN exhibited superior photobleaching resistance, indicating its great potential in bioimaging applications.

Teratoma formation study

The pluripotency of hESCs makes them an important source in regenerative medicine. Teratoma formation assay is the gold standard for *in vivo* assessment of pluripotency of hESCs. To determine whether labeling with QSN affects the pluripotency of H7, we compared the capability of QSN-labeled H7 to form teratomas with H7-wild type (H7-WT). QSN-labeled H7 cells were implanted subcutaneously into

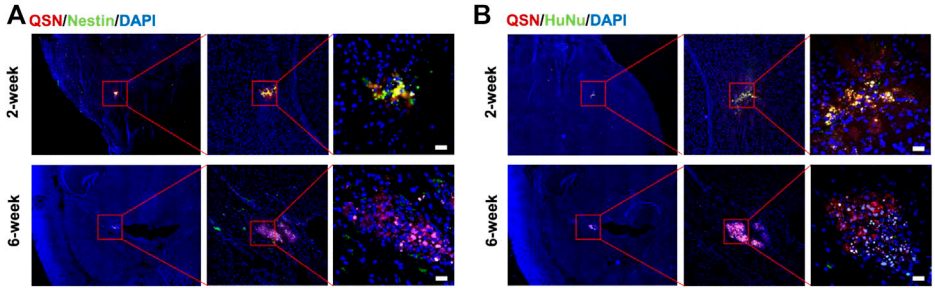

FIGURE 4
Transplantation of QSN-labeled H7NSCs in the mouse brain. QSN-labeled H7NSCs in the mouse brain at 2 and 6 weeks post transplantation were co-stained with **(A)** Nestin, a typical marker of human neuronal stem cells, **(B)** human nuclear marker, and DAPI. Scale bar: 20 μm.

the right flank of non-obese diabetic/ShiLtJGpt-Prkdcem26Cd52Il2rgem26Cd22/Gpt (NCG) mice. As a positive control, the H7-WT was implanted into the left flank of the same NCG mice. We found that QSN-labeled H7 could form teratomas that contain cells derived from each of the three germ layers as same as H7-WT, 6 weeks after transplantation (Supplementary Figure S6), demonstrating that labeling with QSN would not impair the pluripotency of hESCs. In other words, QSN could be used for tracing stem cells without affecting the differentiation potential of stem cells.

In vivo imaging study

As mentioned previously, the therapeutic mechanisms of hNSCs transplanted for the treatment of CNS diseases remain unclear. Owing to the superior photostability and photobleaching resistance of QSN *in vitro*, we suspected that it will be suitable for long-term *in vivo* tracing, which may be conducive to studying the therapeutic mechanism of hNSC transplantation. For confirming this conjecture, first, we labeled H7NSCs with QSN. H7NSCs were incubated with QSN (300 μM) and commercially available DiR dye (1:2500) individually for 15 min at 37°C (labeled as 0 week). Then, the treated cells were transplanted into the nude mice ($n = 3$ per group) *via* intramuscular (IM) injection and hypodermic (H) injection, respectively. After that, the *in vivo* imaging system was used for monitoring fluorescence intensity every 2 weeks. As shown in Figures 3C, D and Supplementary Figure S7A, the fluorescence signal of subcutaneous QSN could still be detected 10 weeks later. Amazingly, the signal is retained in the muscle for even up to 12 weeks. However, the commercially available DiR-dyed fluorescence signals became negligible at the second week and vanished after 4 weeks. In summary, compared with the commercial dye, QSN also showed a longer tracing capability *in vivo*. This capability makes ultralong-term *in vivo* tracing possible.

In situ transplantation study

Considering that the transplantation of hNSCs is usually administered *in situ*, we next investigated the tracing capability of QSN in the brain. At first, we labeled H7NSCs with QSN and DiR, respectively, as previously described. Subsequently, the labeled H7NSCs were transplanted into the null mice brain striatum. At 2 weeks and 6 weeks post transplantation, mice were sacrificed for immunostaining analysis. At respective time points, mice transplanted with DiR-labeled H7NSCs were used as controls. After 2 weeks, grafts were observed with the strong QSN signal when co-stained with the human-specific Nestin antibody and human nuclear antibody, respectively, while fluorescent signals of DiR were almost undetectable (Figure 4; Supplementary Figure S8). Surprisingly, the fluorescence emitted by QSN can even be detected at 6 weeks (Figure 4). This is consistent with our previous results obtained by the *in vivo* imaging system, certifying that QSN exhibited outstanding photostability and endurance to photobleaching compared to commercially available dyes not only *in vitro* but also *in vivo*, suggesting the considerable scope of QSN for *in vivo* ultralong-term tracking of biological processes.

In vivo biochemical analysis study

To determine whether QSN could be a potential probe for further clinical development, biosafety would be a key issue. First, it could be noticed that the body weight of mice did not change significantly after the administration of QSN (Supplementary Figure S7B). Next, we compared H&E staining of organs with QSN-labeled H7NSCs transplanted into null mice with that of normal null mice. We found that QSN-labeled H7NSCs posed nearly no impact on the organs (Supplementary Figure S9). In addition, we performed blood biochemistry analysis to evaluate the liver and kidney function of mice. Among the three groups, there was no significant difference in the levels of alanine transaminase (ALT), aspartate transaminase (AST), albumin (ALB), serum creatinine (Scr), and blood urea nitrogen (BUN) (Supplementary Figure S10). These results indicate that QSN-labeled H7NSCs are biocompatible *in vivo*, thus representing a safe fluorescent probe for *in vivo* application.

Conclusion

In summary, we developed a quinoxalinone-based cell membrane-targeting fluorescent probe with an AIE-active property, strong NIR emission, high photostability, and large Stokes shifts. Additionally, QSN exhibited negligible cellular and systematic toxicity both *in vitro* and *in vivo*. Furthermore, QSN could efficiently label the stem cells

with strong fluorescence emission and photobleaching resistance. Given these excellent characteristics, we trust that QSN could be applied to track biological processes in a long-term fashion. Indeed, it was verified that QSN-labeled stem cells held cellular retention for at least 6 weeks in the mouse brain striatum post transplantation. All these findings demonstrated that QSN would be a potential tool for providing us with a methodology to track the *in vivo* biological process and helping us study the mechanism of *in vivo* stem cell therapy.

Data availability statement

The original contributions presented in the study are included in the article/Supplementary Material; further inquiries can be directed to the corresponding authors.

Ethics statement

The animal study was reviewed and approved by the Animal Ethics Committee of The Eighth Affiliated Hospital, Sun Yat-sen University.

Author contributions

KZ, LS, and XF supervised and supported this project. LS, JC, and DL conceived this project. JC, DL, and HL performed the experiments. LS, JC, DL, and HL analyzed the data. LS, JC, DL, and HL wrote the manuscript. KZ, LS, and XF contributed to revision. All authors discussed and commented on the manuscript.

Acknowledgments

The authors would like to thank the National Natural Science Foundation of China (22105229, 81803438, and 81871197), the Key Program of the National Natural Science Foundation of China (91959204), and the Excellent Technology Innovation Cultivation Program of Shenzhen (RCBS20210609104441067). Experiment protocols involving animals were authorized by the Animal Ethics Committee of The Eighth Affiliated Hospital, Sun Yat-sen University (approval number: A2020-030-01).

Conflict of interest

The authors declare that the research was conducted in the absence of any commercial or financial relationships that could be construed as a potential conflict of interest.

Publisher's note

Supplementary material

The Supplementary Material for this article can be found online at: https://www.frontiersin.org/articles/10.3389/fbioe.2023.1139668/full#supplementary-material

References

Alvarez, M. M., Biayna, J., and Supek, F. (2022). TP53-dependent toxicity of CRISPR/Cas9 cuts is differential across genomic loci and can confound genetic screening. *Nat. Commun.* 13 (1), 4520. doi:10.1038/s41467-022-32285-1

Anzalone, A. V., Koblan, L. W., and Liu, D. R. (2020). Genome editing with CRISPR-Cas nucleases, base editors, transposases and prime editors. *Nat. Biotechnol.* 38 (7), 824–844. doi:10.1038/s41587-020-0561-9

Baloh, R. H., Johnson, J. P., Avalos, P., Allred, P., Svendsen, S., Gowing, G., et al. (2022). Transplantation of human neural progenitor cells secreting GDNF into the spinal cord of patients with ALS: A phase 1/2a trial. *Nat. Med.* 28 (9), 1813–1822. doi:10.1038/s41591-022-01956-3

Borlan, R., Focsan, M., Maniu, D., and Astilean, S. (2021). Interventional NIR fluorescence imaging of cancer: Review on next generation of dye-loaded protein-based nanoparticles for real-time feedback during cancer surgery. *Int. J. Nanomedicine* 16, 2147–2171. doi:10.2147/IJN.S295234

Ceto, S., Sekiguchi, K. J., Takashima, Y., Nimmerjahn, A., and Tuszynski, M. H. (2020). Neural stem cell grafts form extensive synaptic networks that integrate with host circuits after spinal cord injury. *Cell Stem Cell* 27 (3), 430–440.e5. doi:10.1016/j.stem.2020.07.007

Chen, G., Zhang, Y., Li, C., Huang, D., Wang, Q., and Wang, Q. (2018). Recent advances in tracking the transplanted stem cells using near-infrared fluorescent nanoprobes: Turning from the first to the second near-infrared window. *Adv. Healthc. Mater* 7 (20), e1800497. doi:10.1002/adhm.201800497

Cossu, G., Birchall, M., Brown, T., De Coppi, P., Culme-Seymour, E., Gibbon, S., et al. (2018). Lancet Commission: Stem cells and regenerative medicine. *Lancet* 391 (10123), 883–910. doi:10.1016/s0140-6736(17)31366-1

Curtis, E., Martin, J. R., Gabel, B., Sidhu, N., Rzesiewicz, T. K., Mandeville, R., et al. (2018). A first-in-human, phase I study of neural stem cell transplantation for chronic spinal cord injury. *Cell Stem Cell* 22 (6), 941–950.e6. doi:10.1016/j.stem.2018.05.014

Fang, H., Geng, S., Hao, M., Chen, Q., Liu, M., Liu, C., et al. (2021). Simultaneous Zn(2+) tracking in multiple organelles using super-resolution morphology-correlated organelle identification in living cells. *Nat. Commun.* 12 (1), 109. doi:10.1038/s41467-020-20309-7

Ghanim, M., Relitti, N., McManus, G., Butini, S., Cappelli, A., Campiani, G., et al. (2021). A non-toxic, reversibly released imaging probe for oral cancer that is derived from natural compounds. *Sci. Rep.* 11 (1), 14069. doi:10.1038/s41598-021-93408-0

Gong, Y. J., Zhang, X. B., Mao, G. J., Su, L., Meng, H. M., Tan, W., et al. (2016). A unique approach toward near-infrared fluorescent probes for bioimaging with remarkably enhanced contrast. *Chem. Sci.* 7 (3), 2275–2285. doi:10.1039/c5sc04014k

Hayashi, Y., Lin, H. T., Lee, C. C., and Tsai, K. J. (2020). Effects of neural stem cell transplantation in Alzheimer's disease models. *J. Biomed. Sci.* 27 (1), 29. doi:10.1186/s12929-020-0622-x

Hong, G., Antaris, A. L., and Dai, H. (2017). Near-infrared fluorophores for biomedical imaging. *Nat. Biomed. Eng.* 1 (1), 0010. doi:10.1038/s41551-016-0010

Huang, L. Y., Zhu, S., Cui, R., and Zhang, M. (2020). Noninvasive *in vivo* imaging in the second near-infrared window by inorganic nanoparticle-based fluorescent probes. *Anal. Chem.* 92 (1), 535–542. doi:10.1021/acs.analchem.9b04156

Jeong, E. M., Yoon, J. H., Lim, J., Shin, J. W., Cho, A. Y., Heo, J., et al. (2018). Real-time monitoring of glutathione in living cells reveals that high glutathione levels are required to maintain stem cell function. *Stem Cell Rep.* 10 (2), 600–614. doi:10.1016/j.stemcr.2017.12.007

Koch, P., Kokaia, Z., Lindvall, O., and Brüstle, O. (2009). Emerging concepts in neural stem cell research: Autologous repair and cell-based disease modelling. *Lancet Neurology* 8 (9), 819–829. doi:10.1016/s1474-4422(09)70202-9

Li, K., Qin, W., Ding, D., Tomczak, N., Geng, J., Liu, R., et al. (2013). Photostable fluorescent organic dots with aggregation-induced emission (AIE dots) for noninvasive long-term cell tracing. *Sci. Rep.* 3, 1150. doi:10.1038/srep01150

Lu, L., Li, B., Ding, S., Fan, Y., Wang, S., Sun, C., et al. (2020). NIR-II bioluminescence for *in vivo* high contrast imaging and *in situ* ATP-mediated metastases tracing. *Nat. Commun.* 11 (1), 4192. doi:10.1038/s41467-020-18051-1

Pluchino, S., Smith, J. A., and Peruzzotti-Jametti, L. (2020). Promises and limitations of neural stem cell therapies for progressive multiple sclerosis. *Trends Mol. Med.* 26 (10), 898–912. doi:10.1016/j.molmed.2020.04.005

Shi, L., Gao, X., Yuan, W., Xu, L., Deng, H., Wu, C., et al. (2018). Endoplasmic reticulum-targeted fluorescent nanodot with large Stokes shift for vesicular transport monitoring and long-term bioimaging. *Small* 14 (25), e1800223. doi:10.1002/smll.201800223

Tennstaedt, A., Aswendt, M., Adamczak, J., Collienne, U., Selt, M., Schneider, G., et al. (2015). Human neural stem cell intracerebral grafts show spontaneous early neuronal differentiation after several weeks. *Biomaterials* 44, 143–154. doi:10.1016/j.biomaterials.2014.12.038

Yamanaka, S. (2020). Pluripotent stem cell-based cell therapy-promise and challenges. *Cell Stem Cell* 27 (4), 523–531. doi:10.1016/j.stem.2020.09.014

Yang H, H., Han, M., Li, J., Ke, H., Kong, Y., Wang, W., et al. (2022). Delivery of miRNAs through metal-organic framework nanoparticles for assisting neural stem cell therapy for ischemic stroke. *ACS Nano* 16, 14503–14516. doi:10.1021/acsnano.2c04886

Yang J, J., Wang, L., Su, Y., Shen, L., Gao, X., Shi, L., et al. (2022). Color-convertible fluorescent nanoprobe for Parkinson's disease diagnosis. *Chem. Eng. J.* 429, 132368. doi:10.1016/j.cej.2021.132368

Yang, J., Yin, W., Van, R., Yin, K., Wang, P., Zheng, C., et al. (2020). Turn-on chemiluminescence probes and dual-amplification of signal for detection of amyloid beta species *in vivo*. *Nat. Commun.* 11 (1), 4052. doi:10.1038/s41467-020-17783-4

Yang, W., and Chen, S.-L. (2020). Time-gated fluorescence imaging: Advances in technology and biological applications. *J. Innovative Opt. Health Sci.* 13 (03). doi:10.1142/s1793545820300062

Yi, X., Zeng, W., Wang, C., Chen, Y., Zheng, L., Zhu, X., et al. (2022). A step-by-step multiple stimuli-responsive metal-phenolic network prodrug nanoparticles for chemotherapy. *Nano Res.* 15 (2), 1205–1212. doi:10.1007/s12274-021-3626-2

Zhang, P., Kuang, H., Xu, Y., Shi, L., Cao, W., Zhu, K., et al. (2020). Rational design of a high-performance quinoxalinone-based AIE photosensitizer for image-guided photodynamic therapy. *ACS Appl. Mater Interfaces* 12 (38), 42551–42557. doi:10.1021/acsami.0c12670

Zhang, R., Li, Y., Hu, B., Lu, Z., Zhang, J., and Zhang, X. (2016). Traceable nanoparticle delivery of small interfering RNA and retinoic acid with temporally release ability to control neural stem cell differentiation for alzheimer's disease therapy. *Adv. Mater* 28 (30), 6345–6352. doi:10.1002/adma.201600554

Zhang, X., Bloch, S., Akers, W., and Achilefu, S. (2012). Near-infrared molecular probes for *in vivo* imaging. *Curr. Protoc. Cytom.* Chapter 12Unit12 27. doi:10.1002/0471142956.cy1227s60

Zhao, J., Zhong, D., and Zhou, S. (2018). NIR-I-to-NIR-II fluorescent nanomaterials for biomedical imaging and cancer therapy. *J. Mater Chem. B* 6 (3), 349–365. doi:10.1039/c7tb02573d

Zheng, J., Yue, R., Yang, R., Wu, Q., Wu, Y., Huang, M., et al. (2022). Visualization of zika virus infection via a light-initiated bio-orthogonal cycloaddition labeling strategy. *Front. Bioeng. Biotechnol.* 10, 940511. doi:10.3389/fbioe.2022.940511

Zheng, Y., Huang, J., Zhu, T., Li, R., Wang, Z., Ma, F., et al. (2017). Stem cell tracking technologies for neurological regenerative medicine purposes. *Stem Cells Int.* 2017, 1–9. doi:10.1155/2017/2934149

Zhu, J., Chu, C., Li, D., Zhang, Y., Cheng, Y., Lin, H., et al. (2022). Superior fluorescent nanoemulsion illuminates hepatocellular carcinoma for surgical navigation. *Front. Bioeng. Biotechnol.* 10, 890668. doi:10.3389/fbioe.2022.890668

frontiers | Frontiers in Bioengineering and Biotechnology

TYPE Original Research
PUBLISHED 10 February 2023
DOI 10.3389/fbioe.2023.1137199

OPEN ACCESS

EDITED BY
Qitong Huang,
Gannan Medical University, China

REVIEWED BY
Bailong Tao,
The First Affiliated Hospital of Chongqing Medical University, China
Yong Xu,
Technical University Dresden, Germany

*CORRESPONDENCE
Ran Kang,
kangran@njucm.edu.cn
Xin Liu,
liuxin@njucm.edu.cn
Lin Xie,
xielin@njucm.edu.cn

SPECIALTY SECTION
This article was submitted to Tissue Engineering and Regenerative Medicine, a section of the journal Frontiers in Bioengineering and Biotechnology

RECEIVED 05 January 2023
ACCEPTED 26 January 2023
PUBLISHED 10 February 2023

CITATION
Deng R, Kang R, Jin X, Wang Z, Liu X, Wang Q and Xie L (2023), Mechanical stimulation promotes MSCs healing the lesion of intervertebral disc annulus fibrosus.
Front. Bioeng. Biotechnol. 11:1137199.
doi: 10.3389/fbioe.2023.1137199

Mechanical stimulation promotes MSCs healing the lesion of intervertebral disc annulus fibrosus

Rongrong Deng[1], Ran Kang[1,2]*, Xiaoyu Jin[1,3], Zihan Wang[1], Xin Liu[1]*, Qing Wang[4] and Lin Xie[1]*

[1]Third School of Clinical Medicine, Nanjing University of Chinese Medicine, Nanjing, Jiangsu, China, [2]Department of Orthopedics, Nanjing Lishui Hospital of Traditional Chinese Medicine, Nanjing, Jiangsu, China, [3]Department of Sports Medicine and Adult Reconstructive Surgery, Nanjing Drum Tower Hospital, Nanjing, Jiangsu, China, [4]School of Nursing, Nanjing University of Chinese Medicine, Nanjing, Jiangsu, China

Mesenchymal stem cells (MSCs) and scaffolds offer promising perspectives for annulus fibrosus (AF) repair. The repair effect was linked to features of the local mechanical environment related to the differentiation of MSCs. In this study, we established a Fibrinogen-Thrombin-Genipin (Fib-T-G) gel which is sticky and could transfer strain force from AF tissue to the human mesenchymal stem cells (hMSCs) embedded in the gel. After the Fib-T-G biological gel was injected into the AF fissures, the histology scores of intervertebral disc (IVD) and AF tissue showed that Fib-T-G gel could better repair the AF fissure in caudal IVD of rats, and increase the expression of AF-related proteins including Collagen 1 (COL1), Collagen 2 (COL2) as well as mechanotransduction-related proteins including RhoA and ROCK1. To clarify the mechanism that sticky Fib-T-G gel induces the healing of AF fissures and the differentiation of hMSCs, we further investigated the differentiation of hMSCs under mechanical strain *in vitro*. It was demonstrated that both AF-specific genes, including Mohawk and SOX-9, and ECM markers (COL1, COL2, aggrecan) of hMSCs were up-regulated in the environment of strain force. Moreover, RhoA/ROCK1 proteins were also found to be significantly up-regulated. In addition, we further -demonstrated that the fibrochondroinductive effect of the mechanical microenvironment process could be significantly blocked or up-regulated by inhibiting the RhoA/ROCK1 pathway or overexpressing RhoA in MSCs, respectively. Summarily, this study will provide a therapeutic alternative to repair AF tears and provide evidence that RhoA/ROCK1 is vital for hMSCs response to mechanical strain and AF-like differentiation.

KEYWORDS

mesenchymal stem cells, gel scaffold, intervertebral disc annulus fibrosus, mechanical stimulation, RhoA/Rock1 pathway

1 Introduction

Mechanical strain stimulates the development and remodeling of the intervertebral disc (IVD) from mesodermal cells during human body growth and development (Sivakamasundari and Lufkin, 2012; Colombier et al., 2014; Duclos and Michalek, 2017). IVD is structured by the surrounding highly oriented collagenous annulus fibrosus (AF), the central gelatinous nucleus pulposus, and the craniocaudal endplate (Marchand and Ahmed, 1990; Chan et al., 2011b). The integrity of IVD is secured the spine stability to withstand a load of tensile, compression, and shear in our daily life (Schmidt et al., 2007; Chan et al., 2011a). However, disc lesion occurs inevitably along with aging, load fatigue, trauma, etc. (Battié et al., 2007; Wang et al., 2016), resulting in painful disc herniation, reherniation, and degeneration. Repair is necessary,

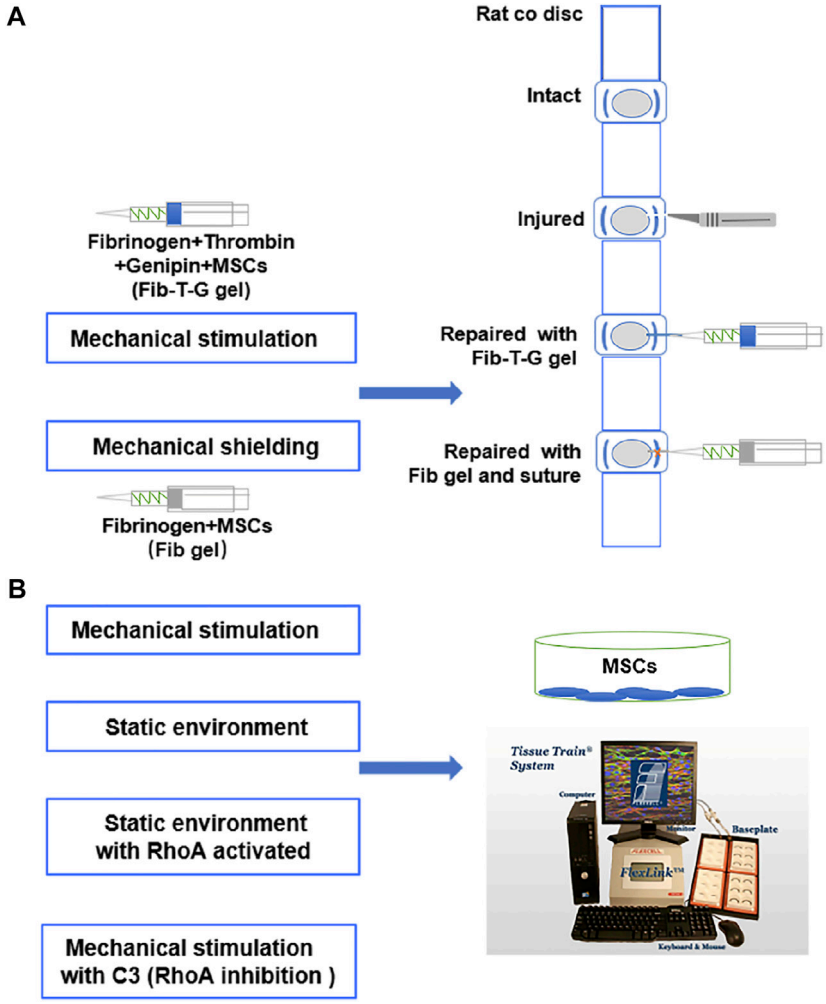

FIGURE 1
(A) Schematic diagram of rat annulus fibrosus injury repair by injectable Fibrinogen-Thrombin-Genipin (Fib-T-G) gel mixed MSCs. **(B)** Schematic diagram of the intrinsic molecular mechanism of MSCs differentiation into annulus fibrosus *in vitro* mechanical stimulation environment.

especially for AF, because anatomically the outer AF holds the central nucleus material and prevents disc herniation and degeneration (Holzapfel et al., 2004).

Suturing, anchoring (Sharifi et al., 2015), and tissue engineering (Bron et al., 2008; Kang et al., 2018) (Chu et al., 2018b; Shamsah et al., 2020)are found to help heal AF lesions, though they are still far from clinical application. The imperfect results may be due to stress shielding by these physical repair methods in the lesion region (Chu et al., 2018a). Mechanically-stimulated tissue regeneration is gaining more attention in musculoskeletal tissue repair strategies. Since extracellular matrix (ECM) components impact stem cell differentiation (Smith et al., 2018; MacDonald et al., 2021), a repair method utilizing biological glue could connect tissue lesions and the microenvironment could transfer strain stress to the immersed seeding cells, such as mesenchymal stem cells (MSCs), to gain more successful differentiation and repair effects (Kang et al., 2017).

MSCs differentiation under proper mechanical stimulation already successfully generates quality cartilage, tendon, bone, and cardiomyogenic tissue (Gu et al., 2017; Kataoka et al., 2020; Liu et al., 2022a; Park et al., 2022; Volz et al., 2022). Recently, the frequency and intensity of mechanical stimulation have been optimized in several studies (Chan et al., 2011a; Lee et al., 2016; Elsaadany et al., 2017). Studies also revealed that the mechanical-related RhoA/ROCK signaling pathway regulation might be the intrinsic mechanism for such a phenomenon (Xu et al., 2012; Peng et al., 2021). More specifically, for AF repair, the tensile stress of 1 HZ frequency and 3% magnitude has been reported to be the favorite mechanical stimulation for MSCs differentiation to AF *in vitro* (Elsaadany et al., 2017). However, few studies specifically compare the repair effect of AF lesions under mechanical shielding and mechanical stimulation, since there is still a lack of a proper biological glue with ideal biocompatibility and sufficient adhesive strength to repair the AF defect.

We established a biological glue composed of Fibrinogen-Thrombin-Genipin (Fib-T-G), which is competent for AF defect repair in a rat model in our pilot study. We further designed the study and investigated the repair quality *in vivo* under two different mechanical conditions: a mechanical stimulation environment by human MSCs (hMSCs) mixed in Fib-T-G sticky glue to fill and connect the annulus lesion; a mechanical shielding environment by

TABLE 1 Primers sequences used for qPCR analyses.

Name		5→sequence→3	Product size	NCBI ReferenCe SequenCes (Ref Seq)
GAPDH	Sense	CCAGAACATCATCCCTGCCT	185	NM_001256799
	Antisense	CCTGCTTCACCACCTTCTTG		
COL1A1	Sense	GTGCTAAAGGTGCCAATGGT	228	NM_000088.3
	Antisense	CTCCTCGCTTTCCTTCCTCT		
RhoA	Sense	TCGTTAGTCCACGGTCTGGT	116	NM_001313941.2
	Antisense	GCCATTGCTCAGGCAACGAA		
ROCK1	Sense	CTGCAACTGGAACTCAACCAAG	100	NM_005406.3
	Antisense	ATTCTTCTACCAATTGCGCTTGC		
Aggrecan	Sense	CCTCTGGACAACCAGGTATTAG	97	NM_001135
	Antisense	CCAGATGTTTCTCCACTCAGAT		
COL2A1	Sense	TCCACGGAAGGCTCCCAGAA		NM_001844.5
	Antisense	CCTGCTATTGCCCTCTGCCC	141	
Mohawk	Sense	CAAGCAAGGATGACACGTATTG	105	NM_001242702.1
	Antisense	GGATGATGCAGCTGGTAGTT		
SOX9	Sense	GAGCTGAGCAGCGACGTCAT	130	NM_000346.4
	Antisense	CGTAGCTGCCCGTGTAGGTG		

hMSCs mixed in Fibrinogen non-sticky solution to fill, and together with suture to connect the annulus lesion. We also studied the molecular reactions of hMSCs in a mechanical stimulation environment as well as the possible intrinsic molecular mechanism of the differentiation of hMSCs towards AF tissue *in vitro* (Figure 1).

2 Materials and methods

2.1 Fib-T-G gel and MSCs preparation

Fibrinogen (F3879, Sigma, United States) dissolved in phosphate-buffered saline (PBS, 0.01 M, pH 7.40) at a concentration of 200 mg/ml, thrombin (T4393, Sigma, United States) dissolved in PBS at a concentration of 100 U/ml, and genipin (G4796, Sigma, United States) dissolved in dimethyl sulfoxide (D2650, Sigma, United States) at a concentration of 400 mg/ml, were prepared for the glue fabrication. This component concentration of Fib-T-G gel was optimized by testing the biocompatibility and mechanical properties with different concentrations of genipin. The Fib-T-G gel contained final concentrations of fibrinogen 140 mg/ml, thrombin 28 U/ml, and genipin 6 mg/ml–these concentrations exhibited the best consistency for biocompatibility and adhesive strength for the following experiment in our pilot study, which was added as Supplementary Data. hMSCs (Passage 2, 15901; purchased from ScienCell Research Laboratories, Carlsbad, CA) routine cultured in Mesenchymal Stem Cell medium (7501, Sciencell, United States) which included DMEM supplemented with 5% fetal bovine serum (FBS, 0025, Sciencell, United States), 1% penicillin-streptomycin (PS, 0503, Sciencell, United States) and Mesenchymal Stem Cell Growth Supplement (MSCGS) (7552, Sciencell, United States) up to passage 6, were used in all the experiments in this study.

2.2 Annulus repair effect with MSCs in mechanical stimulation environment VS. in mechanical stress shied environment *in vivo*

All animal experiments were performed according to the Guidelines for Care and Use of Laboratory Animals established by the Affiliated Hospital of Integrated Traditional Chinese and Western Medicine, Nanjing University of Chinese Medicine. The stroke-bearing protocol was approved by the Committee on the Ethics of Animal Experiments of the Hospital (Ethical Lot Number: AEWC-20191010-82). The experimental procedures were approved by the hospital ethic committee. Twenty male computer-randomized SD rats (average weight 450 ± 20 g) were utilized in this study with 10% chloral hydrate anesthesia. Four caudal intervertebral discs of each rat were exposed from the ventral side for four experimental groups respectively. In brief, a 2 mm width and 2.5 mm depth lesion was punctured by a custom-made blade. Fib-T-G MSCs group: annulus lesion filled and connected by 7 μL Fib-T-G glue mixed with 1.2×10^3 hMSCs. Fibrinogen MSCs(Fib MSCs) group: annulus lesion filled by 7 μL fibrinogen mixed with 1.2×10^3 hMSCs and connected carefully by one micro suture (ETHICON 7-0). Un-repair control: annulus lesion without repair. Intact control: discs exposed without any intervention. All the rats were fed with standardized food and moved freely, and were all sacrificed at 5 weeks.

After the operation, the specimens were fixed with 4% neutralized formalin (BL-G001, Nanjing Senbeijia Biotechnology Co., Ltd, China), then decalcified in 10% nitric acid (USP364, CPA, France). Each segment were separated and transferred to 75% ethanol (64-17-5, Nanjing Chemical Reagent Co., Ltd, China), then embedded in paraffin, cut in the mid-sagittal plane to 5-μm thickness, and stained with hematoxylin and eosin (H&E) for cellular constituents. Histological score of disc degeneration and annulus fibrosus were evaluated based on the following four categories of

10.3389/fbioe.2023.1137199

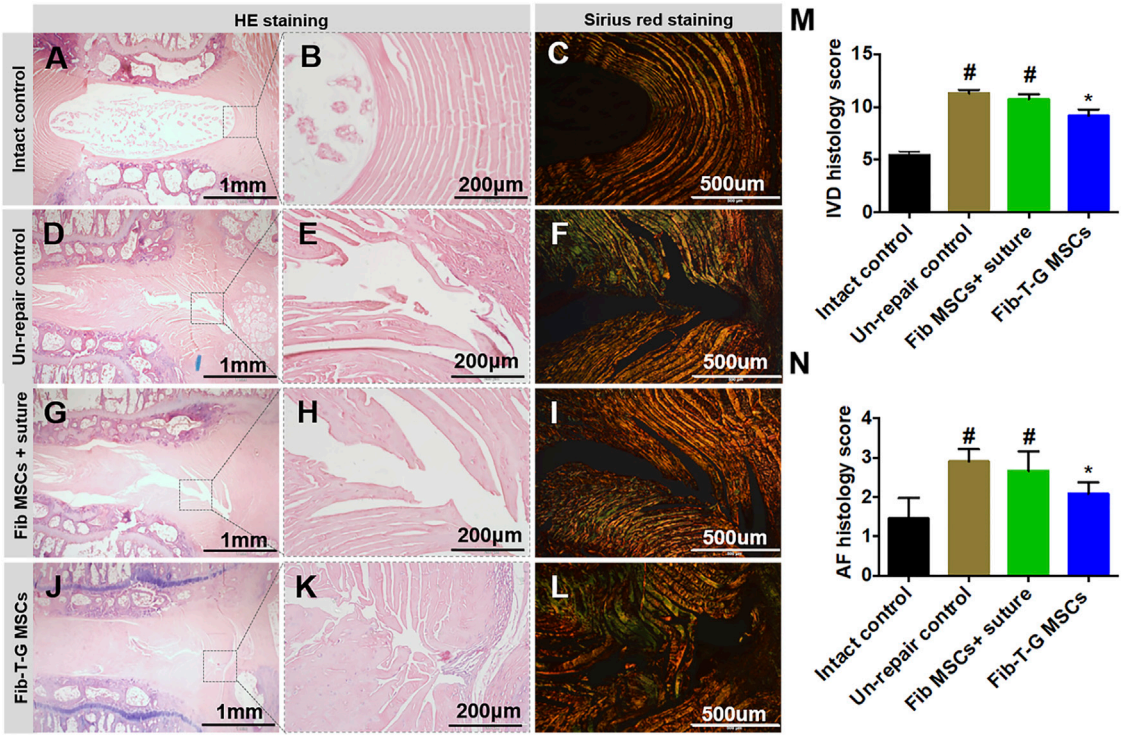

FIGURE 2
Histological assay after 5 weeks of different interventions. **(A–C)** The intact control disc has a loose nucleus matrix and regular annulus fibrous lamellae in HE staining, and continuous annulus lamellae are seen in Sirius red staining. **(D–F)** Unrepair control disc is collapsed with the severe fibrotic nucleus, obvious annulus fissure, irregular fibrous tissue in HE staining, and discontinuous annulus lamellae in Sirius red staining. **(G–I)** Disc repaired by Fib MSCs and suture is also collapsed with the severe fibrotic nucleus, obvious annulus fissure, irregular fibrous tissue in HE staining, and discontinuous annulus lamellae in Sirius red staining. **(J–L)** Disc repaired by Fib-T-G MSCs has a relatively normal structure with a slight fibrotic nucleus, slight annulus fissure in HE staining, and continuous annulus lamellae in Sirius red staining. **(M)** IVD histology score. **(N)** AF histology score. N≥3 * indicates a significant difference between the intervened discs and the unrepair control, $p < 0.05$. # indicates a significant difference between the intervened discs and the Fib-T-G MSCs group, $p < 0.05$.

degenerative changes according to previous study (Masuda et al., 2005): annulus fibrosus, border between the anulus fibrosus and nucleus pulposus, cellularity of the nucleus pulposus, and matrix of the nucleus pulposus. IVD scores range from a normal disc as 4 points to a severely degenerated disc as 12 points, and AF scores range from a normal annulus being 1 point to a more than 30% ruptured or serpentined patterned fibers having 3 points. Picrosirius red (ab150681, Abcam, United States) was stained and assessed under a polarized light microscope for lamellar structure and continuity of collagen. Diaminobenzidine (DAB, ZLI-9018, ZSGB-BIO, China) staining of the main components of annulus fibrosus collagen 1 (COL1) (1:200, ab34710, Abcam, United States), collagen 2 (COL2) (1:200, ab34712, Abcam, United States), mechanical stimulation related protein RhoA (1:100, 10749-1-AP, Proteintech, China) and ROCK1 (1:200, ab97592, Abcam, United States) were conducted according to the product instructions and viewed under a microscope (IX73, Olympus, Japan).

2.3 Differentiation effect of MSCs towards annulus in mechanical stimulation environment VS. in a static environment

The hMSCs were seeded into elastin precoated six-well BioFlex plates (Flexcell International Corporation) with 2.0×10^6 cells/well and cultured in growth media (Dulbecco's modified Eagle medium (DMEM, Gibco, United States) with 10% fetal bovine serum (FBS, Invitrogen, United States) and 1% penicillin-streptomycin (PS, Gibco, United States)) to reach confluence. Then cells were cultured by chondrocyte differentiation medium according to a previous study (Masuda et al., 2005; Lysdahl et al., 2013) (DMEM medium; 10% FBS; 100 nM Dexamethasone, D1756, Sigma; 50 μg/ml Ascorbic Acid-2phosphate, A4544, Sigma; 40 μg/ml L-Proline, P0380, Sigma; 1: 100 ITS Supplement, 10201, Cyagen Biosciences Company; 10 ng/ml TGF-β1, 96-100-21-10, PeproTech; 1% PS), and the fresh medium was changed every 3 days. Cells were differentiated in the following two different mechanical conditions. The mechanical load group: cell cultures were loaded on the Flexercell FX 5000T cell-straining device with 3% strain and 1 HZ mechanical load stimulation for 1 h each day. The stable control group was cell cultures in a static environment.

Three cultures of each group were obtained after 7 days of differentiation. All the mediums in each well were collected to quantify the secreted sGAG and Collagens by Dimethylmethylene blue (DMMB, 341088, Sigma, United States) and Sicol assays (s1000, Biocolor, UK). Total RNA from samples was isolated using Trizol reagent (15596026, Invitrogen, United States) according to the manufacturer's instructions. The RNA was synthesized by reverse transcription kit (E6560, NEB, United States) to cDNA, followed by quantitative real-time PCR (qPCR, ABI StepOnePlus, United States) analysis using SYBR Premix (E3003, NEB, United States) and ABI

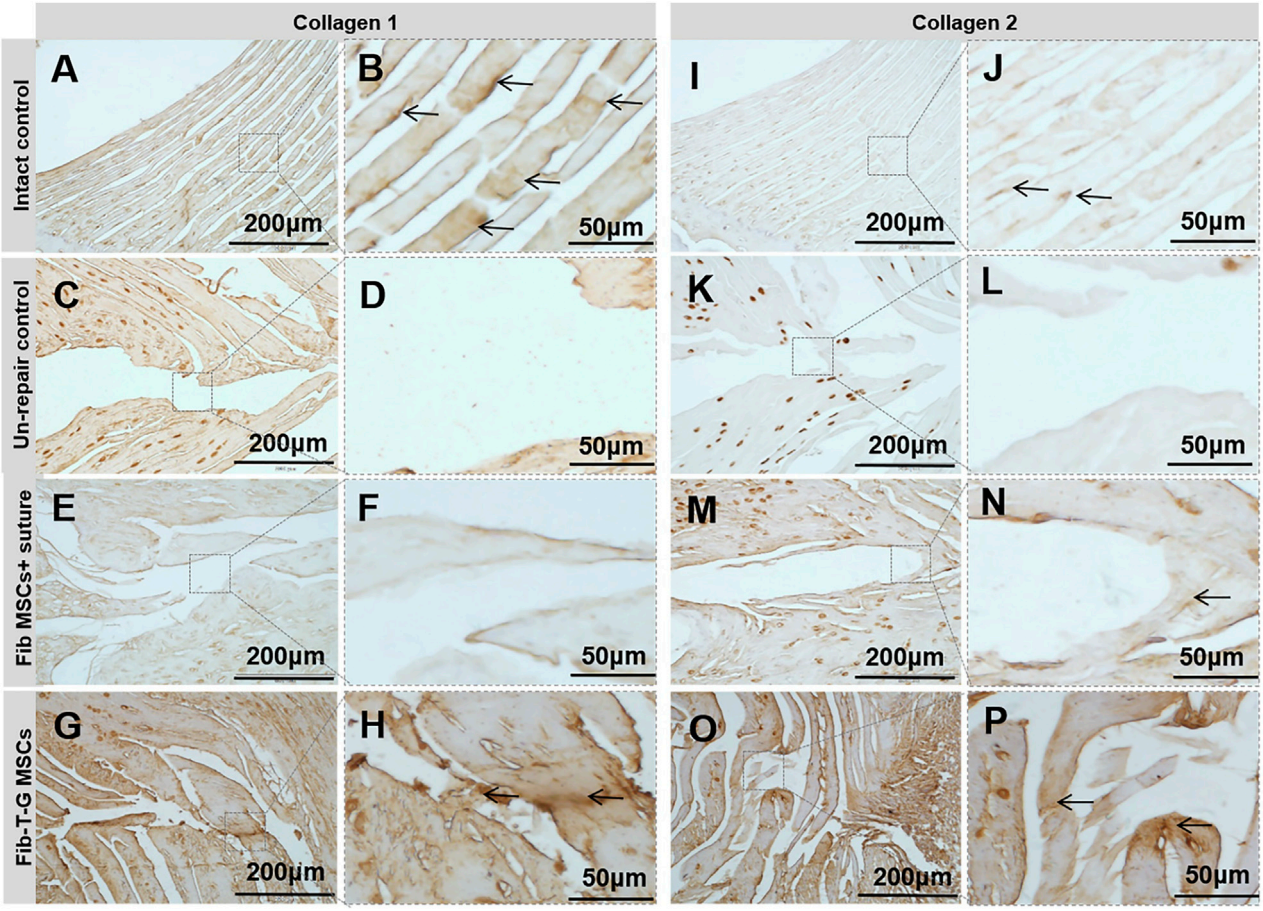

FIGURE 3
DAB staining of collagen 1 and 2 for specimens of different interventions at 5 weeks. Collage 1: **(A, B)** Intact control disc's annulus has a regular, continuous structure with positive staining pointed by arrows. **(C, D)** Unrepair control disc's annulus fissure is obvious with no positive staining. **(E, F)** Disc repaired by Fib MSCs and suture has no positive staining in the annulus fissure. **(G, H)** Disc repaired by Fib-T-G MSCs has a continuous structure with positive matrix staining in the annulus fissure pointed by arrows. Collagen 2: **(I, J)** Intact control disc's annulus has a regular, continuous structure with positive staining pointed by arrows. **(K, L)** Unrepair control disc's annulus fissure is obvious with no positive staining. **(M, N)** Disc repaired by Fib MSCs has some connection tissue with positive matrix staining between the fissure signed by arrows. **(O, P)** Disc repaired by Fib-T-G MSCs has a continuous structure with positive matrix staining in annulus fissure pointed by arrows.

STEPONE PLUS. Gene expression of COL1A1, COL2A1, aggrecan, Mohawk, RhoA, ROCK1, and SOX9 were analyzed by qPCR. 3-phospate dehydrogenase (GAPDH) was used as a reference gene. The sequences of the genes are shown in Table 1.

Another three cultures of each group were obtained after 2 weeks of differentiation. Cell cultures were soaked in 4% paraformaldehyde in PBS with pH 7.4 for 10 min at room temperature and washed with ice-cold PBS three times. Samples were incubated with PBS containing 0.5% Triton X-100 for 10 min and subsequently washed in PBS three times. Then the samples added with 3% BSA in PBS were cultured for 30 min to block the unspecific binding of the antibodies. Samples incubated in the primary antibody COL1, COL2, Aggrecan (1:200, ab36861, Abcam, United States) in PBS-1% BSA solution in a humidified chamber overnight at 4 °C. After removing the primary antibody incubation solution, the cells were washed 3 times with PBS and then coincubated with DAB staining solution at room temperature. Picro Sirius red was stained to assess the alignment of collagen. Finally, all the samples were observed by a fluorescence microscope (IX73, Olympus, Japan).

2.4 MSCs differentiation towards annulus tissue with transfected VS. non-transfected RhoA gene in a static environment

The RhoA gene was transfected to hMSCs. In brief, hMSCs of 2.0×10^6 cells/well were plated into six-well BioFlex culture plates precoated with elastin in culture media and allowed to reach 80% confluence. Transient transfections with the plasmids encoding wild-type RhoA (Public Protein/Plasmid Library, China) and the constitutively active Q63L RhoA were carried out in the RhoA using Lipofectamine™ LTX (15338100, Invitrogen, United States). Transfected cells were allowed to recover for 12 h, then trypsinized (25200, Gibco, United States), and sorted GFP-positive cells to purify only the cells containing transgenes. Sorted cells were centrifuged (1000 rpm/min), washed (PBS as washing solution), and prepared for further study.

RhoA transfected MSCs of 2.0×10^6 each well were plated into six-well BioFlex culture plates and cultured in a differentiation medium (corresponding to 2.3), with normal MSCs culture as control. After 7 days, three samples of each group were

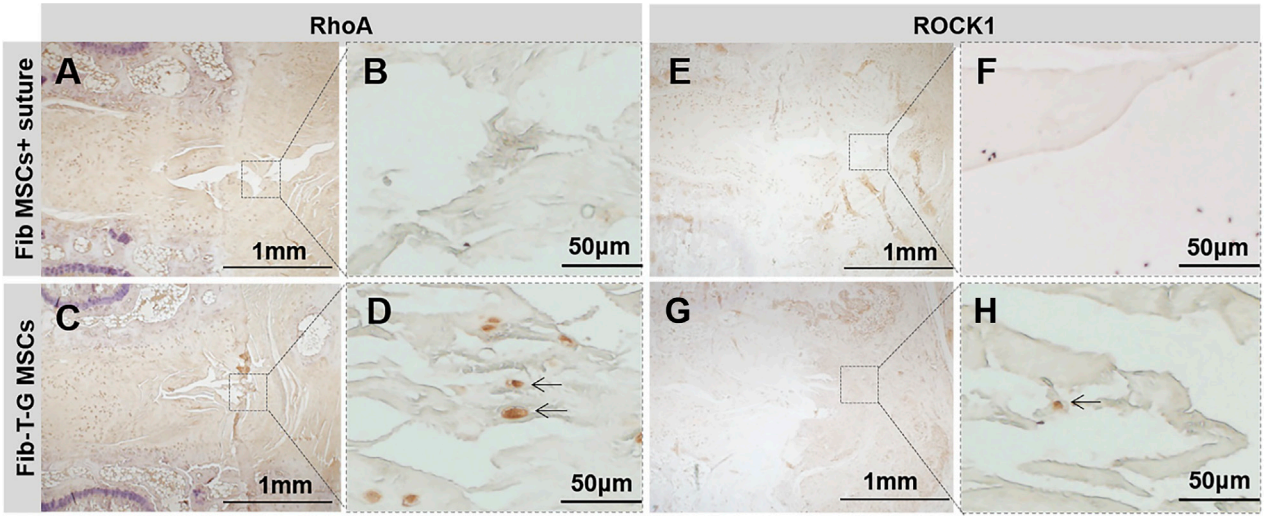

FIGURE 4
DAB staining of RhoA and ROCK1 for specimens of different interventions at 5 weeks. RhoA: **(A, B)** Disc repaired by Fib MSCs and suture has no positive staining in annulus fissure. **(C, D)** Disc repaired by Fib-T-G MSCs has a continuous structure with positive cell staining in annulus fissure pointed by arrows. ROCK1: **(E, F)** Disc repaired by Fib MSCs and suture has no positive staining in annulus fissure. **(G, H)** Disc repaired by Fib-T-G MSCs has a continuous structure with positive cell staining in annulus fissure pointed by arrows.

obtained, and gene expression of COL1, COL2, Aggrecan, Mohawk, RhoA, and R was analysed by qPCR. After 2 weeks, three samples of each group were harvested, and the matrix of COL1, COL2, and aggrecan was determined by DAB staining as above study (corresponding to 2.3).

2.5 MSCs differentiation towards annulus tissue with inhibited VS. non-inhibited RhoA gene in a mechanical stimulation environment

The hMSCs of 2.0×10^6 each well were plated into six-well BioFlex culture plates and cultured in a differentiation medium. In mechanical load with inhibitor C3 group, 3% strain and 1 HZ mechanical load stimulation was conducted for 1 h each day, and Cell Permeable RhoA Inhibitor C3 transferase based (CT04, Cytoskeleton, United States) was added. In the mechanical load group, cells differentiated with a mechanical load but without inhibitor C3. In the control, cells differentiated without mechanical load and without inhibitor C3. After 7 days, we investigated the effect of mechanical strain on AF relative gene expression and the RhoA/ROCK1 by qPCR analysis.

2.6 Statistics analysis

The statistical significance for normally distributed data. Significance was indicated by letters in graphs. For gene expression data, a non-parametric distribution was assumed and presented as mean ± SD for an N ≥ 3. The data were analyzed by one-way ANOVA followed by multiple comparison tests. All tests were performed with GraphPad Prism 6.0 (GraphPad Software, La Jolla, CA, United States).

3 Results

3.1 Healing analysis of groups within mechanical stimulation and mechanical stress shielding *in vivo*

All the discs with lesions have degenerative signs with the fibrotic nucleus, annulus fissure, irregular fibrous tissue in HE and Sirius red staining, while the intact control has healthy loose nucleus matrix and regular annulus fibrous lamellae (Figures 2A–L). After histological disc degenerative scoring, the value 9.167 of the Fib-T-G MSCs group is significantly lower than the unrepaired control group 11.30 ($p \leq 0.01$, and also lower than the 10.73 of the Fib MSCs group ($p < 0.05$) (Figure 2M). After histological annulus fissure degenerative scoring, the value 2.083 of the Fib-T-G MSCs group is significantly lower than the unrepaired control group 2.90 ($p \leq 0.01$, and also lower than the 2.667 of the Fib MSCs group ($p < 0.05$). The lesion is still seen in both repaired groups but less in the Fib-T-G MSCs group at the middle sagittal histological section. The lesion area in the Fib-T-G MSCs group is apparently smaller than that in the Fib MSCs group (Figure 2N). Further, DAB staining in the repaired area of both repaired groups shows relatively more staining of collagen 1/2 (Figure 3) and RhoA/ROCK1 (Figure 4) in the Fib-T-G MSCs group, compared to the Fib MSCs group. Comprehensive results show that the Fib-T-G MSCs group with mechanical stimulation better affects repairing AF lesions.

3.2 Analysis of MSCs differentiation towards AF in mechanical stimulation and static environments *in vitro*

As shown in Figure 5A, after 7 days of culture, the results showed the relative fibrocartilage differentiation gene expression of COL2,

10.3389/fbioe.2023.1137199

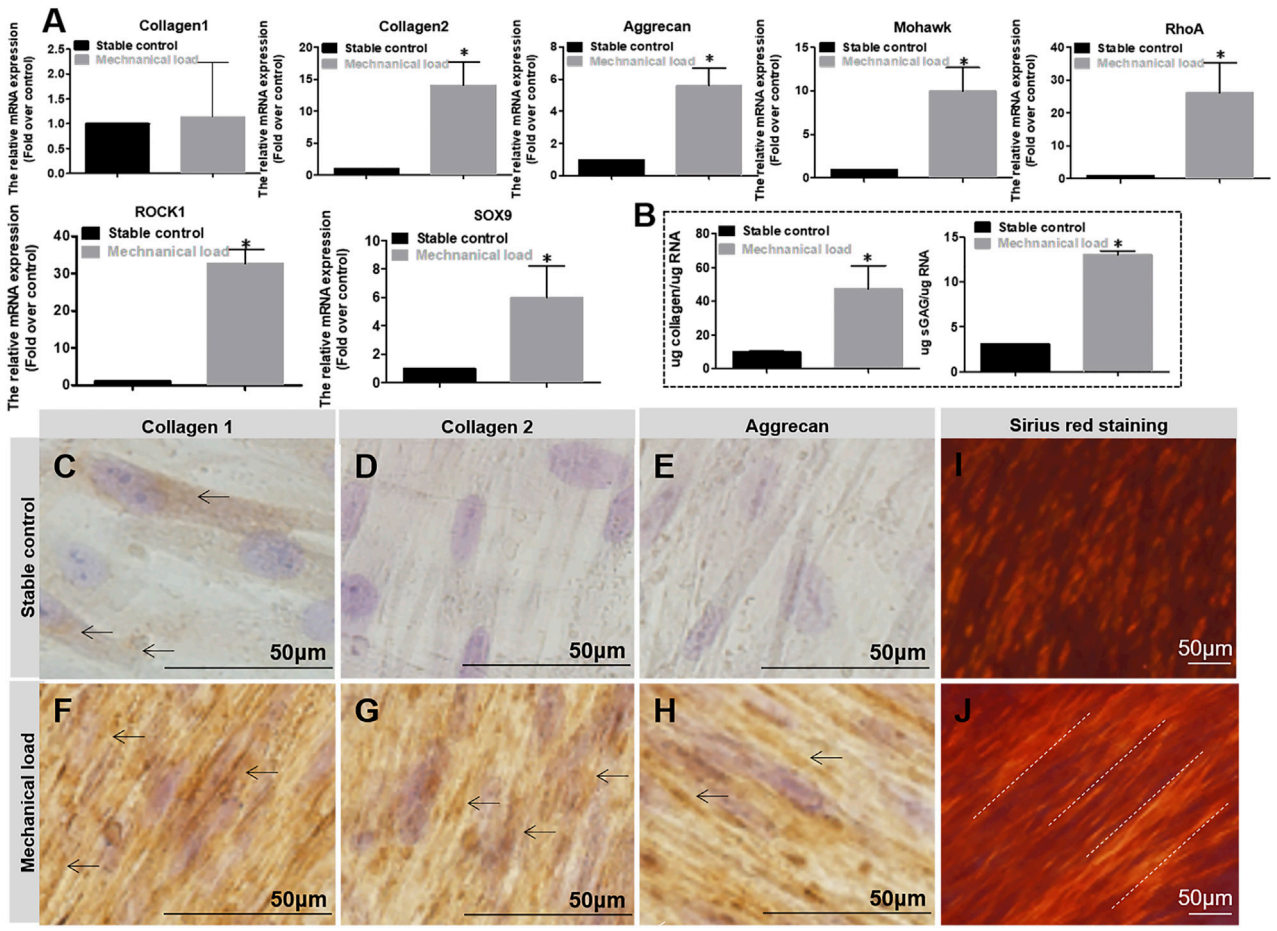

FIGURE 5
(A) Relative gene (Collagen1, Collagen2, Aggrecan, Mohawk, RhoA, ROCK1, SOX9) expression in different mechanical conditions after 7 days of culture. **(B)** Matrix of Collagen and Aggrecan quantification in different mechanical conditions after 7 days of culture. The expression level and quantification are expressed as mean ± SD, (n = 3). **(C–H)** DAB staining of Collagen 1, 2, and Aggrecan for cell culture in different mechanical conditions for 2 weeks. Cell culture differentiation in stable conditions has few positive matrix staining of Collagen 1, 2, and Aggrecan (pointed by arrows), whereas cell culture differentiation in mechanical stimulation conditions has obvious positive matrix staining of Collagen 1, 2, and Aggrecan (pointed by arrows). **(I, J)** Sirius red staining for cell culture in different mechanical conditions for 2 weeks. Collagen stained by Sirius red is positive but without aligned fibers seen under polarized light **(I)**; collagen stained by Sirius red is positive with obviously aligned fibers seen under polarized light (pointed by dotted lines) **(J)**. * indicates a significant difference between the different culture conditions, $p < 0.05$.

aggrecan, Mohawk, RhoA, ROCK1, and SOX9 in the mechanically stimulated environment were significantly higher than those in the static environment. After 2 weeks, the secreted sGAG and collagen contents were measured by Dimethylmethylene blue and Sicol assays (Figure 5B). The results showed that the secretion amount was also significantly higher in the mechanically stimulated environment than in the static environment. In addition, mechanical stimulation promotes hMSCs differentiation with more COL1, COL2, and Aggrecan secretion observed in immunohistostaining compared to the cell culture in the static environment (Figures 5C–H). At the same time, the alignment of collagen was observed by Sirius red staining (Figures 5I, J). Arranged collagen is seen in the mechanical stimulation group under polarized light observation but not in the static group. The comprehensive results demonstrate that **the** differentiation of MSCs towards AF tissue mechanical stimulation benefits the differentiation of hMSCs towards AF tissue, along with the RhoA gene activated.

3.3 Mechanism analysis of mechanical stimulation environment promoting the differentiation of MSCs towards AF tissue

As shown in Figure 6A, in the static environment, gene expression of COL1, COL2, Aggrecan, Mohawk, RhoA, ROCK1, and SOX9 in RhoA transfected hMSCs was significantly higher than that in normal non-RhoA transfected hMSCs after 7 days of culture. Relative more COL1, COL2, and aggrecan secreted by hMSCs by RhoA transfected hMSCs were observed by DAB staining (Figures 6B–G) after 2 weeks in culture. These results suggest that RhoA upregulation can promote AF-related gene expression and protein secretion. As shown in Figure 6H, in the mechanical stimulation environment, C3 Transferase inhibited RhoA signal hinders MSCs differentiation with significantly lower gene expression of collagen 2, aggrecan, Mohawk, ROCK1, SOX9 compared to the cell culture with no C3 Transferase after 7 days of culture. To sum up, without mechanical stimulation, overexpressing RhoA could promote

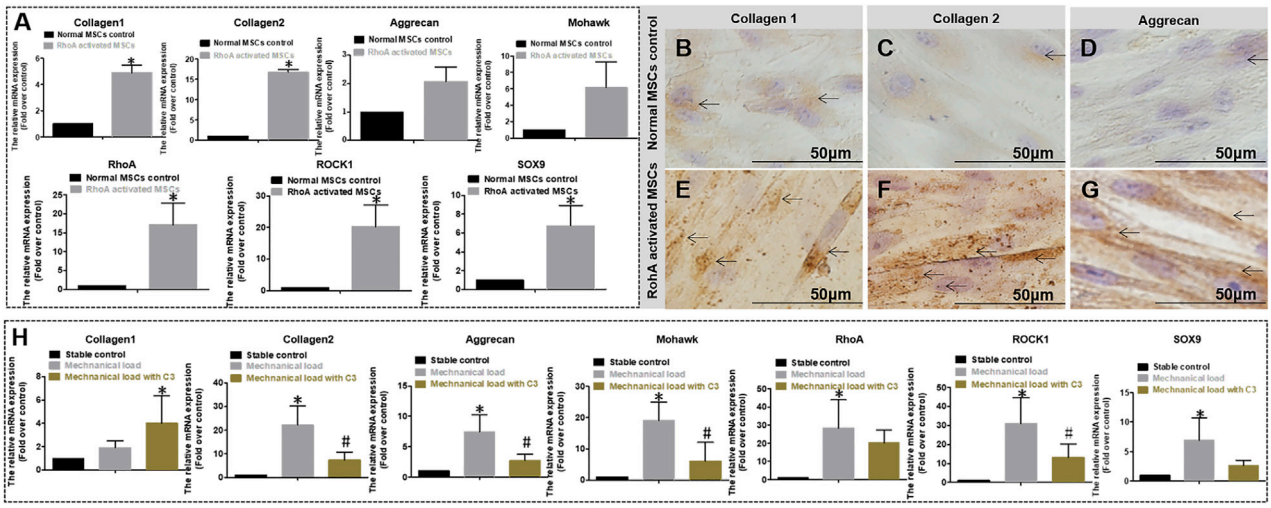

FIGURE 6
(A) Relative gene expression quantified by qPCR of normal and RhoA gene activated MSCs culture both in differentiation medium and without mechanical stimulation for 7 days. The expression level is expressed as mean ± SD, (n = 3) * indicates a significant difference between the different MSCs, $p < 0.05$. **(B–G)** DAB staining of Collagen 1, 2, and Aggrecan for two different cell cultures without mechanical stimulation for 3 weeks. **(B–D)** Normal MSCs differentiation has Collagen 1, 2, and Aggrecan matrix staining (pointed by arrows); **(E–G)** RohA gene-activated MSCs differentiation has obvious positive matrix staining of Collagen 1, 2, and Aggrecan (pointed by arrows). **(H)** Relative gene expression quantified by qPCR of MSCs differentiation without mechanical stimulation, with mechanical stimulation, or with mechanical stimulation and RhoA inhibitor C3 for 7 days. The expression level is expressed as mean ± SD, (n = 3)*indicates a significant difference compared to the cell culture without mechanical stimulation, $p < 0.05$. # indicates a significant difference compared to the cell culture with mechanical stimulation, $p < 0.05$.

differentiation; inhibiting RhoA reduced the differentiation effect with mechanical stimulation.

4 Discussion

Although AF treatment is still at an early stage (Bron et al., 2008), the necessity is increasingly recognized (Huang et al., 2018; Liu et al., 2022b). AF is a stiff ring-shaped structure withstanding complex mechanical strain (Holzapfel et al., 2004), which requires repair strategies to offer sufficient mechanical stability and potential for regenerating AF tissue. Tissues and Cells are exposed to various mechanical forces, mechanical load is very important for the health of IVD. The excessive load could damage IVD; on the other side, an appropriate load could stimulate healing. As reported, appropriate tension strain can reverse degenerated IVD, which is induced by excessive compression *in vivo* (Unglaub et al., 2006). In this study, we also find that mechanical stimulation promotes MSCs healing AF lesions *in vivo*, by means of immersing the cells in biological glue. Further *in vitro* study confirmed that certain strain forces did promote MSCs differentiation to AF-like tissue; meanwhile, RhoA gene activation was observed.

To connect the AF lesion, some stress shielding, and stress retention repair methods have been studied. However, the comparative study of these two methods has not been reported. We used biological glue and sutures to connect the lesion, representing the two mechanical environments for the differentiation of MSCs. However, the biological glue used often exhibits insufficient mechanical properties to meet the application requirements. Therefore, it is necessary to use a cross-linking agent for improvement. Genipin acts as a natural cross-linking agent that can connect tissues or gels at the molecular level. In addition, genipin is also an iridoid compound with multiple active groups, such as hydroxyl and carboxyl groups, which can spontaneously react with amino acids to form blue pigments and maintain a good degree of cross-linking. More importantly, compared to other commonly used cross-linking agents, such as glutaraldehyde (GA), carbodiimide, epoxy compounds, etc., genipin is considered to be the least toxic cross-linking agent, which can effectively reduce the immunogenicity of xenogeic matrices (Oryan et al., 2018). In the degenerative intervertebral disc, genipin crosslinked gel is considered degradate more slowly than gel without genipin (Likhitpanichkul et al., 2014; Likhitpanichkul et al., 2015), and the use of genipin crosslinking has been shown to alter several mechanical parameters (Fujii et al., 2020) and may be advantageous in treating disc pain (Guterl et al., 2013; Guterl et al., 2014; Peng et al., 2020) and disc degeneration (Yu et al., 2021). Thus, we tried genipin and tested Fib-T-G (F140 G6) gel as the best consistency for biocompatibility and adhesive strength; afterward, we applied this biological glue to repair the caudal AF slit injury of rats. It was demonstrated that the Fib-T-G gel helps treat the AF fissure and prevent disc degeneration, more than that, crosslinked sticky gel (Fib-T-G MSCs gel) got better repair results than the unstuck gel (Fib MSCs gel). The result stresses the importance of the mechano-transferred gel and the mechanical stress for the differentiation of the embedded MSCs, which is consistent with published studies (Delaine-Smith and Reilly, 2011). The reason might be that the injected genipin crosslinked hydrogel deforms almost entirely uniformly and transmit physiology tension; thus, the strain force resulting from the repaired disc would be relatively homogeneous on each stem cell throughout the hydrogel scaffold so as to produce continuous ECM to bridge cells and induce the cell differentiation for AF like tissue.

This result predicts a better repair effect of our method in the human body. In general, biological glue provided the initial stabilization of the lesion and stress transmission to the inside MSCs. Along with glue degradation, newly generated tissue gradually filled the lesion. Forces

provide crucial signals to inform cell behavior, to know the intrinsic mechanism, previous studies have implied that the RhoA/ROCK1 signaling pathway may be an important molecular mechanism for differentiating MSCs into skeletal muscle tissue in response to stress stimuli (Heo et al., 2016). Whether mechanical stimulation also regulates the expression of annulus-like genes and proteins in MSCs differentiation is unclear. In order to further explore how the mechanical microenvironment promotes MSCs healing AF, *in vitro* mechanical stimulation was used to simulate the *in vivo* study. Our results demonstrated that genipin crosslinked hydrogels show off better results of disc healing in the repaired zone than the Fibrinogen with suture group in rats, as well as support mechanical strain up-regulated AF tissue markers Mohawk, SOX-9 and ECM markers COL2 and aggrecan after application in MSCs, exhibit trends that are consistent with those reported with regard to fibrous tissues (Baker et al., 2011; Elsaadany et al., 2017). The above study strengthens the evidence that the physical microenvironment plays a vital role in cell differentiation (Raabe et al., 2013; Elsaadany et al., 2017) and extracellular matrix remodeling (Higuchi et al., 2013; Lee et al., 2016). Our study addresses the performance of strain-related mechanotransduction in AF fissure repair of MSCs and explores the mechanical mechanism, the different mechanical strains, and the frequency regulating differentiation of stem cells we refer to previous studies (Elsaadany et al., 2017) and take a preliminary verification.

There are stress-sensitive receptors on the cell surface, which can transmit the induced mechanical signals into the cells through special molecular channels on the cell surface to achieve force-chemical conversion, thereby regulating the physiological functions of cells (Dupont and Wickström, 2022). Some studies have shown that pressure stimulation of the IVD cartilage endplate can activate the RhoA/ROCK1 signaling pathway, leading to changes in gene expression of COL2, Proteoglycan, and SOX9 (Xu et al., 2016). Recent studies have also shown that the RhoA/ROCK signaling pathway is an important molecular mechanism by which MSCs respond to stress stimuli and regulate their differentiation into skeletal muscle tissue (McBeath et al., 2004; Amano et al., 2010; Lessey et al., 2012; Heo et al., 2016). Our study investigated the downstream signaling pathway of RhoA, the expression of ROCK1 and SOX9 were increased in response to mechanical strain. To elucidate whether RhoA controlled strain-induced differentiation, we take overexpression of RhoA, which results in the recruitment of ROCK1 and enhanced differentiation. Evidence also from the other side showed reduced differentiation efficiency when inhibiting RhoA in a mechanical stimulation environment.

There are some limitations in our study. Firstly, rat tail caudal AF fissure models experience much less tension strain and compression force than humans. This does not affect the significance of this study since the healing principle should be similar to humans. And with the quality of adhesion and compatibility of glue improvement by different crosslinking methods (Dare et al., 2009; Cruz et al., 2017; Moriguchi et al., 2018), it will eventually reach the standard for human AF repair. Secondly, although locking cells in the damaged space is the advantage of using biological glue for AF repair, unlike in the control group, where the cells may cause leakage out in the non-stick fibrinogen solution, the resulting different amount of MSCs in each group may affect the comparison study in the rat model. And this is one of the reasons why we need to conduct accurate *in vitro* cell experiments. Thirdly, the exact mechanism of this repair strategy remains to be further verified. Alongside the RhoA/ROCK1 signaling, other pathways may be responsible for mechanotransduction regulating fibrochondrogenic differentiation of MSCs (Wang et al., 2013; Xin et al., 2022) and are worth deep research and further elaboration.

5 Conclusion

Mechanical stimulation promotes MSCs healing of the lesion of AF in the rat model by immersing the cells in the Fib-T-G glue to connect the lesion. Mechanical stimulation is vital for AF tissue regeneration by regulating the differentiation of MSCs, possibly *via* RhoA/ROCK1 signaling.

Data availability statement

The original contributions presented in the study are included in the article/Supplementary Material, further inquiries can be directed to the corresponding authors.

Ethics statement

All animal experiments were performed according to the Guidelines for Care and Use of Laboratory Animals established by the Affiliated Hospital of Integrated Traditional Chinese and Western Medicine, Nanjing University of Chinese Medicine. The stroke-bearing protocol was approved by the Committee on the Ethics of Animal Experiments of the Hospital (Ethical Lot Number: AEWC-20191010-82).

Author contributions

RK: Conceptualization, Methodology, Investigation. RD: Conceptualization, Datum analysis, Writing-original draft. XL: Writing-review and editing. XL, LX, and RK: Writing, Revision, and Supervision.

Funding

This work was financially supported by the National Natural Science of China (81772356), Natural Science Foundation of Jiangsu Province (BK20221420, BK20220464), and Jiangsu Provincial Traditional Chinese Medicine Science and Technology Development Plan Project (2020 ZD202008).

Conflict of interest

The authors declare that the research was conducted in the absence of any commercial or financial relationships that could be construed as a potential conflict of interest.

Publisher's note

All claims expressed in this article are solely those of the authors and do not necessarily represent those of their affiliated

organizations, or those of the publisher, the editors and the reviewers. Any product that may be evaluated in this article, or claim that may be made by its manufacturer, is not guaranteed or endorsed by the publisher.

Supplementary Material

The Supplementary Material for this article can be found online at: https://www.frontiersin.org/articles/10.3389/fbioe.2023.1137199/full#supplementary-material

References

Amano, M., Nakayama, M., and Kaibuchi, K. (2010). Rho-kinase/ROCK: A key regulator of the cytoskeleton and cell polarity. *Cytoskeleton* 67 (9), 545–554. doi:10.1002/cm.20472

Baker, B. M., Shah, R. P., Huang, A. H., and Mauck, R. L. (2011). Dynamic tensile loading improves the functional properties of mesenchymal stem cell-laden nanofiber-based fibrocartilage. *Tissue Eng. Part A* 17 (9-10), 1445–1455. doi:10.1089/ten.TEA.2010.0535

Battié, M. C., Videman, T., Levalahti, E., Gill, K., and Kaprio, J. (2007). Heritability of low back pain and the role of disc degeneration. *Pain* 131 (3), 272–280. doi:10.1016/j.pain.2007.01.010

Bron, J. L., Helder, M. N., Meisel, H.-J., Van Royen, B. J., and Smit, T. H. (2008). Repair, regenerative and supportive therapies of the annulus fibrosus: Achievements and challenges. *Eur. Spine J.* 18 (3), 301–313. doi:10.1007/s00586-008-0856-x

Chan, S. C. W., Ferguson, S. J., and Gantenbein-Ritter, B. (2011a). The effects of dynamic loading on the intervertebral disc. *Eur. Spine J.* 20 (11), 1796–1812. doi:10.1007/s00586-011-1827-1

Chan, W. C. W., Sze, K. L., Samartzis, D., Leung, V. Y. L., and Chan, D. (2011b). Structure and biology of the intervertebral disk in health and disease. *Orthop. Clin. N. Am.* 42 (4), 447–464. doi:10.1016/j.ocl.2011.07.012

Chu, G., Shi, C., Lin, J., Wang, S., Wang, H., Liu, T., et al. (2018a). Biomechanics in annulus fibrosus degeneration and regeneration. *Adv. Exp. Med. Biol.* 1078, 409–420. doi:10.1007/978-981-13-0950-2_21

Chu, G., Shi, C., Wang, H., Zhang, W., Yang, H., and Li, B. (2018b). Strategies for annulus fibrosus regeneration: From biological therapies to tissue engineering. *Front. Bioeng. Biotechnol.* 6, 90. doi:10.3389/fbioe.2018.00090

Colombier, P., Clouet, J., Hamel, O., Lescaudron, L., and Guicheux, J. (2014). The lumbar intervertebral disc: From embryonic development to degeneration. *Jt. Bone Spine* 81 (2), 125–129. doi:10.1016/j.jbspin.2013.07.012

Cruz, M. A., McAnany, S., Gupta, N., Long, R. G., Nasser, P., Eglin, D., et al. (2017). Structural and chemical modification to improve adhesive and material properties of fibrin-genipin for repair of annulus fibrosus defects in intervertebral disks. *J. Biomech. Eng.* 139 (8), 0845011–0845017. doi:10.1115/1.4036623

Dare, E., Griffith, M., Poitras, P., Kaupp, J. A., Waldman, S. D., Carlsson, D. J., et al. (2009). Genipin cross-linked fibrin hydrogels for *in vitro* human articular cartilage tissue-engineered regeneration. *Cells Tissues Organs* 2009 (190), 313–325. doi:10.1159/000209230

Delaine-Smith, R. M., and Reilly, G. C. (2011). The effects of mechanical loading on mesenchymal stem cell differentiation and matrix production. *Vitam. Horm.* 87, 417–480. doi:10.1016/B978-0-12-386015-6.00039-1

Duclos, S. E., and Michalek, A. J. (2017). Residual strains in the intervertebral disc annulus fibrosus suggest complex tissue remodeling in response to *in-vivo* loading. *J. Mech. Behav. Biomed. Mater.* 68, 232–238. doi:10.1016/j.jmbbm.2017.02.010

Dupont, S., and Wickström, S. A. (2022). Mechanical regulation of chromatin and transcription. *Nat. Rev. Genet.* 23 (10), 624–643. doi:10.1038/s41576-022-00493-6

Elsaadany, M., Winters, K., Adams, S., Stasuk, A., Ayan, H., and Yildirim-Ayan, E. (2017). Equiaxial strain modulates adipose-derived stem cell differentiation within 3D biphasic scaffolds towards annulus fibrosus. *Sci. Rep.* 7 (1), 12868. doi:10.1038/s41598-017-13240-3

Fujii, K., Lai, A., Korda, N., Hom, W. W., Evashwick-Rogler, T. W., Nasser, P., et al. (2020). *Ex-vivo* biomechanics of repaired rat intervertebral discs using genipin crosslinked fibrin adhesive hydrogel. *J. Biomechanics* 113, 110100. doi:10.1016/j.jbiomech.2020.110100

Gu, S. R., Kang, Y. G., Shin, J. W., and Shin, J.-W. (2017). Simultaneous engagement of mechanical stretching and surface pattern promotes cardiomyogenic differentiation of human mesenchymal stem cells. *J. Biosci. Bioeng.* 123 (2), 252–258. doi:10.1016/j.jbiosc.2016.07.020

Guterl, C. C., Olivia, M. T., Purmessur, D., Dave, K., Likhitpanichkul, M., Hecht, A. C., et al. (2014). Characterization of mechanics and cytocompatibility of fibrin-genipin annulus fibrosus sealant with the addition of cell adhesion molecules. *Tissue Eng. Part A* 20 (17-18), 2536–2545. doi:10.1089/ten.tea.2012.0714

Guterl, C. C., See, E. Y., Blanquer, S. B. G., Pandit, A., Ferguson, S. J., Benneker, L. M., et al. (2013). Challenges and strategies in the repair of ruptured annulus fibrosus. *Eur. Cells Mater.* 25, 1–21. doi:10.22203/eCM.v025a01

Heo, S.-J., Han, W. M., Szczesny, S. E., Cosgrove, B. D., Elliott, D. M., Lee, D. A., et al. (2016). Mechanically induced chromatin condensation requires cellular contractility in mesenchymal stem cells. *Biophysical J.* 111 (4), 864–874. doi:10.1016/j.bpj.2016.07.006

Higuchi, A., Ling, Q.-D., Chang, Y., Hsu, S.-T., and Umezawa, A. (2013). Physical cues of biomaterials guide stem cell differentiation fate. *Chem. Rev.* 113 (5), 3297–3328. doi:10.1021/cr300426x

Holzapfel, G. A., Schulze-Bauer, C. A. J., Feigl, G., and Regitnig, P. (2004). Single lamellar mechanics of the human lumbar anulus fibrosus. *Biomechanics Model. Mechanobiol.* 3 (3), 125–140. doi:10.1007/s10237-004-0053-8

Huang, Y.-C., Hu, Y., Li, Z., and Luk, K. D. K. (2018). Biomaterials for intervertebral disc regeneration: Current status and looming challenges. *J. Tissue Eng. Regen. Med.* 12 (11), 2188–2202. doi:10.1002/term.2750

Kang, H., Lysdahl, H., Dang, Q., ChenChen, M., Xie, L., et al. (2017). Cyanoacrylate medical glue application in intervertebral disc annulus defect repair: Mechanical and biocompatible evaluation. *J. Biomed. Mater. Res. Part B Appl. Biomaterials* 105 (1), 14–20. doi:10.1002/jbm.b.33524

Kang, R., Li, H., Xi, Z., Ringgard, S., Baatrup, A., Rickers, K., et al. (2018). Surgical repair of annulus defect with biomimetic multilamellar nano/microfibrous scaffold in a porcine model. *J. Tissue Eng. Regen. Med.* 12 (1), 164–174. doi:10.1002/term.2384

Kataoka, K., Kurimoto, R., Tsutsumi, H., Chiba, T., Kato, T., Shishido, K., et al. (2020). *In vitro* neo-genesis of tendon/ligament-like tissue by combination of Mohawk and a three-dimensional cyclic mechanical stretch culture system. *Front. Cell Dev. Biol.* 8, 307. doi:10.3389/fcell.2020.00307

Lee, J.-H., Park, H.-K., and Kim, K. S. (2016). Intrinsic and extrinsic mechanical properties related to the differentiation of mesenchymal stem cells. *Biochem. Biophysical Res. Commun.* 473 (3), 752–757. doi:10.1016/j.bbrc.2015.09.081

Lessey, E. C., Guilluy, C., and Burridge, K. (2012). From mechanical force to RhoA activation. *Biochemistry* 51 (38), 7420–7432. doi:10.1021/bi300758e

Likhitpanichkul, M., Dreischarf, M., Illien-Junger, S., Walter, B. A., Nukaga, T., Long, R. G., et al. (2014). Fibrin-genipin adhesive hydrogel for annulus fibrosus repair: Performance evaluation with large animal organ culture, *in situ* biomechanics, and *in vivo* degradation tests. *Eur. Cell Mater.* 28, 25–38. doi:10.22203/ecm.v028a03

Likhitpanichkul, M., Kim, Y., Torre, O. M., See, E., Kazezian, Z., Pandit, A., et al. (2015). Fibrin-genipin annulus fibrosus sealant as a delivery system for anti-TNFα drug. *Spine J.* 15 (9), 2045–2054. doi:10.1016/j.spinee.2015.04.026

Liu, X., Sun, S., Wang, N., Kang, R., Xie, L., and Liu, X. (2022a). Therapeutic application of hydrogels for bone-related diseases. *Front. Bioeng. Biotechnol.* 10, 998988. doi:10.3389/fbioe.2022.998988

Liu, Z., Bian, Y., Wu, G., and Fu, C. (2022b). Application of stem cells combined with biomaterial in the treatment of intervertebral disc degeneration. *Front. Bioeng. Biotechnol.* 10, 1077028. doi:10.3389/fbioe.2022.1077028

Lysdahl, H. B., Nielsen, A. B., Foldager, C. B., and Bünger, C. (2013). Phenol red inhibits chondrogenic differentiation and affects osteogenic differentiation of human mesenchymal stem cells *in vitro*. *Stem Cell Rev. Rep.* 9 (2), 132–139. doi:10.1007/s12015-012-9417-0

MacDonald, J. A., Woods, D. C., and Tilly, J. L. (2021). Biomechanical strain promotes the differentiation of murine oogonial stem cells. *Stem Cells Dev.* 30 (15), 749–757. doi:10.1089/scd.2021.0086

Marchand, F., and Ahmed, A. M. (1990). Investigation of the laminate structure of lumbar disc anulus fibrosus. *Spine* 15 (5), 402–410. doi:10.1097/00007632-199005000-00011

Masuda, K., Aota, Y., Muehleman, C., Imai, Y., Okuma, M., Thonar, E. J., et al. (2005). A novel rabbit model of mild, reproducible disc degeneration by an anulus needle puncture: Correlation between the degree of disc injury and radiological and histological appearances of disc degeneration. *Spine* 30 (1), 5–14. doi:10.1097/01.brs.0000148152.04401.20

McBeath, R., Pirone, D. M., Nelson, C. M., Bhadriraju, K., and Chen, C. S. (2004). Cell shape, cytoskeletal tension, and RhoA regulate stem cell lineage commitment. *Dev. Cell* 6 (4), 483–495. doi:10.1016/s1534-5807(04)00075-9

Moriguchi, Y., Borde, B., Berlin, C., Wipplinger, C., Sloan, S. R., Kirnaz, S., et al. (2018). *In vivo* annular repair using high-density collagen gel seeded with annulus fibrosus cells. *Acta Biomater.* 79, 230–238. doi:10.1016/j.actbio.2018.07.008

Oryan, A., Kamali, A., Moshiri, A., Baharvand, H., and Daemi, H. (2018). Chemical crosslinking of biopolymeric scaffolds: Current knowledge and future directions of crosslinked engineered bone scaffolds. *Int. J. Biol. Macromol.* 107, 678–688. doi:10.1016/j.ijbiomac.2017.08.184

Park, H., Nazhat, S. N., and Rosenzweig, D. H. (2022). Mechanical activation drives tenogenic differentiation of human mesenchymal stem cells in aligned dense collagen hydrogels. *Biomaterials* 286, 121606. doi:10.1016/j.biomaterials.2022.121606

Peng, Y., Huang, D., Li, J., Liu, S., Qing, X., and Shao, Z. (2020). Genipin-crosslinked decellularized annulus fibrosus hydrogels induces tissue-specific differentiation of bone mesenchymal stem cells and intervertebral disc regeneration. *J. Tissue Eng. Regen. Med.* 14 (3), 497–509. doi:10.1002/term.3014

Peng, Y., Qing, X., Lin, H., Huang, D., Li, J., Tian, S., et al. (2021). Decellularized Disc Hydrogels for hBMSCs tissue-specific differentiation and tissue regeneration. *Bioact. Mater.* 6 (10), 3541–3556. doi:10.1016/j.bioactmat.2021.03.014

Raabe, O., Shell, K., Fietz, D., Freitag, C., Ohrndorf, A., Christ, H. J., et al. (2013). Tenogenic differentiation of equine adipose-tissue-derived stem cells under the influence of tensile strain, growth differentiation factors and various oxygen tensions. *Cell Tissue Res.* 352 (3), 509–521. doi:10.1007/s00441-013-1574-1

Schmidt, H., Kettler, A., Heuer, F., Simon, U., Claes, L., and Wilke, H. J. (2007). Intradiscal pressure, shear strain, and fiber strain in the intervertebral disc under combined loading. *Spine* 32 (7), 748–755. doi:10.1097/01.brs.0000259059.90430.c2

Shamsah, A. H., Cartmell, S. H., Richardson, S. M., and Bosworth, L. A. (2020). Tissue engineering the annulus fibrosus using 3D rings of electrospun PCL:PLLA angle-ply nanofiber sheets. *Front. Bioeng. Biotechnol.* 7, 437. doi:10.3389/fbioe.2019.00437

Sharifi, S., Bulstra, S. K., Grijpma, D. W., and Kuijer, R. (2015). Treatment of the degenerated intervertebral disc; closure, repair and regeneration of the annulus fibrosus. *J. Tissue Eng. Regen. Med.* 9 (10), 1120–1132. doi:10.1002/term.1866

Sivakamasundari, V., and Lufkin, T. (2012). Bridging the gap: Understanding embryonic intervertebral disc development. *Cell Dev. Biol.* 1 (2), 103. doi:10.4172/2168-9296.1000103

Smith, L. R., Cho, S., and Discher, D. E. (2018). Stem cell differentiation is regulated by extracellular matrix mechanics. *Physiology* 33 (1), 16–25. doi:10.1152/physiol.00026.2017

Unglaub, F., Guehring, T., Omlor, G., Lorenz, H., Carstens, C., and Kroeber, M. (2006). Controlled distraction as a therapeutic option in moderate degeneration of the intervertebral disc -- an *in vivo* study in the rabbit-spine model. *Z. für Orthop. ihre Grenzgeb.* 144 (01), 68–73. doi:10.1055/s-2005-836571

Volz, M., Wyse-Sookoo, K. R., Travascio, F., Huang, C.-Y., and Best, T. M. (2022). Mechanobiological approaches for stimulating chondrogenesis of stem cells. *Stem Cells Dev.* 31 (15-16), 460–487. doi:10.1089/scd.2022.0049

Wang, F., Cai, F., Shi, R., Wang, X. H., and Wu, X. T. (2016). Aging and age related stresses: A senescence mechanism of intervertebral disc degeneration. *Osteoarthr. Cartil.* 24 (3), 398–408. doi:10.1016/j.joca.2015.09.019

Wang, Y., Zhong, W., Zhang, W., Wang, S., and Qin, J. (2013). Regulation of fibrochondrogenesis of mesenchymal stem cells in an integrated microfluidic platform embedded with biomimetic nanofibrous scaffolds. *PLoS ONE* 8 (4), e61283. doi:10.1371/journal.pone.0061283

Xin, J., Wang, Y., Zheng, Z., Wang, S., Na, S., and Zhang, S. (2022). Treatment of intervertebral disc degeneration. *Orthop. Surg.* 14 (7), 1271–1280. doi:10.1111/os.13254

Xu, B., Song, G., Ju, Y., Li, X., Song, Y., and Watanabe, S. (2012). RhoA/ROCK, cytoskeletal dynamics, and focal adhesion kinase are required for mechanical stretch-induced tenogenic differentiation of human mesenchymal stem cells. *J. Cell. Physiology* 227 (6), 2722–2729. doi:10.1002/jcp.23016

Xu, H.-G., Ma, M.-M., Zheng, Q., Shen, X., Wang, H., Zhang, S.-F., et al. (2016). P120-Catenin protects endplate chondrocytes from intermittent cyclic mechanical tension induced degeneration by inhibiting the expression of RhoA/ROCK-1 signaling pathway. *Spine* 41 (16), 1261–1271. doi:10.1097/brs.0000000000001532

Yu, L., Liu, Y., Wu, J., Wang, S., Yu, J., Wang, W., et al. (2021). Genipin cross-linked decellularized nucleus pulposus hydrogel-like cell delivery system induces differentiation of ADSCs and retards intervertebral disc degeneration. *Front. Bioeng. Biotechnol.* 9, 807883. doi:10.3389/fbioe.2021.807883

frontiers | Frontiers in Bioengineering and Biotechnology

TYPE Original Research
PUBLISHED 29 March 2023
DOI 10.3389/fbioe.2023.1168192

OPEN ACCESS

EDITED BY
Ziqiang Xu,
Hubei University, China

REVIEWED BY
Md. Rizwanullah,
Jamia Hamdard University, India
Boya Liu,
Boston Children's Hospital and Harvard Medical School, United States

*CORRESPONDENCE
Man Zhou,
baiyuwawa-zhouman@163.com
Xiaoqing Yi,
keyi0115@126.com

SPECIALTY SECTION
This article was submitted to Nanobiotechnology, a section of the journal Frontiers in Bioengineering and Biotechnology

RECEIVED 17 February 2023
ACCEPTED 14 March 2023
PUBLISHED 29 March 2023

CITATION
Wang C, Yang X, Qiu H, Huang K, Xu Q, Zhou B, Zhang L, Zhou M and Yi X (2023), A co-delivery system based on chlorin e6-loaded ROS-sensitive polymeric prodrug with self-amplified drug release to enhance the efficacy of combination therapy for breast tumor cells.
Front. Bioeng. Biotechnol. 11:1168192.
doi: 10.3389/fbioe.2023.1168192

A co-delivery system based on chlorin e6-loaded ROS-sensitive polymeric prodrug with self-amplified drug release to enhance the efficacy of combination therapy for breast tumor cells

Cui Wang[1], Xiaoqing Yang[1], Haibao Qiu[1], Kexin Huang[1], Qin Xu[1], Bin Zhou[1], Lulu Zhang[1], Man Zhou[1]* and Xiaoqing Yi[1,2]*

[1]College of Pharmacy, Gannan Medical University, Ganzhou, China, [2]Key Laboratory of Prevention and Treatment of Cardiovascular and Cerebrovascular Diseases, Gannan Medical University, Ganzhou, China

Background: Recently, various combination therapies for tumors have garnered popularity because of their synergistic effects in improving therapeutic efficacy and reducing side effects. However, incomplete intracellular drug release and a single method of combining drugs are inadequate to achieve the desired therapeutic effect.

Methods: A reactive oxygen species (ROS)-sensitive co-delivery micelle (Ce6@PTP/DP). It was a photosensitizer and a ROS-sensitive paclitaxel (PTX) prodrug for synergistic chemo-photodynamic therapy. Micelles size and surface potential were measured. In vitro drug release, cytotoxicity and apoptosis were investigated.

Results: Ce6@PTP/DP prodrug micelles exhibited good colloidal stability and biocompatibility, high PTX and Ce6 loading contents of 21.7% and 7.38%, respectively. Upon light irradiation, Ce6@PTP/DP micelles endocytosed by tumor cells can generate sufficient ROS, not only leading to photodynamic therapy and the inhibition of tumor cell proliferation, but also triggering locoregional PTX release by cleaving the thioketal (TK) bridged bond between PTX and methoxyl poly (ethylene glycol). Furthermore, compared with single drug-loaded micelles, the light-triggered Ce6@PTP/DP micelles exhibited self-amplified drug release and significantly greater inhibition of HeLa cell growth.

Conclusion: The results support that PTX and Ce6 in Ce6@PTP/DP micelles exhibited synergistic effects on cell-growth inhibition. Thus, Ce6@PTP/DP micelles represent an alternative for realizing synergistic chemo-photodynamic therapy.

KEYWORDS

polymeric prodrug, ROS-sensitive, synergistic chemo-photodynamic therapy, self-amplified drug release, tumor cells

Introduction

Recently, biodegradable and biocompatible amphiphilic polymeric micelle-based drug delivery systems have attracted much interest because of their ability to promote drug utilization and alleviate side effects of chemotherapy has played an important role (Pan et al., 2019; Zhou et al., 2020; Chen et al., 2021). Although the drug delivery systems based on polymer micelles has been extensively studied and applied in the laboratories and the clinics, further advancements are required to overcome the drawbacks of low drug-loading capacity (DLC), premature drug leakage, and insufficient drug release at the normal site. Prodrugs are derivatives of native drugs that temporarily block drug activity by modifying the active site to reduce toxicity to normal tissues, currently accounting for ~10% drugs marketed globally. (Jubeh et al., 2020; Liu et al., 2022). Most chemotherapeutic agents exhibit poor water solubility and a short circulation lifetime owing to their innate hydrophobicity. Conversely, prodrug formulations generally exhibit good water solubility. Self-assembly of an amphiphilic polymeric prodrug can form micelles, which not only improves the dispersion and pharmacokinetic properties of chemotherapeutic drugs in aqueous conditions but also increase drug accumulation *in vivo via* the permeability enhancement and retention (EPR) effect at the lesion site (Wang K. et al., 2019; Wang H. et al., 2020; Peng et al., 2021).

The self-assembled polymeric prodrug micelles are very stable in a physiological environment and can reduce unwanted drug leakage of drugs before reaching tumor tissue, thereby effectively inhibiting side effects of chemotherapeutic drugs on normal cells (Sun et al., 2018; Shukla et al., 2022; Sun et al., 2022). The polymeric prodrug micelles not only have the advantages of improved chemical stability, high DLC and low side effects, but they can also be used as drug carriers, thereby constituting a multidrug codelivery system that can be used for combination therapy and for improving therapeutic efficacy (Li S. et al., 2020; Ma et al., 2021). Furthermore, polymeric prodrugs can be designed for exogenous (e.g., ultrasound and light) or endogenous [e.g., reactive oxygen species (ROS), reducing environment and enzymes] stimulus-responsive drug delivery to activate their toxicity and achieve controlled drug release at the tumor site (Yang et al., 2019; Ye et al., 2019; Cao et al., 2021). Previous studies have reported that the concentration of ROS in tumor cells is 10 times higher than that in normal cells owing to mitochondrial dysfunction and metabolic exuberance (Oddone et al., 2020; Palmer et al., 2020; Liang and Zhou, 2021). Therefore, the development of a ROS-sensitive prodrug micelle delivery system should facilitate the selective release of drugs in cancer cells over normal cells.

However, the concentration of ROS in cancer cells is insufficient to activate prodrug release, which is attributable to several factors, including tumor heterogeneity (Luo et al., 2019; Cao et al., 2021; Guo et al., 2021). Consequently, the frequent use of chemotherapeutic drugs can easily induce drug resistance in tumor cells (Jubeh et al., 2020; Zhang et al., 2021b; Li et al., 2021). Furthermore, single chemotherapy is inadequate for treating cancer (Wang M. et al., 2019; Zhang et al., 2021a; Pang et al., 2022). Therefore, combined chemotherapy and other treatments can effectively reduce the number of drugs used and improve treatment efficacy, such as photodynamic therapy (PDT) (Lee et al., 2021; Lv et al., 2022; Wu et al., 2022). ROS, which can induce tumor cell apoptosis or necrosis, can be produced by the reaction between photosensitizer and dissolved oxygen under light irradiation, defined as PDT. PDT is an important modality of cancer treatment owing to its advantages of minimal invasiveness and modulated phototoxicity that improves the quality of life and median survival time. (Zhou et al., 2020; Yi et al., 2021; Zhou et al., 2021; Zhou et al., 2022). PDT and chemotherapy are now emerging as new approaches to treating solid tumors. (Sun et al., 2020; Zuo et al., 2021). Therefore, ROS-sensitive multidrug polymeric prodrug delivery system can effectively kill two birds with one stone as it can not only perform PDT *via* controllable illumination, but also achieve tumor synergistic therapy by using the generated ROS to trigger the release of prodrugs for self-amplified drug release.

To promote the effectiveness of tumor synergistic therapy, we designed a novel ROS-sensitive polymeric prodrug micelle (Ce6@PTP/DP) with high DLC and self-amplified drug release. The multidrug delivery system comprised three parts: a ROS-sensitive polymeric prodrug methoxyl poly (ethylene glycol)-thioketal-paclitaxel (mPEG-TK-PTX, PTP), DSPE-mPEG (DP), and a traditional photosensitizer of chlorin e6 (Ce6), as illustrated in Scheme 1. The ROS-sensitive polymeric multidrug delivery system has the following advantages: 1) stability in blood circulation, excellent biocompatibility and high DLC (21.7% for PTX and 7.38% for Ce6); 2) PTX release from polymeric prodrug micelles can be effectively triggered under oxidative conditions or light irradiation by breaking the TK bond; 3) the hydrodynamic size of Ce6@PTP/DP micelles was 80.4 nm, which was stable and easily phagocytized by tumor cell; and 4) synergistic therapeutic efficacy of chemotherapy-PDT in HeLa cells.

Materials and methods

Materials

DSPE-mPEG (Mw:2000) and paclitaxel (PTX) were purchased from Xi'an Ruixi Biotechnology Technology Co., Ltd. (Xi'an, China). Methyl sulfoxide (DMSO), suberic acid, N, N′-dicyclohexylcarbodiimide (DCC), 4-dimethylaminopyridine (DMAP), 3-(4,5-dimethylthiazol-2-yl)-2,5-diphenyl tetrazolium bromide (MTT) was obtained from MACKLIN reagent (Shanghai, China). Dichloromethane, petroleum ether, ethyl acetate and the other reagents were analytical or HPLC grade, obtained from Guangdong Guanghua Technology Co., Ltd. (Guangdong, China).

Cell culture

Human cervical cancer carcinoma HeLa cells were cultured in high-glucose DMEM containing 10% fetal bovine serum (FBS) and maintained in a humid environment atmosphere of 5% CO_2 at 37°C.

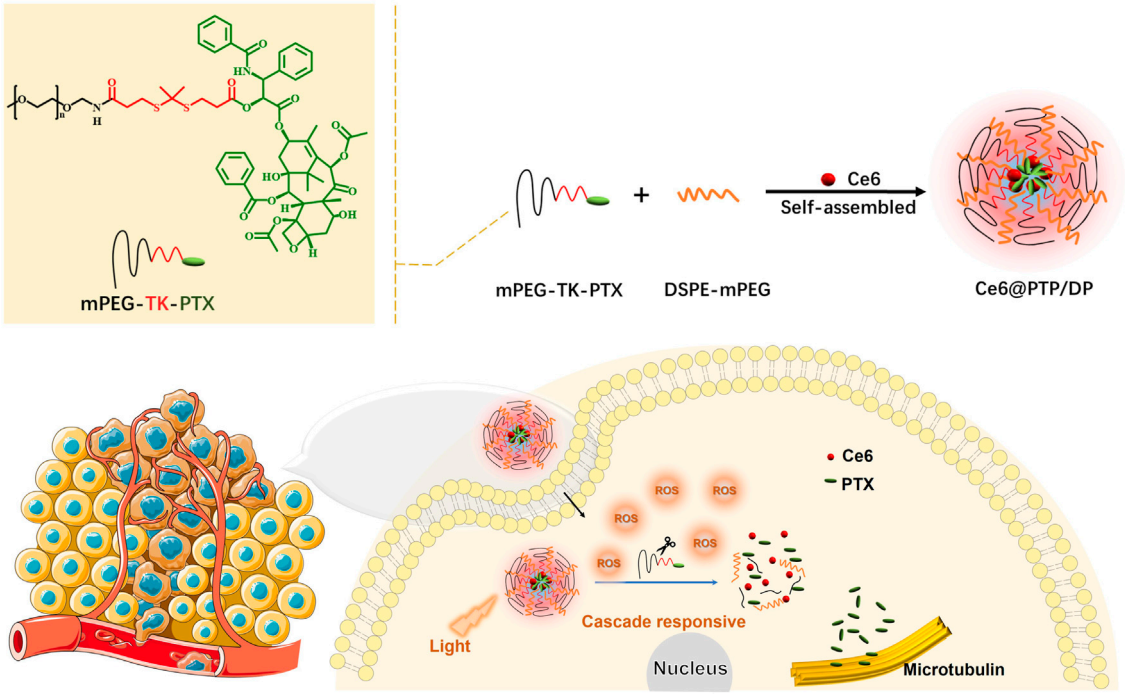

SCHEME 1
Ce6@PTP/DP self-assembly schematic diagram and its application in chemo-photodynamic therapy.

Characterizations

^{1}H NMR spectra (400 MHz, $CDCl_3$) were obtained by a spectrometer (Bruker AV-400, USA). Micelle's size, size distribution in aqueous solution were determined by dynamic light scattering (DLS, ZS90, Malvern). The morphology of the micelles was investigated by means of transmission electron microscopy (FEI Tecnai 12).

Synthesis of Thioketal (TK)

Briefly, 3-mercaptopropionic acid (5.31 g, 50 mmol) and anhydrous acetone (5.81 g, 100 mmol) were dissolved in dry hydrogen chloride and stirred for 3 h at room temperature. After that, when the color of the solution turns orange, it was put back to cold conditions for recrystallization. Then washed several times and the product was filtered with cold petroleum ether and water. Finally, the product was dried under a vacuum (Pei et al., 2018; Liu et al., 2022).

Synthesis of PTX-TK-COOH

The dry PTX (200.00 mg, 2.34 mmol), HOOC-TK-COOH (59.10 mg, 2.34 mmol), DMAP (2.86 mg, 0.234 mmol) were dissolved in 2 mL dry THF to the flask. DCC (531.10 mg, 2.57 mmol) was added slowly dropwise and condensed at 40°C with reflux stirring for 48 h under argon atmosphere. The reaction products were washed with ethyl acetate, then collected the filtrate to evaporated under reduced pressure. Then the crude product was obtained by filtration with ether. Finally, the crude product was purified by column chromatography (ethyl acetate: acetic acid = 100:1).

Synthesis of mPEG-TK-PTX (PTP)

NHS (22.89 mg, 0.20 mmol), EDC (19.69 mg, 0.20 mmol), PTX-TK-COOH (200.00 mg, 0.20 mmol) were dissolved in dry DMF and activated by stirring for 3 h. Then mPEG-NH_2 (200.00 mg, 0.20 mmol) was added and dialyzed after 48 h. The product was purified by HPLC (acetonitrile and water = 1:1).

Preparation of PTP, Ce6@DP and Ce6@PTP/DP Micelles

Typically, PTP (10 mg) was dissolved in DMSO (1 mL) and the mixture was added dropwise to ultrapure water (9 mL) under vigorous stirring. Then continued stirring for 30 min. Next, the solution was transferred to a dialysis bag (Mw:1000) and dialyze overnight to obtain PTP micelles. The same treatment noted that the loading photosensitizer needed to be protected from light: 1) Ce6 loaded DSPE-mPEG, called Ce6@DP. 2) Ce6 loaded mPEG-TK-PTX and DSPE-mPEG, named Ce6@PTP/DP. The concentration of PTX and Ce6 in each micelle was calculated by HPLC and UV-Vis.

Characterization of micelles morphology

The polymer micelles were observed using transmission electron microscopy (TEM). The samples were prepared as follows: the sample micelles of aqueous solution (0.5 mg/mL) were dropped on a copper grid and stained with 0.2% (w/v) phosphotungstic acid solution to observe the micelle morphology.

Measurement of micelles size and distribution and stability

The micelles size and distribution were determined by DLS at 25°C, 173°, and 633 nm with a helium-neon laser source. The concentration of PTP, Ce6@DP, and Ce6@PTP/DP were 1 mg/mL.

Release of PTX from Ce6@PTP/DP micelles

The release of PTX from PTP and Ce6@PTP/DP was measured by HPLC. The measurement was performed as follows: PTX release from PTP and Ce6@PTP/DP was measured by dialysis, 1 mL of freshly prepared PTP and Ce6@PTP/DP micelles solution was transferred into a dialysis bag (Mw: 1000) and then placed into 20 mL of release medium in aqueous solution and gently shaken at 37°C for 150 rpm. 1 mL of release solution was removed at a pre-set time and then supplemented with an equal amount of fresh release medium.

Hydrolysis reactions of Ce6@PTP/DP

The hydrolysis reaction of Ce6@PTP/DP was monitored by incubation in 10 mM H_2O_2 and white light (100 mW cm^{-2}) under different conditions of the hydrodynamic diameter as well as the distribution of Ce6@PTP/DP micelles.

Detection of ROS in solution

ABDA was used to test the generation of ROS. Typically, 15 μL of ABDA solution (4.5 mg/mL, DMSO) were added to the micelle of Ce6@PTP/DP, then the mixed solution (1.5 mL) were put in a small beaker and irradiated with white light (100 mW/cm^{-2}). Finally, the absorbance values were recorded every 1 min of irradiation to monitor the decomposition process of ABDA. The absorbance of ABDA was recorded and obtained the decay rate of the photsensitization process under white light (100 mW/cm^{-2}).

Intracellular ROS generation study at the cellular level

Treated centration of intracellular ROS was detected using 2′,7′-dichlorofluorescein diacetate (DCFH-DA) as a probe. The HeLa cells were seeded in 6-well plates and cultured for 24 h. The cells were incubated with PTP, Ce6@DP and Ce6@PTP/DP for 4 h, respectively. That the cells untreated were the control group. After treatment, the cells were washed three times with PBS. Then 10 μM DCFH-DA was added to replace the medium at 37°C for 30 min, followed by white light (100 mW/cm^{-2}, 10 min). Finally, the cells were cleaned three times with PBS, and then the fluorescence of DCFH-DA in the cells was detected with CLSM.

Cell uptake

HeLa cells were inoculated in cell culture dishes and incubated for 24 h Ce6@DP and Ce6@PTP/DP micelles were then added separately and incubated for another 4 h. The above cells were washed three times with PBS using Hoechst 33258, and then incubated for 20 min. Finally, the cells were further washed three times with pre-chilled PBS for CLSM observation.

Cytotoxicity assay

In vitro cytotoxicity of all drug forms on cancer HeLa cells was assayed by MTT. HeLa cells were inoculated on 96-well plates at a density of 5×10^3 cells per well and cultured overnight. First, the cells were treated with different concentrations of PTX, PTP, Ce6@DP and Ce6@PTP/DP. After 48 h of incubation, 10 μL of MTT (5 mg/mL) was added to each well and further incubated for 4 h. Finally, the absorbance of each well at 490 nm was measured by microplate readout. In another experiment, the cells were incubated with PTX, PTP, Ce6@DP and Ce6@PTP/DP for 4 h, followed by irradiation at white light (100 mW/cm^{-2}, 10 min). After further incubation for 48 h, cell viability was determined by MTT method.

Apoptosis detection

Annexin V-FITC and PI were used to assess the cell viability of the HeLa cells. The cells were cultured overnight in 6-well plates at 2.0×10^5 cells per well. Then, the cells were incubated with PTP, Ce6@DP and Ce6@PTP/DP (PTX or Ce6 equivalent dose 5 μg/mL and 1.7 μg/mL) for 24 h. After 15 min of reaction at room temperature according to the instructions of the Annexin V-FITC Apoptosis Assay Kit. Finally, the samples mixed and placed on the ice were detected by flow cytometry (BD FACS Canto II, USA) within 1 h.

Hemolysis assays

The hemocompatibility of PTP, Ce6@DP and Ce6@PTP/DP at different concentrations were studied by hemolysis assay. Freshly mice blood was diluted by PBS and centrifuged to collect red blood cells (RBCs). 2% RBC suspension was used for hemolysis study. Then, these micelles were added and mixed by vortex and incubated at 37°C for 6 h. Then mixtures were centrifuged at 1200 rpm for 10 min. The supernatant was collected and amount of hemoglobin released was recorded on an enzyme Markers at 510 nm and 540 nm. Double-distilled water was used as positive control and PBS was used as negative control.

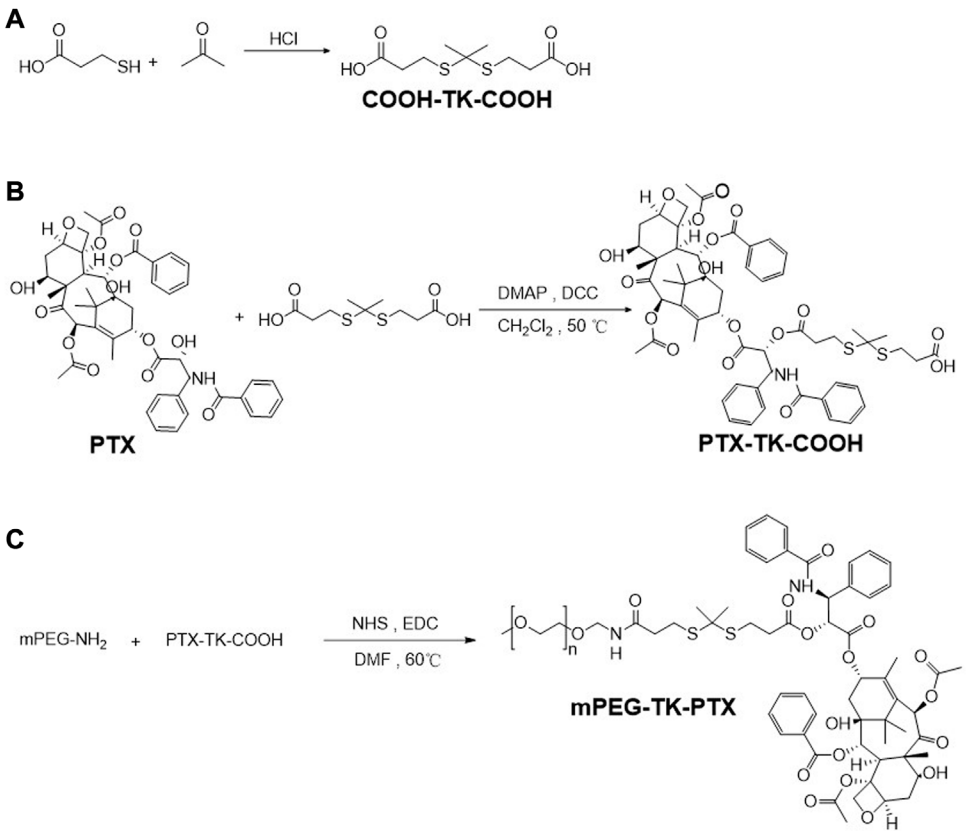

FIGURE 1
The synthesis routs of TK **(A)**, PTX-TK-COOH **(B)**, and mPEG-TK-PTX **(C)**, respectively.

The hemolysis ratio of RBCs was calculated according to the following formula: Hemolysis (%) = $(A_{sample}–A_{negative})/(A_{positive}–A_{negative}) \times 100\%$, where, A_{sample} was the absorbance of sample, $A_{negative}$ was the absorbance of negative control and $A_{positive}$ was the absorbance of positive control. All hemolysis experiments were carried out in triplicate.

Statistical analysis and data availability

All values in the text are described as mean ± standard deviation (SD) and were analyzed using GraphPadPrism 5.01 software. Statistical analysis was performed using one-way ANOVA followed by Dunnett's comparison test. $p < 0.05$ is different (*), $p < 0.01$ is significantly different (**), $p < 0.001$ is significantly different (***).

Results and discussion

Synthesis of TK, PTX-TK-COOH, mPEG-TK-PTX (PTP)

To obtain the ROS-sensitive polymeric prodrug micelle (Ce6@PTP/DP), Ce6 with excellent capacity for PDT and ROS-sensitive PTX prodrug for enhanced chemotherapy-PDT were utilized. The polymeric prodrug PTP was synthesized, and its detailed synthesis is presented in Figure 1. First, the ROS-sensitive linker of TK was synthesized, and the ^{1}H NMR spectrum of TK was consistent with that reported in previous reports (Supplementary Figure S1) (Li Y. et al., 2020; Xu et al., 2020; Zhang et al., 2022). Then, the ROS-sensitive prodrug PTX-TK-COOH was obtained *via* a condensation reaction between PTX (^{1}H NMR result shown in Supplementary Figure S2) and TK, and the chemical framework of PTX-TK-COOH was clarified using the ^{1}H NMR result (Figure 2A) which revealed that the peak of the 2′-hydroxyl group of PTX at 3.6 ppm vanished and the signal of 2′-CH shifted from 4.7 to 5.9 ppm (Cao et al., 2018; Chang et al., 2020). Furthermore, the signals at δ 1.52 and δ 5.52 were attributed to methyl protons belonging to the TK structure and methyne proton belonging to the C2′(CH)-OH of PTX, respectively. Moreover, the appearance of the mass spectrum peak at 1105.4036 ($[M + NH_4]^+$, calculated 1105.4032) and 1110.3577 ($[M + Na]^+$, calculated 1110.3586) confirmed that PTX-TK-COOH was successfully synthesized and that the esterification reaction between PTX and TK occurred at the 2′-hydroxyl group of PTX (Figure 2B). Then, the ROS-sensitive polymeric prodrug of PTP was synthesized by reacting mPEG-NH_2 (^{1}H NMR result shown in Supplementary Figure S3) with PTX-TK-COOH. The characteristic signals of PEG, TK, and PTX at δ 3.57, 2.5–2.8, and 7.31–8.10, respectively, appeared in the spectrum of PTP (Figure 2C), indicating its successful preparation. Furthermore, the matrix-assisted laser desorption/ionization time

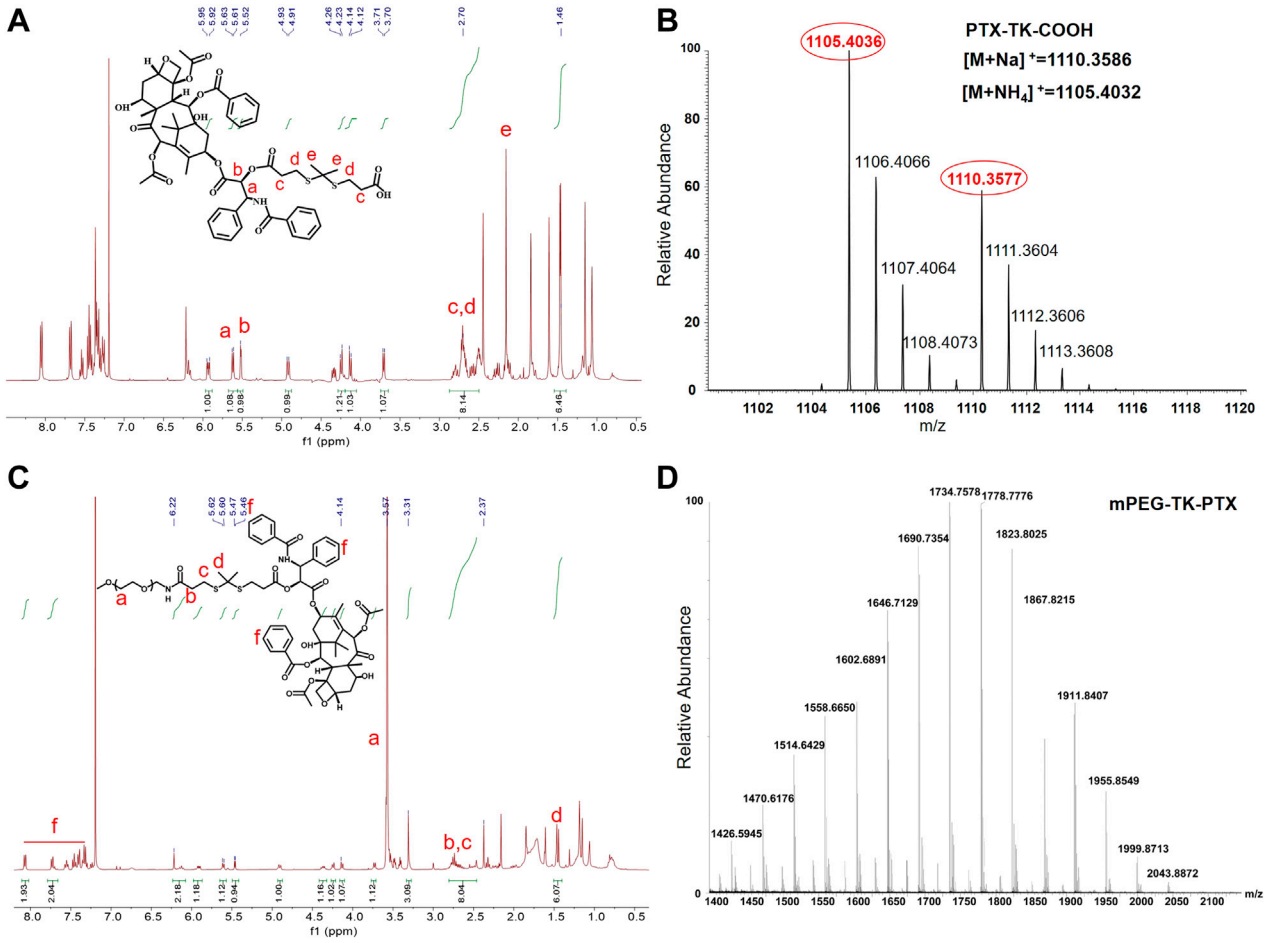

FIGURE 2
(A) ^{1}H NMR spectrum (400 MHz, $CDCl_3$) of PTX-TK-COOH. **(B)** Mass spectrum (MS) of PTX-TK-COOH. **(C)** ^{1}H NMR spectrum (400 MHz, $CDCl_3$) of mPEG-TK-PTX. **(D)** MS of mPEG-TK-PTX.

of flight mass spectrometry spectrum revealed that the molecular weight of PTP was 1734.8 Da (Figure 2D). These findings imply that the ROS-sensitive amphiphilic polymer prodrug PTP was successfully synthesized.

Preparation PTP, Ce6@DP and Ce6@PTP/DP micelles

The ROS-sensitive multifunction polymeric micelles with the function of self-amplified drug release comprising Ce6, PTP and DP, were termed Ce6@PTP/DP. The control micelles without the chemotherapeutic drug PTX comprised Ce6 and DP, and were referred to as Ce6@DP. Only PTP constituted another control micelle without the function of ROS generation. The above micelles were acquired *via* dialysis in aqueous solution. The characterizations of PTP, Ce6@DP and Ce6@PTP/DP micelles are shown in Figure 3A; Table 1. The hydrodynamic sizes of PTP, Ce6@DP and Ce6@PTP/DP micelles were 30.9 ± 1.3 nm (PDI = 0.057 ± 0.038), 29.4 ± 1.0 nm (PDI = 0.134 ± 0.053), and 80.4 ± 2.2 nm (PDI = 0.217 ± 0.006), respectively.

Stability evaluation of the micelles

The stability of the Ce6@PTP/DP micelles for synergistic chemo-photodynamic therapy was monitored at room temperature for 1 week. The hydrodynamic size of Ce6@DP and Ce6@PTP/DP micelles did not significantly change during a week (Supplementary Figure S4; Figure 3B), indicating that the Ce6@PTP/DP micelles with PEG shell exhibited good stability in an aqueous environment, and their adequate size enabled their enrichment at the tumour site owing to improved enhanced permeability and retention (EPR) effect. Furthermore, transmission electron miscroscopy (TEM) images confirmed that the Ce6@DP and Ce6@PTP/DP micelles exhibited obvious spherical boundaries (Figures 3C,D), with sizes of ~10 and 20 nm, respectively. The smaller size measured *via* TEM compared with that measured *via* dynamic light scattering (DLS) results can be primarily attributed to the shrinkage of the PEG shell upon drying. The absorption peak of the Ce6@PTP/DP micelles in aqueous solution at 402 nm was mainly attributed to the characteristic absorption of Ce6, and a strong fluorescence peak was observed at 684 nm (Supplementary Figures S5, S6). The DLC of Ce6 in the

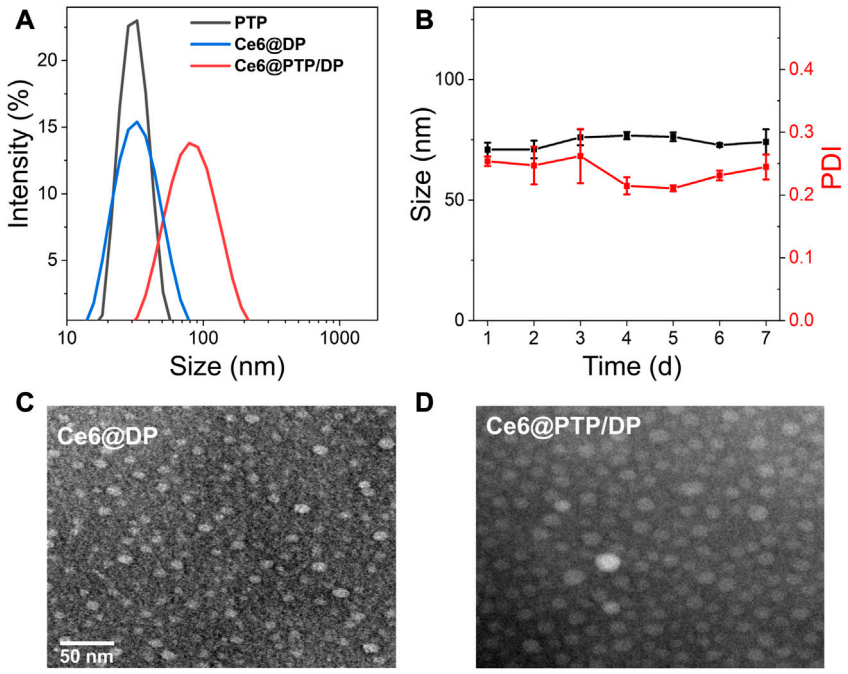

FIGURE 3
(A) Size distribution PTP, Ce6@DP and Ce6@PTP/DP. **(B)** Seven-day size change of Ce6@PTP/DP. Data represent the mean ± s.d (n = 3). **(C, D)** TEM images of Ce6@DP and Ce6@PTP/DP. Scale bar: 50 nm.

TABLE 1 Properties of the PTP, Ce6@DP and Ce6@PTP/DP micelles.

Samples	DLC (wt%)		Mass ration (PTX: Ce6)	Size (nm)	PDI
	PTX	Ce6			
PTP	46.9	/[a]	/[a]	30.9 ± 1.3	0.057 ± 0.038
Ce6@DP	/[b]	6.42	/[b]	29.4 ± 1.0	0.134 ± 0.053
Ce6@PTP/DP	21.7	7.38	2.94	80.4 ± 2.2	0.217 ± 0.006

[a]No Ce6 was encapsulated in the PTP, micelles.
[b]No PTX, was encapsulated in the Ce6@DP, micelles.

Ce6@DP and Ce6@PTP/DP micelles were determined using the standard curve of UV-Vis absorption of Ce6, which were 6.42% and 7.38%, respectively (Table 1; Supplementary Figure S7). The PTP and Ce6@PTP/DP micelles exhibited high DLC for PTX, reaching up to 46.9% and 21.7%, respectively, which were significantly higher than that of conventional nanomedicine (usually ≤10%, w/w). These results indicate that the prepared polymeric prodrug micelles have good stability and excellent DLC for synergistic chemo-photodynamic therapy.

ROS production in solution

The production of ROS under light irradiation was analyzed in an aqueous solution using the ROS indicator, 9,10-anthracenediylbis (methylene)dimalonic acid (ABDA) *via* UV-Vis spectrophotometer. ABDA effectively merges with ROS, lowering its characteristic UV-Vis absorption peaks at 378 and 400 nm. Therefore, the reduction in the characteristic peak absorption intensity of ABDA is equivalent to the amount of ROS produced under light irradiation. The characteristic peaks at 378 and 400 nm of the anthracene moiety in ABDA reduced with increasing of irradiation duration (Supplementary Figure S8). After 5.5 min of light irradiation, the absorption intensity at 400 nm declined by ≥ 40%. When the illumination time was extended to 10.5 min, the absorption intensity decreased by ~60%, thereby confirming that the polymeric prodrug micelles stacked with the photosensitizer Ce6 exhibited satisfactory ROS production under light irradiation for PDT.

In vitro release of PTX from PTP and Ce6@PTP/DP micelles

The effects of different environments on the *in vitro* release of PTX from PTP and Ce6@PTP/DP micelles were investigated under

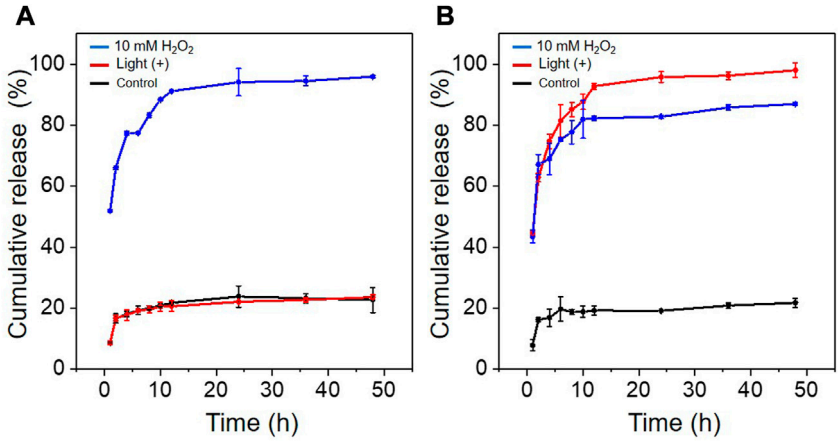

FIGURE 4
(A) Cumulative release of PTX from PTP under different conditions. **(B)** Cumulative release of PTX from Ce6@PTP/DP under different conditions: control (without light and H_2O_2); white light, 100 mW/cm^{-2}, 10 min; 10 mM H_2O_2.

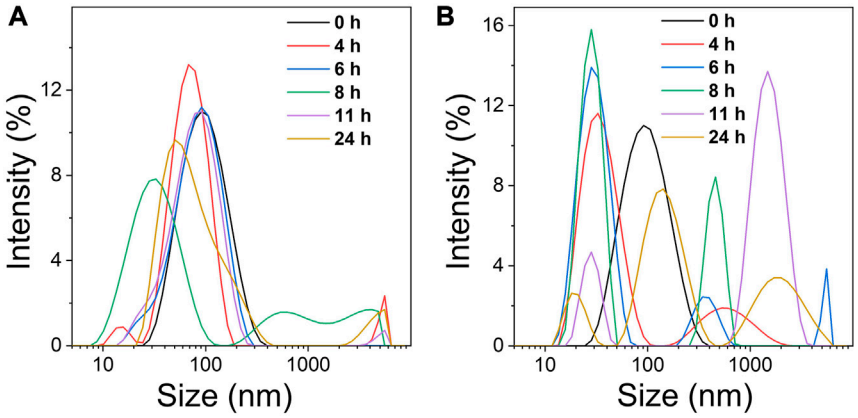

FIGURE 5
(A) Changes in the micelle size distribution of Ce6@PTP/DP at different times under 10 mM H_2O_2. **(B)** Changes in the micelle size distribution of Ce6@PTP/DP at different times under white light (100 mW/cm^{-2}), respectively.

the condition of 10 mM H_2O_2 and light irradiation by HPLC. As shown in Figures 4A, B, When PTP and Ce6@PTP/DP micelles were not treated by light irradiation or H_2O_2, the release of PTX was greatly inhibited, 21.74% and 22.62% of PTX was released within 48 h, which indicated that the polymeric prodrug micelles had good stability and sufficient protection ability for drug leakage of PTX. However, the release of PTX increased considerably under 10 mM H_2O_2 and light stimulation, as can be seen in the PTP micelles with 23.6% and 95.9% release within 48 h, respectively. However, Ce6@PTP/DP micelles released 86.9% and 98.0% within 48 h. This indicates that the release capacity of PTX can be stimulated under oxidative conditions, which helps to achieve the controlled release of drugs and improve the therapeutic efficiency. The reason why the release of PTX can be triggered under oxidative conditions is mainly attributed to the fact that the TK functional group is oxidized and the link between PTX and PEG is cut off. The above shows that light irradiation can not only perform PDT, but also trigger the release of PTX to achieve self-amplified release of drug.

Light-triggered changes of the Ce6@PTP/DP micelles

TK, a sulfhydryl-based ROS-sensitive functional group, has often been used for ROS-sensitive drug delivery (Wang D. et al., 2020). The introduction of TK between PEG and PTX to prepare the prodrug PTP, induces a cascade reaction which cleaves PTP upon ROS production. Thus, the ROS produced *via* PDT induces the degradation of the Ce6@PTP/DP micelles to facilitate PTX release. Consequently, DLS was used to assess the behavior of ROS production of the Ce6@PTP/DP micelles. The change in the

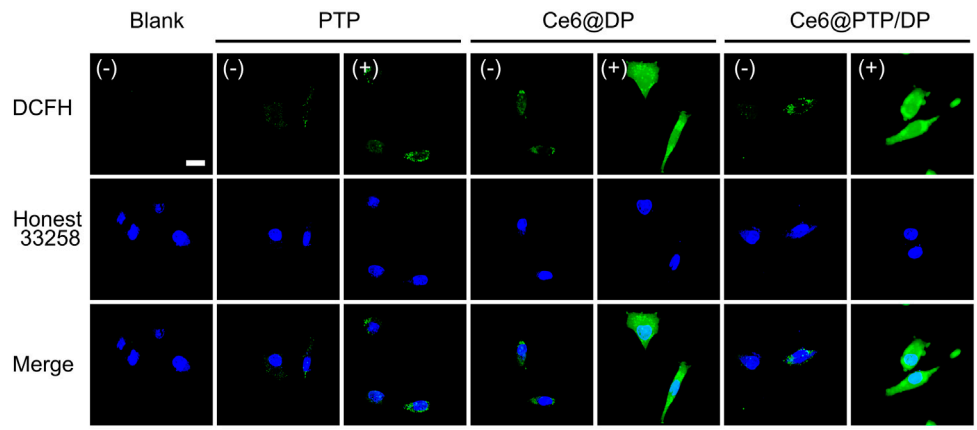

FIGURE 6
ROS generation studies of PTP, Ce6@DP and Ce6@PTP/DP micelles in HeLa cells. Using DCFH-DA as general ROS fluorescence indicators (green) and the nuclei were stained by Hoechst 33258 (blue), respectively.

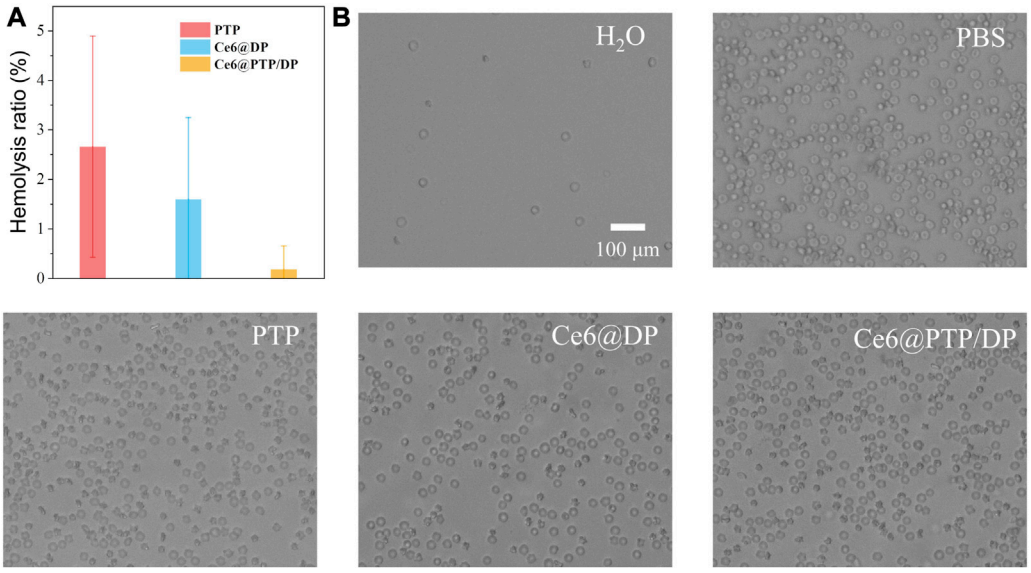

FIGURE 7
(A) The hemolysis ratio induced by PTP, Ce6@DP, Ce6@PTP/DP micelles incubated at 37°C for 6 h in dark. Data represent the mean ± s.d (n = 3). **(B)** Optical microscopic observation of the dispersion states of the erythrocytes after incubated with H_2O, PBS, PTP, Ce6@DP, Ce6@PTP/DP micelles for 6 h. Scale bar: 100 μm.

size of the Ce6@PTP/DP micelles in response to H_2O_2 and light irradiation was monitored over time. The Ce6@PTP/DP micelles exhibited significant size change at a H_2O_2 concentration of 10 mM (Figure 5A). After the micelles were infused with H_2O_2 for 4 h, the maximum size of the multiple peaks increased up to ~5000 nm, probably owing to the oxidation of the TK group by H_2O_2, which influences to the separation of hydrophilic and hydrophobic chain segments of the Ce6@PTP/DP micelles, leading to the breakdown of the micellar structure. Furthermore, the change in size of the Ce6@PTP/DP micelles in response to light irradiation was identified *via* DLS (Figure 5B). As ROS produced *via* PDT under light irradiation can influence the degradation of the TK group, thereby disrupting the self-assembly of the Ce6@PTP/DP micelles, as presumed, the signal of DLS becomes more complex. For example, after 4 h of light irradiation, a new signal peak of ~800 nm appears. Furthermore, a new signal peak at ~5000 nm appears after 6 h of light irradiation. These findings indicate that the prepared Ce6@PTP/DP micelles undergo oxidation in response to H_2O_2 and light irradiation,

10.3389/fbioe.2023.1168192

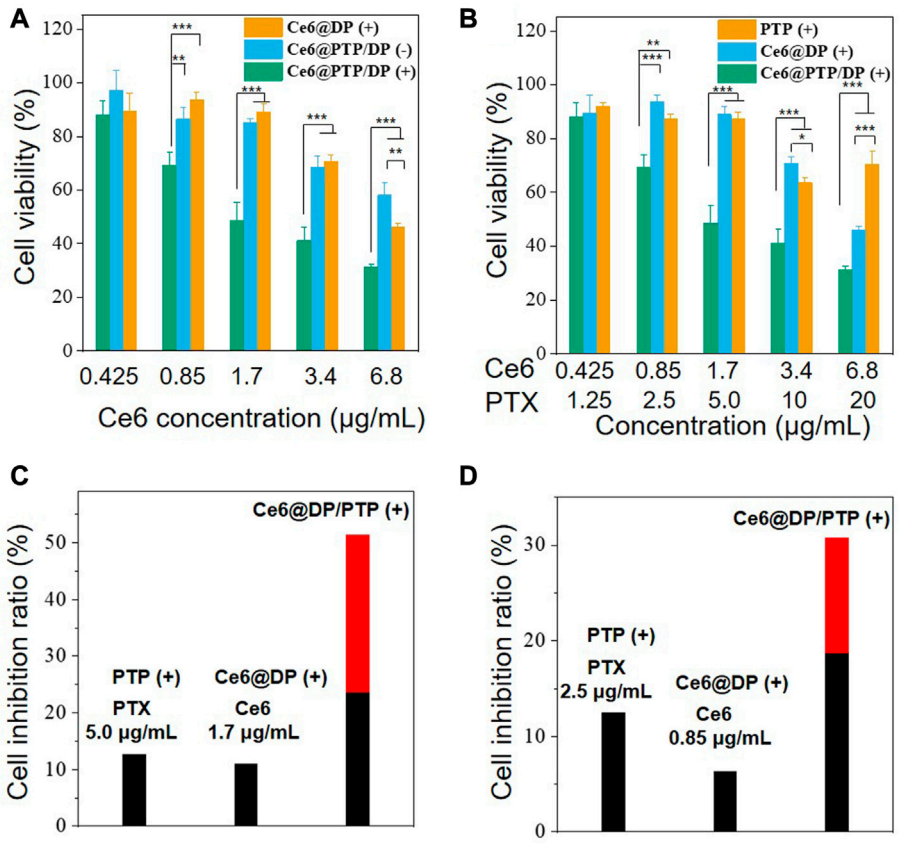

FIGURE 8
(A) MTT assay of Free PTX, PTP, and PTP (+) (white light, 100 mW cm^{-2}, 10 min) in HeLa cells after incubation for 48 h **(B)** MTT assay of Ce6@PTP/DP, Ce6@DP (+) and Ce6@PTP/DP (+) (white light, 100 mW cm^{-2}, 10 min) in HeLa cells after incubation for 48 h. Data represent the mean ± s.d (n = 3), $*p < 0.05$, $**p < 0.01$, $***p < 0.001$, respectively. **(C, D)** The inhibition ratios of PTP (+), Ce6@DP (+), Ce6@PTP/DP (+) micelles treated cells upon light (white light, 100 mW cm^{-2}, 10 min). The red bar denotes the additional cell inhibition ratio gained whenCe6@PTP/DP micelles upon light irradiation are combined, compared with the sum of PTP, Ce6@DP micelles upon light irradiation (white light, 100 mW cm^{-2}, 10 min), respectively.

suggesting that ROS produced *via* PDT can influence the degradation of micelles.

ROS production of the prepared micelles *in vivo*

Efficient drug uptake by tumor cells is a recommended feature of prepared micelles. The cellular uptake of the Ce6@PTP/DP and Ce6@DP micelles was observed *via* confocal laser scanning microscopy (CLSM) in HeLa cells. Bright fluorescence signals for the Ce6@PTP/DP and Ce6@DP micelles were observed in the cytoplasm *via* CLSM, whereas almost no fluorescence signals were observed in the nuclear region (Supplementary Figure S9). This may be because of the fact that the diameter of the nuclear pore complex is 10 nm, and the size of the Ce6@PTP/DP and Ce6@DP micelles is much larger than that, which is why fluorescence signals of the nano-micelle is hardly detected in the cell nucleus area. CLSM was used to determine the ROS production ability of the PTP, Ce6@DP and Ce6@PTP/DP micelles under white light irradiation using 2′, 7-dichlorofluorescein acetate (DCFH-DA) as a fluorescence probe. The intrinsic fluorescence intensity of DCFH-DA is very low, however, it can be oxidized to DCF with strong green fluorescence in the presence of ROS. Therefore, the ability of the prepared polymeric micelles to produce ROS can be indirectly demonstrated by monitoring the fluorescence intensity of intracellular DCF. When the cells were treated with DCFH-DA only in the absence of light, there was some green fluorescence in the cells. This was because intracellular enzymes or natural antioxidants scavenge these oxygen radicals in normal cells. The fluorescence signals detected *via* CLSM after all the micelles were incubated with HeLa cells were very weak without light irradiation, suggesting that the proportion of ROS produced was very small, and insufficient to oxidize the ROS fluorescent probe DCFH-DA (Figure 6). However, the green fluorescence signals of the Ce6@DP and Ce6@PTP micelles were incubated in HeLa cells under light irradiation were markedly improved, thereby signifying that the polymeric micelles loaded with Ce6 produced a large proportion of ROS and could oxidize DCFH-DA. However, unlike the Ce6@DP andCe6@PTP/DP micelles, the fluorescence signals of the PTP micelles in HeLa cells were very weaker following light irradiation. These results indicate that the Ce6@PTP/DP micelles exhibit satisfactory ROS production in cells and can be further employed for combination therapy.

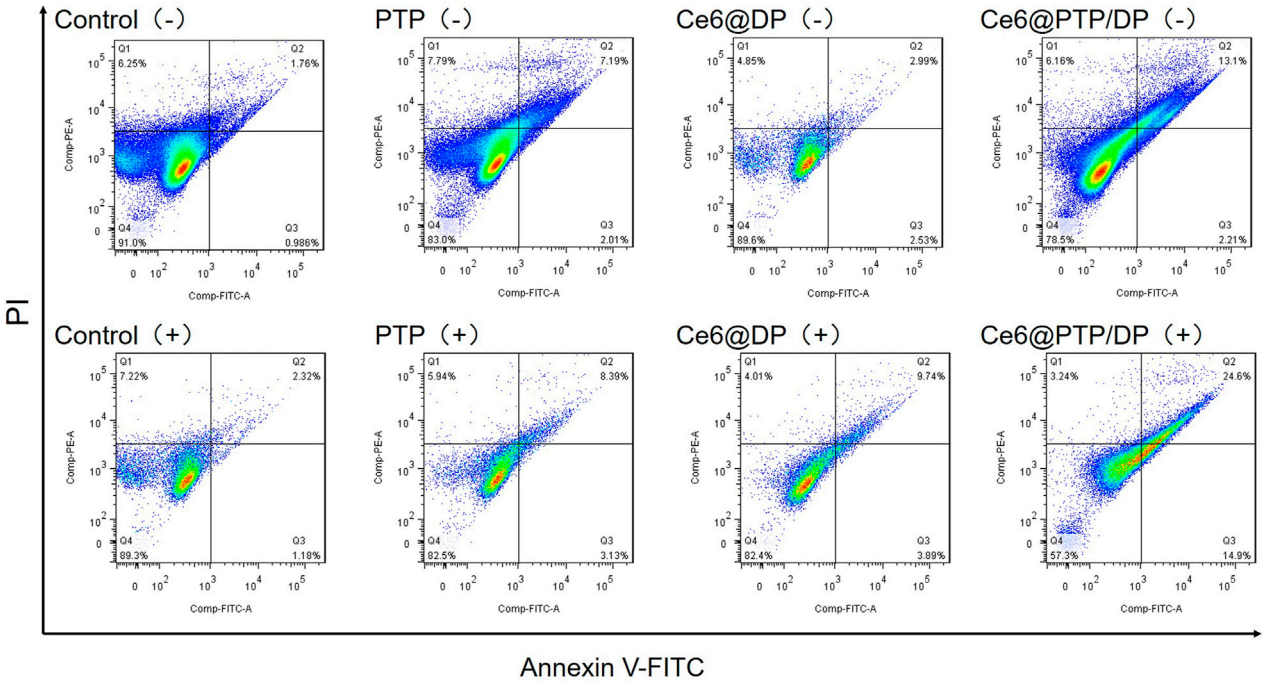

FIGURE 9
Apoptosis of HeLa cells induced by PTP, Ce6@DP, Ce6@PTP/DP for 48 h (–) (without light irradiation), and (+) (white light, 100 mW cm^{-2}, 10 min).

Hemolysis test

Good blood compatibility is a prerequisite of polymeric prodrug micelles for clinical application. The PTP, Ce6@DP and Ce6@PTP/DP were incubated with red blood cell solution at 37°C for 6 h in the dark, and the rate of hemolysis was determined *via* UV-Vis measurement of the hemoglobin released from damaged red blood cells (Figure 7). Generally, the lower the rate of hemolysis, better the blood biocompatibility of polymeric prodrug micelles, and these micelles can be intravenously administered when the hemolysis rate is ≤ 10%. Almost no heme was found to be released into the supernatant after the PTP, Ce6@DP and Ce6@PTP/DP micelles were incubated with the red blood cells (Supplementary Figure S10). Furthermore, the hemolysis rate of the PTP, Ce6@DP and Ce6@PTP/DP micelles was <5%, morphology of the red blood cells was intact after following incubation, and proportion of red blood cells was equivalent to phosphate-buffered saline. These findings suggest that the Ce6@PTP/DP micelles have good blood biocompatibility, and can be delivered to the lesion site in a passively targeted manner *via* intravenous administration.

In vitro cytotoxicity assay

To investigate the synergistic effect of the PTX prodrug and Ce6 photosensitizer, an MTT assay was performed to determine the cytotoxicity of free PTX, and the PTP, Ce6@DP, and Ce6@PTP/DP micelles in HeLa cells. Compared with the condition of without light irradiation, cell viability did not reduce following light irradiation, and cell viability was >90%, implying that the HeLa cell activity was not hindered following light irradiation for 10 min (white light, 100 mW cm^{-2}) (Supplementary Figure S11). Furthermore, the cytotoxicity of free PTX, PTP (–) (without light irradiation), and PTP (+) (white light, 100 mW cm^{-2}, 10 min) was dose-dependent. Compared with the PTP (–) and PTP (+) groups, free PTX demonstrated more inhibition, probably owing to the extended release of PTX from PTP (Supplementary Figure S12). There was no substantial difference between the effect of PTP (–) and PTP (+) on HeLa cell proliferation signifying that irradiation did not affect the cytotoxicity of the PTP micelles. Subsequently, for the Ce6@DP micelles, Ce6@DP (–) exhibited minimal effects on cell proliferation, with a concentration of Ce6 up to 6.8 μg mL^{-1}, whereas Ce6@DP (+) effectively hinders tumor cell growth, implying that the ROS produced by Ce6@DP under light irradiation can effectively kill tumor cells and play a role in PDT (Supplementary Figure S13; Figure 8A). For the Ce6@PTP/DP micelles, their inhibitory effect was augmented by light irradiation, comparable with that of the Ce6@DP micelles (Figure 8A). The cytotoxicity of the PTP, Ce6@DP, and Ce6@PTP/DP micelles in HeLa cells under light irradiation was further used to assess the synergistic effect of chemo-photodynamic therapy. Ce6@PTP/DP (+) demonstrated enhanced cytotoxicity compared with that of PTP (+) and Ce6@DP (+) (Figure 8B). This result indicates that the codelivery system comprising the photosensitizer and chemotherapeutic prodrug can effectively merge chemo-photodynamic therapy to achieve synergistic treatment. Furthermore, the chemo-photodynamic therapy group of Ce6@PTP/DP (+) produced a higher cell inhibition ratio than that of the sum of the chemotherapy group of PTP (+) and the PDT group

of Ce6@DP (+) at the concentrations of PTX and Ce6 of 2.63 and 1.42 μg mL^{-1}, respectively (red bar represents the increased cell inhibition ratio) (Figure 8C). The findings of the cell inhibition ratio was comparable with that of PTP (+), Ce6@PTP (+), and Ce6@PTP/DP (+) with the concentrations of PTX and Ce6 of 2.5 and 0.85 μg mL^{-1}, respectively, in HeLa cells (Figure 8D). Thus, these results indicate that the ROS-sensitive cascaded multi-drug delivery system Ce6@PTP/DP micelles exhibit great potential for synergistic chemo-photodynamic therapy.

Subsequently, the ability of micelles to induce apoptosis in HeLa cells under various treatments was evaluated using Annexin V-FITC/PI. Apoptosis was calculated as the percentage of early and late apoptosis. As was shown in Figure 9, control (−) and control (+) were 2.75% and 3.50%, which expressed the similar rate before and after light exposure. Apoptosis increased to 9.20% and 11.52% for the chemotherapy group of PTP (−) and PTP (+) respectively compared to the control group. The release of PTX from PTP is thought to be responsible for the inhibition observed. Then the PDT group of Ce6@DP (−) and Ce6@DP (+) were 5.52% and 13.62%. We demonstrate that apoptosis of cells can occur in PDT. But the chemo-PDT group of Ce6@PTP/DP (−) and Ce6@PTP/DP (+) showed increasingly grow from 15.31% to 39.30%. We also acknowledge that the rate of apoptosis in the Ce6@PTP/DP group under light condition was higher than that in any of the PDT and chemotherapy group. Finally, examination results illustrate that PTP, Ce6@DP and Ce6@PTP/DP micelles have the same trend in apoptosis and cytotoxicity, which verifies our results from another view that the ROS-sensitive cascaded co-delivery system Ce6@PTP/DP micelles have amplify the release of chemotherapy drugs potential in synergistic chemotherapy-phototherapy.

Conclusion

In conclusion, we designed a polymeric prodrug co-delivery system, named Ce6@PTP/DP, which comprises ROS-sensitive PTX and Ce6 photosensitizer for the synergistic chemo-PDT against tumor cells. The Ce6@PTP/DP micelles produced a considerable amount of ROS with under light irradiation, which stimulated PDT, inhibited tumor cell proliferation, and triggered PTX release from the prodrug PTP, thereby improving its therapeutic effecacy. The Ce6@PTP/DP micelles exhibited good size uniformity in aqueous conditions; good stability and biocompatibility, satisfactory DLC for PTX and Ce6, which can be easily taken up by tumor cells; and excellent ROS production under light irradiation, which influences PTX release. Moreover, light irradiated Ce6@PTP/DP micelles significantly inhibited HeLa cell growth compared with single drug-loaded micelles of PTP and Ce6@DP. Thus, this ROS-sensitive cascaded multi-drug delivery system demonstrated a synergistic effect on HeLa cell growth inhibition. Overall, our findings demonstrated a facile strategy to develop ROS-sensitive co-delivery micelles with a cascade reaction to stimulate the adequate release of chemotherapeutic drugs that for synergistic chemo-photodynamic therapy.

Data availability statement

The original contributions presented in the study are included in the article/Supplementary Material, further inquiries can be directed to the corresponding authors.

Author contributions

XYi and MZ designed the research. CW, MZ, and XYi carried out the experiments. CW, QX, BZ, LZ, MZ, and XYi performed data analysis. XYa, HQ, and KH participated in cell experiments. CW, MZ, and XYi wrote the paper. All the authors checked the manuscript.

Funding

This research was supported by the Natural Science Foundation of Jiangxi Province of China (20224BAB216113), the Open Project of Key Laboratory of Prevention and Treatment of Cardiovascular and Cerebrovascular Diseases, Ministry of Education (Nos. XN201911; XN202018), the Research Fund of Gannan Medical University (No. QD201903), the Postgraduate Innovation Special Fund Project Fund of Gannan Medical University (No. YC2021-X016), the Science and Technology Project of the Education Department of Jiangxi Province (No. GJJ211537), University Student Innovation and Entrepreneurship Training Project Jiangxi Province (No. 202110413004), Undergraduate Science and Technology Innovation Project of Gannan Medical University (Nos. BKSZR001, BKSZR004, BKSRW10, BKSZR38).

Conflict of interest

The authors declare that the research was conducted in the absence of any commercial or financial relationships that could be construed as a potential conflict of interest.

Publisher's note

Supplementary material

The Supplementary Material for this article can be found online at: https://www.frontiersin.org/articles/10.3389/fbioe.2023.1168192/full#supplementary-material

References

Cao, Z., Li, D., Wang, J., and Yang, X. (2021). Reactive oxygen species-sensitive polymeric nanocarriers for synergistic cancer therapy. *Acta. Biomater.* 130, 17–31. doi:10.1016/j.actbio.2021.05.023

Cao, Z., Ma, Y., Sun, C., Lu, Z., Yao, Z., Wang, J., et al. (2018). ROS-sensitive polymeric nanocarriers with red light-activated size shrinkage for remotely controlled drug release. *Chem. Mater* 30 (2), 517–525. doi:10.1021/acs.chemmater.7b04751

Chang, N., Zhao, Y., Ge, N., and Qian, L. (2020). A pH/ROS cascade-responsive and self-accelerating drug release nanosystem for the targeted treatment of multi-drug-resistant colon cancer. *Drug Deliv.* 27 (1), 1073–1086. doi:10.1080/10717544.2020.1797238

Chen, E., Wang, T., Zhang, J., Zhou, X., Niu, Y., Liu, F., et al. (2021). Mitochondrial targeting and pH-responsive nanogels for Co-delivery of lonidamine and paclitaxel to conquer drug resistance. *Front. Bioeng. Biotechnol.* 9, 787320. doi:10.3389/fbioe.2021.787320

Guo, J., Dai, J., Peng, X., Wang, Q., Wang, S., Lou, X., et al. (2021). 9,10-Phenanthrenequinone: A promising kernel to develop multifunctional antitumor systems for efficient type I photodynamic and photothermal synergistic therapy. *ACS Nano* 15 (12), 20042–20055. doi:10.1021/acsnano.1c07730

Jubeh, B., Breijyeh, Z., and Karaman, R. (2020). Antibacterial prodrugs to overcome bacterial resistance. *Molecules* 25 (7), 1543–3049. doi:10.3390/molecules25071543

Lee, D., Jang, S.-y., Kwon, S., Lee, Y., Park, E., and Koo, H. (2021). Optimized combination of photodynamic therapy and chemotherapy using gelatin nanoparticles containing tirapazamine and pheophorbide a. *ACS Appl. Mat. Inter.* 13 (9), 10812–10821. doi:10.1021/acsami.1c02316

Li, C., Wang, Y., Zhang, S., Zhang, J., Wang, F., Sun, Y., et al. (2021). pH and ROS sequentially responsive podophyllotoxin prodrug micelles with surface charge-switchable and self-amplification drug release for combating multidrug resistance cancer. *Drug Deliv.* 28 (1), 680–691. doi:10.1080/10717544.2021.1905750

Li, S, S., Shan, X., Wang, Y., Chen, Q., Sun, J., He, Z., et al. (2020). Dimeric prodrug-based nanomedicines for cancer therapy. *J. Control. Release* 326, 510–522. doi:10.1016/j.jconrel.2020.07.036

Li, Y, Y., Chen, M., Yao, B., Lu, X., Song, B., Vasilatos, S. N., et al. (2020). Dual pH/ROS-responsive nanoplatform with deep tumor penetration and self-amplified drug release for enhancing tumor chemotherapeutic efficacy. *Small* 16 (32), e2002188. doi:10.1002/smll.202002188

Liang, B., and Zhou, D. (2021). ROS-activated homodimeric podophyllotoxin nanomedicine with self-accelerating drug release for efficient cancer eradication. *Drug Deliv.* 28 (1), 2361–2372. doi:10.1080/10717544.2021.1995076

Liu, Y., Zhang, H., Cui, H., Zhang, F., Zhao, L., Liu, Y., et al. (2022). Combined and targeted drugs delivery system for colorectal cancer treatment: Conatumumab decorated reactive oxygen species sensitive irinotecan prodrug and quercetin Co-loaded nanostructured lipid carriers. *Drug Deliv.* 29 (1), 342–350. doi:10.1080/10717544.2022.2027573

Luo, C., Sun, B., Wang, C., Zhang, X., Chen, Y., Chen, Q., et al. (2019). Self-facilitated ROS-responsive nanoassembly of heterotypic dimer for synergistic chemo-photodynamic therapy. *J. Control. Release* 302, 79–89. doi:10.1016/j.jconrel.2019.04.001

Lv, J., Wang, S., Qiao, D., Lin, Y., Hu, S., and Li, M. (2022). Mitochondria-targeting multifunctional nanoplatform for cascade phototherapy and hypoxia-activated chemotherapy. *J. Nanobiotechnology* 20 (1), 42. doi:10.1186/s12951-022-01244-9

Ma, J., Chen, Y., Liang, W., Li, L., Du, J., Pan, C., et al. (2021). ROS-Responsive dimeric prodrug-based nanomedicine targeted therapy for gastric cancer. *Drug Deliv.* 28 (1), 1204–1213. doi:10.1080/10717544.2021.1937380

Oddone, N., Boury, F., Garcion, E., Grabrucker, A. M., Martinez, M. C., Da Ros, F., et al. (2020). Synthesis, characterization, and *in vitro* studies of an reactive oxygen species (ROS)-Responsive methoxy polyethylene glycol-thioketal-melphalan prodrug for glioblastoma treatment. *Front. Pharmacol.* 11, 574. doi:10.3389/fphar.2020.00574

Palmer, J. E., Brietske, B. M., Bate, T. C., Blackwood, E. A., Garg, M., Glembotski, C. C., et al. (2020). Reactive oxygen species (ROS)-Activatable prodrug for selective activation of ATF6 after ischemia/reperfusion injury. *ACS Med. Chem. Lett.* 11 (3), 292–297. doi:10.1021/acsmedchemlett.9b00299

Pan, Y., Wang, X., and Yin, Z. (2019). Synthesis and evaluation of cationic polymeric micelles as carriers of lumbrokinase for targeted thrombolysis. *Asian J. Pharm. Sci.* 14 (2), 144–153. doi:10.1016/j.ajps.2018.03.004

Pang, L., Zhang, L., Zhou, H., Cao, L., Shao, Y., and Li, T. (2022). Reactive oxygen species-responsive nanococktail with self-amplificated drug release for efficient Co-delivery of paclitaxel/cucurbitacin B and synergistic treatment of gastric cancer. *Front. Chem.* 10, 844426. doi:10.3389/fchem.2022.844426

Pei, Q., Hu, X., Zheng, X., Liu, S., Li, Y., Jing, X., et al. (2018). Light-activatable red blood cell membrane-camouflaged dimeric prodrug nanoparticles for synergistic photodynamic/chemotherapy. *ACS Nano* 12 (2), 1630–1641. doi:10.1021/acsnano.7b08219

Peng, J., Yin, Y., Liang, H., Lu, Y., Zheng, H., Wu, G., et al. (2021). Tumor microenvironment responsive pepper mild mottle virus-based nanotubes for targeted delivery and controlled release of paclitaxel. *Front. Bioeng. Biotechnol.* 9, 763661. doi:10.3389/fbioe.2021.763661

Shukla, S. K., Sarode, A., Wang, X., Mitragotri, S., and Gupta, V. (2022). Particle shape engineering for improving safety and efficacy of doxorubicin -A case study of rod-shaped carriers in resistant small cell lung cancer. *Biomater. Adv.* 137, 212850. doi:10.1016/j.bioadv.2022.212850

Sun, B., Luo, C., Yu, H., Zhang, X., Chen, Q., Yang, W., et al. (2018). Disulfide bond-driven oxidation- and reduction-responsive prodrug nanoassemblies for cancer therapy. *Nano Lett.* 18 (6), 3643–3650. doi:10.1021/acs.nanolett.8b00737

Sun, L., Zhao, P., Chen, M., Leng, J., Luan, Y., Du, B., et al. (2022). Taxanes prodrug-based nanomedicines for cancer therapy. *J. Control. Release* 348, 672–691. doi:10.1016/j.jconrel.2022.06.004

Sun, Y., Zhao, D., Wang, G., Wang, Y., Cao, L., Sun, J., et al. (2020). Recent progress of hypoxia-modulated multifunctional nanomedicines to enhance photodynamic therapy: Opportunities, challenges, and future development. *Acta Pharm. Sin. B* 10 (8), 1382–1396. doi:10.1016/j.apsb.2020.01.004

Wang, D., Wang, S., Xia, Y., Liu, S., Jia, R., Xu, G., et al. (2020). Preparation of ROS-responsive core crosslinked polycarbonate micelles with thioketal linkage. *Colloids Surf. B Biointerfaces* 195, 111276. doi:10.1016/j.colsurfb.2020.111276

Wang, H., Wang, K., He, L., Liu, Y., Dong, H., and Li, Y. (2020). Engineering antigen as photosensitiser nanocarrier to facilitate ROS triggered immune cascade for photodynamic immunotherapy. *Biomaterials* 244, 119964. doi:10.1016/j.biomaterials.2020.119964

Wang, K., Yang, B., Ye, H., Zhang, X., Song, H., Wang, X., et al. (2019). Self-strengthened oxidation-responsive bioactivating prodrug nanosystem with sequential and synergistically facilitated drug release for treatment of breast cancer. *ACS Appl. Mat. Inter.* 11 (21), 18914–18922. doi:10.1021/acsami.9b03056

Wang, M., Zhai, Y., Ye, H., Lv, Q., Sun, B., Luo, C., et al. (2019). High Co-loading capacity and stimuli-responsive release based on cascade reaction of self-destructive polymer for improved chemo-photodynamic therapy. *ACS Nano* 13 (6), 7010–7023. doi:10.1021/acsnano.9b02096

Wu, Y., Li, J., Zhong, X., Shi, J., Cheng, Y., He, C., et al. (2022). A pH-sensitive Supramolecular Nanosystem with Chlorin e6 and Triptolide Co-delivery for Chemo-photodynamic Combination Therapy. *Asian J. Pharm. Sci.* 17 (2), 206–218. doi:10.1016/j.ajps.2021.12.003

Xu, C., Song, R., Lu, P., Chen, J., Zhou, Y., Shen, G., et al. (2020). <p>A pH-responsive charge-reversal drug delivery system with tumor-specific drug release and ROS generation for cancer therapy</p>. *Int. J. Nanomedicine* 15, 65–80. doi:10.2147/IJN.S230237

Yang, B., Chen, Y., and Shi, J. (2019). Reactive oxygen species (ROS)-Based nanomedicine. *Chem. Rev.* 119 (8), 4881–4985. doi:10.1021/acs.chemrev.8b00626

Ye, H., Zhou, Y., Liu, X., Chen, Y., Duan, S., Zhu, R., et al. (2019). Recent advances on reactive oxygen species-responsive delivery and diagnosis system. *Biomacromolecules* 20 (7), 2441–2463. doi:10.1021/acs.biomac.9b00628

Yi, X., Zeng, W., Wang, C., Chen, Y., Zheng, L., Zhu, X., et al. (2021). A step-by-step multiple stimuli-responsive metal-phenolic network prodrug nanoparticles for chemotherapy. *Nano Res.* 15 (2), 1205–1212. doi:10.1007/s12274-021-3626-2

Zhang, B., Xue, R., and Sun, C. (2022). Rational design of ROS-responsive nanocarriers for targeted X-ray-induced photodynamic therapy and cascaded chemotherapy of intracranial glioblastoma. *Nanoscale* 14 (13), 5054–5067. doi:10.1039/d2nr00436d

Zhang, L., Du, X. F., Liu, B., Li, C., Long, J., Zhao, M. X., et al. (2021b). Engineering supramolecular nanomedicine for targeted near infrared-triggered mitochondrial dysfunction to potentiate cisplatin for efficient chemophototherapy. *ACS Nano* 16, 1421–1435. doi:10.1021/acsnano.1c09555

Zhang, L., Zhang, S., Li, M., Li, Y., Xiong, H., Jiang, D., et al. (2021a). Reactive oxygen species and glutathione dual responsive nanoparticles for enhanced prostate cancer therapy. *Mat. Sci. Eng. C. Mat. Biol. Appl.* 123, 111956. doi:10.1016/j.msec.2021.111956

Zhou, H., Li, Q., Cheng, X., Zhang, C., Sun, J., Du, L., et al. (2020). A janus upconverting nanoplatform with biodegradability for glutathione depletion, near-infrared light induced photodynamic therapy and accelerated excretion. *J. Mat. Chem. B* 8 (40), 9251–9257. doi:10.1039/d0tb01357a

Zhou, M., Wen, L., Wang, C., Lei, Q., Li, Y., and Yi, X. (2022). Recent advances in stimuli-sensitive amphiphilic polymer-paclitaxel prodrugs. *Front. Bioeng. Biotechnol.* 10, 875034. doi:10.3389/fbioe.2022.875034

Zhou, Y., Ren, X., Hou, Z., Wang, N., Jiang, Y., and Luan, Y. (2021). Engineering A photosensitizer nanoplatform for amplified photodynamic immunotherapy via tumor microenvironment modulation. *Nanoscale Horiz.* 6 (2), 120–131. doi:10.1039/d0nh00480d

Zuo, S., Wang, Z., An, X., Wang, J., Zheng, X., Shao, D., et al. (2021). Self-assembly engineering nanodrugs composed of paclitaxel and curcumin for the combined treatment of triple negative breast cancer. *Front. Bioeng.Biotechnol.* 9, 747637. doi:10.3389/fbioe.2021.747637

frontiers | Frontiers in Bioengineering and Biotechnology

TYPE Original Research
PUBLISHED 30 May 2023
DOI 10.3389/fbioe.2023.1208693

OPEN ACCESS

EDITED BY
Qitong Huang,
Gannan Medical University, China

REVIEWED BY
Xing-Huo Wang,
Qingdao University, China
Chenhui Wang,
Chongqing University, China

*CORRESPONDENCE
Qing Li,
1515012032@163.com
Zhiye Li,
xclzy@126.com
Hongqi Lin,
lhq9988@126.com

†These authors have contributed equally to this work

RECEIVED 19 April 2023
ACCEPTED 11 May 2023
PUBLISHED 30 May 2023

CITATION
Xu H, Ding X, Li L, Li Q, Li Z and Lin H (2023), Tri-element nanozyme PtCuSe as an ingenious cascade catalytic machine for the amelioration of Parkinson's disease-like symptoms.
Front. Bioeng. Biotechnol. 11:1208693.
doi: 10.3389/fbioe.2023.1208693

Tri-element nanozyme PtCuSe as an ingenious cascade catalytic machine for the amelioration of Parkinson's disease-like symptoms

Hongdang Xu[1†], Xin Ding[2†], Lingrui Li[3†], Qing Li[3*], Zhiye Li[3*] and Hongqi Lin[1*]

[1]Department of Anesthesiology, Henan Provincial People's Hospital, People's Hospital of Henan University, Central China Fuwai Hospital, Central China Fuwai Hospital of Zhengzhou University, Zhengzhou, Henan, China, [2]Department of Anesthesiology, Pain and Perioperative Medicine, The First Affiliated Hospital of Zhengzhou University, Zhengzhou, Henan, China, [3]The Application Center for Precision Medicine, The Second Affiliated Hospital of Zhengzhou University, Zhengzhou, Henan, China

Parkinson's disease (PD), as the second most common neurodegenerative disease after Alzheimer's, has become intractable with the increasing aging global population. The exploration of nanomedicine has broadened the opportunities for developing novel neuroprotective therapies. In particular, polymetallic functional nanomaterials have been widely used in the biomedicine field in recent years, exhibiting flexible and diversified functions and controllable properties. In this study, a tri-element nanozyme (PtCuSe nanozyme) has been developed with desirable CAT- and SOD-like activities for the cascade scavenging of reactive oxygen species (ROS). In particular, the nanozyme is suitable for relieving nerve cell damage by removing reactive oxygen species in cells and mitigating the behavioral and pathological symptoms in animal models of Parkinson's disease. Therefore, this ingenious tri-element nanozyme may have potential in the treatment of Parkinson's disease and other neurodegenerative diseases.

KEYWORDS

Parkinson's disease, nanozyme, PtCuSe, nerve cell damage, reactive oxygen species

1 Introduction

Reactive oxygen species (ROS), which are generated in the oxygen metabolism process, contain various species, including hydroxyl radical ($OH^{\cdot}$), monomorphic oxygen ($^1O_2$), hydrogen peroxide radical ($LOO^{\cdot}$), hydrogen peroxide lipid (LOOH), nitroperoxyl ($ONOO^-$), hypochlorous acid (HOCl), and ozone (O_3), (Han et al., 2022; Zhang et al., 2022). Although a moderate amount of ROS can promote cell growth and energy metabolisms, excessive ROS would damage cell structures like mitochondria and DNA, causing cell death or apoptosis. It is generally believed that the pathophysiological processes of many neurodegenerative diseases, such as Parkinson's disease, Alzheimer's disease, and amyotrophic lateral sclerosis, are also closely related with ROS (Li et al., 2022a; Emin et al., 2022).

Parkinson's disease (PD), as one of the most common neurodegenerative diseases worldwide, affects approximately 2% of people over 60 years of age (He et al., 2022a; Yuan

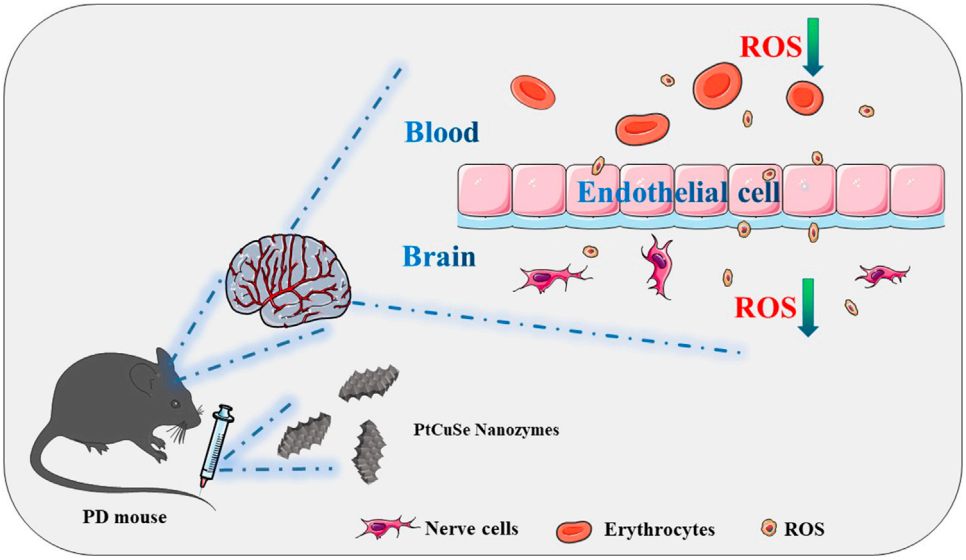

SCHEME 1
Schematic illustration of the application of the tri-element nanozyme PtCuSe as the cascade catalytic machine for PD symptom relief by ROS depletion.

et al., 2022). It is characterized by a wide spectrum of motor and non-motor symptoms, including resting tremors, bradykinesia, rigidity, cognitive impairments, and sleep disorders (Dilliard and Siegwart, 2023). It is believed that PD is caused by genetic and environmental factors, and the major neuropathological hallmark of PD is dopaminergic neuronal loss in the substantia nigra pars compacta (SNpc) (Wu et al., 2021; Cheng et al., 2022). However, recent studies have found that the occurrence and development of PD are closely related to oxidative stress and free radical generation. Patients with PD have high dopamine oxidation during metabolism to produce a large number of ROS, such as H_2O_2 and ultra-oxygen anion in the substantia nigra Fe^{2+}catalytic, to further generate hydroxyl free radicals with higher toxicity (Xiong et al., 2020; Olson et al., 2021). Therefore, solving the problem of accumulation of excess free radicals to reduce the intracellular ROS level and alleviate neuronal degeneration damage is expected to be an effective strategy for treating the symptoms and root causes of PD based on an antioxidant system (Bengoa-Vergniory et al., 2020).

As a promising natural enzyme substitute, nanozymes possess both enzymatic activities and the characteristics of nanomaterials (Li et al., 2021; He et al., 2022b). PtCu bimetallic nanoalloys (PtCu NAs) are a new kind of bimetallic alloy nanozyme. Compared with traditional metal nanozymes, the noble metal has stable surface properties and adjustable size, which is supposed to artificially control the active structure of the nanozymes, giving them higher biocompatibility and cell uptake rate. PtCu NAs have been proven to have a variety of enzymatic activities, including superoxide dismutase, and the ability to remove intracellular reactive oxygen species and reduce intracellular oxidative stress (Li et al., 2022b; Gao et al., 2023; Yang et al., 2023). Previous studies have shown that PtCu NAs play a decisive role in blocking the prion-like spreading of nerve cells, and this mechanism has been reported in Alzheimer's disease studies (Liu et al., 2021; Chen et al., 2022; Zhu et al., 2022). Obviously, in the future, PtCu NAs will play an irreplaceable role in more fields. Selenium is a constituent of glutathione peroxidase (GSH-Px) (Niu et al., 2021). Every mole of GSH-PX contains 4 g of selenium. Selenium is an important cofactor in GSH-PX and plays an unmatched role in catalyzing the redox reaction of reducing glutathione (GSH) with peroxide (Dringen et al., 2015; Peter et al., 2015; Sun et al., 2016). Therefore, it is an important cellular free radical scavenger in introducing selenium into PtCu nanozymes, which can improve biocompatibility and reduce biological toxicity (Huang et al., 2017; Hu et al., 2022). Therefore, PtCuSe shows great potential in catalyzing the generation of oxygen from over-produced hydrogen peroxide in cells, which reduces the damage caused by hydrogen peroxide to tissues and cells, solves the problem of accumulation of excess free radicals in order to reduce the intracellular ROS level and alleviate neuronal degeneration damage, and solves the problem of apoptosis in neurons in PD to a large extent (Ding et al., 2021; Xue et al., 2022; Yu et al., 2022).

Herein, the tri-element nanozyme PtCuSe was constructed as an ingenious cascade catalytic machine for the amelioration of Parkinson's disease-like symptoms. This catalytic machine was employed as the ROS scavenger both in *in vitro* and *in vivo*, effectively relieving oxidative damage and inflammatory reaction of nerve cells and significantly mitigating the behavioral and pathological symptoms of a PD mouse model (Scheme 1).

2 Results and discussion

PtCuSe nanozyme is a successful conversion based on PtCu nanoparticles, which not only retains the original advantages of low cytotoxicity but also has higher biological activity.

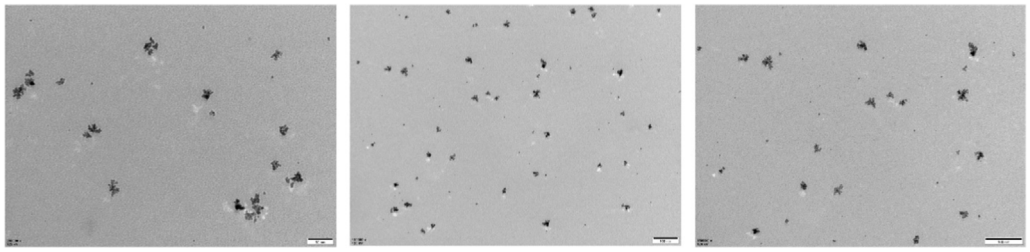

FIGURE 1
Transmission electron microscope (TEM) images of PtCuSe nanozymes.

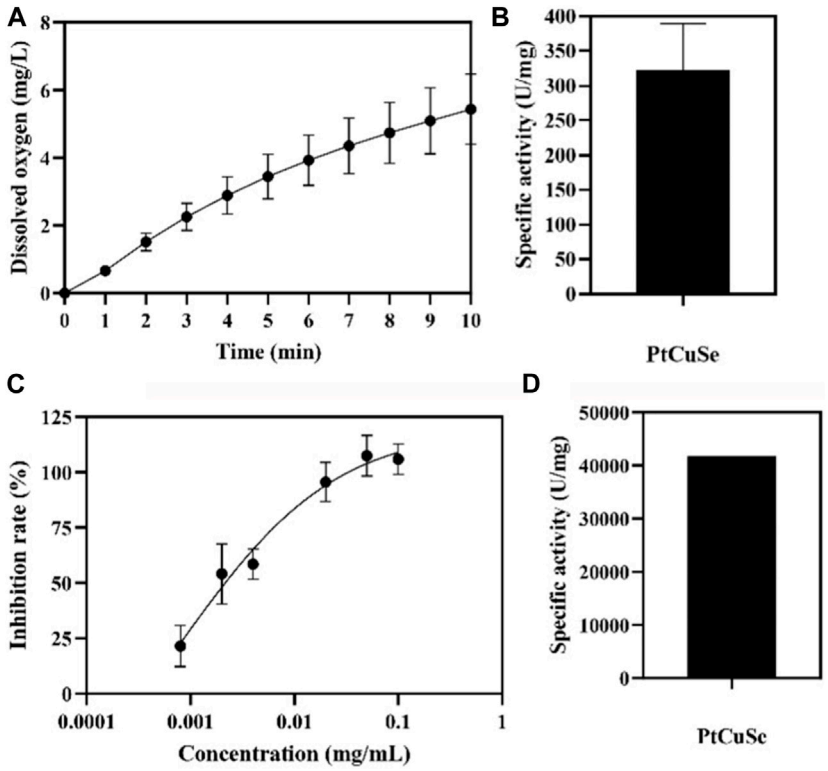

FIGURE 2
Enzymatic-like activity characterization of PtCuSe nanozyme. **(A,B)** CAT-like activity and **(C,D)** SOD-like activity of PtCuSe nanozyme.

Observation under an electron microscope showed that the structure of PtCuSe is regular and well-dispersed, and its surface character is of obvious consistency (Figure 1). The antioxidant capacity of PtCuSe is reflected in its catalytic activity for hydrogen peroxide reduction (CAT-like), superoxide dismutase (SOD-like), and free radical scavenging. PtCuSe predominantly achieves antioxidant function through the following two aspects: first, it encourages the decomposition of H_2O_2, which is a CAT-like activity and well reflected through the detection of the dissolved oxygen level. The dissolved oxygen content demonstrated a positive correlation with time and increased gradually. At the beginning of the recording, the dissolved oxygen content was 0, and when the reaction progresses, the dissolved oxygen approached 6 mg/L at 10 min. This exciting curve confirmed that PtCuSe is stable, strongly efficient, and extremely durable, and even if the concentration is very low, it still reaches a high level of enzyme activity. According to calculations, the catalytic capacity of H_2O_2 decomposition into H_2O and O_2 per mg of PtCuSe is almost identical to 320 U CAT. This result is amazing because such a high biological enzyme equivalent is considerably beyond expectations, which indicates that PtCuSe has substantial biological activity and broad research value (Figures 2A, B, respectively).

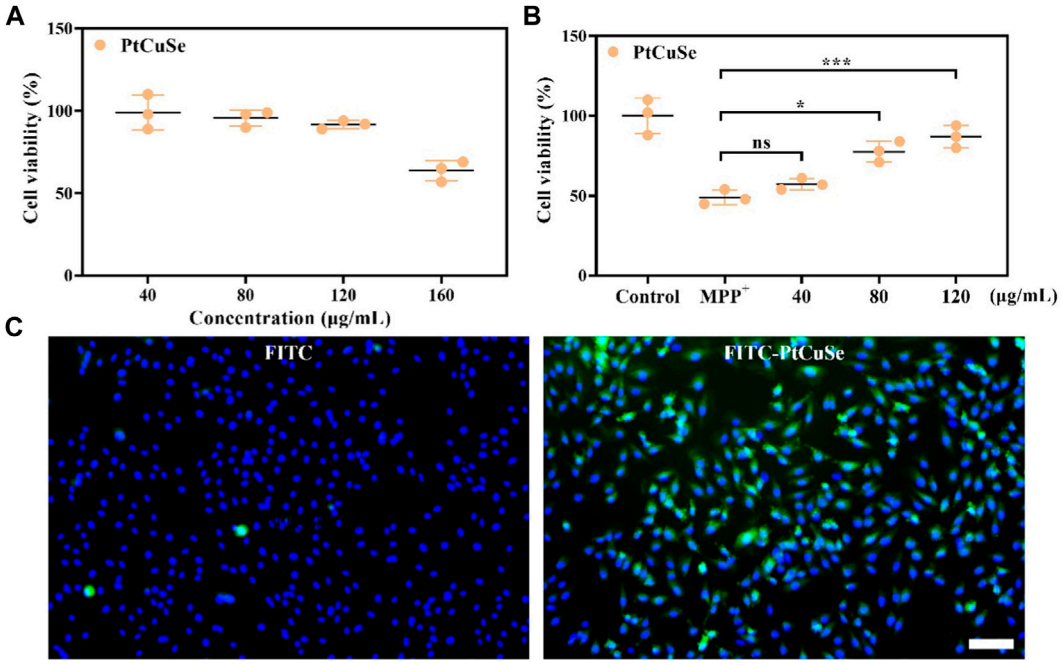

FIGURE 3
In vitro studies showing the neuron protection and cell uptake ability of PtCuSe. **(A)** Cell viability of SH-SY5Y cells under PtCuSe treatments of various concentrations. **(B)** Cell viability of SH-SY5Y cells under different treatment strategies and various concentrations. **(C)** Cell uptake of PtCuSe detected by fluorescent staining. The scale bar is 50 μm.

The rate of superoxide anion reduction is strongly associated with the activity of xanthine oxidase which is inhibited by SOD. Therefore, SOD-like activity is normally reflected by detecting the degree of inhibition of xanthine oxidase. The inhibition rate gradually increases with the increase in concentration and reaches 100% when the concentration of PtCuSe is 0.1 mg/mL. According to the inhibition curve, the SOD activity in the sample was calculated, and the activity of PtCuSe nanozyme per milligram was more than 40,000 U SOD. In conclusion, PtCuSe not only obtains an extremely high CAT-like activity but also possesses a potent superoxide dismutase activity, which prevents intracellular oxygen overload and reactive oxygen retention in numerous ways, plays a highly efficient antioxidant role, and blocks the pathological process believed to lead to PD (Figures 2C, D).

MTT assay was then employed to detect the cytotoxicity of PtCuSe in *in vitro* culture with different PtCuSe concentration gradients, and the appropriate concentration was determined by cell viability. When the concentration was less than 120 μg/mL, the cytotoxicity was negligible, so we concluded that this was an adequate dosing concentration for experimental requirements (Figure 3A). MTT assay also suggested that the cell viability was significantly reduced after treatment with MPP^+. However, when we incubated these cells with a range of concentrations of PtCuSe (40–120 μg/mL) in advance, a dose-dependent increase in cell viability could be observed (Figure 3B). Afterward, PtCuSe was again labeled with FITC to form FITC–PtCuSe composites and administered into cultured cells *in vitro*. A bright green fluorescence was observed under the laser confocal microscope, and after adjusting the field of view, it was found with great satisfaction that these fluorescence signals were located in the cell interior. The reason why there was high fluorescence in cells is that the unique nanometer scale of PtCuSe is satisfactory for cell endocytosis, so it is competent to have an extremely high cellular uptake rate, and it is this excellent cellular uptake rate that is the premise of PtCuSe to play an efficient role in the cell (Figure 3C).

Based on these successful data, we attempt to investigate the scavenging capability of PtCuSe for intracellular ROS. 1-Methyl-4-phenylpyridinium (MPP^+) was selected as a neurotoxin to generate neuronal cell damage phenotypes, which can lead to the increase in intracellular reactive oxygen species concentration and induce apoptosis of human neuroblastoma SH-SY5Y. A measure of 2 mM MPP^+ was added to the cell culture medium and co-incubated with the cells. As shown in the figure, the cell death was clearly evident. However, if the cells were treated with PtCuSe in advance and then co-incubated with MPP^+, the cell survival rate was substantially increased, which verified that PtCuSe had an excellent anti-neurotoxin MPP^+ effect. Then, 2-7-dichlorodihydrofluorescein diacetic acid (DCFH-DA) was added to monitor the oxidation status of cells to reflect the ROS content and to investigate the role of ROS in cell death induced by neurotoxin MPP^+ and the protection of cells by PtCuSe. The high content of ROS in MPP^+-treated SH-SY5Y cells occurred during cell death corresponding to SH-SY5Y incubated with PtCuSe composites. The content of ROS significantly diminished, which was comparable to the result of MPP^+, and confirmed the capability of PtCuSe composites to clear ROS (Figure 4A). Caspase-3 is an apoptotic protein, which plays

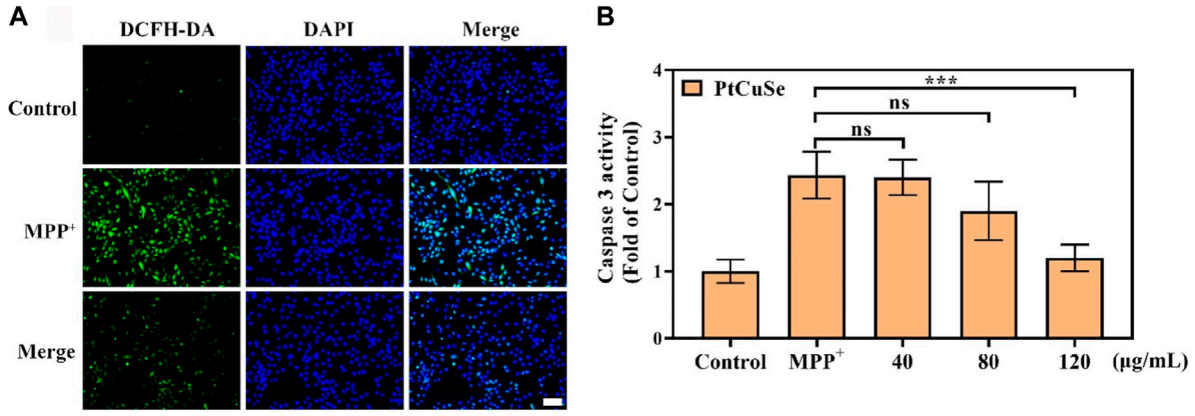

FIGURE 4
ROS clearance and protective ability against cell apoptosis after treatment with PtCuSe. **(A)** Intracellular ROS levels stained by DCFH-DA and detected using a laser scanning confocal microscope. The scale bar is 50 μm. **(B)** Caspase-3 activity in SH-SY5Y cells after various treatments.

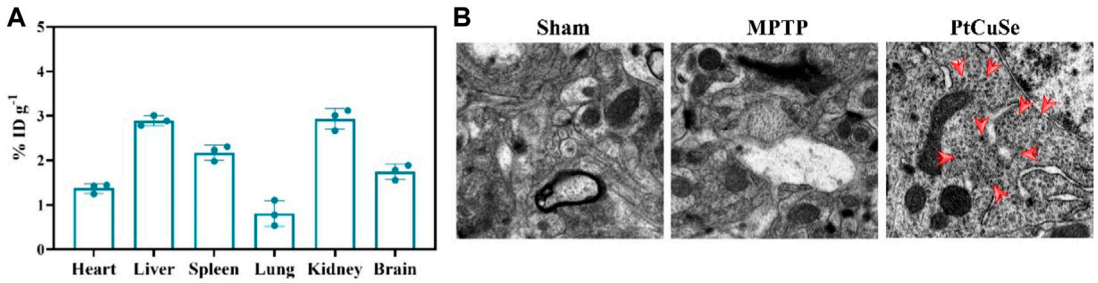

FIGURE 5
Biological distribution and brain enrichment effects after intravenous injection of PtCuSe nanoparticles. **(A)** Biodistribution of PtCuSe nanoparticles in major organs and brain detected by ICP-MS. **(B)** Bio-TEM images of the ultrathin section of brain lesion areas. The red arrows show the distribution of PtCuSe nanoparticles in the brain.

an irreplaceable role in the occurrence and regulation of cell apoptosis. Detection of its expression variation is capable of demonstrating the defensive effect of PtCuSe on MPP^+. As shown in the diagram, caspase-3 expression was significantly increased in SH-SY5Y cells treated with MPP^+ alone and markedly lower in PtCuSe-treated cells (Figure 4B). In conclusion, MPP^+ neurotoxin increased the content of intracellular ROS and caspase-3 and induced cell apoptosis, but PtCuSe promoted the decomposition of ROS to decrease intracellular ROS, prevented the expression of caspase-3, and diminished cell apoptosis.

BBB plays an important role in maintaining the healthy physiological state of the brain. However, BBB also influences or even prohibits the availability of PD therapeutic drugs by the brain. Thus, we then examined the BBB traverse ability of the nanosystem by detecting the biodistribution of PtCuSe in the brain and other organs. PD mouse models were established, and inductively coupled plasma mass spectrometry (ICP-MS) analysis was performed after *i.v.* administration of nanoparticles and obtaining major organs. As shown in Figure 5A, PtCuSe had desirable normalized dosage accumulation. Notably, most of the injected PtCuSe accumulated in the liver and kidney, which might attribute to the renal and hepatic uptake due to its nano-sized hydrophilicity diameter. In addition, bio-TEM also showed that the PtCuSe nanoparticles with high contrast inside the brain, indicating the desirable brain targeting capability of PtCuSe (Figure 5B).

Subsequently, the PD mouse model was established by MPTP stimulation, and PD-associated behaviors were assessed by the Morris water maze and open field test after treatment. These animals were divided into three groups: healthy mice (Sham group), MPTP-induced PD mice (MPTP), and PD mice *i.v.* injected with PtCuSe nanozymes (PtCuSe). PD mice exhibited random and disordered motor pathways and could not find the platform timely (Figure 6A). In contrast, the PtCuSe-treated mice reached the platform in a spatially oriented manner. Furthermore, the PtCuSe-treated mice showed improved mean speed (Figure 6B) and target of occupancy (Figure 6C) after treatment, indicating that PtCuSe significantly rescued motor impairments and memory loss in PD mice.

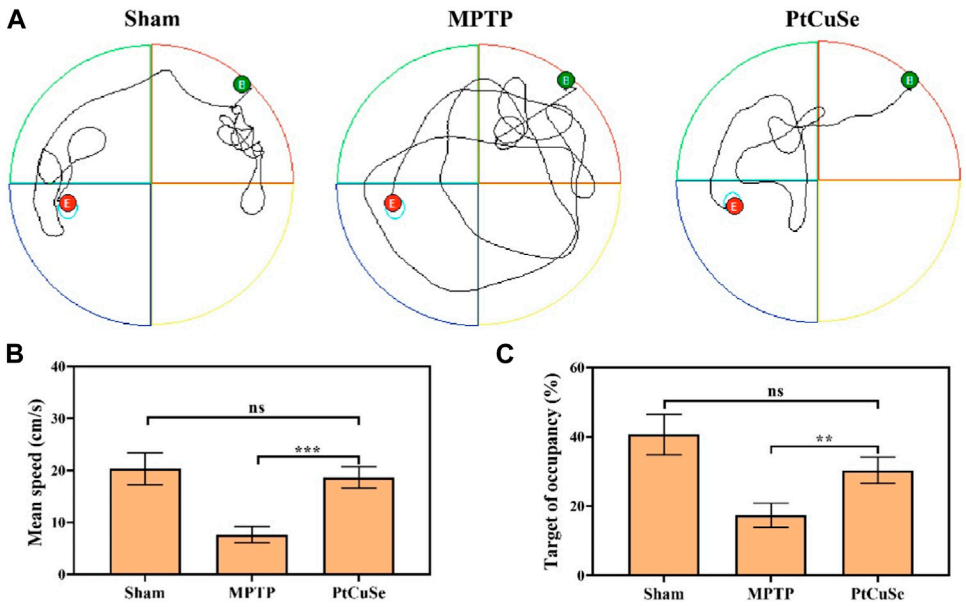

FIGURE 6
Behavioral assessment of PD mice after treatment with different formulations. The Morris water maze test was used to investigate the athletic and memory ability of PD mice. **(A)** Representative path tracing of mice, **(B)** mean time spent on the target quadrant, **(C)** and the relative time spent on the target quadrant.

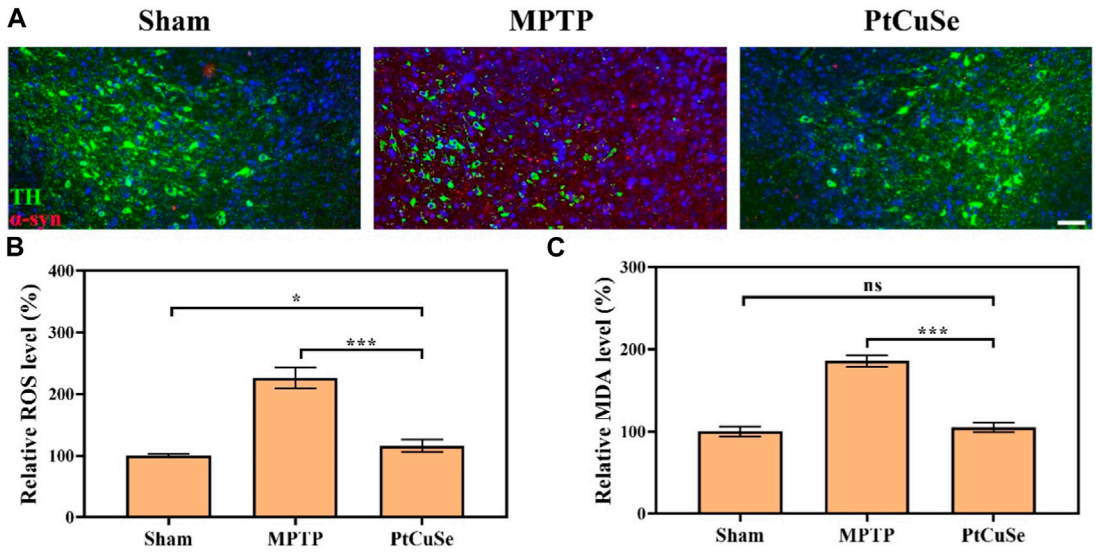

FIGURE 7
Pathological evaluation of PD mice after treatment with different formulations. **(A)** Co-immunoreactivity analysis after staining the brain sections with an anti-α-syn antibody and anti-TH antibody. The scale bar is 50 μm. **(B)** ROS levels in the SNpc. **(C)** MDA levels in the SNpc region.

To explore the therapeutic efficacy of PtCuSe, the PD mouse model was established via intraperitoneal injection of MPTP. The loss of dopaminergic neurons is the most immediate characteristic of PD, which is reflected by the reduction of TH-positive neurons in SNpc. In addition, the severity of PD can also be reflected by α-syn accumulation as the result of its close relationship with the loss of TH-positive neurons. Therefore, we evaluated the TH and α-syn levels in the SNpc and ST of different groups by co-immunofluorescence. Immunofluorescence in the SNpc suggested that the MPTP-treated mice showed reduced TH+ neurons but elevated α-syn levels, while the contents were reversed after PtCuSe treatment to an extent similar to those of healthy mice (Figure 7A). In addition, ROS and malondialdehyde (MDA) levels were also detected. It suggested that MPTP significantly elevated the peroxidation levels in the lesion site of the brain, which was reversed by the treatment of PtCuSe nanozymes (Figures 7B, C).

3 Conclusion

In conclusion, we successfully synthesized PtCuSe nanozymes with SOD- and CAT-like activities, which can be applied as an excellent cascade catalytic machine for the depletion of ROS in the lesion site of PD. The PtCuSe nanozyme has efficient cellular uptake in neurons, consistently and stably removing intracellular ROS and substantially enhancing cell viability. In addition, *in vivo* studies suggest that the PtCuSe nanozyme has satisfactory brain enrichment, thus alleviating both behavioral and pathological symptoms in PD mice after intravenous administration. Therefore, it is believed that PtCuSe provides a novel approach to the treatment and research of PD and opens up avenues for the application of a three-element nanozyme in the treatment of PD and other neurodegenerative diseases. In the future, PtCuSe is expected to be used in the treatment of early Parkinson's disease by injection to achieve the therapeutic goal of early treatment, early prevention, and early rehabilitation.

4 Materials and methods

4.1 Materials

DMEM and FBS were purchased from Gibco. Thiazolyl blue tetrazolium bromide (MTT) was purchased from Sigma-Aldrich. SH-SY5Y cells were purchased from Wuhan Pricella Life Technology Co., Ltd. 1-Methyl-4-phenyl-1,2,3,6-tetrahydropyridine (MPTP) hydrochloride and 2′,7'-dichlorodihydrofluorescein diacetate (DCFH-DA) were purchased from Sigma-Aldrich.

4.2 ROS detection

SH-SY5Y cells were treated with drugs at optimized concentrations for 6 h, followed by incubation with MPP^+ for another 4 h, and then stained with 3 μM DCFH-DA for 60 min at 37°C. Afterward, the ROS content in the cells was evaluated using a confocal laser scanning microscope (FV1200, Olympus, Japan).

4.3 Cell viability assay

SH-SY5Y cells were seeded into 96-well plates at a density of 8,000 cells/well overnight. Drugs were added to the cells for 6 h, and then, 2 mM MPP^+ was subsequently added and incubated for another 24 h. A measure of 20 μL of MTT solution (5 mg/mL) was added into each well and incubated at 37°C for another 4 h. Finally, dimethyl sulfoxide (DMSO) was used to dissolve the formed formazan crystal, and the absorbance at 492 nm was measured using a GF-M3000 microplate reader (Caihong, Shandong, China).

4.4 Construction and treatment of the Parkinson's disease (PD) model

All animal experiments were approved by the Institution Animal Ethics Committee of Zhengzhou University. Six week old C57BL/6 mice (Sipeifu Biotechnology Co., Ltd., Beijing, China) were fed in cages with controlled temperature and humidity. Before the investigation, the mice were subjected to rotarod performance on the rotation rod, and the mice which exhibited behavioral consistency were selected for subsequent studies. The mice were subjected to intraperitoneal MPTP injection (35 mg/kg/day for 5 consecutive days) to induce a PD-like phenotype.

4.5 Brain tissue distribution

PD-like phenotype mice were injected with PtCuSe (8 mg/kg) through the tail vein. Afterward, the mice in each group were euthanized, and the main organs were collected 24 h after injection. Then, the tissues were weighed and homogenized to calculate the percentage of injected dose per gram of tissue (%ID g^{-1}) by ICP-MS (Agilent 7800, China). Three mice from each group were euthanized for brain tissue collection.

4.6 Immunofluorescence analysis

The brains of the treated mice were collected and fixed with 4% paraformaldehyde for 72 h. Then, the SNpc tissues were embedded, and paraffin sections of 10 μm thickness were obtained. The block process was performed after antigen retrieval, in which the slides were incubated in 10% rabbit serum for 30 min at room temperature. Then, primary antibodies for TH (GB12181, Servicebio, China) and α-syn (ab212184, Abcam, China) were applied, and then the slices were washed and incubated with secondary antibodies. After counterstaining with DAPI for 10 min and sealing, the slides were observed using a panoramic section scanner.

4.7 Statistical analysis

GraphPad Prism 8.0.2 was utilized for all statistical analyses. The outcomes were compared via Student's *t*-tests. The significance was measured as $^*p < 0.01$, $^{**}p < 0.005$, $^{***}p < 0.001$, and $^{****}p < 0.0001$.

Data availability statement

The original contributions presented in the study are included in the article/Supplementary Material; further inquiries can be directed to the corresponding authors.

Ethics statement

All animal experiments were approved by the Institution Animal Ethics Committee of Zhengzhou University (License No. ZZU-LAC20221114).

Author contributions

HX and XD: complete research and manuscript writing; QL, ZL, and HL: proposed design concepts and manuscript writing; LL: reviewed the manuscript. All authors listed have made a substantial, direct, and intellectual contribution to the work and approved it for publication.

Funding

The authors acknowledge the financial support from the Youth Science Foundation Project of Henan Province (232300421285) and the Joint Project of Medical Science and Technology of Henan Province (LHGJ20220498).

Conflict of interest

The authors declare that the research was conducted in the absence of any commercial or financial relationships that could be construed as a potential conflict of interest.

Publisher's note

References

Bengoa-Vergniory, N., Faggiani, E., Ramos-Gonzalez, P., Kirkiz, E., Connor-Robson, N., Brown, L. V., et al. (2020). CLR01 protects dopaminergic neurons *in vitro* and in mouse models of Parkinson's disease. *Nat. Commun.* 11 (1), 4885. doi:10.1038/s41467-020-18689-x

Chen, J., Zhang, S., Chen, X., Wang, L., and Yang, W. (2022). A self-assembled fmoc-diphenylalanine hydrogel-encapsulated Pt nanozyme as oxidase- and peroxidase-like breaking pH limitation for potential antimicrobial application. *Chem* 28 (26), e202104247. doi:10.1002/chem.202104247

Cheng, G., Liu, Y., Ma, R., Cheng, G., Guan, Y., Chen, X., et al. (2022). Anti-parkinsonian therapy: Strategies for crossing the blood-brain barrier and nano-biological effects of nanomaterials. *Nanomicro Lett.* 14 (1), 105. doi:10.1007/s40820-022-00847-z

Dilliard, S. A., and Siegwart, D. J. (2023). Passive, active and endogenous organ-targeted lipid and polymer nanoparticles for delivery of genetic drugs. *Nat. Rev. Mater* 8, 282–300. doi:10.1038/s41578-022-00529-7

Ding, S., Liu, Z., Huang, C., Zeng, N., Jiang, W., and Li, Q. (2021). Novel engineered bacterium/black phosphorus quantum dot hybrid system for hypoxic tumor targeting and efficient photodynamic therapy. *ACS Appl. Mater Interfaces* 13 (8), 10564–10573. doi:10.1021/acsami.0c20254

Dringen, R., Brandmann, M., Hohnholt, M., and Blumrich, E. (2015). Glutathione-dependent detoxification processes in astrocytes. *Neurochem. Res.* 40, 2570–2582. doi:10.1007/s11064-014-1481-1

Emin, D., Zhang, Y. P., Lobanova, E., Miller, A., Li, X., Xia, Z., et al. (2022). Small soluble α-synuclein aggregates are the toxic species in Parkinson's disease. *Nat. Commun.* 13 (1), 5512. doi:10.1038/s41467-022-33252-6

Gao, X., Liu, Y., Li, Y., Jin, B., Jiang, P., Chen, X., et al. (2023). Piezoelectric nanozyme for dual-driven catalytic eradication of bacterial biofilms. *ACS Appl. Mater Interfaces* 15 (11), 14690–14703. doi:10.1021/acsami.2c21901

Han, G., Bai, K., Yang, X., Sun, C., Ji, Y., Zhou, J., et al. (2022). "Drug-Carrier" synergy therapy for amyloid- β clearance and inhibition of tau phosphorylation via biomimetic lipid nanocomposite assembly. *Adv. Sci. (Weinh)* 9 (14), e2106072. doi:10.1002/advs.202106072

He, C., Lin, X., Mei, Y., Luo, Y., Yang, M., Kuang, Y., et al. (2022). Recent advances in carbon dots for *in vitro*/vivo fluorescent bioimaging: A mini-review. *Front. Chem.* 10, 905475. doi:10.3389/fchem.2022.905475

He, X., Wang, X., Yang, L., Yang, Z., Yu, W., Wang, Y., et al. (2022). Intelligent lesion blood-brain barrier targeting nano-missiles for Alzheimer's disease treatment by anti-neuroinflammation and neuroprotection. *Acta Pharm. Sin. B* 12 (4), 1987–1999. doi:10.1016/j.apsb.2022.02.001

Hu, Y., Wang, K., and Ye, C. (2022). Four-in-One" nanozyme and natural enzyme symbiotic system of Cu(2-x) Se-GOx for cervical cancer therapy. *Chem* 28 (1), e202102885. doi:10.1002/chem.202102885

Huang, Y., Liu, C., Pu, F., Liu, Z., Ren, J., and Qu, X. (2017). A GO-Se nanocomposite as an antioxidant nanozyme for cytoprotection. *Chem. Commun. (Camb)* 53 (21), 3082–3085. doi:10.1039/c7cc00045f

Li, Q., Liu, Y., Dai, X., Jiang, W., and Zhao, H. (2021). Nanozymes regulate redox homeostasis in ROS-related inflammation. *Front. Chem.* 9, 740607. doi:10.3389/fchem.2021.740607

Li, Q., Shao, X., Dai, X., Guo, Q., Yuan, B., Liu, Y., et al. (2022). Recent trends in the development of hydrogel therapeutics for the treatment of central nervous system disorders. *NPG Asia Mater* 14 (1), 14. doi:10.1038/s41427-022-00362-y

Li, Q., Wu, T., Fan, X., Guo, X., Jiang, W., and Fan, K. (2022). Multifaceted nanozymes for synergistic antitumor therapy: A review. *Mater. Des.* 224, 111430. doi:10.1016/j.matdes.2022.111430

Liu, Y.-Q., Mao, Y., Xu, E., Jia, H., Zhang, S., Dawson, V. L., et al. (2021). Nanozyme scavenging ROS for prevention of pathologic α-synuclein transmission in Parkinson's disease. *Nano Today* 36, 101027. doi:10.1016/j.nantod.2020.101027

Niu, B., Liao, K., Zhou, Y., Wen, T., Quan, G., Pan, X., et al. (2021). Application of glutathione depletion in cancer therapy: Enhanced ROS-based therapy, ferroptosis, and chemotherapy. *Biomater* 277, 121110. doi:10.1016/j.biomaterials.2021.121110

Olson, K. E., Namminga, K. L., Lu, Y., Thurston, M. J., Schwab, A. D., de Picciotto, S., et al. (2021). Granulocyte-macrophage colony-stimulating factor mRNA and Neuroprotective Immunity in Parkinson's disease. *Biomater* 272, 120786. doi:10.1016/j.biomaterials.2021.120786

Peter, C., Braidy, N., Zarka, M., Welch, J., and Bridge, W. (2015). Therapeutic approaches to modulating glutathione levels as a pharmacological strategy in Alzheimer's disease. *Curr. Alzheimer Res.* 12, 298–313. doi:10.2174/1567205012666150302160308

Sun, H., Wang, Y., Hao, T., Wang, C., Wang, Q., and Jiang, X. (2016). Efficient GSH delivery using PAMAM-GSH into MPP-induced PC12 cellular model for Parkinson's disease. *Regen. Biomater.* 3, 299–307. doi:10.1093/rb/rbw032

Wu, J., Cui, X., Ke, P. C., Mortimer, M., Wang, X., Bao, L., et al. (2021). Nanomaterials as novel agents for amelioration of Parkinson's disease. *Nano Today* 41, 101328. doi:10.1016/j.nantod.2021.101328

Xiong, S., Liu, W., Zhou, Y., Mo, Y., Liu, Y., Chen, X., et al. (2020). Enhancement of oral bioavailability and anti-Parkinsonian efficacy of resveratrol through a nanocrystal formulation. *Asian J. Pharm. Sci.* 15 (4), 518–528. doi:10.1016/j.ajps.2019.04.003

Xue, Z. Y., Yu, J. L., Xia, Q. Q., Zhu, Y. Q., Wu, M. X., Liu, X., et al. (2022). Color-tunable binary copolymers manipulated by intramolecular aggregation and hydrogen bonding. *ACS Appl. Mater Interface* 14, 53359–53369. doi:10.1021/acsami.2c17600

Yang, Q. Y., Wan, C. Q., Wang, Y. X., Shen, X. F., and Pang, Y. H. (2023). Bismuth-based metal-organic framework peroxidase-mimic nanozyme: Preparation and mechanism for colorimetric-converted ultra-trace electrochemical sensing of chromium ion. *J. Hazard Mater* 451, 131148. doi:10.1016/j.jhazmat.2023.131148

Yu, J. L., Wu, M. X., Xue, Z. Y., Xia, Q. Q., Liu, X., and Wang, X. H. (2022). Supramolecular assembly-induced emission enhancement vesicles regulated by pincer-like hosts containing pillar[5]arenes. *Adv. Opt. Mater* 10, 2201496. doi:10.1002/adom.202201496

Yuan, J., Liu, H., Zhang, H., Wang, T., Zheng, Q., and Li, Z. (2022). Controlled activation of TRPV1 channels on microglia to boost their autophagy for clearance of alpha-Synuclein and enhance therapy of Parkinson's disease. *Adv. Mater* 34 (11), e2108435. doi:10.1002/adma.202108435

Zhang, Y., Li, Q., Han, C., Geng, F., Zhang, S., Qu, Y., et al. (2022). Superoxide dismutase@zeolite imidazolate framework-8 attenuates noise-induced hearing loss in rats. *Front. Pharmacol.* 13, 885113. doi:10.3389/fphar.2022.885113

Zhu, Y., Wang, Z., Zhao, R., Zhou, Y., Feng, L., Gai, S., et al. (2022). Pt decorated $Ti_3C_2T_x$ MXene with NIR-II light amplified nanozyme catalytic activity for efficient phototheranostics. *ACS Nano* 16 (2), 3105–3118. doi:10.1021/acsnano.1c10732

frontiers | Frontiers in Bioengineering and Biotechnology

TYPE Review
PUBLISHED 13 July 2023
DOI 10.3389/fbioe.2023.1233476

OPEN ACCESS

EDITED BY
Youbin Zheng,
Technion Israel Institute of Technology, Israel

REVIEWED BY
Leilei Shi,
Sun Yat-sen University, China
Bingxia Zhao,
Southern Medical University, China

*CORRESPONDENCE
Huaimin Liu,
huaiminliu@sina.com
Jingwen Tang,
tjw0371@163.com
Lihan Zhang,
13909421681@163.com

†These authors have contributed equally to this work and share first authorship

RECEIVED 02 June 2023
ACCEPTED 29 June 2023
PUBLISHED 13 July 2023

CITATION
Zhang L, Li X, Yue G, Guo L, Hu Y, Cui Q, Wang J, Tang J and Liu H (2023), Nanodrugs systems for therapy and diagnosis of esophageal cancer. *Front. Bioeng. Biotechnol.* 11:1233476. doi: 10.3389/fbioe.2023.1233476

Nanodrugs systems for therapy and diagnosis of esophageal cancer

Lihan Zhang[1*†], Xing Li[2†], Guangxing Yue[1], Lihao Guo[3], Yanhui Hu[1], Qingli Cui[1], Jia Wang[1], Jingwen Tang[1*] and Huaimin Liu[1*]

[1]Department of Integrated Chinese and Western Medicine, The Affiliated Cancer Hospital of Zhengzhou University and Henan Cancer Hospital, Zhengzhou, China, [2]Department of General Surgery, The Affiliated Cancer Hospital of Zhengzhou University and Henan Cancer Hospital, Zhengzhou, China, [3]Interdisciplinary Research Center of Smart Sensors, School of Advanced Materials and Nanotechnology, Xidian University, Xi'an, China

With the increasing incidence of esophageal cancer, its diagnosis and treatment have become one of the key issues in medical research today. However, the current diagnostic and treatment methods face many unresolved issues, such as low accuracy of early diagnosis, painful treatment process for patients, and high recurrence rate after recovery. Therefore, new methods for the diagnosis and treatment of esophageal cancer need to be further explored, and the rapid development of nanomaterials has brought new ideas for solving this problem. Nanomaterials used as drugs or drug delivery systems possess several advantages, such as high drug capacity, adjustably specific targeting capability, and stable structure, which endow nanomaterials great application potential in cancer therapy. However, even though the nanomaterials have been widely used in cancer therapy, there are still few reviews on their application in esophageal cancer, and systematical overview and analysis are deficient. Herein, we overviewed the application of nanodrug systems in therapy and diagnosis of esophageal cancer and summarized some representative case of their application in diagnosis, chemotherapy, targeted drug, radiotherapy, immunity, surgery and new therapeutic method of esophageal cancer. In addition, the nanomaterials used for therapy of esophageal cancer complications, esophageal stenosis or obstruction and oesophagitis, are also listed here. Finally, the challenge and the future of nanomaterials used in cancer therapy were discussed.

KEYWORDS

nanomaterials, esophageal cancer, chemotherapy, radiotherapy, diagnosis

1 Introduction

Esophageal cancer ranks seventh globally in terms of its incidence in 2020, with 604,000 new cases reported, and it is the sixth leading cause of death, resulting in 544,000 fatalities. With approximately one in every 18 cancer-related deaths can be attributed to esophageal cancer (Sung et al., 2021), it poses a significant public health burden worldwide. The 5-year survival rate for esophageal cancer ranges from 10% to 30% in most countries, which is 29.7% in China and shows an improvement of 6%–10% since 2000. China is a high-incidence region for esophageal squamous cell carcinoma (ESCC). Currently, surgical intervention remains the primary treatment approach for resectable ESCC, but the efficacy of single-surgery is suboptimal, e.g., approximately 80% of patients experience

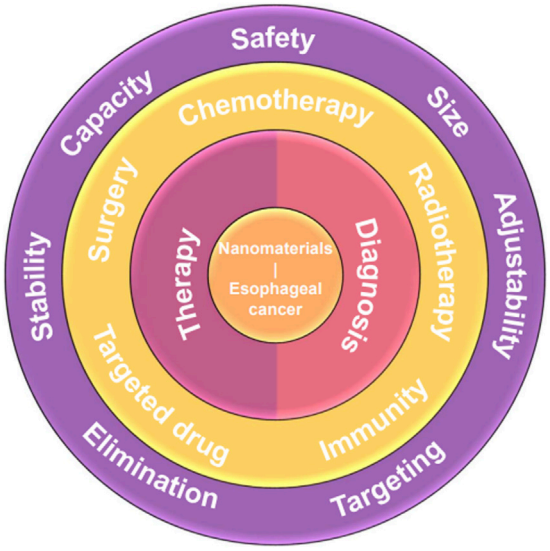

FIGURE 1
Schema of the main direction of nanomaterials for therapy and diagnosis of esophageal cancer. The nanomaterials for esophageal cancer (core) can be divided into two types, i.e., therapy and diagnosis (first ring). The nanomaterials for therapy of esophageal cancer can be specific to five aspects, i.e., chemotherapy, radiotherapy, targeted drugs, surgery, and immunity (second ring). The crucial criteria should be adhered in constructing nanocarriers for drug delivery systems.

recurrence or metastasis within 2 years post-operation. While radiotherapy and chemotherapy have shown promise in enhancing treatment outcomes, the efficacy of single-agent chemotherapy is 10%–20% far from satisfactory, and using combination regimens can only improve the efficacy to approximately 45%, accompanied by significant adverse effects. Consequently, there is an urgent need to explore novel and clinically effective treatment modalities to improve the therapeutic efficacy of patients diagnosed with esophageal cancer and inhibit recurrence.

Nanotechnology has paved a novel way in the medical field, and using nanocarriers as drug delivery systems has shown extraordinary potential to address many clinical difficulties, e.g., poor therapeutic efficacy and high recurrence rate. Using nanocarriers as drug delivery systems has been extensively researched both experimentally and clinically, and the outstanding properties of nanocarriers drug delivery systems, e.g., high drug capacity, adjustably specific targeting capability, stable structure, etc., endow nanocarriers with high performance with great application potential in treatment and diagnosis of cancer such as esophageal cancer, breast cancer, liver cancer, and so on. The relationship between the characteristics, synthesis, and properties of nanocarriers are relevant to their therapeutic/diagnosis performance. It has been proved that the characteristics and synthesis methods of different nanomaterials play a crucial role in determining the size, structure, and transport capabilities of these nanocarriers, which is critical factor to design and construct the optimal drug delivery systems (Lee et al., 2017). The nanoscale dimensions and controllably modified property of nanocarriers in these delivery systems present significant advantages in enhancing both the pharmacokinetics and pharmacodynamics of drugs and further improve treatment outcomes (Bozzuto and Molinari, 2015). Notably, extensive advancements have been made in the field of nanocarriers for drug delivery systems, showcasing their immense potential in prolonging drug circulation time, improving bioavailability, enhancing drug accumulation at tumor sites, reducing drug resistance, minimizing adverse reactions associated with anticancer medications, etc. (Figure 1) (Patra et al., 2018).

To facilitate effective treatment and diagnosis of cancer, the construction of nanocarriers for drug delivery systems should adhere to several crucial criteria (Tang et al., 2017), including:

1) Safety: Nanocarriers must be composed of non-toxic and biocompatible materials to ensure their safety and compatibility within biological systems.
2) Size: The size of nanocarriers should be appropriate to enhance passive targeting efficiency to the bone marrow. While some researchers have proposed that the optimum size of nanocarriers should be smaller than 150 nm (Moghimi, 1995), a universally agreed-upon standard has yet to be established.
3) Capacity: Nanocarriers should possess an adequate drug-loading capacity to achieve therapeutic doses.
4) Stability: To accomplish targeted delivery and therapeutic tasks, the nanocarriers should maintain a period of circulation time within the physiological system. Thus, the nanocarriers should be tolerant in the physiological environment, i.e., the stability, surface functionalization, and dispersity of nanocarriers must withstand in drug effective time resisting aggregation induced by solution acidity/alkalinity, temperature, ionic strength, and interactions with macromolecules. Moreover, the excellent stability of nanocarriers ensures the prevention of drugs rapid degradation or clearance within the bloodstream.
5) Elimination: Nanocarriers should possess appropriate clearance mechanisms after fulfilling their intended functions to avoid long-term accumulation and triggered systemic adverse effects. Meanwhile, timely eduction can effectively ease the excessive burden on excretory organs.
6) Targeting: Targeting capabilities of nanocarriers consist of active targeting and passive targeting progress. The highly specific targeting capabilities can allow the drug to preferentially accumulate at the diseased site while minimize adverse effects on healthy tissues.
7) Adjustability: Leveraging the characteristic differences between cancer cells and normal cells in terms of extracellular and intracellular environments (such as pH, redox potential, and enzymatic activity), responsive nanocarriers can be stimulated to facilitate the controlled release of encapsulated drugs specifically within the target tissue and cells. Therefore, the design of suitable nanocarriers can exploit the unique physiological conditions associated with the disease.

By meeting these stringent criteria, nanocarriers for drug delivery systems hold great promise for improving cancer therapy and diagnosis. Even though the correlational researches about nanocarriers applied in drug delivery systems are explored and developed ceaselessly, the systematic overview about the nanocarriers used as drug delivery systems for therapeutic and

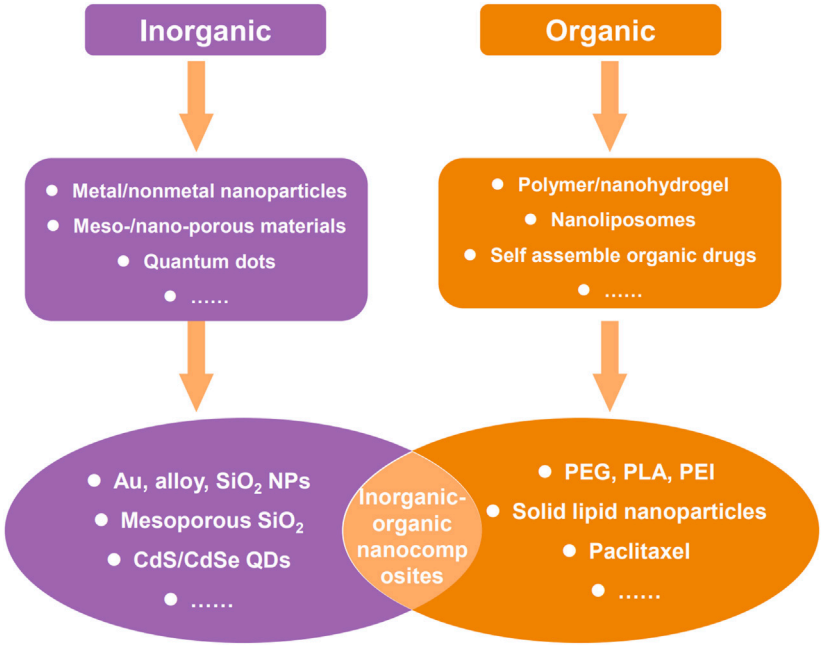

FIGURE 2
Common two types of nanomaterials for therapy and diagnosis of cancer, and some typical examples.

diagnosis of esophageal cancer is still lack. Herein, we reviewed some instructive researches about the application of nanocarriers drug delivery systems in therapeutic and diagnosis of esophageal cancer and its complications. In brief, the representative cases about nanocarriers drug delivery systems used in esophageal cancer, i.e., diagnosis, chemotherapy, targeted drug, radiotherapy, immunity, surgery, and new therapeutic method, were generalized while their applications in esophageal stenosis or obstruction and oesophagitis were also summarized, and the nanomaterials used in Chinese patent medicine were firstly overviewed (Figure 1). Moreover, we also discussed the challenge and the future of nanocarriers drug delivery systems in the end. Hence, this omnibearing review is significative to drive the development of therapeutic and diagnosis of esophageal cancer, and may be enlightening for other cancer therapeutic.

2 The applications of nanocarriers in therapeutic and diagnosis of esophageal cancer

Nanocarriers employed in drug delivery systems can be broadly categorized into two major classes: organic nanocarriers and inorganic nanocarriers. Organic nanocarriers encompass polymers, liposomes, and proteins, and inorganic nanocarriers include various nanoparticles such as gold nanoparticles, silicon nanoparticles, iron nanoparticles, selenium nanoparticles, copper nanoparticles, and other inorganic salt nanoparticles. Both organic nanocarriers and inorganic nanocarriers possess different characteristics but equal importance in drug delivery systems, so there are also many examples using organic-inorganic nanocomposite as nanocarriers to realize functional complementarity (Figure 2). Thus, to roundly summarize and analyze the effect of nanocarriers in the therapeutic and diagnosis of esophageal cancer, all of organic nanocarriers, inorganic nanocarriers, and composite nanocarriers were reviewed in subsequent content.

2.1 The applications of nanocarriers in esophageal cancer diagnosis

When using nanocarriers as a diagnostic tools for esophageal cancer, they are typically prepared as nanoprobes for direct diagnosis or utilized for enhancing existing diagnostic measures through their unique properties. As for direct diagnosis, the fluorescent substances are combined with nanoparticles or nanocapsules to prepare imaging probes with high contrast and high resolution which can be used to detect tumors, cell activity, and vascular activity. Furthermore, for another way, i.e., using nanocarriers to enhance/assist diagnosis, the nanocarriers are always introduced into existing diagnostic measure such as computerized tomography (CT), nuclear magnetic resonance (NMR) imaging, Surface-Enhanced Raman Scattering (SERS), etc. For example, magnetic nanoparticles can be prepared as nanoprobes for magnetic resonance imaging, and these probes can improve image contrast and sensitivity, thus allowing for better detection of tumors and other diseases.

Li et al. established a novel method based on resonance Rayleigh scattering (RRS) to detect the overexpression of epidermal growth factor receptor (EGFR) in esophageal cancer cells. In this strategy, a multifunctional gold nanoparticle probe (Apt-Au nanoparticles-Ab)

TABLE 1 The clinical trials for cancer diagnosis and treatment using nanodrugs based on magnetic iron oxide nanoparticle (by May 2023; Source: clinicaltrials.gov) (Liang et al., 2020).

Project ID	Methods	Cancer type	Stage	Start/end date	State
NCT02689401	MRI to detect lymph node metastases	Esophageal cancer	Phase 1	2016/2016	Withdrawn
NCT02857218	MRI before neoadjuvant chemoradiation therapy and again before esophagectomy	Esophageal cancer (Stage IIB-IIIC)	Early Phase 1	2018/2021	Withdrawn
NCT02253602	Innovative MRI Techniques to Improve Treatment Stratification of Patients With Esophageal Cancer	Esophageal Neoplasms	Phase 1	2014/2018	Completed

was developed by multi-functionalizing Au nanoparticles with aptamers and anti-EGFR antibodies which was subsequently delivered into EGFR positive cancer cell. The diagnostic results show that, remarkably, the RRS intensity significantly increased upon mixing the probe with Eca-109 esophageal cancer cells meaning that this RRS-based detection platform provides a valuable tool for identifying EGFR-positive cancer cells and exhibits substantial potential for clinical diagnostics (Li et al., 2021). Gai et al. conducted research on the development of a novel targeted dual-specific antibody system encapsulated in chitosan-Fe_3O_4 nanoparticles, specifically targeting fibroblast growth factor receptor (FGFR) and vascular endothelial growth factor receptor (VEGFR). As a result, both *in vivo* and *in vitro* experiments, this system demonstrated its ability to enhance the resolution of CT imaging and improve the accuracy of diagnosis for early detection and final confirmation of suspected cases (Gai et al., 2018). Moreover, Duo et al. employed surface-enhanced Raman scattering (SERS) based on silver nanoparticles to analyze and classify SERS spectra obtained from both normal and cancerous plasma samples, and the diagnostic accuracy achieved was notably high, approximately 90%, making this approach holds promising potential as a label-free and straightforward blood test for the detection of esophageal cancer (Lin et al., 2014). The magnetic nanocarriers are frequently used to improve diagnostic accuracy through enhancing image contrast and sensitivity in NMR imaging process. The introduction of gadolinium-iron nanoparticles as drug delivery carriers is associated with various parameters (e.g., nanoparticle size, hydrophobicity/hydrophilicity, surface charge, core composition, coating properties, administration route, and dosage) that influence their biodistribution. Because of this particular phenomenon and the magnetic properties of these nanoparticles, the real-time monitoring of drug delivery and treatment responses can be realized (Alphandéry, 2019). Li et al. developed a polyethylene glycol-b-poly (1-(3-aminopropyl)-3-(2-methacryloyloxypropyl)imidazolium bromide) (PAMPImB) complex carrier for DNA loading and magnetofection which consists of four layers, i.e., Fe_3O_4 nanoparticle core, Au shell, internal PAMPImB block, and PEG corona. In this four layers structure, each layer is designed to perform different functions: the Fe_3O_4 nanoparticle core can facilitate cellular uptake through magnetic acceleration; the Au shell promotes copolymer binding via Au-S bonds; the internal PAMPImB blocks for DNA condensation; and the PEG corona enhances colloidal stability. Transfection efficiency studies conducted on human esophageal cancer cells (EC-109) revealed that the nanocomplex exhibited high transfection efficiency within a shorter incubation time when subjected to an external magnetic field, which was caused by enhanced cellular uptake through magnetic acceleration, providing a feasible method for rapid cancer diagnosis (Li et al., 2017). Furthermore, Fe_3O_4 nanoparticle-modified CdSe/CdS/ZnS nanocrystals can be utilized for the immediate optomagnetic detection of cancer biomarkers, including esophageal cancer, in serum samples (Qureshi et al., 2020). In addition, the clinical trials for cancer diagnosis and treatment using nanodrugs based on magnetic iron oxide nanoparticle were shown in Table 1.

2.2 The applications of nanocarriers in chemotherapy of esophageal cancer

Chemotherapy is a crucial systemic treatment for esophageal cancer, and currently, commonly used chemotherapy drugs include paclitaxel, platinum agents, and fluoropyrimidine drugs. However, these chemotherapy drugs exhibit similar concentrations in both plasma and tumor tissues, leading to various toxic side effects that render long-term chemotherapy intolerable for patients. Moreover, tumor blood vessels exhibit distinct pathological and physiological characteristics that are not typically observed in normal vasculature, including substantial increase in proliferating endothelial cells, enlarged and tortuous structures, the absence of pericyte coverage, and abnormal basement membranes. Thus, the therapeutic efficacy of traditional chemotherapy drugs may be weakened while the therapeutic process may be accompanied by the adverse side effect causing harmful consequence. Given these unique traits, nanoparticle-based drug delivery systems hold great potential for the chemotherapy of esophageal cancer. Nanocarriers drug delivery systems possess several distinguishing properties that set them apart from conventional cancer therapies, such as 1) the ability to act as both therapeutic agents and diagnostic tools for cancer, which can realize real-time monitoring of drug delivery and treatment responses; 2) the capacity to encapsulate multiple anti-cancer drug molecules, enabling synergistic therapeutic effects; 3) the potential to enhance specificity to tumor cells through passive and active targeting mechanisms; 4) the ability to achieve controlled drug release, thereby increasing drug concentrations within cancer cells while reducing toxicity to normal cells, ultimately leading to improved therapeutic outcomes and reduced systemic toxicity. Hence, using nanocarriers as a chemotherapeutic drug delivery systems can effectively maximize drug efficacy, prolong drug action time, and reduce harmful side effects.

2.2.1 The targeting process of nanocarriers in chemotherapy

The targeting process of nanocarriers can be divided into two types, i.e., passive targeting and active targeting, and these two types of targeting process experience different mechanisms. For passive Targeting, the enhanced permeability and retention effect (EPR) arises from the formation of leaky blood vessels and impaired lymphatic drainage in rapidly growing tumors, which contributes to the accumulation of nanoparticles and microparticles within the tumor. Extensive research has been conducted on nanosized drug carriers, such as liposomes, dendrimers, polymer-drug conjugates, polymer micelles, and inorganic nanoparticles, for drug delivery in cancer chemotherapy using this distinctive approach (Akhter et al., 2018). Due to their specific size range (typically between 1 nm and 200 nm), these nanoparticles preferentially accumulate at the tumor site by exploiting the highly permeable blood vessels and leveraging the EPR effect (Liao et al., 2020)]. Distinguishing with passive targeting, the active targeting employs surface-conjugated ligands that interact with cell membrane receptors, and nanocarriers facilitate receptor-mediated endocytosis, leading to increased drug concentrations within the target cells (Hejmady et al., 2020). Tumor cells often exhibit overexpression of specific receptors, making these receptors ideal targets for active targeting using ligand-functionalized nanoparticles (Juan et al., 2020). Consequently, both tumor cells and endothelial cells are considered viable cellular targets for active targeting strategies. Additionally, nanoparticles have the potential to address these limitations by leveraging the EPR effect to accumulate anticancer drugs specifically within tumor tissues, and nanoparticles can prolong the half-life of drugs, enhance the solubility of hydrophobic drugs, and reduce potential immunogenicity (Shi et al., 2010). Thus, through active targeting, nanocarriers can mitigate the non-specific distribution of drugs, enhance drug accumulation within the tumor, and improve treatment safety and efficacy.

2.2.2 The applications of nanocarriers combined with chemotherapy drugs used in chemotherapy

Dohmitsu et al. conducted a study to evaluate the antitumor activity of TAC-1043, a thermosensitive liposome containing encapsulated cisplatin within large unilamellar vesicles composed of a 9:1 ratio of dipalmitoyl phosphatidylcholine and distearoyl phosphatidylcholine, and the results demonstrated that the combined administration of TAC-1043 and hyperthermia significantly inhibited tumor cell proliferation (Dohmitsu et al., 1991). Wang et al. developed a novel nanoplatform for the treatment of esophageal cancer based on ATP-responsive drug release. The chemotherapeutic drug doxorubicin was inserted into an ATP aptamer (Ap) to form a double-stranded DNA ("DNA duplex") which was subsequently condensed using polyethyleneimine (PEI) to construct the final nanoplatform (PEI-Ap-DNA-DOX). After internalization by cancer cells, the doxorubicin-loaded DNA duplex can be opened and released within the intracellular environment rich in ATP (Wang et al., 2020c). Similarly, Huang et al. developed a novel formulation of docetaxel, called trimethyl chitosan-DTX (TMC-DTX) applying to the treatment of esophageal cancer, and investigated its effects. TMC-DTX exhibited remarkable inhibition of cell proliferation and promoted apoptosis in EC cells, effectively reducing tumor volume in a xenograft mouse model (Huang et al., 2015). Moreover, solid lipid nanoparticles (SLNs) coated with trimethyl chitosan were prepared using ultrasonication and thermal shear homogenization techniques for the encapsulation of erlotinib with a three layers structure, i.e., trimethyl chitosan-coated erlotinib-loaded SLNs (TMC-IRN-SLN). The presence of trimethyl chitosan on the SLN surface facilitated electrostatic interactions with the lipid layer and increased the particle internalization, resulting in sustained release of the drug in an acidic environment, and these nanoparticles exhibited excellent cytotoxicity against EC9706 cells, leading to an increased proportion of apoptotic cells in both early and late-stage apoptosis. This formulation aimed to enhance stability, improve drug payload, and achieve prolonged drug release in esophageal cancer cells (Ji et al., 2018).

NK012 is a novel micellar nanoparticle formulation containing SN-38, an analogue of irinotecan, and it exhibits superior anti-esophageal cancer activity and induces longer survival compared to traditional CPT-11, with a lower clearance rate. The experimental result shows that the concentration of polymer-bound SN-38 and released SN-38 in tumor tissue remains sustained for an extended period. Thus, with its specific distribution and prolonged release of SN-38 within the tumor, NK012 may represent a promising approach for treating esophageal cancer by exerting time-dependent antitumor activity (Hamaguchi et al., 2010). In a phase I clinical trial conducted by Hamaguchi et al., the anticancer efficacy of NK012 was evaluated in adult patients with solid tumors, and three patients with esophageal cancer participated in the trial, and one refractory patient achieved an objective response and continued the study treatment for 5 months (Hamaguchi et al., 2010). The recommended dose of NK012 was determined to be 28 mg/m^2, administered every 3 weeks as a treatment cycle. Recently, an open-label phase I clinical trial evaluated the safety and efficacy of eribulin liposomes in Japanese patients with advanced solid tumors, including esophageal cancer. The findings indicated that eribulin liposomes administered at a dose of 2.0 mg/m^2 every 3 weeks were well tolerated, suggesting the need for further large-scale investigations in these patient populations (Udagawa et al., 2023).

Recently, Liu et al. prepared a chemotherapy drug based on inorganic Au nanomaterials and Rhus coriaria L. fruit aqueous extract. This composite drug can treat several types of esophageal cancer, such as human esophageal squamous cell carcinoma, human Caucasian esophageal carcinoma, adenocarcinoma of the gastroesophageal junction, and distal esophageal adenocarcinoma. The excellent antioxidant and anti-esophageal cancer activities let this composite drug indicate suitable antitumor property without any cytotoxicity effect on the normal cell (Liu J. et al., 2020). Moreover, more and more natural extracts have been used in chemotherapy.

2.2.3 The applications of nanocarriers based on paclitaxel used in chemotherapy

Paclitaxel (PTX) is a naturally derived compound widely used in the treatment of various types of cancer due to its unique mechanism of action, which involves blocking cell cycle progression, preventing mitosis, and inhibiting cancer cell growth. However, the administration of PTX is associated with potential adverse effects such as peripheral neuropathy, cardiac toxicity, and hepatic toxicity,

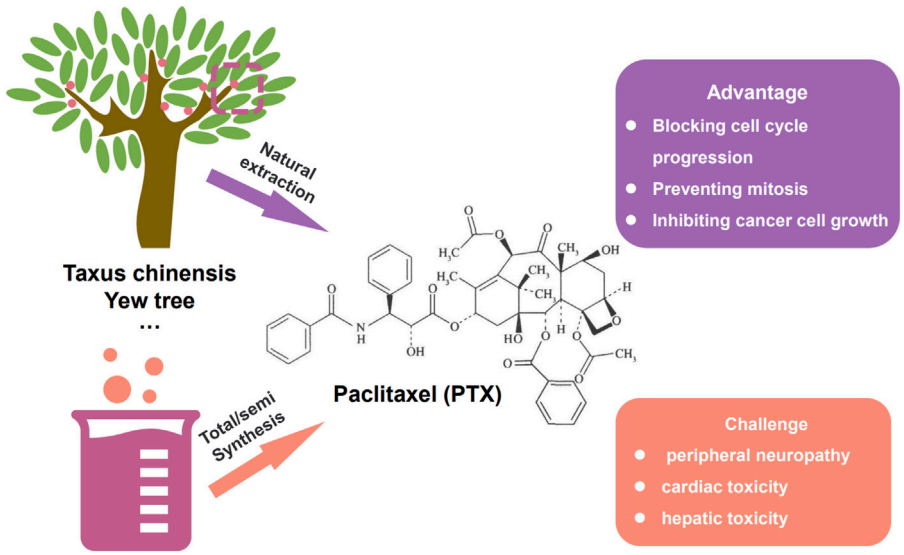

FIGURE 3
The way to gain paclitaxel (PTX), i.e., natural extraction and total/semi synthesis. The advantage and existing challenge of paclitaxel.

TABLE 2 Representative commercial materials for PTX applications.

Materials	Trade name	Characteristic	Application
polyoxyethylated castor oil	Cremophor® EL	toxicity	
PEG-*b*-PLA/PTX micellar	Genexol-PM®	lower toxicity (with a maximum tolerated dose determined to be 2 to 3 times higher)	breast cancer and non-small cell lung cancer
mPEG-b-PDLLA/PTX amphiphilic micellar	Nanoxel®	lower toxicity and hydrosoluble	breast cancer, ovarian cancer, and non-small cell lung cancer

which are major drawbacks of this highly effective drug (Figure 3). Specifically, peripheral neuropathy can manifest as shooting or burning pain (particularly in the hands and feet), sensory loss, numbness, and tingling sensations (Wang et al., 2017). To address the adverse issues of single PTX, several nanocarrier formulations have been developed to mitigate the adverse effects of PTX and improve its water solubility without the commonly used solvent Cremophor® EL which has been associated with toxicity (Kiss et al., 2013) (Table 2). Genexol-PM® is a polyethylene glycol (PEG)-b-poly (D,L-lactide) (PEG-PLA) micellar formulation of PTX, approved in 2007 in Korea for the treatment of breast cancer and non-small cell lung cancer. This formulation exhibits lower toxicity compared to PTX formulated with Cremophor® EL, with a maximum tolerated dose determined to be 2 to 3 times higher (Table 2). Besides, Nanoxel®, a polymer-based amphiphilic micellar formulation of PTX, has received clinical approval in India in 2006 and is currently undergoing FDA-approved clinical trials (ClinicalTrials.gov Identifier: NCT04066335), and Apealea, approved for use in the European Union in 2018, utilizes a PTX conjugate with poly-l-glutamic acid. However, despite these formulation advancements, peripheral neuropathy remains a clinical challenge, emphasizing the need for further optimization (Riedel et al., 2021).

Researchers have discovered that the expression level of PI3K is higher in ESCC patients compared to normal individuals, so by using nanoparticles loaded with a PI3K inhibitor (AZD8186) and docetaxel (DTX) on esophageal squamous cell carcinoma cells, synergistic effects between nanoparticles and drugs have been observed, along with a significant reduction in hematological toxicity (Wang et al., 2018). Some scholars conducted *in vitro* studies, as well as subcutaneous tumor transplantation and peritoneal metastasis tumor survival models in mice with esophageal adenocarcinoma, and found that compared to conventional paclitaxel, nanoparticle-bound albumin-paclitaxel showed significantly improved *in vivo* antitumor efficacy and overall survival rates, whether used alone or in combination therapy (Hassan et al., 2017). In another study, Cui et al. developed albumin-based microspheres incorporating magnetic Fe_3O_4 nanoparticles as carriers for paclitaxel. These microspheres demonstrated excellent targeting ability and sustained release of paclitaxel, effectively inhibiting the growth of Eca109 cells (Cui et al., 2012).

TABLE 3 Representative nanomaterials used in chemotherapy of esophageal cancer.

Materials	Types	Features and findings	Application	References
PEI-Ap-DNA-DOX	Organic	ATP-responsive drug release	esophageal cancer	Wang et al. (2020c)
Trimethyl chitosan-DTX	Organic	Remarkable inhibition of cell proliferation and promoted apoptosis in EC cells, effectively reducing tumor volume in a xenograft mouse model	esophageal cancer	Huang et al. (2015)
Trimethyl chitosan-coated erlotinib-loaded solid lipid nanoparticles	Organic	Excellent cytotoxicity against EC9706 cells	early and late-stage apoptosis	Ji et al. (2018)
Nanoparticles loaded with a PI3K inhibitor (AZD8186) and docetaxel (DTX)	Organic	Significant reduction in hematological toxicity	esophageal squamous cell carcinoma cells	Wang et al. (2018)
Nanoparticle-bound albumin-paclitaxel	Organic	significantly improved *in vivo* antitumor efficacy and overall survival rates	esophageal adenocarcinoma	Hassan et al. (2017)
Albumin-based microspheres incorporating magnetic Fe_3O_4 NPs as carriers for paclitaxel	Inorganic-organic nanocomposites	excellent targeting ability and sustained release of paclitaxel, effectively inhibiting the growth of Eca109 cells	esophageal cancer	Cui et al. (2012)
Nab-paclitaxel combined with cisplatin	Inorganic-organic nanocomposites	significant efficacy of the nab-paclitaxel plus cisplatin regimen, with a disease control rate of 87.9%, an objective response rate of 60.0%, a median overall survival of 15.5 months, and a median progression-free survival of 6.2 months	esophageal cancer	Shi et al. (2013)

Nowadays, the combination regimen of nab-paclitaxel and cisplatin has emerged as an effective and well-tolerated first-line treatment option treatment option for esophageal cancer in China (Wu et al., 2017). Shi et al. conducted a clinical study to investigate the efficacy and safety of nab-paclitaxel combined with cisplatin in patients with metastatic esophageal cancer, which contained a total of 33 patients with metastatic disease were included in the study (Shi et al., 2013). The results demonstrated significant efficacy of the nab-paclitaxel plus cisplatin regimen, with a disease control rate of 87.9%, an objective response rate of 60.0%, a median overall survival of 15.5 months, and a median progression-free survival of 6.2 months. Nab-paclitaxel, a novel nanoparticle-based drug, is a 130 nm albumin-bound formulation of paclitaxel that offers enhanced water solubility and solvent-free delivery of paclitaxel (Yuan et al., 2015), and unlike conventional paclitaxel formulations, nab-paclitaxel utilizes albumin as a stable carrier for paclitaxel, eliminating the need for toxic solvents such as ethanol and polyoxyethylated castor oil (Cremophor® EL) (Zhao et al., 2022). These solvents have been associated with severe side effects, including peripheral neuropathy and hypersensitivity reactions while the use of solvents can limit the drug's efficacy and bioavailability. Therefore, the solvent-free nab-paclitaxel represents a promising advancement in paclitaxel therapy, offering reduced adverse reactions and improved therapeutic outcomes. A study by Hassan et al. investigated the anti-tumor effects of nab-paclitaxel on esophageal cancer cells through *in vitro* and *in vivo* experiments revealing that nab-paclitaxel significantly suppressed the proliferation of esophageal cancer cells and induced higher rates of apoptosis compared to paclitaxel alone or the control group (Hassan et al., 2018).

Additionally, in mouse models of subcutaneous xenograft and peritoneal metastasis, nab-paclitaxel exhibited a significant increase in survival rates. Overall, nab-paclitaxel and albumin-based paclitaxel formulations offer promising prospects for the treatment of esophageal cancer, with improved therapeutic efficacy and reduced adverse effects. Further exploration and optimization of these formulations are necessary to fully realize their potential in clinical applications. While nab-paclitaxel has been widely utilized as a nanomedicine in the treatment of esophageal cancer, research exploring the application of other nanocarriers, such as viral capsids and dendrimers, in this context remains limited and requires further investigation (Li et al., 2022). The representative nanomaterials used in chemotherapy of esophageal cancer were summarized in Table 3.

2.3 The applications of nanocarriers in radiotherapy of esophageal cancer

Concurrent chemoradiotherapy is an essential modality for the local treatment of unresectable esophageal cancer, but due to the anatomical position of esophagus is in close proximity to vital organs such as the lungs, heart, and spinal cord, it presents challenges in escalating the local radiation dose without causing adverse effects like radiation-induced lung injury and cardiac toxicity. Furthermore, although chemotherapy drugs are used as radiosensitizers to synergize with radiation therapy, suboptimal outcomes are normally observed due to similar drug concentrations in both plasma and tumor tissue. Additionally, the majority of esophageal cancer patients are at risk of developing malnutrition, and during radiation therapy, they are susceptible to life-threatening complications, including perforation, bleeding, and tracheoesophageal fistula formation, which magnifies the adverse side effects of chemotherapy drugs and radio. Consequently, achieving satisfactory precisely local control of radiotherapy with minimized adverse side effect remains a

challenge, and considering these limitations, the exploration of novel breakthroughs in the field of radiation therapy for esophageal cancer is in an urgent demand to improve therapeutic efficacy and simultaneously alleviate patient's pain and sufferings.

2.3.1 The applications of organic nanocarriers used in radiotherapy

The above-mentioned paclitaxel is also commonly used as a radiosensitizer in the treatment of various tumors, and the application of paclitaxel in (chemo) radiotherapy shows great potential in cancer therapy. Moreover, more and more researchers put their attention on improving the radiotherapy effectiveness of paclitaxel to achieve better therapeutic efficacy. A novel approach has been developed by linking recombinant protein anti-EGFR and internalizing arginine-glycine-aspartic acid (IRGD) to the surface of paclitaxel-loaded red blood cell membrane nanoparticles (IE-PR nanoparticles). This innovative nanoscale radiosensitizer has demonstrated increased sensitization rates of 1.32-fold in EGFR-overexpressing esophageal cancer cells and 1.25-fold in EGFR-low-expressing cells compared to paclitaxel alone suggesting that this strategy has the potential to overcome the current limitations in esophageal cancer treatment (Ai et al., 2018). In a similar vein, some researchers have also explored the use of modified with anti-EGFR-iRGD fusion protein red blood cell membrane nanoparticles loaded with paclitaxel. *In vitro* tumor studies have shown that these nanoparticles enhance the radiosensitizing effects by effectively arresting more tumor cells in the radiation-sensitive G/M phase, which leads to an increased production of reactive oxygen species and the formation of more lethal DNA double-strand breaks (Ren et al., 2018). In a retrospective clinical study conducted at a single center, the efficacy and feasibility of liposomal paclitaxel combined with cisplatin in the treatment of locally advanced squamous cell carcinoma of the esophagus were evaluated. The results suggested that the use of liposomal paclitaxel in combination with cisplatin for chemoradiotherapy yielded good tolerability and effectiveness in managing locally advanced squamous cell carcinoma of the esophagus (Yi et al., 2022). Besides, another retrospective clinical study analyzed the efficacy and safety of neoadjuvant chemotherapy based on liposomal paclitaxel in conjunction with platinum in patients with locally advanced resectable esophageal squamous cell carcinoma. The study demonstrated that a satisfactory R0 resection rates, survival rates, and significant tumor downstaging effects can be achieved while maintaining a good safety profile (Wang et al., 2022). In a single-center retrospective clinical study, the use of liposomal paclitaxel and cisplatin in synchronous chemotherapy was found to improve the prognosis of patients with locally advanced esophageal squamous cell carcinoma undergoing intensity-modulated radiotherapy (Liu et al., 2019). The therapeutic value of combined chemoradiotherapy in the treatment of locally advanced esophageal squamous cell carcinoma still require larger prospective studies to validate.

Due to the limited retention time of radiation in tumor tissues the radiotherapy effectiveness of the traditional *in vivo* irradiation techniques has been hampered, but by leveraging nanodrug delivery technology, it is possible to enhance the targeted action of radioisotopes, resulting in improved local control rates and reduced adverse reactions. In a preclinical animal model of esophageal cancer, Chang et al. have employed rhenium-188 (188 Re) nano-liposomes in combination with external beam irradiation (beta radiation), which show an effective inhibition of the growth of tumor tissues without significant adverse reactions or biological toxicity (Chang et al., 2015). The combination of external beam radiation therapy and 188Re-liposomes exhibited a greater inhibitory effect on tumor regeneration compared to each treatment alone. Furthermore, this combined therapy showed no significant adverse effects or notable biotoxicity on parameters such as white blood cell count, body weight, or liver and kidney function. Even though iodine-125 (^{125}I) brachytherapy has emerged as a highly effective palliative treatment option for advanced esophageal cancer, the development of resistance to ^{125}I brachytherapy due to tumor hypoxia and activation of the hypoxia-inducible factor 1 (HIF-1) signaling pathway poses a significant limitation in the management of esophageal cancer. To overcome these challenges, Yao and colleagues have devised a novel approach to enhance the radiosensitivity of brachytherapy by co-encapsulating catalase (CAT) and the HIF-1 inhibitor, i.e., acriflavine (ACF), within the hydrophilic cavity of liposomes, creating a formulation termed (ACF-CAT@Lipo). ACF-CAT@Lipo exhibits remarkable properties when stimulated by overexpressed H_2O_2 in the tumor microenvironment and generates a significant amount of O_2 both *in vitro* and *in vivo*, effectively alleviating tumor hypoxia. Furthermore, the synergistic effect of ACF substantially reduces the expression of hypoxia-related proteins, including HIF-1α, VEGF, and MMP-2. More importantly, this combined effect enhances the radiosensitivity of ^{125}I brachytherapy, leading to improved therapeutic outcomes and potential eradication of esophageal cancer *in vivo* (Yao et al., 2022).

2.3.2 The applications of inorganic nanocarriers used in radiotherapy

Moreover, a novel nanomaterial composed of graphdiyne (GDY) anchored with cerium oxide (CeO_2) nanoparticles was also used, known as GDY-CeO_2 nanocomposites. This unique composite material demonstrates exceptional catalase activity in decomposing H_2O_2 into O_2, offering a significant advantage in mitigating tumor hypoxia. In addition, the GDY-CeO_2 nanocomposites promote radiation-induced DNA damage, thereby inhibiting tumor growth and potentially reversing radioresistance in esophageal cancer treatment (Zhou et al., 2021). A pH-responsive nano-system possessing capability of aggregating and carrying doxorubicin (DOX) has been developed for enhanced radiosensitization and synergistic radiochemotherapy in esophageal cancer. Within the acidic microenvironment of the tumor, the size of nano-aggregates increase and the reflux of gold nanoparticles (Au NPs) into the bloodstream can be impeded. Consequently, tumor accumulation and retention of Au NPs are enhanced, resulting in higher concentrations and larger sizes of Au NPs within the tumor, and in turn, significantly improves the radiosensitizing effect. Simultaneously, the DOX payload is selectively delivered and released into tumor cells triggered by the acidic microenvironment as a synergistic approach to radiochemotherapy. *In vitro* experiments have demonstrated that the pH-responsive Au NPs intensify radiation-induced DNA damage, promote cell apoptosis, induce cell cycle arrest, and

TABLE 4 Representative nanomaterials for radiotherapy of esophageal cancer.

Crucial component	Materials	Features and findings	Application	References
miRNA	Sulfuric fish gelatin nanoparticles as carriers for miR-203	Targeting specific molecules such as Ran and DNp63, increasing local drug concentrations, and efficiently suppressing tumor proliferation and invasion	esophageal squamous cell carcinoma	Cao et al. (2013)
siRNA	PEI coated mesoporous Si NPs loaded with siRNA by EC-9706 tumor cells	Significant inhibition of EC-9706 tumor cells proliferation	esophageal cancer	Sun et al. (2017)
	Carboxymethyl chitosan-auristatin and siRNA	Targeting MVP and BCL2, inhibited cancer cell growth and tumor development in both cultured esophageal squamous cell carcinoma cells and xenograft models of mice	esophageal squamous cell carcinoma	Zhang et al. (2022)
polypeptide	NGR/PEI/TANOL	Pronounced enhancement in the uptake by well-differentiated human esophageal adenocarcinoma cells	esophageal cancer	(MOFFATT and WANGARI)
small molecule	Reversible disulfide crosslinked micelles-docetaxel and the PI3K inhibitor AZD8186	Minimizing premature release into the bloodstream and reducing nonspecific toxicity, synergistic antitumor effect of the DCM-loaded docetaxel and AZD8186	esophageal squamous cell carcinoma	Wang et al. (2017)

reduce colony-forming ability. Notably, *in vivo* studies have also shown a marked enhancement in the anti-tumor efficacy (Luan et al., 2022). The representative nanomaterials for radiotherapy of esophageal cancer were summarized in Table 4.

2.4 The applications of nanocarriers in targeted therapy of esophageal cancer

In recent years, molecular targeted therapy has emerged as a significant breakthrough in the treatment of various malignant tumors, particularly lung cancer, colorectal cancer, and liver cancer. In terms of targeted therapy, for HER-2 positive advanced esophagogastric junction cancer, trastuzumab can be considered as a treatment option after the third-line of treatment. Targeted drugs against angiogenesis can also be used as treatment options, with apatinib being recommended for advanced esophagogastric junction cancer after the third-line of treatment. For second-line treatment of advanced esophageal squamous cell carcinoma, anlotinib or apatinib are viable options. However, the effective small molecule targeted drugs for esophageal cancer are scarce due to the high heterogeneity of esophageal tumor cells, making it challenging to effectively target them. miRNAs as a class of endogenous non-coding small RNA molecules play a crucial role in the development, progression, and metastasis of esophageal cancer, and they have become promising biomarkers for diagnosing and treating this disease (Chen et al., 2018; Pennathur et al., 2019). To address these challenges, researchers have explored the use of nanotechnology, specifically nanoparticle-based delivery systems, to enhance the effectiveness of small molecule targeted drugs in esophageal cancer treatment.

Research has identified abnormal expression levels of approximately 50 miRNAs in esophageal cancer tissues, among which about 7 miRNAs can distinguish between normal and malignant tissues. Notably, the downregulation of miR-203 in esophageal cancer suggests its close association with the initiation and progression of the disease (Zhang et al., 2019). The nanoparticles have been proved as a suitable carriers to load miRNA and achieve targeting delivery. For instance, utilizing sulfuric fish gelatin nanoparticles as carriers for miR-203, targeted therapy can be achieved to target specific molecules such as Ran and DNp63 in esophageal squamous cell carcinoma (ESCC), leading to the repair of tumor cells (Cao et al., 2013). This approach holds promise in effectively delivering therapeutic agents to esophageal tumor cells, increasing local drug concentrations, and efficiently suppressing tumor proliferation and invasion. Mesoporous silica nanoparticles (MSNP) synthesized through sol-gel method have been utilized as carriers which demonstrate the effective uptake of nano-complexes loaded with small interfering RNA (siRNA) by EC-9706 tumor cells, leading to a significant inhibition of cell proliferation *in vitro* experiments (Sun et al., 2017). Meanwhile, the positively charged polyethyleneimine (PEI) coating on the surface of silica nanoparticles can facilitate the binding with negatively charged ESCCAL-1 siRNA and effectively inhibit the growth of EC-9706 esophageal cancer cells. In addition, a novel nanoparticle carrier (NGR/PEI/TANOL) was developed by incorporating PEI into a TANOL nanoparticle formulation and subsequently modifying it with a tumor-targeting peptide, NGR. This composite exhibited a pronounced enhancement in the uptake by well-differentiated human esophageal adenocarcinoma cells, thereby facilitating more efficient targeting of tumor tissue *in vivo* (MOFFATT and WANGARI, 2018). These findings highlight the potential of utilizing nanoparticle carriers, whether loaded with small molecule targeted drugs or chemotherapy drugs, to effectively target heterogeneous esophageal tumor cells and provide a new paradigm for systemic treatment of esophageal cancer. In addition, Zhang et al. designed a multifunctional self-assembling nanoparticle platform based on carboxymethyl chitosan facilitating the simultaneous delivery of auristatin and siRNA targeting two genes associated with multidrug resistance in esophageal squamous cell carcinoma, i.e., MVP and BCL2. The synthesized nanoparticles successfully inhibited cancer cell growth and tumor development in both cultured esophageal squamous cell carcinoma cells and xenograft models of mice (Zhang et al., 2022).

Wang et al. used reversible disulfide crosslinked micelles (DCM) as targeted nanocarriers to deliver a potent combination of docetaxel

TABLE 5 Representative nanomaterials used in target drugs of esophageal cancer.

Types	Materials	Features and findings	Application	References
Radiosensitizer	Linking recombinant protein anti-EGFR IRGD to the surface of paclitaxel-loaded red blood cell membrane NPs (IE-PR NPs)	Increased sensitization rates of 1.32-fold in EGFR-overexpressing esophageal cancer cells and 1.25-fold in EGFR-low-expressing cells compared to paclitaxel	esophageal cancer	Ai et al. (2018)
	Anti-EGFR-iRGD fusion protein red blood cell membrane nanoparticles loaded with paclitaxel	Enhance the radiosensitizing effects by effectively arresting more tumor cells in the radiation-sensitive G/M phase, lead to an increased production of reactive oxygen species and the formation of more lethal DNA double-strand breaks	esophageal cancer	Ren et al. (2018)
Chemoradiotherapy drugs	Liposomal paclitaxel combined with cisplatin	Good tolerability and effectiveness in managing locally advanced squamous cell carcinoma of the esophagus	esophageal squamous cell carcinoma	Yi et al. (2022)
Radioisotopes	188 Re nano-liposomes	effective inhibition of the growth of tumor tissues without significant adverse reactions	esophageal cancer	Chang et al. (2015)
	Co-encapsulating catalase (CAT) and acriflavine within the hydrophilic cavity of liposomes (ACF-CAT@Lipo)	Generates a significant amount of O_2 both *in vitro* and *in vivo*, effectively alleviating tumor hypoxia, reduces the expression of hypoxia-related proteins, including HIF-1α, VEGF, and MMP-2, enhances the radiosensitivity of 125I brachytherapy	esophageal cancer	Yao et al. (2022)
Synergistic approach	graphdiyne anchored with CeO_2 NPs	Significant advantage in mitigating tumor hypoxia, promote radiation-induced DNA damage inhibiting tumor growth and potentially reversing radioresistance	esophageal cancer	Zhou et al. (2021)
	Au NPs	Improves the radiosensitizing effect, intensify radiation-induced DNA damage, promote cell apoptosis, induce cell cycle arrest, and reduce colony-forming ability	esophageal cancer	Luan et al. (2022)

and the PI3K inhibitor AZD8186, and for the first time, the effective inhibition of esophageal cancer cell growth in a mouse xenograft model. The use of DCM allowed for controlled drug release at the tumor site, minimizing premature release into the bloodstream and reducing nonspecific toxicity (Wang et al., 2017). The results showed a synergistic antitumor effect of the DCM-loaded docetaxel and AZD8186, highlighting their potential for targeted therapy of esophageal squamous cell carcinoma. More importantly, the study provided valuable insights into reducing systemic toxicity associated with the treatment (Li et al., 2022). In another work, folate-targeted paclitaxel-loaded micelles were evaluated for their efficacy in esophageal cancer treatment. When compared to free paclitaxel and conventional paclitaxel-loaded micelles, the folate-mediated polymer micelles exhibited superior effectiveness in inhibiting subcutaneous xenograft tumors and prolonging the survival of tumor-bearing nude mice. These findings suggest that folate-targeted micelles loaded with paclitaxel hold great promise as a potential therapeutic approach for human esophageal cancer (Wu et al., 2012). Additionally, Dai et al. developed a novel poly (ε-caprolactone)-Pluronic micelle system capable of encapsulating both doxorubicin and miR-34a, and the results demonstrated that the PCL-Pluronic micelles significantly enhanced the uptake of doxorubicin by esophageal cancer cells *in vitro*, leading to increased drug accumulation within the cells. The synergistic effect of the combined treatment of doxorubicin and miR-34a-loaded micelles was found to be superior to monotherapy, providing a promising strategy for improving the outcomes of esophageal cancer treatment (Dai et al., 2018). The representative nanomaterials for target drugs of esophageal cancer were summarized in Table 5. Recently, a novel T7 peptide-modified pH-responsive targeting nano-system was developed by Deng et al., and in this nano-system the docetaxel and curcumin were co-loaded. As a result, T7-NP-DC was synthesized successfully with 100 nm diameter, good colloidal stability, and pH-responsive drug release property. The loading rate of docetaxel and curcumin is 10% and 6.1%, respectively, and good biosafety was observed, even when the concentration was high. In addition, the therapeutic efficacy of T7-NP-DC was better than NP-DC and docetaxel in terms of growth suppression in the KYSE150 esophageal cancer model (Deng et al., 2020).

2.5 The applications of nanocarriers in immunity of esophageal cancer

The immune system, as an important component in the treatment of esophageal cancer, also possesses great research value. However, even though the nanodrugs have great application potential in immunity of esophageal cancer, the relevant references are still scarce. Utilizing immunostimulants activate immune cells of autosomatic immunity can effectively enhance the immune response and improve the anti-tumor ability within the body. In addition, the nanocarriers are appropriate as platform to long term and precisely deliver immunostimulants and the safety and efficacy of immunotherapy are improved while reducing side effects and complications of

immune response. The immunosuppressive agents such as PD-1 can be delivered using nanodrugs, which can effectively suppress the immune escape of tumor cells, enhance the immune response in patients, and improve the efficacy of immunotherapy. Moreover, the standard first-line treatment for advanced esophageal cancer involves the use of immune checkpoint inhibitors in combination with chemotherapy. In the case of advanced esophageal and gastroesophageal junction cancer (including both squamous cell carcinoma and adenocarcinoma), the recommended first-line therapy includes combining pembrolizumab with platinum-based chemotherapy and fluoropyrimidine. For patients with advanced adenocarcinoma of the gastroesophageal junction, the recommended first-line treatment involves combining nivolumab with oxaliplatin and fluoropyrimidine. Lastly, for patients with advanced esophageal squamous cell carcinoma, the recommended first-line treatment is to combine camrelizumab with paclitaxel and platinum-based chemotherapy. Even though immune checkpoint inhibitor (ICI) is one of the most important tumor treatment methods, the application of nanodrugs in the immunotherapy of esophageal cancer is still limited, and immune nano-drugs delivery system can improve the therapeutic effect of immune checkpoint inhibitors on tumors (Qian et al., 2022). So, a large number of clinical trials are still necessary to verify the role of nanodrugs in the immunotherapy of esophageal cancer.

2.6 The applications of nanocarriers in esophageal cancer surgery

Local recurrence and lymph node metastasis are crucial factors affecting the survival rate of patients with esophageal cancer. However, in patients who experience recurrence after curative surgery for esophageal cancer, the majority present with lymph node metastasis, with a remarkably high proportion of 44.5% (Wang et al., 2010). Currently, in China, the main surgical approaches for esophageal cancer involve two routes: via left thoracic and via right thoracic. Nevertheless, it has been revealed that the left thoracic approach is associated with a high incidence of lymph node metastasis in the upper mediastinum and supraclavicular region, ranging from 30% to 40%. In contrast, via the right thoracic approach, encompassing a complete lymph node dissection of the chest and/or neck, can significantly reduce the rate of lymph node metastasis and recurrence. However, despite the complete lymph node clearance achieved with this approach, it is accompanied by prolonged surgical time, increased trauma, and a higher likelihood of irreversible and fatal complications, without necessarily improving the quality of life and survival benefits for some patients. Hence, it is of utmost clinical importance to selectively remove suspicious positive metastatic lymph nodes in patients with esophageal cancer, avoiding excessive lymph node dissection.

Nanocarbon lymph node tracers represent a novel type of lymphatic tissue-active dye designed for identifying sentinel lymph nodes, observing lymphatic drainage patterns, and guiding curative surgery (Wang C. et al., 2020; Lin et al., 2020). Meanwhile, the nanocarbon lymph node tracers possessing high affinity for lymph nodes and carbon adsorption capacity can effectively adsorb specific chemotherapeutic drugs, facilitate lymphatic-targeted preoperative or intraoperative chemotherapy, and ultimately enhance the quality of life for individuals with tumors. In the context of endoscopic esophageal cancer curative surgery, the use of nanocarbon tracers has been found to increase the number of dissected lymph nodes and detect more metastatic lymph nodes, resulting in reduced postoperative bleeding, drainage, and recurrent laryngeal nerve injury compared to the control group without nanocarbon tracers (Liu P. et al., 2020). Since chemotherapy drugs face challenges in reaching lymph nodes through the bloodstream, the efficacy of systemic chemotherapy for metastatic lymph nodes is limited, resulting in insufficient improvement in survival rates for some patients even if they undergo surgery. Consequently, targeted preoperative or intraoperative chemotherapy for lymph node metastasis assumes paramount significance. By leveraging the characteristics of large molecular substances and particles that are easily engulfed by the lymphatic system, preoperative or intraoperative lymphatic-targeted chemotherapy utilizing drug-loaded nanoparticles enhances the drug concentration within local lymph nodes, prolongs drug action duration, and mitigates drug toxicity and side effects. Although the application of nanocarbon in esophageal cancer surgery is currently limited, the aforementioned studies collectively demonstrate that nanocarbon improves the quality of life and prolongs survival time for patients undergoing curative surgery for esophageal cancer, underscoring its immense value in this therapeutic context.

Endoscopic submucosal dissection (ESD), is an advanced minimally invasive technique using various electrosurgical knives and endoscopy for the meticulous submucosal dissection of the *en bloc* resection of lesions larger than 2 cm. ESD offers several advantages over traditional surgical approaches, including accurate pathological staging, shorter operation time, faster recovery, shorter hospital stay, and reduced medical costs (Kantsevoy et al., 2008). Even though ESD has become the preferred treatment modality for early-stage gastrointestinal cancers and precancerous lesions, the major challenges associated with ESD are the higher risk of bleeding and perforation (Yamamoto, 2012). To mitigate these complications, injecting appropriate submucosal injection media, a thick liquid or gas cushion, allows for effective and prolonged separation between the lesion and muscular layer playing a critical role, which is crucial for successful ESD. Traditional submucosal injection media, such as physiological saline, are quickly absorbed by the surrounding tissue, necessitating repeated injections during the ESD procedure (Zhou et al., 2014), while hypertonic solutions can cause tissue damage (Fujishiro et al., 2005; Katsinelos et al., 2008). In contrast, hyaluronic acid (nano-)hydrogel has many advantages such as maintaining a favorable submucosal fluid cushion and excellent safety, making it the preferred choice for submucosal injection during ESD (Jung and Park, 2013). Similarly, hydroxyethyl cellulose, a synthetic product, can trigger antigen-antibody reactions (Lenz et al., 2010), while fibrinogen mixture carries the risk of viral transmission, including hepatitis (Uraoka et al., 2009). Recent advancements in submucosal injection media have introduced novel options. For example, carbon dioxide gas has shown promising results as a submucosal buffering agent, significantly extending the elevation time of the submucosal layer compared to physiological saline (Uraoka et al., 2011). Sodium alginate (nano-) hydrogel has emerged as a potential alternative

to hyaluronic acid, exhibiting favorable characteristics as a submucosal injection medium (Kang et al., 2013). Additionally, elastic polymer submucosal layer elevation has demonstrated superior performance over physiological saline, providing greater elevation height and promoting effective post-ESD mucosal healing (Tran et al., 2012). Moreover, a new approach involves using DMEM/F12 cross-linked chitosan hydrogel, which can be transformed into an insoluble hydrogel through brief exposure to ultraviolet irradiation. Compared to hypertonic saline and hyaluronic acid, this hydrogel exhibits sustained elevation and clear margins, enabling precise endoscopic submucosal dissection without complications such as bleeding or perforation. However, because of the longer degradation time its prolonged degradation time *in vivo* may delay wound healing (Kumano et al., 2012). In summary, ESD has revolutionized the treatment of early-stage gastrointestinal cancers and precancerous lesions. To address the challenges of bleeding and perforation, the selection of suitable submucosal injection media is crucial. While traditional options have limitations, recent advancements, such as (nano-) hydrogel hyaluronic acid, sodium alginate, cross-linked chitosan hydrogel and carbon dioxide gas, offer promising alternatives with improved safety and efficacy. Continued research in this field is essential to optimize the outcomes of ESD and further enhance patient care.

2.7 The applications of nanocarriers in new treatment of esophageal cancer

Nowadays, there are two common new methods used for non-surgical tumor therapy, i.e., photothermal therapy (PTT) and photodynamic therapy (PDT). In PTT, tumor cells are eliminated by subjecting a photosensitizer to light of a specific wavelength, which induces localized heating and subsequent cell death, and as for PDT, a photosensitizer that, upon exposure to specific light, generates a high concentration of reactive oxygen species (ROS) leading to tumor cell eradication. While the use of photosensitizers is essential in PDT, PTT offers the advantage of enhanced therapeutic efficacy and outcomes without the need for exogenous heat-generating agents.

2.7.1 The PTT nanocarriers in esophageal cancer

Tumor hyperthermia therapy employs various techniques such as ultrasound, microwave, radiofrequency, and magnetic field to heat tumor tissue. This treatment approach demonstrates a higher specificity towards tumors due to their inherent heat tolerance, but the therapy efficacy is limited because the damage to adjacent healthy tissues should be minimized (Gonçalves et al., 2020). Photothermal therapy (PTT) has emerged as a promising solution to overcome this challenge by utilizing photothermal agents to precisely heat the targeted area and restrict thermal damage to the tumor tissue. However, the effectiveness of PTT relies on improved light absorption and enhanced photothermal conversion efficiency (Wang et al., 2020b). Noble metal nanoparticles, commonly employed as photothermal agents for *in vivo* therapy, offer a less invasive experimental technique that ensures effective cancer treatment (Huang et al., 2006). The efficacy of PTT depends on two primary factors: i) the light source, such as lasers, which enable deeper tissue penetration by emitting light in the spectral range of 650–900 nm, and ii) light-absorbing nanoparticles that facilitate photothermal ablation through efficient conversion of light into heat within picosecond timescales (Chen et al., 2007). These nanoparticles exhibit strong absorption in the near-infrared (NIR) region of the electromagnetic spectrum, particularly in the range of 650–900 nm, due to their surface plasmon resonance (SPR) effect, and notably, the absorption coefficient of nanoparticles is 4–5 times higher than that of photothermal dyes owing to their SPR characteristics (Jain et al., 2008). Spherical gold nanoparticles typically exhibit their maximum SPR absorption peak in the visible spectrum, around 520 nm. Huang et al. identified gold nanorods as effective photothermal agents due to their longitudinal absorption bands in the NIR region resulting from SPR oscillation (Huang et al., 2010). Specifically, small-diameter gold nanorods are preferred as NIR photothermal converters for *in vivo* applications due to their high absorption cross-section beyond the tissue absorption spectrum. Moreover, the nanorods hold promise as an ablative component for cancer treatment, as it enables NIR light transmission through human skin and tissue (Kuo et al., 2010). Another approach involves utilizing silica-gold with core-shell structure to enhance the photothermal effect within cancer cells because of the controlled thermotherapy generated under laser (Terentyuk et al., 2009). A research by Chen et al. explored a gold nanoshell-based system for cancer targeting and PTT in HER2-overexpressing and drug-resistant ovarian cancer cells (OVCAR3). This nanomaterial was designed to facilitate simultaneous fluorescence optical imaging and magnetic resonance imaging, and the study revealed selective killing of OVCAR3 cells upon NIR laser irradiation using the nanocomposite system (Chen et al., 2010). Additionally, Arnfield et al. conducted an observational clinical trial involving core-shelled gold-silica induced hyperthermia, followed by NIR light exposure, in patients with squamous cell carcinoma of the head and neck (Arnfield et al., 1992). In another study, McGrath et al. conducted research on the synthesis and efficacy of palladium-gold nanocomposites for enhanced photothermal therapy (PTT) applications (McGrath et al., 2015). They successfully demonstrated the potential of PTT by combining these nanocomposites with 808 nm diode laser radiation, leading to the effective eradication of HeLa cells *in vitro* and the destruction of cervical cancer cells in HeLa tumor xenografts in male B9 mice. Similarly, Shen et al. reported the effects of photothermal ablation mediated by magnetic nanoparticle clusters on both *in vitro* and *in vivo* cancer models (Shen et al., 2015). Their findings revealed that clustered Fe_3O_4 nanoparticles exhibited significantly enhanced NIR absorption compared to magnetic Fe_3O_4 nanoparticles alone, and the clustered nanoparticles achieved higher cellular toxicity against A549 cells by generating elevated temperatures after NIR irradiation at 808 nm. Furthermore, an *in vivo* study of photothermal therapy in a tumor-bearing mouse model (A549) also demonstrated that clustered Fe_3O_4 nanoparticles had superior therapeutic efficacy compared to individual free Fe_3O_4 nanoparticles (Alshehri et al., 2020). As well as Fe_3O_4 nanoparticles, the dispersive gold nanoparticles have no damage to tissues while once they aggerate and irradiated by near-infrared (NIR) light, malignant tissues can be selectively destroyed. Yan Li et al. investigated the feasibility of using chitosan-coated gold/gold sulfide (CS-GGS) nanoparticles for photothermal ablation therapy of esophageal

adenocarcinoma. In their study, a rat model of esophagojejunostomy was employed for *in vivo* ablation experiments, and three human esophageal cell lines were utilized to assess the response of cancerous and benign cells to NIR light following treatment with CS-GGS nanoparticles. The results demonstrated that both cancer tissue and cancer cells exhibited higher uptake of gold nanoparticles, resulting in complete ablation upon exposure to NIR light. In contrast, benign tissue and non-cancerous cells exhibited lower nanoparticle uptake and maintained viability after NIR light exposure. Therefore, CS-GGS nanoparticles represent a promising intracavitary treatment option for NIR light-mediated ablation of esophageal cancer (Li et al., 2013). Moreover, the silica nanostructures were effectively covered onto the synthesized Cu_9S_5 to form Cu_9S_5@MS core-shell nanostructures. This nano-system successfully utilized for photothermal removal of esophageal squamous carcinoma cells and NIR therapy with good biocompatibility (Wang et al., 2019).

2.7.2 The PDT nanocarriers in esophageal cancer

Photodynamic therapy (PDT) is gaining attention as a promising treatment modality for oral diseases due to its numerous advantages, and this physical therapy has now evolved into a viable treatment option within the realm of cancer chemotherapy. PDT has been explored as a treatment approach for various cancer types, including skin cancer, head and neck cancer, esophageal cancer, gastric cancer, pancreatic cancer, bladder cancer, prostate cancer, and lung cancer. PDT involves the localized application or systemic administration of a photosensitizer, which accumulates in the target tissue and undergoes a light-induced photochemical reaction, resulting in irreversible tissue damage or necrosis. PDT exploits the ability of photosensitizers to absorb specific wavelengths of light, generating oxygen-based molecular species that induce cytotoxic effects, and these reactive species cause damage to cellular membranes and subcellular organelles, ultimately leading to cell death through apoptosis, necrosis, or autophagy. The effectiveness of PDT relies on the photosensitizers' capacity to selectively produce singlet oxygen at therapeutic concentrations within the tumor site (Chen et al., 2020). A wide range of organic photosensitizers, including porphyrins, dipyrrolemethene or phthalocyanine derivatives, curcumin, etc., have been extensively investigated for PDT in clinical and preclinical settings. To enhance the *in vivo* therapeutic efficacy of nanoparticle-mediated PDT in cancer, these photosensitizers are often encapsulated within nanocarriers.

Furthermore, in recent years, nanomaterials with inherent photodynamic properties, such as graphene, quantum dots (QDs), and titanium dioxide (TiO_2) nanoparticles, have emerged as potential alternatives to overcome the limitations associated with hydrophobic photosensitizers (Sivasubramanian et al., 2019). Unterweger et al. conducted a study to develop iron oxide nanoparticles loaded with curcumin as carriers for photodynamic therapy (PDT) (Unterweger et al., 2015). Flow cytometry analysis of Jurkat human T-cell leukemia cell line demonstrated that the pure nanoparticle system and curcumin alone did not exhibit toxicity when cells were not exposed to light. However, when curcumin was delivered in combination with the nanoparticles and light irradiation was applied, concentration- and time-dependent cancer cell death was induced due to the formation of reactive oxygen species. In another study, Li et al. developed hybrid nanoparticles consisting of thiolated heparin-deprotonated chlorophyll A (PhA) conjugated iron oxide and gold nanoparticles (Fe_3O_4/Au-NP) for efficient monitoring of PDT (Li L. et al., 2014). Experimental results showed that A549 cancer cells treated with the hybrid nanoparticles and subjected to light irradiation displayed significant phototoxicity and strong fluorescence signals. Furthermore, Shen et al. designed a novel nanocomposite for tumor targeting, composed of quantum dot-zinc-porphyrin nanocomplexes encapsulated in folate-modified phospholipid polymers (Shen et al., 2017). This system exhibited a high payload of porphyrin, leading to a significantly increased production of singlet oxygen, and *in vivo* studies demonstrated the preferential accumulation of the developed nanoparticle system in tumor tissue, allowing for effective monitoring of PDT using non-invasive fluorescence imaging techniques in a mouse model. Additionally, Murakami et al. investigated the ability of semiconductor-rich and metal-rich single-walled carbon nanotubes to generate reactive oxygen species under near-infrared light (808 nm) irradiation (Murakami et al., 2012). Their findings indicated that the semiconductor-rich single-walled carbon nanotubes exhibited a stronger photodynamic effect compared to the metal-rich counterparts. The representative nanomaterials for new treatment of esophageal cancer were summarized in Table 6.

3 The applications of nanocarriers in complications of esophageal cancer

3.1 Esophageal stenosis or esophageal obstruction

Dysphagia, a prominent symptom in the majority of advanced esophageal cancer patients who have eliminated the occasion of curative surgical interventions. Although the insertion of esophageal stents can alleviate eating difficulties to some extent, it fails to address tumor control. To explore new treatment avenues for late-stage esophageal cancer patients, researchers have incorporated nanoparticles into stents coated with a fibrous membrane. Subsequently, through intracavity photodynamic therapy, they observed a substantial increase in animal survival time, presenting a novel therapeutic direction. Zhao et al. reported that a patient with esophageal squamous cell carcinoma experienced local progression following chemoradiotherapy, resulting in nutritional deficiencies and mild anemia due to impaired eating. Facilitated by innovative localization techniques, i.e., X-ray fluoroscopy and albumin-bound paclitaxel, photodynamic therapy was employed to this patient, leading to positive clinical outcomes (Zhao et al., 2022). Li et al. explored the application of polydopamine (PDA) and polyethyleneimine (PEI) coatings on 317L stainless steel (317LSS) esophageal stents, and after modification the surface exhibited tumor growth inhibition, endowing the stents with sustained anticancer functionality, thus offering an ideal strategy for mitigating esophageal restenosis (Zhang et al., 2017). Similarly, Bai et al. coated the surface of 317LSS esophageal stents with a layer composed of polydopamine/polyethyleneimine/5-fluorouracil (PDA/PEI/5-Fu), demonstrating strong antitumor and anti-restenosis properties

TABLE 6 Representative nanomaterials for new therapy method of esophageal cancer.

Types	Materials	Features and findings	Application	References
PTT	Gold nanoshell	facilitate simultaneous fluorescence optical imaging and magnetic resonance imaging, selectively kill of OVCAR3 cells upon NIR laser irradiation	Ovarian cancer cells	Chen et al. (2010)
	Palladium-gold nanocomposites	Lead to the effective eradication of HeLa cells *in vitro* and the destruction of cervical cancer cells in HeLa tumor xenografts in male B9 mice	Cervical cancer	McGrath et al. (2015)
	Clustered Fe_3O_4 NPs	enhance NIR absorption and achieve higher cellular toxicity against A549 cells by generating elevated temperatures after NIR irradiation at 808 nm	Lung cancer	Alshehri et al. (2020)
	Chitosan-coated gold/gold sulfide NPs	Complete ablation upon exposure to NIR light	Esophageal cancer	Li et al. (2013)
PDT	Iron oxide NPs loaded with curcumin	Generate reactive oxygen species after light irradiation and induce concentration- and time-dependent cancer cell death	T-cell leukemia	Unterweger et al. (2015)
	Thiolated heparin-deprotonated chlorophyll A (PhA) conjugated Fe_3O_4/Au-NPs	A549 cancer cells treated with the hybrid nanoparticles and subjected to light irradiation display significant phototoxicity and strong fluorescence signals	Lung cancer	Li et al. (2014a)
	Quantum dot-zinc-porphyrin nanocomplexes encapsulated in folate-modified phospholipid polymers	High payload of porphyrin, lead to a significantly increased production of singlet oxygen, and accumulate the developed nanoparticle system in tumor tissue, allow for effective monitoring of PDT using non-invasive fluorescence imaging techniques in a mouse model		Shen et al. (2017)

(Bai et al., 2018). In a related study, Zhang et al. also found that the PDA/PEI/5-Fu composite layer on the esophageal stents inhibited the viability of pathological cells and the expression of E-cadherin, thus blocking the NF-κB signaling pathway. Additionally, the loaded 5-Fu suppressed the release of inflammatory factors (TNF-α and IL-1β), promoted macrophages to release anti-inflammatory/anti-tumor factors (IL-10 and IL-4), and inhibited the migration of pathological cells. Both PEI and 5-Fu contributed to the upregulation of Bax and Caspase-3 (pro-apoptotic factors) and the downregulation of Bcl-2 (anti-apoptotic factor) in esophageal tumor cells. These comprehensive findings suggest that the PDA/PEI/5-Fu coating holds significant potential for multi-pathway anticancer and anti-inflammatory effects in the surface modification of esophageal stents (Zhang et al., 2020). Song and co-workers developed an innovative approach involving the application of a highly efficient gold nanoshell (AuNS) coating on stents, and in brief, the surface of the stents was coated with polydopamine to serve as an anchor and template for Au^{3+} ions. The resulting AuNS-coated stents exhibited enhanced temperature elevation upon near-infrared (NIR) laser irradiation in pork and pig intestines. Compared to bare metal stents, these AuNS-modified stents hold immense potential for clinical implementation, as they can facilitate duct channel opening and impede tumor growth (Song et al., 2016).

Cho et al. developed a self-expanding metal stent coated with gold nanoparticles for photothermal therapy under near-infrared laser irradiation, which successfully treated granulation tissue formation after stent placement in the rat esophagus (Cho et al., 2021). In another study, Liu et al. designed a biodegradable composite scaffold by coating poly (lactic-co-glycolic acid) (PLGA) with paclitaxel (PTX) onto a magnesium-based woven scaffold. Compared to scaffolds without PTX-PLGA coating, the PTX-PLGA scaffolds exhibited higher radial force and faster degradation in an acidic environment, effectively promoting fibroblast apoptosis *in vitro* (Liu et al., 2022).

3.2 Oesophagitis

The clinical results show that during the radiotherapy process, there is a risk of oesophagitis which is an adverse concomitant disease hindering therapy. Thus, inhibiting concomitant oesophagitis becomes a research focus. Michael W. et al. administered intragastric injections of manganese superoxide dismutase (MnSOD)-plasmid/liposome complexes into experimented C3H/HeNsd mice. The results showed that this treatment effectively prevented radiation-induced esophagitis (Epperly et al., 2001). Additionally, Niu et al. investigated the effects of MnSOD-plasmid/liposome complexes in mice and found that they improved esophageal radiation tolerance by enhancing the engraftment and self-renewal of bone marrow-derived progenitor cells in the esophageal squamous epithelium (Niu et al., 2008). Furthermore, in an *in vitro* study, Michael W. et al. also transfected human esophageal segments with the MnSOD-plasmid/liposome complexes, demonstrating their ability to prevent cell apoptosis induced by ionizing radiation and alleviate radiation-induced esophagitis (Epperly et al., 2000).

4 The exploration of nanocarriers in Chinese patent medicine

The rapid development of nanomaterials provides excellent carriers for Chinese patent medicine which is also widely used to treat cancer including esophageal cancer, and the exploration of nanocarriers used in Chinese patent medicine has never stopped.

For instance, Hu et al. prepared a nanocomposite material comprising chitosan-sodium alginate-polyethylene glycol-crocin which can inhibit the growth of KYSE-150 esophageal cancer cells by effectively increasing the generation of reactive oxygen species (ROS) and inducing apoptotic cell death (Hu et al., 2022). Moreover, Al-Hazmi et al. purified cyanine dye from *Pseudomonas aeruginosa* and immobilized it onto nanochitosan. The anticancer activity of dissociative cyanine dye and nanocyanine dye was evaluated against CLS-145 gastric cancer cells, AsPC-1 pancreatic cancer cells, HCT116 colon cancer cells, KYSE-410 esophageal cancer cells, and HepG2 liver cancer cells, and the antibacterial activity of these dyes against bacteria associated with gastrointestinal cancer biopsies, including *Helicobacter pylori*, *Fusobacterium* nucleatum, enterohemorrhagic *Escherichia coli*, *Clostridium difficile*, and Porphyromonas gingivalis, was also examined. The results demonstrated notable anticancer and antibacterial effects for both dissociative cyanine dye and nanocyanine dye, and the nanocyanine dye exhibiting superior activity in suppressing cancer growth and combating bacterial strains (Al-Hazmi and Naguib, 2022). Furthermore, Li et al. synthesized two novel polymer-drug conjugates, docetaxel-polyvinyl alcohol and docetaxel-chitosan, via alcoholysis reactions. These nanocomposites exhibited dose-dependent inhibition of ECA-109 human esophageal cancer cells and EMT6 mouse mammary cancer cells and they induced apoptosis in ECA-109 cells and caused cell cycle arrest at the S phase. Notably, the conjugates demonstrated significant antitumor activity in an EMT6 tumor-bearing mouse model, surpassing the tumor suppression rates of free docetaxel (Li M. et al., 2014). Martin et al. investigated the synthesis and characterization of a novel nanosystem comprising gold nanorods loaded with curcumin and then incorporating them into polymer nanoparticles (Martin et al., 2015). The viability of adenocarcinoma cells was significantly reduced because both gold nanorods and curcumin exhibited effective photothermal effects. Therefore, the combination of gold nanorods and curcumin presents a safe and effective approach for eradicating precancerous esophageal adenocarcinoma (Li et al., 2022). Zhan encapsulated β-elemene within the pores of mesoporous silica nanoparticles, while artemisinin was electrostatically adsorbed onto the nanoparticle surface, resulting in a synergistic dual-drug nanosystem. This nanosystem demonstrated excellent antitumor effects both *in vitro* and *in vivo*, offering a promising therapeutic option for esophageal cancer treatment (Zhan et al., 2020). Zou et al. employed a simple biosynthetic method to prepare copper oxide nanoparticles (CuO nanoparticles) using an extract from Astragalus membranaceus at ambient temperature. These nanoparticles exhibited cytotoxicity against the human esophageal cancer cell line KYSE30, while no significant cytotoxicity was observed in human dermal fibroblasts (Zou et al., 2020). Zhang et al. successfully synthesized nickel nanoparticles using the aqueous extract of Calendula officinalis leaves in a water-based medium, which demonstrated significant inhibitory and antioxidant effects against esophageal cancer cell lines (Zhang et al., 2021). Jiang et al. synthesized biogenic zinc oxide nanoparticles (ZnO nanoparticles) using a plant extract obtained from Arisaema heterophyllum showing good biocompatibility and exhibited anti-esophageal cancer activity (Jiang et al., 2020). Cyclin D1 is commonly overexpressed in esophageal squamous cell carcinoma and plays a crucial role in tumor development and proliferation (Dey et al., 2015). Curcumin possesses anti-inflammatory, antioxidant, and anticancer properties and has been shown to have therapeutic effects against esophageal cancer. The bioavailability of curcumin in free form is limited, but in contrast, nanocurcumin significantly reduced the proliferation of esophageal squamous cell carcinoma KYSE-30 cells without affecting the proliferation of normal esophageal cell lines. Furthermore, it downregulated the expression of Cyclin D1 (Hosseini et al., 2018).

Pi et al. devised a strategy to enhance the anticancer efficacy by targeting cancer cells with overexpressed epidermal growth factor receptor (EGFR) using GE11 peptide-conjugated selenium nanoparticles for the delivery of colchicine (Pi et al., 2017). This study revealed that this method achieved efficient loading of GE11 peptide-conjugated selenium nanoparticles, resulting in enhanced uptake by tumor cells and improved tumor suppression while reducing nonspecific toxicity. The nanoparticles exhibited preferential accumulation in lysosomes, enabling the release of colchicine in acidic conditions. Subsequently, upon translocation to the cytoplasm, they induced disruption of membrane integrity (Li et al., 2022).

5 The toxicity of inorganic nanocarriers

Even though there are extensive preclinical studies conducted over the past two decades have demonstrated the distinct diagnostic and therapeutic opportunities offered by inorganic and metallic nanoparticles because of their unique physicochemical properties, setting them apart from polymer and lipid nanoparticles. These inorganic nanoparticles are well-positioned to address several challenges that remain unresolved in clinical applications. However, the issue of toxicity has overshadowed their potential therapeutic and diagnostic benefits, warranting careful consideration. In general, nanomaterials tend to accumulate within various cell types, including macrophage-like cells such as tissue and blood phagocytes, as well as reticuloendothelial system (RES) cells, and their deposition has been observed in tissues such as lymph nodes, bone marrow, brain, spleen, adrenal glands, liver, and kidneys, highlighting their widespread distribution. The impact of physicochemical properties of inorganic nanoparticles, including size, shape, solubility, surface charge, chemical structure, reactivity, and surface modifications, has been extensively investigated and is well-documented (Mohammadpour et al., 2019), and their safety concerns associated with nanomedicines are well-documented, particularly regarding DNA damage and oxidative stress (Damasco et al., 2020). In this discussion, we focus on the biocompatibility issues pertaining to commonly used and promising inorganic nanoparticles (NPs). Taking gold nanoparticles (AuNPs) as an illustrative example, it has been observed that colloidal AuNPs with sizes ranging from 10 to 50 nm may exhibit greater toxicity compared to larger particles measuring 100–200 nm. Specifically speaking, AuNPs within the size range of 2.8–38 nm have been found to induce heightened toxicity and immune responses (Yen et al., 2009). Conversely, there is an exception that AuNPs measuring 15 nm demonstrate no toxicity to cells, even at concentrations 60 times higher than the IC50 of smaller AuNPs (Dauty and Verkman, 2005). These findings

underscore the size-dependent toxicity of AuNPs. Specifically, smaller AuNPs, especially those below 15 nm, have been found to significantly upregulate pro-inflammatory genes such as interleukin-1, interleukin-6, and tumor necrosis factor-α, resulting in a reduction in macrophage population (Adewale et al., 2019). The relationship between AuNP shape and toxicity has also been investigated, with a study conducted by Sun et al. revealing shape-dependent *in vivo* toxicity of AuNPs, i.e., rod-shaped AuNPs demonstrated the highest toxicity, followed by cubic AuNPs, while spherical AuNPs exhibited the best biocompatibility. (Sun et al., 2011). Additionally, the study highlighted the preferential accumulation of all AuNPs in the liver and spleen, and consistent with the biodistribution patterns of other nanomedicines, AuNPs, following intestinal absorption, exhibit high distribution in the blood, brain, lungs, heart, kidneys, liver, and spleen (Qiu et al., 2010). Moreover, positively charged spherical AuNPs exhibited greater toxicity compared to negatively charged particles of the same size.

Moving on to other widely explored inorganic nanoparticles with significant safety concerns, Quantum Dots (QDs) have been extensively investigated for their diagnostic and therapeutic potential. However, it is known that QDs composed of heavy metal ions such as Cd^{2+}, released from QDs lacking polymer protection when exposed to ultraviolet radiation, can induce lung and kidney damage (Schmid et al., 2017). *In vitro* studies on CdSe QDs have shown acute toxicity to primary liver cells, attributed to the release of free Cd^{2+} ions (Kargozar et al., 2020). Among the metal-based nanoparticles, Superparamagnetic Iron Oxide Nanoparticles (SPIONs) have garnered considerable attention due to their biodegradability and relatively lower toxicity under *in vivo* conditions (Lee et al., 2010). SPIONs have been extensively evaluated and developed for diagnostic applications, and more recently, they have shown promise in the field of magnetic hyperthermia therapy. However, some iron oxide materials have been withdrawn from use due to toxicity concerns or a lack of clinical benefits. Toxicity levels of SPIONs have been a subject of debate among researchers, primarily based on viability test results, and the biodistribution studies have shown the accumulation of SPIONs in various tissues and organs, including the brain. Nevertheless, a clear understanding of acute toxicity, genetic toxicity, immune toxicity, reproductive toxicity, and neurotoxicity of SPIONs is still lacking, and results vary across different animal models. Lastly, gadolinium (Gd), commonly used as a contrast agent in clinical settings, including cancer treatment, deserves discussion. Despite its widespread use, gadolinium nanoparticles have raised concerns regarding human toxicity, and patients with pre-existing renal impairment may develop Nephrogenic Systemic Fibrosis (NSF), a condition characterized by systemic tissue fibrosis, following the administration of gadolinium (Alshehri et al., 2020). It is crucial to further investigate the toxicity profile of gadolinium nanoparticles, considering their potential applications in theragnostic.

6 Challenges for clinical translational and approval of cancer nanomedicine

The process of translating cancer nanomedicines from laboratory research to clinical applications and commercialization is a time-consuming and resource-intensive endeavor. While a limited number of nanomedicines, including Doxil®, Myocet®, Abraxane®, Depocyt®, and Genexol®, have successfully obtained regulatory approval for use in chemotherapy, the overall number remains relatively low. This phenomenon highlights the significant disparity that exists between the laboratory-level development of nanomedicines and their subsequent translation into clinical practice and large-scale industrial production (Ferrari, 2005).

The following paragraphs aim to address the critical issues that impede the clinical development and regulatory approval of cancer nanomedicines: 1) One major and pivotal drawback lies in our limited understanding of the pathological and physiological complexities and heterogeneity of tumor sites that influence patient selection. Identifying which patients are most likely to benefit from nanoparticle-based chemotherapy remains a challenge (Maeda, 2015). 2) Additionally, our knowledge of the behavior of nanoparticles inside the body is predominantly based on animal data, and the animal models used often fail to accurately replicate the true *in vivo* conditions. 3) Typically, systemically administered nanoparticles accumulate in solid tumors via the enhanced permeability and retention (EPR) effect, but several crucial aspects related to the interpretation of EPR have been significantly overlooked, including nanoparticle-protein interactions, blood circulation, tumor tissue penetration, and cellular internalization. Furthermore, the behavior of nanoparticles *in vivo* is greatly influenced by their characteristics, such as size, geometry, surface features, and consequently, there are numerous factors governing the EPR-driven *in vivo* behavior of nanoparticles that cannot be reliably predicted solely from animal data. In summary, these challenges underscore the complex nature of translating nanomedicines into clinical applications. To overcome these hurdles, a more profound understanding of tumor heterogeneity, as well as the impact of nanoparticle properties on their *in vivo* behavior, is imperative. This necessitates further research and exploration to bridge the gap between preclinical studies and clinical translation.

In addition, one of the key obstacles lies in optimizing the physicochemical parameters necessary for the successful development of therapeutic nanoparticles. This optimization process is essential but presents a significant barrier to the rapid and reproducible synthesis of large quantities of nanoparticles with distinct characteristics due to the involvement of multiple steps or intricate techniques. To overcome this challenge, new scaling strategies and alternative approaches to formulation development must be explored (Karnik et al., 2008). Additionally, the clinical development of nanomedicines faces ambiguity in the requirements of chemistry, manufacturing, and controls (CMC) and good manufacturing practice (GMP). Scaling up the production of more complex nanomedicines introduces challenges in maintaining compliance with CMC and GMP standards. This necessitates improvisation and adaptation of existing manufacturing processes to meet regulatory requirements (Rolland et al., 2005). To date, the evaluation of the enhanced permeability and retention (EPR) effect and nanoparticle penetration in human tumor metastasis models has proven to be of significant importance, considering the impact of tumor metastasis on cancer-related mortality (Zuckerman et al., 2014). The successful clinical translation of cancer nanomedicines heavily relies on the introduction of animal models that faithfully replicate

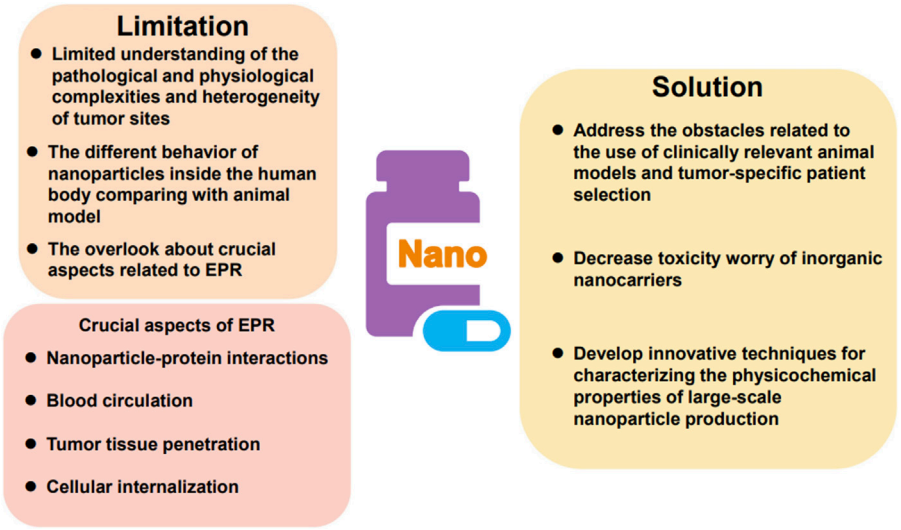

FIGURE 4
The limitation and solution of nanomaterials for therapy and diagnosis of esophageal cancer.

the heterogeneity and anatomical histology observed in human tumors (Meads et al., 2009).

In summary, addressing the obstacles related to the use of clinically relevant animal models, tumor-specific patient selection, decrease toxicity worry of inorganic nanocarriers and the development of innovative techniques for characterizing the physicochemical properties of large-scale nanoparticle production are crucial steps towards the successful clinical translation of cancer nanomedicines (Figure 4).

7 Discussion and outlook

The field of cancer nanomedicine encompasses two primary areas: cancer nanotherapy and nanodiagnostics. Over the past four decades, significant advancements have been made in cancer treatment through the development of cancer nanomedicines including extending overall survival, improving quality of life, and reducing toxicity. The approval of liposomal doxorubicin (Doxil®) as the first cancer nanomedicine two decades ago marked a turning point, leading to substantial investment and research in this field by both industry and academia. However, translating the promising preclinical results of cancer nanomedicines into clinical success has proven to be a challenging task. Despite these challenges, there have been recent approvals of nanomedicine products for the treatment of orphan cancers, as well as ongoing developments in cancer nanomedicines for cancer immunotherapy, while the approval of lipid nanoparticle-formulated mRNA as a vaccine for COVID-19 in late December 2020 has also reignited interest in cancer nanomedicines and renewed hopes for the development of non-viral cancer vaccines. The field of cancer nanomedicine has garnered more interest and investment compared to any other therapeutic area reflected in the global revenue trends and forecasts in the nanomedicine market since 2016, where the market share of cancer nanomedicine is significantly higher than that of other therapeutic areas. Currently, there are 18 approved cancer nanomedicines, many of which have shown positive results in Phase III trials holding great promise for improving cancer treatment. Additionally, the successful approval of nanoanalogue for several cancer nanomedicines is helping to alleviate the high financial burden associated with cancer treatment. It is anticipated that the use of generic drugs will further enhance affordability and accessibility of nanomedicines in the near future. In conclusion, the field of cancer nanomedicine has made significant progress in improving cancer treatment, and despite the challenges faced in translating preclinical success to clinical efficacy, there is a continued drive for research and development in this field. The potential of nanomedicines to revolutionize cancer therapy and their growing market presence highlight the importance of ongoing investment and exploration in cancer nanomedicine.

The field of nanotheranostics and nanodiagnosis are rapidly evolving research areas that has not yet reached clinical standards. While some nanodiagnostic systems exhibit significant diagnostic efficacy, they often lack therapeutic capabilities, and on the other hand, certain systems have demonstrated primary therapeutic indicators but limited imaging capabilities. To overcome these limitations, extensive efforts have been made to explore various nanomaterials and modification techniques, assessing their *in vivo* performance and paving the way for potential clinical trials. Currently, most research in nanodiagnostics focuses on evaluating their diagnostic and therapeutic applications using animal models, yielding promising results. However, the translation of these systems to human subjects has proven challenging due to differences in the diffusion mechanisms between animals and humans. Moreover, the potential toxicity and safety concerns associated with nanotheranostics when used in humans have been a significant area of investigation, such as nanodiagnostic systems based on carbon nanotubes and metal nanoparticles have raised safety concerns due to their slow degradation and potential *in vivo* accumulation. In response, researchers have explored strategies such as surface coating with biocompatible/biodegradable polymers or synthesizing nanodiagnostic systems using clinically approved nanomaterials to enhance their *in vivo* efficacy and address

safety concerns. While substantial progress has been made in designing complex nanotheranostic systems worldwide, significant efforts are still needed before their widespread clinical application becomes a reality. Nevertheless, the future of nanotheranostics in clinical practice is within reach, and with continued dedication and research, further advancements can be expected.

Author contributions

LZ, XL, JT, and HL contributed to conception and design. LZ, XL, GY, YH, QC, and JW review the literature. LZ, XL, GY, LG, YH, QC, and JW arrange the literature and plots. LZ, XL, LG, JT, and HL wrote, reviewed, and/or revised the manuscript. All authors contributed to the article and approved the submitted version.

Funding

This work was supported by Henan Medical Science and Technology Research Project (No. 212102310338), Henan Medical Science and Technology Project Jointly Built by the Ministry and the Province (No. LHGJ20190673), Postdoctoral Research Project of Henan Province (No. 202002077), National Natural Science Foundation of China (No. 82205217) and Natural Science Foundation of Henan Province (No. 222300420364).

Conflict of interest

The authors declare that the research was conducted in the absence of any commercial or financial relationships that could be construed as a potential conflict of interest.

Publisher's note

All claims expressed in this article are solely those of the authors and do not necessarily represent those of their affiliated organizations, or those of the publisher, the editors and the reviewers. Any product that may be evaluated in this article, or claim that may be made by its manufacturer, is not guaranteed or endorsed by the publisher.

References

Adewale, O. B., Davids, H., Cairncross, L., and Roux, S. (2019). Toxicological behavior of gold nanoparticles on various models: Influence of physicochemical properties and other factors. *Int. J. Toxicol.* 38 (5), 357–384. doi:10.1177/1091581819863130

Ai, D., Chen, Y., Liu, Q., Zhang, J., Deng, J., Zhu, H., et al. (2018). Comparison of paclitaxel in combination with cisplatin (TP), carboplatin (TC) or fluorouracil (TF) concurrent with radiotherapy for patients with local advanced oesophageal squamous cell carcinoma: A three-arm phase III randomized trial (ESO-Shanghai 2). *BMJ open* 8 (10), e020785. doi:10.1136/bmjopen-2017-020785

Akhter, M. H., Rizwanullah, M., Ahmad, J., Ahsan, M. J., Mujtaba, M. A., and Amin, S. (2018). Nanocarriers in advanced drug targeting: Setting novel paradigm in cancer therapeutics. *Artif. Cells Nanomed. B* 46 (5), 873–884. doi:10.1080/21691401.2017.1366333

Al-Hazmi, N. E., and Naguib, D. M. (2022). Microbial azurin immobilized on nano-chitosan as anticancer and antibacterial agent against gastrointestinal cancers and related bacteria. *J. Gastrointest. Canc.* 53 (3), 537–542. doi:10.1007/s12029-021-00654-6

Alphandéry, E. (2019). Biodistribution and targeting properties of iron oxide nanoparticles for treatments of cancer and iron anemia disease. *Nanotoxicology* 13 (5), 573–596. doi:10.1080/17435390.2019.1572809

Alshehri, S., Imam, S. S., Rizwanullah, M., Akhter, S., Mahdi, W., Kazi, M., et al. (2020). Progress of cancer nanotechnology as diagnostics, therapeutics, and theranostics nanomedicine: Preclinical promise and translational challenges. *Pharmaceutics* 13 (1), 24. doi:10.3390/pharmaceutics13010024

Arnfield, M., Mathew, R., Tulip, J., and McPhee, M. (1992). Analysis of tissue optical coefficients using an approximate equation valid for comparable absorption and scattering. *Phys. Med. Biol.* 37 (6), 1219–1230. doi:10.1088/0031-9155/37/6/002

Bai, Y., Zhang, K., Xu, R., Liu, H., Guan, F., Luo, H., et al. (2018). Surface modification of esophageal stent materials by a drug-eluting layer for better anti-restenosis function. *Coatings* 8 (6), 215. doi:10.3390/coatings8060215

Bozzuto, G., and Molinari, A. (2015). Liposomes as nanomedical devices. *Int. J. Nanomed.* 10, 975–999. doi:10.2147/ijn.s68861

Cao, M., Deng, X., Su, S., Zhang, F., Xiao, X., Hu, Q., et al. (2013). Protamine sulfate–nanodiamond hybrid nanoparticles as a vector for MiR-203 restoration in esophageal carcinoma cells. *Nanoscale* 5 (24), 12120–12125. doi:10.1039/c3nr04056a

Chang, C.-H., Liu, S.-Y., Chi, C.-W., Yu, H.-L., Chang, T.-J., Tsai, T.-H., et al. (2015). External beam radiotherapy synergizes ^{188}Re-liposome against human esophageal cancer xenograft and modulates ^{188}Re-liposome pharmacokinetics. *Int. J. Nanomed.* 10, 3641–3649. doi:10.2147/IJN.S80302

Chen, F., Zhou, H., Wu, C., and Yan, H. (2018). Identification of miRNA profiling in prediction of tumor recurrence and progress and bioinformatics analysis for patients with primary esophageal cancer: Study based on TCGA database. *Pathol. Res. Pract.* 214 (12), 2081–2086. doi:10.1016/j.prp.2018.10.009

Chen, J., Fan, T., Xie, Z., Zeng, Q., Xue, P., Zheng, T., et al. (2020). Advances in nanomaterials for photodynamic therapy applications: Status and challenges. *Biomaterials* 237, 119827. doi:10.1016/j.biomaterials.2020.119827

Chen, J., Wang, D., Xi, J., Au, L., Siekkinen, A., Warsen, A., et al. (2007). Immuno gold nanocages with tailored optical properties for targeted photothermal destruction of cancer cells. *Nano Lett.* 7 (5), 1318–1322. doi:10.1021/nl070345g

Chen, W., Bardhan, R., Bartels, M., Perez-Torres, C., Pautler, R. G., Halas, N. J., et al. (2010). A molecularly targeted theranostic probe for ovarian cancer. *Mol. Cancer Ther.* 9 (4), 1028–1038. doi:10.1158/1535-7163.MCT-09-0829

Cho, Y. C., Kang, J. M., Park, W., Kim, D.-H., Shin, J. H., Kim, D. H., et al. (2021). Photothermal therapy via a gold nanoparticle-coated stent for treating stent-induced granulation tissue formation in the rat esophagus. *Sci. Rep.* 11 (1), 10558–8. doi:10.1038/s41598-021-90182-x

Cui, S., Lin, B. L., and Shen, X. D. (2012). "Preparation of paclitaxel-loaded microspheres with Fe_3O_4 nanoparticles and study of their target-orientation and sustained-release property," in *Advanced materials research* (Switzerland: Trans Tech Publ), 521–524. doi:10.4028/www.scientific.net/AMR.535-537.521

Dai, S., Ye, Z., Wang, F., Yan, F., Wang, L., Fang, J., et al. (2018). Doxorubicin-loaded poly (ε-caprolactone)-Pluronic micelle for targeted therapy of esophageal cancer. *J. Cell. Biochem.* 119 (11), 9017–9027. doi:10.1002/jcb.27159

Damasco, J. A., Ravi, S., Perez, J. D., Hagaman, D. E., and Melancon, M. P. (2020). Understanding nanoparticle toxicity to direct a safe-by-design approach in cancer nanomedicine. *Nanomaterials* 10 (11), 2186. doi:10.3390/nano10112186

Dauty, E., and Verkman, A. S. (2005). Actin cytoskeleton as the principal determinant of size-dependent DNA mobility in cytoplasm: A new barrier for non-viral gene delivery. *J. Biol. Chem.* 280 (9), 7823–7828. doi:10.1074/jbc.M412374200

Deng, L., Zhu, X. J., Yu, Z. J., Li, Y., Qin, L. Y., Liu, Z. L., et al. (2020). <p>Novel T7-modified pH-responsive targeted nanosystem for Co-delivery of docetaxel and curcumin in the treatment of esophageal cancer</p>. *Int. J. Nanomed.* 15, 7745–7762. doi:10.2147/IJN.S257312

Dey, B., Raphael, V., Khonglah, Y., and GiriLynrah, K. (2015). Expression of cyclin D1 and p16 in esophageal squamous cell carcinoma. *Middle East J. Dig. Dis.* 7 (4), 220–225.

Dohmitsu, K., Akiyama, S., Kawasaki, S., Kataoka, M., Kondoh, K., Yamauchi, M., et al. (1991). Hyper-thermo chemotherapy of esophageal cancer with thermosensitive liposome, TAC-1043. *Gan Kagaku ryoho. Cancer & Chemother.* 18 (11), 1760–1763.

Epperly, M. W., Gretton, J. A., DeFilippi, S. J., Sikora, C. A., Liggitt, D., Koe, G., et al. (2001). Modulation of radiation-induced cytokine elevation associated with esophagitis and esophageal stricture by manganese superoxide dismutase-plasmid/liposome (SOD2-PL) gene therapy. *Radiat. Res.* 155 (1), 2–14. doi:10.1667/0033-7587(2001)155[0002:MORICE]2.0.CO;2

Epperly, M. W., Sikora, C., Defilippi, S., Bray, J., Koe, G., Liggitt, D., et al. (2000). Plasmid/liposome transfer of the human manganese superoxide dismutase transgene prevents ionizing irradiation-induced apoptosis in human esophagus organ explant culture. *Int. J. Cancer* 90 (3), 128–137. doi:10.1002/1097-0215(20000620)90:3<128::AID-IJC2>3.0.CO;2-U

Ferrari, M. (2005). Cancer nanotechnology: Opportunities and challenges. *Nat. Rev. cancer* 5 (3), 161–171. doi:10.1038/nrc1566

Fujishiro, M., Yahagi, N., Kashimura, K., Matsuura, T., Nakamura, M., Kakushima, N., et al. (2005). Tissue damage of different submucosal injection solutions for EMR. *Gastrointest. Endosc.* 62 (6), 933–942. doi:10.1016/j.gie.2005.07.052

Gai, J., Gao, Z., Song, L., Xu, Y., Liu, W., and Zhao, C. (2018). Contrast-enhanced computed tomography combined with Chitosan-Fe3O4 nanoparticles targeting fibroblast growth factor receptor and vascular endothelial growth factor receptor in the screening of early esophageal cancer. *Exp. Ther. Med.* 15 (6), 5344–5352. doi:10.3892/etm.2018.6087

Gonçalves, A. S., Rodrigues, C. F., Moreira, A. F., and Correia, I. J. (2020). Strategies to improve the photothermal capacity of gold-based nanomedicines. *Acta Biomater.* 116, 105–137. doi:10.1016/j.actbio.2020.09.008

Hamaguchi, T., Doi, T., Eguchi-Nakajima, T., Kato, K., Yamada, Y., Shimada, Y., et al. (2010). Phase I study of NK012, a novel SN-38–incorporating micellar nanoparticle, in adult patients with solid tumors. *Clin. Cancer Res.* 16 (20), 5058–5066. doi:10.1158/1078-0432.CCR-10-0387

Hassan, M. S., Awasthi, N., Li, J., Williams, F., Schwarz, M. A., Schwarz, R. E., et al. (2018). Superior therapeutic efficacy of nanoparticle albumin bound paclitaxel over cremophor-bound paclitaxel in experimental esophageal adenocarcinoma. *Transl. Oncol.* 11 (2), 426–435. doi:10.1016/j.tranon.2018.01.022

Hassan, M. S., Awasthi, N., Schwarz, R. E., Schwarz, M. A., and Holzen, U. v. (2017). Abstract 2040: Superior therapeutic efficacy of nanoparticle albumin-bound paclitaxel over cremophor-bound paclitaxel in experimental esophageal adenocarcinoma. *Cancer Res.* 77 (13), 2040. doi:10.1158/1538-7445.AM2017-2040

Hejmady, S., Pradhan, R., Alexander, A., Agrawal, M., Singhvi, G., Gorain, B., et al. (2020). Recent advances in targeted nanomedicine as promising antitumor therapeutics. *Drug Discov. Today* 25 (12), 2227–2244. doi:10.1016/j.drudis.2020.09.031

Hosseini, S., Chamani, J., Rahimi, H., Azmoodeh, N., Ghasemi, F., and Abadi, P. H. (2018). An *in vitro* study on curcumin delivery by nano-micelles for esophageal squamous cell carcinoma (KYSE-30). *Rep. Biochem. Mol. Biol.* 6 (2), 137–143.

Hu, A., Alarfaj, A. A., Hirad, A. H., Veeraraghavan, V. P., Surapaneni, K. M., Hussein-Al-Ali, S. H., et al. (2022). Chitosan-sodium alginate-polyethylene glycol-crocin nanocomposite treatment inhibits esophageal cancer KYSE-150 cell growth via inducing apoptotic cell death. *Arab. J. Chem.* 15 (6), 103844. doi:10.1016/j.arabjc.2022.103844

Huang, X., El-Sayed, I. H., and El-Sayed, M. A. (2010). Applications of gold nanorods for cancer imaging and photothermal therapy. *Cancer Nanotechnol. methods Protoc.* 624, 343–357. doi:10.1007/978-1-60761-609-2_23

Huang, X., Jain, P. K., El-Sayed, I. H., and El-Sayed, M. A. (2006). Determination of the minimum temperature required for selective photothermal destruction of cancer cells with the use of immunotargeted gold nanoparticles. *Photochem. Photobiol.* 82 (2), 412–417. doi:10.1562/2005-12-14-RA-754

Huang, Z.-J., Yang, N., Xu, T.-W., and Lin, J.-Q. (2015). Antitumor efficacy of docetaxel-loaded nanocarrier against esophageal cancer cell bearing mice model. *Drug Res.* 65 (08), 403–409. doi:10.1055/s-0034-1385907

Jain, P. K., Huang, X., El-Sayed, I. H., and El-Sayed, M. A. (2008). Noble metals on the nanoscale: Optical and photothermal properties and some applications in imaging, sensing, biology, and medicine. *Acc.Chem. Res.* 41 (12), 1578–1586. doi:10.1021/ar7002804

Ji, C., Ju, S., Zhang, D., and Qiang, J. (2018). Nanomedicine based N-trimethyl chitosan entangled solid lipid nanoparticle loaded with Irinotecan to enhance the therapeutic efficacy in esophageal cancer cells. *J. Biomater. Tiss. Eng.* 8 (8), 1195–1200. doi:10.1166/jbt.2018.1846

Jiang, M., Li, Q., Cui, X., Long, F., Ye, F., Gu, L., et al. (2020). Bio-fabricated bioactive arisaema triphyllum aqueous extract-loaded nano-ZnO particles improve the nursing care of esophageal cancer. *Mat. Express* 10 (10), 1620–1627. doi:10.1166/mex.2020.1800

Juan, A., Cimas, F. J., Bravo, I., Pandiella, A., Ocaña, A., and Alonso-Moreno, C. (2020). Antibody conjugation of nanoparticles as therapeutics for breast cancer treatment. *Int. J. Mol. Sci.* 21 (17), 6018. doi:10.3390/ijms21176018

Jung, Y. S., and Park, D. I. (2013). Submucosal injection solutions for endoscopic mucosal resection and endoscopic submucosal dissection of gastrointestinal neoplasms. *Gastrointest. Interv.* 2 (2), 73–77. doi:10.1016/j.gii.2013.09.003

Kang, K. J., Min, B.-H., Lee, J. H., Kim, E. R., Sung, C. O., Cho, J. Y., et al. (2013). Alginate hydrogel as a potential alternative to hyaluronic acid as submucosal injection material. *Dig. Dis. Sci.* 58, 1491–1496. doi:10.1007/s10620-012-2555-z

Kantsevoy, S. V., Adler, D. G., Conway, J. D., Diehl, D. L., Farraye, F. A., Kwon, R., et al. (2008). Endoscopic mucosal resection and endoscopic submucosal dissection. *Gastrointest. Endosc.* 68 (1), 11–18. doi:10.1016/j.gie.2008.01.037

Kargozar, S., Hoseini, S. J., Milan, P. B., Hooshmand, S., Kim, H. W., and Mozafari, M. (2020). Quantum dots: A review from concept to clinic. *Biotechnol. J.* 15 (12), 2000117. doi:10.1002/biot.202000117

Karnik, R., Gu, F., Basto, P., Cannizzaro, C., Dean, L., Kyei-Manu, W., et al. (2008). Microfluidic platform for controlled synthesis of polymeric nanoparticles. *Nano Lett.* 8 (9), 2906–2912. doi:10.1021/nl801736q

Katsinelos, P., Kountouras, J., Paroutoglou, G., Chatzimavroudis, G., Zavos, C., Pilpilidis, I., et al. (2008). A comparative study of 50% dextrose and normal saline solution on their ability to create submucosal fluid cushions for endoscopic resection of sessile rectosigmoid polyps. *Gastrointest. Endosc.* 68 (4), 692–698. doi:10.1016/j.gie.2008.02.063

Kiss, L., Walter, F. R., Bocsik, A., Veszelka, S., Ózsvári, B., Puskás, L. G., et al. (2013). Kinetic analysis of the toxicity of pharmaceutical excipients Cremophor EL and RH40 on endothelial and epithelial cells. *J. Pharm. Sci.* 102 (4), 1173–1181. doi:10.1002/jps.23458

Kumano, I., Ishihara, M., Nakamura, S., Kishimoto, S., Fujita, M., Hattori, H., et al. (2012). Endoscopic submucosal dissection for pig esophagus by using photocrosslinkable chitosan hydrogel as submucosal fluid cushion. *Gastrointest. Endosc.* 75 (4), 841–848. doi:10.1016/j.gie.2011.10.035

Kuo, W. S., Chang, C. N., Chang, Y. T., Yang, M. H., Chien, Y. H., Chen, S. J., et al. (2010). Gold nanorods in photodynamic therapy, as hyperthermia agents, and in near-infrared optical imaging. *Angew. Chem. Int.Edit.* 49 (15), 2711–2715. doi:10.1002/anie.200906927

Lee, J. J., Saiful Yazan, L., and Che Abdullah, C. A. (2017). A review on current nanomaterials and their drug conjugate for targeted breast cancer treatment. *Int. J. Nanomed.* 12, 2373–2384. doi:10.2147/ijn.s127329

Lee, P.-W., Hsu, S.-H., Wang, J.-J., Tsai, J.-S., Lin, K.-J., Wey, S.-P., et al. (2010). The characteristics, biodistribution, magnetic resonance imaging and biodegradability of superparamagnetic core–shell nanoparticles. *Biomaterials* 31 (6), 1316–1324. doi:10.1016/j.biomaterials.2009.11.010

Lenz, L., Di Sena, V., Nakao, F. S., Andrade, G. P. d., Rohr, M. R. d. S., and Ferrari, A. P., Jr (2010). Comparative results of gastric submucosal injection with hydroxypropyl methylcellulose, carboxymethylcellulose and normal saline solution in a porcine model. *Arq. Gastroenterol.* 47, 184–187. doi:10.1590/s0004-28032010000200013

Li, J., Wang, S., Kang, W., Li, N., Guo, F., Chang, H., et al. (2021). Multifunctional gold nanoparticle based selective detection of esophageal squamous cell carcinoma cells using resonance Rayleigh scattering assay. *Microchem. J.* 163, 105905. doi:10.1016/j.microc.2020.105905

Li, J., Zou, S., Gao, J., Liang, J., Zhou, H., Liang, L., et al. (2017). Block copolymer conjugated Au-coated Fe3O4 nanoparticles as vectors for enhancing colloidal stability and cellular uptake. *J. Nanobiotechnol.* 15 (1), 56–11. doi:10.1186/s12951-017-0290-5

Li, L., Nurunnabi, M., Nafiujjaman, M., Jeong, Y. Y., Lee, Y.-k., and Huh, K. M. (2014a). A photosensitizer-conjugated magnetic iron oxide/gold hybrid nanoparticle as an activatable platform for photodynamic cancer therapy. *J. Mat. Chem. B* 2 (19), 2929–2937. doi:10.1039/c4tb00181h

Li, M., Xu, X., Lu, F., and Guo, S. (2014b). Primary *in vitro* and *in vivo* evaluation of norcantharidin-chitosan/poly (vinyl alcohol) for cancer treatment. *Drug Deliv.* 21 (4), 293–301. doi:10.3109/10717544.2013.840692

Li, X., Chen, L., Luan, S., Zhou, J., Xiao, X., Yang, Y., et al. (2022). "The development and progress of nanomedicine for esophageal cancer diagnosis and treatment," in *Seminars in cancer biology* (Netherlands: Elsevier). doi:10.1016/j.semcancer.2022.01.007

Li, Y., Gobin, A. M., Dryden, G. W., Kang, X., Xiao, D., Li, S. P., et al. (2013). Infrared light-absorbing gold/gold sulfide nanoparticles induce cell death in esophageal adenocarcinoma. *Int. J. Nanomed.* 8, 2153–2161. doi:10.2147/IJN.S37140

Liang, C., Zhang, X., Cheng, Z., Yang, M., Huang, W., and Dong, X. (2020). Magnetic iron oxide nanomaterials: A key player in cancer nanomedicine. *View* 1 (3), 20200046. doi:10.1002/VIW.20200046

Liao, J., Jia, Y., Wu, Y., Shi, K., Yang, D., Li, P., et al. (2020). Physical-, chemical-, and biological-responsive nanomedicine for cancer therapy. *Wiley Interdiscip. Rev. Nanomedicine Nanobiotechnology* 12 (1), e1581. doi:10.1002/wnan.1581

Lin, D., Feng, S., Huang, H., Chen, W., Shi, H., Liu, N., et al. (2014). Label-free detection of blood plasma using silver nanoparticle based surface-enhanced Raman spectroscopy for esophageal cancer screening. *J. Biomed. Nanotechnol.* 10 (3), 478–484. doi:10.1166/jbn.2014.1750

Lin, N., Yu, C., Yang, J., and Wang, Y. (2020). Nano-carbon and titanium clip combined labeling assisted surgery before neoadjuvant radiotherapy and chemotherapy for rectal cancer. *Asian J. Surg.* 43 (1), 383–384. doi:10.1016/j.asjsur.2019.09.003

Liu, J., Zangeneh, A., Zangeneh, M. M., and Guo, B. H. (2020a). Antioxidant, cytotoxicity, anti-human esophageal squamous cell carcinoma, anti-human Caucasian esophageal carcinoma, anti-adenocarcinoma of the gastroesophageal junction, and anti-distal esophageal adenocarcinoma properties of gold nanoparticles green synthesized by Rhus coriaria L. fruit aqueous extract. *J. Exp. Nanosci.* 15 (1), 202–216. doi:10.1080/17458080.2020.1766675

Liu, L.-L., Qin, J., Zeng, C.-H., Du, R.-J., Pan, T., Ji, J.-J., et al. (2022). Biodegradable PTX-PLGA-coated magnesium stent for benign esophageal stricture: An experimental study. *Acta Biomater.* 146, 495–505. doi:10.1016/j.actbio.2022.04.038

Liu, P., Tan, J., Tan, Q., Xu, L., He, T., and Lv, Q. (2020b). <p>Application of carbon nanoparticles in tracing lymph nodes and locating tumors in colorectal cancer: A concise review</p>. *Int. J. Nanomed.* 15, 9671–9681. doi:10.2147/ijn.s281914

Liu, S., Ren, S.-N., Ding, W.-X., Ge, X.-L., Cao, Y.-D., Zhang, S., et al. (2019). Concurrent liposomal paclitaxel and cisplatin chemotherapy improved outcomes for locally advanced esophageal squamous cell carcinoma treated with intensity-modulated radiotherapy. *Ann. Transl. Med.* 7 (14), 331. doi:10.21037/atm.2019.06.45

Luan, S., Xie, R., Yang, Y., Xiao, X., Zhou, J., Li, X., et al. (2022). Acid-responsive aggregated gold nanoparticles for radiosensitization and synergistic chemoradiotherapy in the treatment of esophageal cancer. *Small* 18 (19), 2200115. doi:10.1002/smll.202200115

Maeda, H. (2015). Toward a full understanding of the EPR effect in primary and metastatic tumors as well as issues related to its heterogeneity. *Adv. Drug Deliv. Rev.* 91, 3–6. doi:10.1016/j.addr.2015.01.002

Martin, R. C., Locatelli, E., Li, Y., Zhang, W., Li, S., Monaco, I., et al. (2015). Gold nanorods and curcumin-loaded nanomicelles for efficient *in vivo* photothermal therapy of Barrett's esophagus. *Nanomedicine* 10 (11), 1723–1733. doi:10.2217/nnm.15.25

McGrath, A. J., Chien, Y.-H., Cheong, S., Herman, D. A., Watt, J., Henning, A. M., et al. (2015). Gold over branched palladium nanostructures for photothermal cancer therapy. *ACS Nano* 9 (12), 12283–12291. doi:10.1021/acsnano.5b05563

Meads, M. B., Gatenby, R. A., and Dalton, W. S. (2009). Environment-mediated drug resistance: A major contributor to minimal residual disease. *Nat. Rev. cancer* 9 (9), 665–674. doi:10.1038/nrc2714

Moffatt, S., and Wangari, M. (2018). "Enhanced targeting of polyethyleneimine (PEI)-Based tumor-specific antisense," in *Nano-oligonucleotides (tanol) in cancer therapy*.

Moghimi, S. M. (1995). Exploiting bone marrow microvascular structure for drug delivery and future therapies. *Adv. Drug Deliv. Rev.* 17 (1), 61–73. doi:10.1016/0169-409X(95)00041-5

Mohammadpour, R., Dobrovolskaia, M. A., Cheney, D. L., Greish, K. F., and Ghandehari, H. (2019). Subchronic and chronic toxicity evaluation of inorganic nanoparticles for delivery applications. *Adv. Drug Deliv. Rev.* 144, 112–132. doi:10.1016/j.addr.2019.07.006

Murakami, T., Nakatsuji, H., Inada, M., Matoba, Y., Umeyama, T., Tsujimoto, M., et al. (2012). Photodynamic and photothermal effects of semiconducting and metallic-enriched single-walled carbon nanotubes. *J. Am. Chem. Soc.* 134 (43), 17862–17865. doi:10.1021/ja3079972

Niu, Y., Epperly, M., Shen, H., Smith, T., Wang, H., and Greenberger, J. (2008). Intraesophageal MnSOD-plasmid liposome enhances engraftment and self-renewal of bone marrow derived progenitors of esophageal squamous epithelium. *Gene Ther.* 15 (5), 347–356. doi:10.1038/sj.gt.3303089

Patra, J. K., Das, G., Fraceto, L. F., Campos, E. V. R., Rodriguez-Torres, M. D. P., Acosta-Torres, L. S., et al. (2018). Nano based drug delivery systems: Recent developments and future prospects. *J. Nanobiotech* 16 (1), 71. doi:10.1186/s12951-018-0392-8

Pennathur, A., Godfrey, T. E., and Luketich, J. D. (2019). The molecular biologic basis of esophageal and gastric cancers. *Surg. Clin. N. Am.* 99 (3), 403–418. doi:10.1016/j.suc.2019.02.010

Pi, J., Jiang, J., Cai, H., Yang, F., Jin, H., Yang, P., et al. (2017). GE11 peptide conjugated selenium nanoparticles for EGFR targeted oridonin delivery to achieve enhanced anticancer efficacy by inhibiting EGFR-mediated PI3K/AKT and Ras/Raf/MEK/ERK pathways. *Drug Deliv.* 24 (1), 1549–1564. doi:10.1080/10717544.2017.1386729

Qian, X. Y., Hu, W., and Yan, J. (2022). Nano-Chemotherapy synergize with immune checkpoint inhibitor- A better option? *Front. Immunol.* 13, 963533. doi:10.3389/fimmu.2022.963533

Qiu, Y., Liu, Y., Wang, L., Xu, L., Bai, R., Ji, Y., et al. (2010). Surface chemistry and aspect ratio mediated cellular uptake of Au nanorods. *Biomaterials* 31 (30), 7606–7619. doi:10.1016/j.biomaterials.2010.06.051

Qureshi, A., Tufani, A., Corapcioglu, G., and Niazi, J. H. (2020). CdSe/CdS/ZnS nanocrystals decorated with Fe_3O_4 nanoparticles for point-of-care optomagnetic detection of cancer biomarker in serum. *Sensors Actuat. B Chem.* 321, 128431. doi:10.1016/j.snb.2020.128431

Ren, W., Sha, H., Yan, J., Wu, P., Yang, J., Li, R., et al. (2018). Enhancement of radiotherapeutic efficacy for esophageal cancer by paclitaxel-loaded red blood cell membrane nanoparticles modified by the recombinant protein anti-EGFR-iRGD. *J.Biomater. Appl.* 33 (5), 707–724. doi:10.1177/0885328218809019

Riedel, J., Calienni, M. N., Bernabeu, E., Calabro, V., Lázaro-Martinez, J. M., Prieto, M. J., et al. (2021). Paclitaxel and curcumin co-loaded mixed micelles: Improving *in vitro* efficacy and reducing toxicity against Abraxane. *J. Drug Deliv. Sci. Tech.* 62, 102343. doi:10.1016/j.jddst.2021.102343

Rolland, J. P., Maynor, B. W., Euliss, L. E., Exner, A. E., Denison, G. M., and DeSimone, J. M. (2005). Direct fabrication and harvesting of monodisperse, shape-specific nanobiomaterials. *J. Am. Chem. Soc.* 127 (28), 10096–10100. doi:10.1021/ja051977c

Schmid, G., Kreyling, W. G., and Simon, U. (2017). Toxic effects and biodistribution of ultrasmall gold nanoparticles. *Arch. Toxicol.* 91, 3011–3037. doi:10.1007/s00204-017-2016-8

Shen, S., Wang, S., Zheng, R., Zhu, X., Jiang, X., Fu, D., et al. (2015). Magnetic nanoparticle clusters for photothermal therapy with near-infrared irradiation. *Biomaterials* 39, 67–74. doi:10.1016/j.biomaterials.2014.10.064

Shen, Y., Sun, Y., Yan, R., Chen, E., Wang, H., Ye, D., et al. (2017). Rational engineering of semiconductor QDs enabling remarkable 1O2 production for tumor-targeted photodynamic therapy. *Biomaterials* 148, 31–40. doi:10.1016/j.biomaterials.2017.09.026

Shi, J., Votruba, A. R., Farokhzad, O. C., and Langer, R. (2010). Nanotechnology in drug delivery and tissue engineering: From discovery to applications. *Nano Lett.* 10 (9), 3223–3230. doi:10.1021/nl102184c

Shi, Y., Qin, R., Wang, Z.-K., and Dai, G.-H. (2013). Nanoparticle albumin-bound paclitaxel combined with cisplatin as the first-line treatment for metastatic esophageal squamous cell carcinoma. *OncoTargets Ther.* 6, 585–591. doi:10.2147/OTT.S44406

Sivasubramanian, M., Chuang, Y. C., and Lo, L.-W. (2019). Evolution of nanoparticle-mediated photodynamic therapy: From superficial to deep-seated cancers. *Molecules* 24 (3), 520. doi:10.3390/molecules24030520

Song, J., Hu, H., Jian, C., Wu, K., and Chen, X. (2016). New generation of gold nanoshell-coated esophageal stent: Preparation and biomedical applications. *ACS Appl. Mat. Interfaces* 8 (41), 27523–27529. doi:10.1021/acsami.6b09104

Sun, L., Xia, T., and Cao, W. (2017). Preparation and *in vitro* study of ESCCAL_1-targeted siRNA gene delivery of nanocomposite for treating esophageal cancer EC-9706. *Chin. Pharmacol. Bull.*, 1749–1753. doi:10.3969/j.issn.1001-1978.2017.12.024

Sun, Y.-N., Wang, C.-D., Zhang, X.-M., Ren, L., and Tian, X.-H. (2011). Shape dependence of gold nanoparticles on *in vivo* acute toxicological effects and biodistribution. *J. Nanosci. Nanotech.* 11 (2), 1210–1216. doi:10.1166/jnn.2011.3094

Sung, H., Ferlay, J., Siegel, R. L., Laversanne, M., Soerjomataram, I., Jemal, A., et al. (2021). Global cancer statistics 2020: GLOBOCAN estimates of incidence and mortality worldwide for 36 cancers in 185 countries. *CA-Cancer J. Clin.* 71 (3), 209–249. doi:10.3322/caac.21660

Tang, X., Loc, W. S., Dong, C., Matters, G. L., Butler, P. J., Kester, M., et al. (2017). The use of nanoparticulates to treat breast cancer. *Nanomedicine* 12 (19), 2367–2388. doi:10.2217/nnm-2017-0202

Terentyuk, G. S., Maslyakova, G. N., Suleymanova, L. V., Khlebtsov, N. G., Khlebtsov, B. N., Akchurin, G. G., et al. (2009). Laser-induced tissue hyperthermia mediated by gold nanoparticles: Toward cancer phototherapy. *J. Biomed. Opt.* 14 (2), 021016–021019. doi:10.1117/1.3122371

Tran, R. T., Palmer, M., Tang, S.-J., Abell, T. L., and Yang, J. (2012). Injectable drug-eluting elastomeric polymer: A novel submucosal injection material. *Gastrointest. Endosc.* 75 (5), 1092–1097. doi:10.1016/j.gie.2011.12.009

Udagawa, H., Takahashi, S., Hirao, M., Tahara, M., Iwasa, S., Sato, Y., et al. (2023). Liposomal eribulin for advanced adenoid cystic carcinoma, gastric cancer, esophageal cancer, and small cell lung cancer. *Cancer Med.* 12 (2), 1269–1278. doi:10.1002/cam4.4996

Unterweger, H., Subatzus, D., Tietze, R., Janko, C., Poettler, M., Stiegelschmitt, A., et al. (2015). Hypericin-bearing magnetic iron oxide nanoparticles for selective drug delivery in photodynamic therapy. *Int. J. Nanomed.* 10, 6985–6996. doi:10.2147/IJN.S92336

Uraoka, T., Kawahara, Y., Ohara, N., Kato, J., Hori, K., Okada, H., et al. (2011). Carbon dioxide submucosal injection cushion: An innovative technique in endoscopic submucosal dissection. *Dig. Endosc.* 23 (1), 5–9. doi:10.1111/j.1443-1661.2010.01038.x

Uraoka, T., Saito, Y., Yamamoto, K., and Fujii, T. (2009). Submucosal injection solution for gastrointestinal tract endoscopic mucosal resection and endoscopic submucosal dissection. *Drug Des. Dev. Ther.* 2, 131–138. doi:10.2147/dddt.s3219

Wang, C., Wang, X., and Liu, L. (2020a). Clinical application of carbon nanoparticles suspension in operation of papillary thyroid carcinoma. *Lin. Chung Er Bi Yan Hou Tou Jing Wai Ke Za Zhi* 34 (2), 165–169. doi:10.13201/j.issn.1001-1781.2020.02.016

Wang, F., Porter, M., Konstantopoulos, A., Zhang, P., and Cui, H. (2017). Preclinical development of drug delivery systems for paclitaxel-based cancer chemotherapy. *J. Control. Release* 267, 100–118. doi:10.1016/j.jconrel.2017.09.026

Wang, J., Han, C., Zhu, S., Gao, C., and Li, X. (2010). The pattern of lymphatic metastasis and influencing factors of thoracic esophageal carcinoma. *Chin. J. Clin. Oncol.* 90-93.

Wang, J., Wu, X., Shen, P., Wang, J., Shen, Y., Shen, Y., et al. (2020b). <p>Applications of inorganic nanomaterials in photothermal therapy based on combinational cancer treatment</p>. *Int. J. Nanomed.* 15, 1903–1914. doi:10.2147/IJN.S239751

Wang, J., Xu, L., Liu, X., Yang, R., and Wang, D. (2020c). A facile adenosine triphosphate-responsive nanoplatform for efficacious therapy of esophageal cancer. *Oncol. Lett.* 20 (4), 1. doi:10.3892/ol.2020.11969

Wang, S. F., Liu, J. L., Qiu, S. F., and Yu, J. M. (2019). Facile fabrication of Cu-9-S-5 loaded core-shell nanoparticles for near infrared radiation mediated tumor therapeutic strategy in human esophageal squamous carcinoma cells nursing care of esophageal cancer patients. *J. Photoch. Photobio. B* 199, 111583. doi:10.1016/j.jphotobiol.2019.111583

Wang, W., Yi, Y., Jia, Y., Dong, X., Zhang, J., Song, X., et al. (2022). Neoadjuvant chemotherapy with liposomal paclitaxel plus platinum for locally advanced esophageal squamous cell cancer: Results from a retrospective study. *Thorac. Cancer* 13 (6), 824–831. doi:10.1111/1759-7714.14328

Wang, X.-s., Ding, X.-z., Li, X.-c., He, Y., Kong, D.-j., Zhang, L., et al. (2018). A highly integrated precision nanomedicine strategy to target esophageal squamous cell cancer molecularly and physically. *Nanomed.-Nanotechnol.* 14 (7), 2103–2114. doi:10.1016/j.nano.2018.06.008

Wu, W., Zheng, Y., Wang, R., Huang, W., Liu, L., Hu, X., et al. (2012). Antitumor activity of folate-targeted, paclitaxel loaded polymeric micelles on a human esophageal EC9706 cancer cell line. *Int. J. Nanomed.* 7, 3487–3502. doi:10.2147/IJN.S32620

Wu, Y., Feng, J., Hu, W., and Luo, Q. (2017). A randomized placebo-controlled clinical study of nab-paclitaxel as second-line chemotherapy for patients with advanced non-small cell lung cancer in China. *Biosci. Rep.* 37 (4). doi:10.1042/bsr20170020

Yamamoto, H. (2012). Endoscopic submucosal dissection—Current success and future directions. *Nat. Rev. Gastro. Hepat.* 9 (9), 519–529. doi:10.1038/nrgastro.2012.97

Yao, X., Lu, S., Feng, C., Suo, R., Li, H., Zhang, Y., et al. (2022). Tumor oxygenation nanoliposome synergistic hypoxia-inducible-factor-1 inhibitor enhanced Iodine-125 seed brachytherapy for esophageal cancer. *Biomaterials* 289, 121801. doi:10.1016/j.biomaterials.2022.121801

Yen, H. J., Hsu, S. h., and Tsai, C. L. (2009). Cytotoxicity and immunological response of gold and silver nanoparticles of different sizes. *Small* 5 (13), 1553–1561. doi:10.1002/smll.200900126

Yi, Q., Liu, C., Cui, Y., Yang, Y., Li, Y., Fan, X., et al. (2022). Chemoradiotherapy with paclitaxel liposome plus cisplatin for locally advanced esophageal squamous cell carcinoma: A retrospective analysis. *Cancer Med.* 12 (6), 6477–6487. doi:10.1002/cam4.5416

Yuan, Y., Zhang, Y., Shi, L., Mei, J.-F., Feng, J.-E., and Shen, B. (2015). Clinical research on albumin-bound paclitaxel-based chemotherapy for advanced esophageal cancer. *Asian pac. J. Cancer p.* 16 (12), 4993–4996. doi:10.7314/apjcp.2015.16.12.4993

Zhan, W., Li, H., Guo, Y., Du, G., Wu, Y., and Zhang, D. (2020). Construction of biocompatible dual-drug loaded complicated nanoparticles for *in vivo* improvement of synergistic chemotherapy in esophageal cancer. *Front. Oncol.* 10, 622. doi:10.3389/fonc.2020.00622

Zhang, K., Bai, Y., Wang, X., Li, Q., Guan, F., and Li, J. (2017). Surface modification of esophageal stent materials by a polyethyleneimine layer aiming at anti-cancer function. *J. Mat. Sci.-Mater. M.* 28, 125–128. doi:10.1007/s10856-017-5939-y

Zhang, K., Bai, Y., Xu, R., Li, J., and Guan, F. (2020). The mechanism of PDA/PEI/5-Fu coated esophageal stent material on inhibiting cancer associated pathological cells. *J. Biomed. Mat. Res. A* 108 (3), 814–821. doi:10.1002/jbm.a.36860

Zhang, Q., Liang, Y., Yuan, H., Li, S., Wang, J.-B., Li, X.-M., et al. (2019). Integrated analysis of lncRNA, miRNA and mRNA expression profiling in patients with systemic lupus erythematosus. *Arch. Med. Sci.* 15 (4), 872–879. doi:10.5114/aoms.2018.79145

Zhang, X., Wang, M., Feng, J., Qin, B., Zhang, C., Zhu, C., et al. (2022). Multifunctional nanoparticles co-loaded with Adriamycin and MDR-targeting siRNAs for treatment of chemotherapy-resistant esophageal cancer. *J. Nanobiotechnol.* 20 (1), 166–184. doi:10.1186/s12951-022-01377-x

Zhang, Y., Mahdavi, B., Mohammadhosseini, M., Rezaei-Seresht, E., Paydarfard, S., Qorbani, M., et al. (2021). Green synthesis of NiO nanoparticles using Calendula officinalis extract: Chemical charactrization, antioxidant, cytotoxicity, and anti-esophageal carcinoma properties. *Arab. J. Chem.* 14 (5), 103105. doi:10.1016/j.arabjc.2021.103105

Zhao, W., Zhao, J., Kang, L., Li, C., Xu, Z., Li, J., et al. (2022). Fluoroscopy-guided salvage photodynamic therapy combined with nanoparticle albumin-bound paclitaxel for locally advanced esophageal cancer after chemoradiotherapy. *Cancer bio. Radio* 37 (5), 410–416. doi:10.1089/cbr.2020.4595

Zhou, P.-H., Schumacher, B., Yao, L.-Q., Xu, M.-D., Nordmann, T., Cai, M.-Y., et al. (2014). Conventional vs. waterjet-assisted endoscopic submucosal dissection in early gastric cancer: A randomized controlled trial. *Endoscopy* 46 (10), 836–843. doi:10.1055/s-0034-1377580

Zhou, X., You, M., Wang, F., Wang, Z., Gao, X., Jing, C., et al. (2021). Multifunctional graphdiyne–cerium oxide nanozymes facilitate microRNA delivery and attenuate tumor hypoxia for highly efficient radiotherapy of esophageal cancer. *Adv. Mat.* 33 (24), 2100556. doi:10.1002/adma.202100556

Zou, X., Cheng, S., You, B., and Yang, C. (2020). Bio-mediated synthesis of copper oxide nanoparticles using Pogestemon benghalensis extract for treatment of the esophageal cancer in nursing care. *J. Drug Deliv. Sci. Tech.* 58, 101759. doi:10.1016/j.jddst.2020.101759

Zuckerman, J. E., Gritli, I., Tolcher, A., Heidel, J. D., Lim, D., Morgan, R., et al. (2014). Correlating animal and human phase Ia/Ib clinical data with CALAA-01, a targeted, polymer-based nanoparticle containing siRNA. *Proc. Natl. Acad. Sci.* 111 (31), 11449–11454. doi:10.1073/pnas.1411393111

frontiers | Frontiers in Bioengineering and Biotechnology

TYPE Mini Review
PUBLISHED 08 August 2023
DOI 10.3389/fbioe.2023.1251713

OPEN ACCESS

EDITED BY
Miaomiao Yuan,
Sun Yat-sen University, China

REVIEWED BY
Judun Zheng,
Southern Medical University, China
Qing Li,
Second Affiliated Hospital of Zhengzhou University, China

*CORRESPONDENCE
Jun Liu,
liujun448153798@126.com
Xiaojun Fang,
fxjainll@163.com
Xiaofeng Lin,
linxf@gmu.edu.cn

RECEIVED 02 July 2023
ACCEPTED 28 July 2023
PUBLISHED 08 August 2023

CITATION
Jiang M, Liao J, Liu C, Liu J, Chen P, Zhou J, Du Z, Liu Y, Luo Y, Liu Y, Chen F, Fang X and Lin X (2023), Metal-organic frameworks/metal nanoparticles as smart nanosensing interfaces for electrochemical sensors applications: a mini-review.
Front. Bioeng. Biotechnol. 11:1251713.
doi: 10.3389/fbioe.2023.1251713

Metal-organic frameworks/metal nanoparticles as smart nanosensing interfaces for electrochemical sensors applications: a mini-review

Min Jiang[1], Jing Liao[1], Chenghao Liu[1], Jun Liu[2,3]*, Peixian Chen[4], Jia Zhou[1], Zhizhi Du[1], Yan Liu[1], Yan Luo[1], Yangbin Liu[1], Fei Chen[1], Xiaojun Fang[1]* and Xiaofeng Lin[1]*

[1]Key Laboratory of Prevention and Treatment of Cardiovascular and Cerebrovascular Diseases of Ministry of Education, Key Laboratory of Biomaterials and Biofabrication in Tissue Engineering of Jiangxi Province, Key Laboratory of Biomedical Sensors of Ganzhou, School of Medical and Information Engineering, School of Pharmacy, Scientific Research Center, Gannan Medical University, Ganzhou, China, [2]Department of Neurosurgery, The Second Affifiliated Hospital of Nanchang University, Nanchang, China, [3]Department of Neurosurgery, The Affiliated Ganzhou Hospital of Nanchang University, Ganzhou, China, [4]Department of Health Services, Fujian Hwa Nan Women's College, Fuzhou, China

Metal-organic frameworks (MOFs) are porous materials with huge specific surface area and abundant active sites, which are composed of metal ions or clusters and organic ligands in the form of coordination bonds. In recent years, MOFs have been successfully applied in many fields due to their excellent physical, chemical, and biological properties. Electrochemical sensors have advantages such as economy, portability, and sensitivity, making them increasingly valued in the field of sensors. Many studies have shown that the electrode materials will affect the performance of electrochemical sensors. Therefore, the research on electrode materials is still one of the hotspots. MOFs are also commonly used to construct electrochemical sensors. However, electrochemical sensors prepared from single MOFs have shortcomings such as insufficient conductivity, low sensitivity, and poor electrochemical catalytic ability. In order to compensate for these defects, a new type of nanocomposite material with very ideal conductivity was formed by adding metal nanoparticles (MNPs) to MOFs. The combination of the two is expected to be widely applied in the field of sensors. This review summarizes the applications of various MNPs/MOFs composites in the field of electrochemical sensors and provides some references for the development of MNPs/MOFs composites-based electrochemical sensors in the future.

KEYWORDS

metal-organic frameworks, metal nanoparticles, composite, smart nanosensing, electrochemical sensor

1 Introduction

Coordination polymers are framework materials with a periodic spatial network structure, consisting of metal ions (or metal clusters) assembled with multi-dentate ligands through coordination bonds (Liu J.-Q. et al., 2020; Daniel et al., 2022). Metal-organic frameworks (MOFs), a subset of coordination polymers, are a class of coordination

networks with both organic ligands and potential pores (Falsafi et al., 2021; Kajal et al., 2022). In comparison with other inorganic porous materials, such as zeolites, porous silica, and carbon materials, MOFs possess some unique structural advantages, including structural diversity, huge specific surface area, and high porosity, abundant unsaturated metal sites and good biocompatibility (Liu C.-S. et al., 2020; Çorman et al., 2022; Zhang W. et al., 2023). Based on these attractive structural and performance advantages, MOFs have attracted many researchers to investigate the structural features and functions of MOFs and explore their potential applications in gas adsorption, multiphase catalysis, drug delivery, biomedical imaging, and chemical sensing (Lu et al., 2018; Lin et al., 2020; Bag et al., 2021; Kumari et al., 2022).

The electrochemical sensor is a kind of special analysis and detection platform, which applies electrochemical detection technology to the sensor. It consists of three parts: an identification probe, a power converter, and a data analyzer. It works by first modifying the identification materials on the electrode surface by chemical or physical methods. And then the target molecules on the surface of the electrode are captured through intermolecular-specific recognition. Finally, their concentration signals are converted into recognizable electrical signals, such as current, voltage and impedance, etc. Due to their simple operation, economy, convenient detection, high sensitivity, and fast response, electrochemical biosensors have been widely used in biomedicine, food engineering, environmental monitoring, and other fields (Chen et al., 2018; Huang et al., 2020; Lin et al., 2021a; Lin et al., 2021b; Mei et al., 2022a; Mei et al., 2022b; Huang et al., 2022). It is well known that the sensor interface materials of electrochemical sensors play an important role in the efficient and sensitive detection of different target molecules. Accordingly, the reasonable choice of sensing interface materials will determine the performance of electrochemical sensors.

At present, some MOFs meet the requirements of electrochemical sensing that can be directly used to construct sensing interfaces. For example, MOFs with electroactivity can be used as electrocatalysts to detect small molecule compounds such as H_2O_2(Li et al., 2022), glucose (Adeel et al., 2021), ascorbic acid (Wang H. et al., 2021), nitrite (Yang et al., 2022), dopamine (Ma J. et al., 2021), etc. Nevertheless, MOFs have some drawbacks that cannot be ignored. For instance, their physical and chemical stability tends to be poorer than that of conventional inorganic porous materials, which limits the application scope of MOFs to a certain extent. As a result, the frameworks of MOFs have been functionally modified to form composites to obtain specific functions and make up for some shortcomings of MOFs. For the practical application of MOFs-modified electrodes, the performance of MOFs can be improved in two ways by improving the electrical conductivity of MOF-based materials and designing MOF-based materials with redox activity (Zhou et al., 2022). The porous nature of MOFs enables them to be integrated with a variety of functional materials such as metal nanoparticles, carbon nanomaterials, polymers, biomolecules, etc., to form composites that combine the advantages of MOFs with other active materials and exhibit superior electrocatalytic/electrochemical sensing properties than MOFs alone.

Metal nanoparticles (MNPs) have become a hot topic of current research (Mourdikoudis et al., 2018; Yi et al., 2022; Zhang et al., 2022; Zhang Z. et al., 2023). MNPs have outstanding optical and conductive properties (Wang et al., 2020), which have been extensively applied in the sensing field in recent years. The large surface area and ordered porous structure of MOFs enable functionalized metal nanoparticles (MNPs) to be anchored on the surface of MOFs or encapsulated in cavities/pores to form MNPs/MOFs composites (Liu C.-S. et al., 2020). The combination of large specific surface area and size-limiting effect of MOFs and catalytic activity and conductivity of MNPs provides more catalytic active sites and a good microenvironment, making MNPs/MOFs composites excellent in both catalytic and sensing properties (Wu and Zhao, 2017; Jiao et al., 2018; Zhong et al., 2019; Zhang W. et al., 2020; Hao et al., 2021; Zhang et al., 2021; Guo M. et al., 2022; Guo T. et al., 2022; Xu et al., 2023). Here, this review summarizes the relevant literature that has been reported on the preparation of MNPs/MOFs composites for electrochemical sensors (Table 1).

This paper has reviewed the research progress of electrochemical sensors based on MNPs/MOFs in recent years. Meanwhile, the future challenges and opportunities for the preparation of electrochemical sensors based on MNPs/MOFs are briefly discussed. In conclusion, we aim to provide some new ideas for opening up MNPs/MOFs' high-performance electrochemical sensors.

2 MOFs/MNPs-based electrochemical sensors

In recent years, MOFs are often used as a carrier to encapsulate MNPs, which not only effectively prevent MNPs agglomeration but also have the following functions: 1) as a protective layer, they effectively prevent the aggregation and migration of MNPs. 2) Their inherent large surface area and porosity can facilitate the migration of reactants on the MNPs' surface. 3) Maintaining the catalytic activity of MNPs in multiple catalytic cycles. Compared with pure MOFs, MNPs@MOFs composites with core-shell heterogeneous structures have better catalytic and adsorption properties, and are beneficial for improving selectivity due to their size-screening effect. There are three general methods for the synthesis of MNPs@MOFs composites (Li et al., 2018). The first method is to confine the MNPs to the cavity or pore of the MOFs in the form of a ship-in-a-bottle, and the common methods include impregnation, coprecipitation, and deposition-precipitation. Unfortunately, some precursors may be deposited on the outer surface of MOFs to form aggregates, making them difficult to precisely control the MNPs at the loading position of MOFs. The second and third methods are more commonly used to encapsulate the MNPs in a bottle-around-ship form by MOFs. In the second method, MNPs with a well-defined structure are first synthesized and then mixed with the precursor solution of MOFs to obtain an encapsulated structure. Thus, the most important point to obtain a well-defined structure is to avoid agglomeration of MNPs and self-core of MOFs, The third method, in which the MNPs are embedded in the MOFs framework by one-pot synthesis, is considered the preferred method due to their low production cost/time and ease of scale-up. Commonly used metal nanoparticles in electrochemical sensors are gold nanoparticles, silver nanoparticles, copper nanoparticles, nickel nanoparticles, etc.

TABLE 1 Electrochemical sensors based on MNPs/MOFs composites.

Materials	Targets	Electrochemical methods	Linear range	Detection limit	Ref
PtNi@Cu-TCPP(Fe)	calprotectin	CV, EIS	200 fg/mL-50 ng/mL	137.7 fg/mL	Dong et al. (2020)
AuNPs/Co-MOF/MWCNT	nitrite	CV, EIS	1-1,000 μmol/L	0.4 μmol/L	Lei et al. (2021)
CoNi-MOF	miRNA-126	EIS	1.0 fmol/L-10.0 nmol/L	0.14 fmol/L	Hu et al. (2021)
Ce-Zn-MOF/MWCNT	bisphenol A	CV, EIS, DPV	0.1–100 μmol/L	7.2 nmol/L	Huang et al. (2021a)
Co-MOFs	glucose	CV	10–1,200 μmol/L	3.2 μmol/L	Ma et al. (2021b)
Au NPs/UiO-66	H_2O_2	CV, EIS	0.2–23 mmol/L	0.045 μmol/L	Wang et al. (2021b)
Pd@UiO-66	microRNA-21	DPV	20 fmol/L-600 pmol/L	0.713 fmol/L	Meng et al. (2020a)
Ag@MOF	Cu(II)	CV	—	0.68 μmol/L	Kwon and Kim (2021)
Ag@MOF	Pb(II)	CV	—	0.64 μmol/L	Kwon and Kim (2021)
USAuNPs@AuZn-MOF	estrone	CV, EIS, DPV	0.05 μmol/L-5 μmol/L	12.3 nmol/L	Chai et al. (2021)
Ag-ZIF-67p	Acetaminophen	CV, DPV	—	0.2 μmol/L	Tang et al. (2020)
Ag-ZIF-67p	dopamine	CV, DPV	—	0.05 μmol/L	Tang et al. (2020)
Ag-CoNi-MOF	luteolin	CV, DPV	0.002–1.0 μmol/L	0.4 nmol/L	Tang et al. (2022)
Co_xNi_{3-x} $(HITP)_2$	enrofloxacin	CV, EIS	0.001–1 pg/mL	0.2 fg/mL	Song et al. (2021)
Cu@C@ZIF-8	nitrite	CV, EIS, DPV	0.1–300.0 μmol/L	0.033 μmol/L	Gao et al. (2022)
CoP@C/NCS/GCE	dopamine	SWV	5.0–400.0 μmol/L	0.03 μmol/L	Xiao et al. (2021)
NiCu-MOF-6	glucose	CV	0.02-4.93 mmol/L	15 μmol/L	Pan et al. (2021)
Ni@Cu-MOF	glucose	CV	5–2,500 μmol/L	1.67 μmol/L	Xue et al. (2020)
Au@ZIF-8	dopamine	CV, DPV	0.1–50 μmol/L	0.01 μmol/L	Lu et al. (2020)
Ni-MOF	dopamine	DPV	0.2–100 μmol/L	60 nmol/L	Huang et al. (2021b)
CuCo-MOFs/NF	glucose	CV	—	0.23 mmol/L	Du et al. (2022)
Au/Co-BDC/MoS_2	Cardiac troponin I	EIS	10 fg/mL–100 ng/mL	3.02 fg/mL	Zhao et al. (2021)
Au@MOFs	Neuron-specific enolase	DPV, EIS	10 fg/mL–100 ng/mL	4.17 fg/mL	Ma et al. (2020)
Au NPs@ZIF-8	carcinoembryonic antigen	DPV, EIS	5 pg/mL-400 ng/mL	1.3 pg/mL	Ye et al. (2020)
Au@UiO-66(NH_2)	HBsAg	CV, DPV	1.13–fg/mL-100 ng/mL	1.13 fg/mL	Bajpai et al. (2021)
Au/UiO-66-NH_2	streptomycin	CV, DPV	0.005-150 ng/mL	2.6 pg/mL	Meng et al. (2020b)
MIP/Pt-UiO-66/CPME	phosalone	CV, DPV	0.50–nmol/L-20 μmol/L	0.078 nmol/L	Xu et al. (2020)
AgNPs/PCN-224	telomerase	CV, EIS, DPV	1.0×10^{-7}-1.0×10^{-1} IU/L	5.4×10^{-8} IU/L	Wang et al. (2021c)
Fe-Cu-BTC	bisphenol A	CV, DPV	0.1-1.0 μM	18 nM	Nguyen et al. (2022)
Fe-rich FeCoNi-MOF	imidaclopri	CV, DPV	1 pmol/L–120 μmol/L	0.04 pmol/L	Shu et al. (2023)
Mn_3O_4@ZIF-67	glucose	Amperometric method	0.0008–6.0 mM	0.24 μM	Dong et al. (2022)
Fe@YAU-101	Cd^{2+}	CV, EIS, DPV	0.003–42 μM	1 nM	Liang et al. (2023)
Fe@YAU-101	Pb^{2+}	CV, EIS, DPV	0.004–80 μM	1.33 nM	Liang et al. (2023)
Fe@YAU-101	Hg^{2+}	CV, EIS, DPV	0.045–66 μM	15 nM	Liang et al. (2023)
Au-CH@MOF-5	topotecan (TPT)	CV, EIS, DPV	0.4–70.0 nM	0.298 nM	Mehmandoust et al. (2023)
NiMn-LDH-MOF	glucose	CV	4.9 μM–2.2 mM	0.87 μM	Wei et al. (2023)

(Continued on following page)

TABLE 1 (*Continued*) **Electrochemical sensors based on MNPs/MOFs composites.**

Materials	Targets	Electrochemical methods	Linear range	Detection limit	Ref
Ni/Co-FAMOF	glucose	CV, EIS	0.006–1.004 mM	2 μM	Song et al. (2023)
Ag@MOF-199	Ni^{2+}	CV	-	6.06 nM	Bodkhe et al. (2023)
AuNPs/Zr-MOF-Graphene	sunset yellow	CV, DPV	0.1–1,000 μM	0.1 μM	Sun et al. (2023)
AuNPs/Zr-MOF-Graphene	Sudan I	CV, DPV	0.1–800 μM	0.1 μM	Sun et al. (2023)
AuNP/Cu-TCPP(Fe)	lactate (LA)	CV, EIS	0.013 nM-100 mM	0.91 p.m.	Ji et al. (2023)

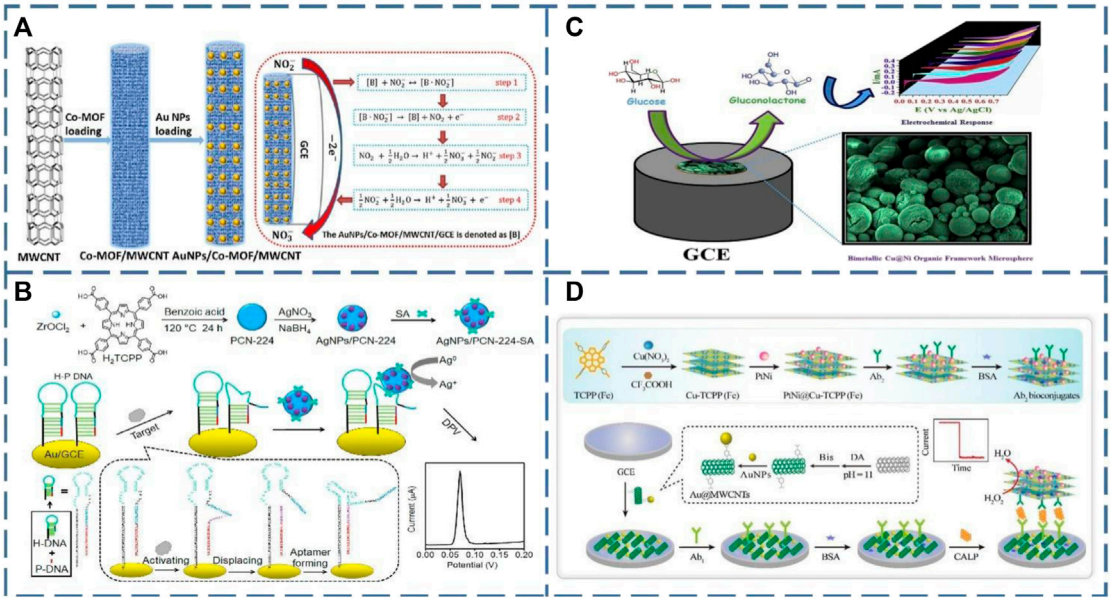

FIGURE 1
(A) Schematic illustration of the synthesizing process for the AuNPs/Co-MOF/MWCNT and the sensing mechanism of nitrite (Lei et al., 2021); **(B)** A schematic diagram of the electrochemical sensing strategy of telomerase activity based on the construction of streptavidin (SA) modified AgNPs/PCN-224 (Dong et al., 2019); **(C)** Pictorial representation of bimetallic Cu@Ni organic framework for electrochemical glucose oxidation (Kim and Muthurasu, 2020); **(D)** Schematic illustration of the construction process of the sandwich electrochemical immunosensor (Dong et al., 2020).

2.1 MOFs/Au NPs-based electrochemical sensors

To the best of our knowledge, there have been a large number of literature reports on the application of Au@MOFs in electrochemical sensors for the detection of different targets (Chen et al., 2019; Meng X. et al., 2020; Bajpai et al., 2021; Lei et al., 2021). At the same time, the introduction of carbon materials can efficiently improve the conductivity of pristine MOFs and limit their growth and aggregation. Consequently, the hybridization of MNPs@MOFs with carbon materials will also produce sensors with excellent stability and conductivity and give MNPs@MOFs template effect. For example, Zhang and his colleagues used Au nanoparticles to modify ZIF-8 as a basis for building a sensing platform to detect carcinoembryonic antigens (CEA). The Au@ZIF-8 that was successfully synthesized helped to increase the loading of the antibody. Ordered mesoporous carbon, a novel carbon nanomaterial with ordered pores, which was then attached to the electrode surface to enhance the conductivity of this sensor (Zhang Y. et al., 2020). Furthermore, Lei and his teams prepared ternary composites consisting of multi-walled carbon nanotubes (MWCNT) as a substrate, cobalt-based metal-organic backbone (Co-MOF), and gold nanoparticles (AuNPs/Co-MOF/MWCNT) (Figure 1A), which exhibited efficient catalytic activity and highly sensitive response to nitrite (Lei et al., 2021). Small Co-MOF nanoplates were first grown *in situ* on the surface of conducting multi-walled carbon nanotubes, which could absorb a large amount of Au^{+}. The reduced AuNPs can be uniformly restricted to Co-MOF/MWCNT. On the one hand, the binding of multi-walled carbon nanotubes to Co-MOF can markedly enhance the electron transport capacity of Co-MOF. On the other hand, the AuNPs distributed on Co-MOF can reduce the working voltage and significantly improve its catalytic activity for nitrite oxidation.

2.2 MOFs/Ag NPs-based electrochemical sensors

In addition to Au nanoparticles, Ag nanoparticles are also suitable as classical electrochemical detection labels. For instance, Wang and his colleagues took advantage of the fact that Ag nanoparticles are not easily oxidized and modified them on a porphyrin Zr-MOF (PCN-224) surface (AgNPs/PCN-224), functionalizing the surface with a streptavidin (SA) recognition element (Wang Y. et al., 2021). A hairpin structure of DNA is then modified on the electrode, and the developed sensor can be used to detect telomerase activity in cancer cells (Figure 1B). Zheng and his co-workers were also successful in embedding AgNPs into the ZIF-67 framework to form an ideal Ag@ZIF-67 core/shell material. The porous structure and large surface area of ZIF-67 provide abundant active sites for H_2O_2 adsorption and reduction as well as fast H_2O_2 diffusion channels (Dong et al., 2019). Moreover, the excellent electrical conductivity of AgNPs accelerates the electron transfer capability during H_2O_2 reduction, resulting in a highly sensitive electrochemical H_2O_2 sensor.

2.3 MOFs/Pt NPs-based electrochemical sensors

Pt nanoparticles, as noble metal nanoparticles, also have salient electrical conductivity and electrocatalytic activity and are among the superior materials for enhancing the conductivity of MOF-based sensors. Ma and his colleagues reported the synthesis of nanocomposite Pt@UiO-66-NH_2 by immobilizing Pt NPs on the surface of UiO-66-NH_2 and applying it to the preparation of acetylcholinesterase (AChE) biosensors (Ma et al., 2019). The pores of UiO-66-NH_2 can restrict the aggregation of Pt NPs and help the transfer of Pt NPs. At the same time, it can also provide more AChE active sites. Thus, the sensor can achieve sensitive detection of organophosphorus pesticides (OPs). Deng and his colleagues reported a one-pot hydrothermal reduction of metals with three different ligand lengths of Zr-MOF(Deng et al., 2018). And TEM results demonstrated that the Pt@UiO-66 composites maintained the integrity of the UiO-66 framework with some Pt NPs dispersed within the framework. Meanwhile, aggregated Pt NPs were observed in the Pt@UiO-68 composites, which could be attributed to the exudation and aggregation of Pt nanoparticles due to the large pore size of UiO-68. However, the doping of Pt NPs led to the collapse of the UiO-67 crystal structure. The framework structure of Pt@Zr-MOF has a great influence on the electrocatalytic activity and induction of N_2H_4, where Pt@ UiO-66 has the best performance, followed by Pt@UiO-68, and Pt@UiO-67 has the worst electrocatalytic performance.

2.4 MOFs/Ru NPs-based electrochemical sensors

Ruthenium belongs to the platinum group of noble metals along with platinum. Although ruthenium nanoparticles have the advantages of electrochemical catalysis, charge storage, and electrode modification, they usually suffer from the defects such as poor porosity, poor stability, and low electron transfer rate (Abdelwahab et al., 2020). Therefore, bimetallic nanoparticles, especially bimetallic Pt and Ru nanoparticles possess more attractive electrocatalytic properties, large specific surface area, good stability, and higher sensitivity than single Ru nanoparticles (Lavanya et al., 2020). Cao and his colleagues prepared nanocomposites of MOFs encapsulating bimetallic nanoparticles (PtRu/UiO66-NH_2) by embedding PtRu bimetallic nanoparticles (PtRu NPs) in UiO66-NH_2(Cao et al., 2020). Subsequently, PtRu/UiO66-NH_2 was subjected to high-temperature carbonization to synthesize PtRu-PC for the detection of uranium in aqueous solution. Among them, UiO66-NH_2 could not only limit the aggregation and migration of PtRu NPs, but also improve the electrical conductivity. Raju et al. (2023) also synthesized a novel nanocomposite of ZIF-67-modified bimetallic platinum and ruthenium nanoparticles (Pt-Ru@C/ZIF-67) and constructed a biosensor based on this composite for the detection of saxitoxin (STX)). ZIFs are a class of MOFs consisting of imidazolyl ligands and transition metal cations, which have the advantages of high stability, large surface area, and tunable pore structure. The electrochemical conductivity of the Pt-Ru@C/ZIF-67 nanocomposites was improved by the synergistic interaction between bimetallic PtRu NPs and ZIF-67. In addition, the unique porous structure of the composite and the presence of Co easily adsorb STX adsorption, thus facilitating STX detection.

2.5 MOFs/Cu NPs-based electrochemical sensors

Although noble metal nanoparticles (such as Au, Ag, Pt, etc.) are excellent materials for building sensors, their scarcity and high cost are disadvantages that do not facilitate their dissemination. Hence, researchers started to explore the possibility of non-precious metal nanoparticles (e.g., Cu, Co, Ni, etc.). In 2016, Shi and his colleagues informed for the first time that their team utilized the *in situ* synthesis of Cu NPs inside the ZIF-8 cavity. The Cu NPs@ZIF-8 nanocomposite was successfully applied to construct a novel electrochemical glucose sensor (Shi et al., 2016). In addition, due to the low loading of MNPs on MOFs and slow electron migration during encapsulation, Kim and his colleagues synthesized a metal-organic bimetallic skeleton structure based on a Cu@Ni solid spherical structure using a two-step hydrothermal method to solve these problems. They then modified it on a glassy carbon electrode (GCE), which can be regarded as a non-enzymatic sensor for glucose detection in an alkaline solution (Figure 1C) (Kim and Muthurasu, 2020). The sensor displayed better electrocatalytic activity for glucose oxidation compared to the sensors prepared from individual material. Its excellent catalytic performance for glucose mainly depends on the synergistic effect of Cu and Ni MOF. It also effectively prevents the oxidation of common interfering biomolecules, including ascorbic acid, dopamine and uric acid. This bimetallic Cu@Ni organic backbone microsphere electrode has high reliability and accuracy and is suitable as an alternative electrode for non-enzymatic glucose sensors.

2.6 MOFs/other NPs-based electrochemical sensors

In addition to these common MOF-based electrochemical sensors constructed with metal nanoparticles, there are also

bimetallic MOFs, which exhibit even more excellent electrochemical properties. Dong and his co-workers designed a novel composite with high electrocatalytic activity by functionalizing 2D ultra-thin Cu-TCPP(Fe) nanoflakes (PtNi@Cu-TCPP(Fe)) with PtNi nanospheres (Dong et al., 2020). The bimetallic Cu-TCPP(Fe) nanosheets have a huge specific surface area and a good deal of accessible active centers, allowing multiple PtNi to attach to their surfaces. Not only does it strengthen enzyme-free catalysis and conductivity, but it also provides junction sites for the immobilization of antibodies modified with fiducials. They constructed a sandwich-type calcium-binding protein immunosensor by exploiting the dual electrocatalytic activity of Cu-TCPP (Fe) and PtNi to amplify the signal for H_2O_2 reduction (Figure 1D). However, the immobilization of MNPs on the MOFs surface by simple sonication or surface self-assembly strategies will inevitably lead to the aggregation of some metal nanoparticles, which reduces the catalytic activity of MNPs. To further improve the analytical performance of electrochemical sensors, more effective active sites, and electrocatalysts are needed to be uniformly dispersed on the electrode surface. To achieve this goal, Chen and his colleagues used electrodeposition to uniformly disperse a large number of Au NPs (<200 nm) on the surface of Cu-MOF. Compared with the nitrite electrochemical sensor prepared by these two composites, the electrochemical sensor with electrodeposited Au/Cu-MOF has a wider linear detection range (Chen et al., 2019).

3 Conclusion and prospects

Within the last few years, the literature related to electrochemical sensors based on MNPs/MOFs composites has increased dramatically, and most of them focus mainly on the detection of glucose, hydrogen peroxide, and dopamine. The innovation of this mini-review is to systematically summarize the studies on electrochemical sensors related to MNPs/MOFs composites. The synthesis of MNPs/MOFs composites and the advantages of electrochemical sensors prepared using these composites are also briefly discussed. In addition, more detailed statistics of the studies on the detection of various analytes using the sensors are also presented. In addition, MNPs/MOFs composites utilize the synergistic effect between MNPs and MOFs: 1) MNPs act as active centers and MOFs play a stabilizing role. 2) MOFs limit the aggregation of MNPs. However, the sensor also has some drawbacks. First, MNPs or bimetallic nanoparticles composed of noble and non-precious metals are scarce and expensive, and cannot be applied on a large scale. Therefore, subsequent studies should consider affordable alternatives to MNPs or use non-precious metal particles. Secondly, based on MNPs/MOFs composites, efforts should be devoted to the development of electrochemical sensors with more sensitivity, better stability, and reproducibility. In conclusion, the nanocomposites synthesized by attaching MNPs on the surface of MOFs or encapsulating them internally have largely improved the sensing performance of electrochemical sensors and have a bright future in the sensing field.

Author contributions

MJ: defined the focus of the review. JL, CL, and ZD: writing. YLu, YLo, and Yb L: editing. PC, JZ, and FC: reviewing. JL, XF, and XL: writing, reviewing and editing. All authors contributed to the article and approved the submitted version.

Funding

This work has been supported by the National Natural Science Foundation of China (No. 82060599), the Natural Science Foundation of Jiangxi (No. 20224BAB206091), the Science and Technology Project of the Education Department of Jiangxi Province (Nos. GJJ2201406, GJJ2201453, GJJ211517, GJJ2201457), the Science and Technology Project of Jiangxi Health Committee (No. 202131033), The teaching reform of higher education in Jiangxi province (No. JXJG-22-13-30). The Natural Science Foundation of Ganzhou (No. 202101034482), the Natural Science Foundation of Gannan Medical University (No. YB201945), the Program of Innovation and Entrepreneurship Training for Undergraduate (No. 202310413001, 202310413003), and the Special Fund for Graduate Innovation in Jiangxi Province (No. YC2022-X017).

Conflict of interest

The authors declare that the research was conducted in the absence of any commercial or financial relationships that could be construed as a potential conflict of interest.

Publisher's note

References

Abdelwahab, A. A., Naggar, A. H., Abdelmotaleb, M., and Emran, M. Y. (2020). Ruthenium nanoparticles uniformly-designed chemically treated graphene oxide nanosheets for simultaneous voltammetric determination of dopamine and acetaminophen. *Electroanalysis* 32 (10), 2156–2165. doi:10.1002/elan.202060126

Adeel, M., Asif, K., Rahman, M. M., Daniele, S., Canzonieri, V., and Rizzolio, F. (2021). Glucose detection devices and methods based on metal-organic frameworks and related materials. *Adv. Funct. Mater.* 31 (52), 2106023. doi:10.1002/adfm.202106023

Bag, P. P., Singh, G. P., Singha, S., and Roymahapatra, G. (2021). Synthesis of metal-organic frameworks (MOFs) and their applications to biology, catalysis and electrochemical charge storage: A mini review. *Eng. Sci.* 13, 1–10. doi:10.30919/es8d1166

Bajpai, V. K., Haldorai, Y., Khan, I., Sonwal, S., Singh, M. P., Yadav, S., et al. (2021). Au@Zr-based metal-organic framework composite as an immunosensing platform for determination of hepatitis B virus surface antigen. *Microchim. Acta* 188 (11), 365. doi:10.1007/s00604-021-05022-6

Bodkhe, G. A., Khandagale, D. D., More, M. S., Deshmukh, M. A., Ingle, N. N., Sayyad, P. W., et al. (2023). Ag@MOF-199 metal organic framework for selective detection of nickel ions in aqueous media. *Ceram. Int.* 49 (4), 6772–6779. doi:10.1016/j.ceramint.2022.10.135

Cao, X., Sun, Y., Wang, Y., Zhang, Z., Dai, Y., Liu, Y., et al. (2020). PtRu bimetallic nanoparticles embedded in MOF-derived porous carbons for efficiently electrochemical sensing of uranium. *J. Solid State Electrochem.* 25 (2), 425–433. doi:10.1007/s10008-020-04668-1

Chai, C., Gao, J., Zhao, G., Li, L., Tang, Y., Wu, C., et al. (2021). *In-situ* synthesis of ultrasmall Au nanoparticles on bimetallic metal-organic framework with enhanced electrochemical activity for estrone sensing. *Anal. Chim. Acta* 1152, 338242. doi:10.1016/j.aca.2021.338242

Chen, B. S., Chen, D. J., Li, F. M., Lin, X. F., and Huang, Q. T. (2018). Graphitic porous carbon: Efficient synthesis by a combustion method and application as a highly selective biosensor. *J. Mater. Chem. B* 6 (46), 7684–7691. doi:10.1039/c8tb02139b

Chen, H., Yang, T., Liu, F., and Li, W. (2019). Electrodeposition of gold nanoparticles on Cu-based metal-organic framework for the electrochemical detection of nitrite. *Sensors Actuators B Chem.* 286, 401–407. doi:10.1016/j.snb.2018.10.036

Çorman, M. E., Ozcelikay, G., Cetinkaya, A., Kaya, S. I., Armutcu, C., Özgür, E., et al. (2022). Metal-organic frameworks as an alternative smart sensing platform for designing molecularly imprinted electrochemical sensors. *TrAC Trends Anal. Chem.* 150, 116573. doi:10.1016/j.trac.2022.116573

Daniel, M., Mathew, G., Anpo, M., and Neppolian, B. (2022). MOF based electrochemical sensors for the detection of physiologically relevant biomolecules: An overview. *Coord. Chem. Rev.* 468, 214627. doi:10.1016/j.ccr.2022.214627

Deng, M., Bo, X., and Guo, L. (2018). Encapsulation of platinum nanoparticles into a series of zirconium-based metal-organic frameworks: Effect of the carrier structures on electrocatalytic performances of composites. *J. Electroanal. Chem.* 815, 198–209. doi:10.1016/j.jelechem.2018.03.021

Dong, L., Yin, L., Tian, G., Wang, Y., Pei, H., Wu, Q., et al. (2020). An enzyme-free ultrasensitive electrochemical immunosensor for calprotectin detection based on PtNi nanoparticles functionalized 2D Cu-metal organic framework nanosheets. *Sensors Actuators B Chem.* 308, 127687. doi:10.1016/j.snb.2020.127687

Dong, Q., He, Z., Tang, X., Zhang, Y., Yang, L., Huang, K., et al. (2022). One-step synthesis of Mn_3O_4@ZIF-67 on carbon cloth: As an effective non-enzymatic glucose sensor. *Microchem. J.* 175, 107203. doi:10.1016/j.microc.2022.107203

Dong, Y., Duan, C., Sheng, Q., and Zheng, J. (2019). Preparation of Ag@zeolitic imidazolate framework-67 at room temperature for electrochemical sensing of hydrogen peroxide. *Analyst* 144 (2), 521–529. doi:10.1039/C8AN01641K

Du, Q., Liao, Y., Shi, N., Sun, S., Liao, X., Yin, G., et al. (2022). Facile synthesis of bimetallic metal-organic frameworks on nickel foam for a high performance non-enzymatic glucose sensor. *J. Electroanal. Chem.* 904, 115887. doi:10.1016/j.jelechem.2021.115887

Falsafi, M., Saljooghi, A. S., Abnous, K., Taghdisi, S. M., Ramezani, M., and Alibolandi, M. (2021). Smart metal organic frameworks: Focus on cancer treatment. *Biomaterials Sci.* 9 (5), 1503–1529. doi:10.1039/D0BM01839B

Gao, F., Tu, X., Yu, Y., Gao, Y., Zou, J., Liu, S., et al. (2022). Core-shell Cu@C@ZIF-8 composite: A high-performance electrode material for electrochemical sensing of nitrite with high selectivity and sensitivity. *Nanotechnology* 33 (22), 225501. doi:10.1088/1361-6528/ac3da7

Guo, M., Du, Y., Zhang, M., Wang, L., Zhang, X., and Li, G. (2022a). Breaking the activity-selectivity trade-off of Pt nanoparticles encapsulated in UiO-66 for hydrogenation by constructing suitable hierarchical structure. *ACS Sustain. Chem. Eng.* 10 (23), 7485–7499. doi:10.1021/acssuschemeng.2c00098

Guo, T., Huang, Y., Zhang, N., Chen, T., Wang, C., Xing, X., et al. (2022b). Modulating the chemical microenvironment of Pt nanoparticles within ultrathin nanosheets of isoreticular MOFs for enhanced catalytic activity. *Inorg. Chem.* 61 (5), 2538–2545. doi:10.1021/acs.inorgchem.1c03425

Hao, L., Xia, Q., Zhang, Q., Masa, J., and Sun, Z. (2021). Improving the performance of metal-organic frameworks for thermo-catalytic CO_2 conversion: Strategies and perspectives. *Chin. J. Catal.* 42 (11), 1903–1920. doi:10.1016/S1872-2067(21)63841-X

Hu, M., Zhu, L., Li, Z., Guo, C., Wang, M., Wang, C., et al. (2021). CoNi bimetallic metal-organic framework as an efficient biosensing platform for miRNA 126 detection. *Appl. Surf. Sci.* 542, 148586. doi:10.1016/j.apsusc.2020.148586

Huang, D., Huang, X., Chen, J., Ye, R., Lin, Q., and Chen, S. (2021a). An electrochemical bisphenol: A sensor based on bimetallic Ce-Zn-mof. *Electrocatalysis* 12 (4), 456–468. doi:10.1007/s12678-021-00659-6

Huang, Q., Lin, X., Chen, D., and Tong, Q.-X. (2022). Carbon Dots/α-Fe_2O_3-Fe_3O_4 nanocomposite: Efficient synthesis and application as a novel electrochemical aptasensor for the ultrasensitive determination of aflatoxin B1. *Food Chem.* 373, 131415. doi:10.1016/j.foodchem.2021.131415

Huang, Q., Lin, X., Tong, L., and Tong, Q.-X. (2020). Graphene quantum dots/multiwalled carbon nanotubes composite-based electrochemical sensor for detecting dopamine release from living cells. *ACS Sustain. Chem. Eng.* 8 (3), 1644–1650. doi:10.1021/acssuschemeng.9b06623

Huang, Z., Zhang, L., Cao, P., Wang, N., and Lin, M. (2021b). Electrochemical sensing of dopamine using a Ni-based metal-organic framework modified electrode. *Ionics* 27 (3), 1339–1345. doi:10.1007/s11581-020-03857-2

Ji, G., Zhu, W., Jia, X., Ji, S., Han, D., Gao, Z., et al. (2023). AuNP/Cu-TCPP(Fe) metal-organic framework nanofilm: A paper-based electrochemical sensor for non-invasive detection of lactate in sweat. *Nanoscale* 15 (10), 5023–5035. doi:10.1039/d2nr06342e

Jiao, L., Wang, Y., Jiang, H.-L., and Xu, Q. (2018). Metal-organic frameworks as platforms for catalytic applications. *Adv. Mater.* 30 (37), 1703663. doi:10.1002/adma.201703663

Kajal, N., Singh, V., Gupta, R., and Gautam, S. (2022). Metal organic frameworks for electrochemical sensor applications: A review. *Environ. Res.* 112320, 112320. doi:10.1016/j.envres.2021.112320

Kim, S. E., and Muthurasu, A. (2020). Metal-organic framework-assisted bimetallic Ni@Cu microsphere for enzyme-free electrochemical sensing of glucose. *J. Electroanal. Chem.* 873, 114356. doi:10.1016/j.jelechem.2020.114356

Kumari, V., Pal Singh, P., and Kaushal, S. (2022). Synthesis and applications of metal-organic frameworks and graphene-based composites: A review. *Polyhedron* 214, 115645. doi:10.1016/j.poly.2021.115645

Kwon, D., and Kim, J. (2021). Ag metal organic frameworks nanocomposite modified electrode for simultaneous electrochemical detection of copper (II) and lead (II). *J. Appl. Electrochem.* 51 (8), 1207–1216. doi:10.1007/s10800-021-01569-7

Lavanya, A. L., Bala Kumari, K. G., Prasad, K. R. S., and Brahman, P. K. (2020). Fabrication of electrochemical sensor based on electrochemically co-deposited Ru-Co bimetallic nanoparticles on glassy carbon electrode: An analytical measurement tool for monitoring of hydrazine in water samples. *Int. J. Environ. Anal. Chem.* 102 (3), 720–735. doi:10.1080/03067319.2020.1726333

Lei, H., Zhu, H., Sun, S., Zhu, Z., Hao, J., Lu, S., et al. (2021). Synergistic integration of Au nanoparticles, Co-MOF and MWCNT as biosensors for sensitive detection of low-concentration nitrite. *Electrochimica Acta* 365, 137375. doi:10.1016/j.electacta.2020.137375

Li, G., Zhao, S., Zhang, Y., and Tang, Z. (2018). Metal-organic frameworks encapsulating active nanoparticles as emerging composites for catalysis: Recent progress and perspectives. *Adv. Mater.* 30 (51), 1800702. doi:10.1002/adma.201800702

Li, Y., Li, J.-J., Zhang, Q., Zhang, J.-Y., Zhang, N., Fang, Y.-Z., et al. (2022). The multifunctional bodipy@Eu-mof nanosheets as bioimaging platform: A ratiometric fluorescencent sensor for highly efficient detection of F-H_2O_2 and glucose. *Sensors Actuators B Chem.* 354, 131140. doi:10.1016/j.snb.2021.131140

Liang, Q., Xiao, W., Zhang, C., Zhu, D., Wang, S. L., Tian, S. Y., et al. (2023). MOFs-based Fe@YAU-101/GCE electrochemical sensor platform for highly selective detecting trace multiplex heavy metal ions. *Talanta* 259, 124491. doi:10.1016/j.talanta.2023.124491

Lin, X., Lian, X., Luo, B., and Huang, X.-C. (2020). A highly sensitive and stable electrochemical HBV DNA biosensor based on ErGO-supported Cu-MOF. *Inorg. Chem. Commun.* 119, 108095. doi:10.1016/j.inoche.2020.108095

Lin, X., Mei, Y., He, C., Luo, Y., Yang, M., Kuang, Y., et al. (2021a). Electrochemical biosensing interface based on carbon dots-Fe_3O_4 nanomaterial for the determination of *Escherichia coli* O157:H7. *Front. Chem.* 9 (903), 769648. doi:10.3389/fchem.2021.769648

Lin, X., Xiong, M., Zhang, J., He, C., Ma, X., Zhang, H., et al. (2021b). Carbon dots based on natural resources: Synthesis and applications in sensors. *Microchem. J.* 160, 105604. doi:10.1016/j.microc.2020.105604

Liu, C.-S., Li, J., and Pang, H. (2020a). Metal-organic framework-based materials as an emerging platform for advanced electrochemical sensing. *Coord. Chem. Rev.* 410, 213222. doi:10.1016/j.ccr.2020.213222

Liu, J.-Q., Luo, Z.-D., Pan, Y., Kumar Singh, A., Trivedi, M., and Kumar, A. (2020b). Recent developments in luminescent coordination polymers: Designing strategies, sensing application and theoretical evidences. *Coord. Chem. Rev.* 406, 213145. doi:10.1016/j.ccr.2019.213145

Lu, K., Aung, T., Guo, N., Weichselbaum, R., and Lin, W. (2018). Nanoscale metal-organic frameworks for therapeutic, imaging, and sensing applications. *Adv. Mater.* 30 (37), 1707634. doi:10.1002/adma.201707634

Lu, S., Hummel, M., Chen, K., Zhou, Y., Kang, S., and Gu, Z. (2020). Synthesis of Au@ZIF-8 nanocomposites for enhanced electrochemical detection of dopamine. *Electrochem. Commun.* 114, 106715. doi:10.1016/j.elecom.2020.106715

Ma, E., Wang, P., Yang, Q., Yu, H., Pei, F., Zheng, Y., et al. (2020). Electrochemical immunosensors for sensitive detection of neuron-specific enolase based on small-size trimetallic Au@Pd-Pt nanocubes functionalized on ultrathin MnO_2 nanosheets as signal labels. *ACS Biomaterials Sci. Eng.* 6 (3), 1418–1427. doi:10.1021/acsbiomaterials.9b01882

Ma, J., Bai, W., Liu, X., and Zheng, J. (2021a). Electrochemical dopamine sensor based on bi-metallic Co/Zn porphyrin metal-organic framework. *Microchim. Acta* 189 (1), 20. doi:10.1007/s00604-021-05122-3

Ma, L., He, Y., Wang, Y., Wang, Y., Li, R., Huang, Z., et al. (2019). Nanocomposites of Pt nanoparticles anchored on UiO66-NH_2 as carriers to construct acetylcholinesterase biosensors for organophosphorus pesticide detection. *Electrochimica Acta* 318, 525–533. doi:10.1016/j.electacta.2019.06.110

Ma, Z.-Z., Ma, Y., Liu, B., Xu, L., and Jiao, H. (2021b). A high-performance Co-MOF non-enzymatic electrochemical sensor for glucose detection. *New J. Chem.* 45 (45), 21350–21358. doi:10.1039/D1NJ04480J

Mehmandoust, M., Tiris, G., Pourhakkak, P., Erk, N., Soylak, M., Kanberoglu, G. S., et al. (2023). An electrochemical sensing platform with a molecularly imprinted polymer based on chitosan-stabilized metal@metal-organic frameworks for topotecan detection. *Microchim. Acta* 190 (4), 142. doi:10.1007/s00604-023-05722-1

Mei, Y., He, C., Zeng, W., Luo, Y., Liu, C., Yang, M., et al. (2022a). Electrochemical biosensors for foodborne pathogens detection based on carbon nanomaterials: Recent advances and challenges. *Food Bioprocess Technol.* 15 (3), 498–513. doi:10.1007/s11947-022-02759-7

Mei, Y., Lin, X., He, C., Zeng, W., Luo, Y., Liu, C., et al. (2022b). Recent progresses in electrochemical DNA biosensors for SARS-CoV-2 detection. *Front. Bioeng. Biotechnol.* 10, 952510. doi:10.3389/fbioe.2022.952510

Meng, T., Shang, N., Nsabimana, A., Ye, H., Wang, H., Wang, C., et al. (2020a). An enzyme-free electrochemical biosensor based on target-catalytic hairpin assembly and Pd@UiO-66 for the ultrasensitive detection of microRNA-21. *Anal. Chim. Acta* 1138, 59–68. doi:10.1016/j.aca.2020.09.022

Meng, X., Gu, H., Yi, H., He, Y., Chen, Y., and Sun, W. (2020b). Sensitive detection of streptomycin in milk using a hybrid signal enhancement strategy of MOF-based bio-bar code and target recycling. *Anal. Chim. Acta* 1125, 1–7. doi:10.1016/j.aca.2020.05.041

Mourdikoudis, S., Pallares, R. M., and Thanh, N. T. J. N. (2018). Characterization techniques for nanoparticles: Comparison and complementarity upon studying nanoparticle properties. *Nanoscale* 10 (27), 12871–12934. doi:10.1039/c8nr02278j

Nguyen, M. B., Anh, N. H., Thi Thu, V., Thi Hai Yen, P., Hong Phong, P., Quoc Hung, L., et al. (2022). A novel bimetallic MOFs combined with gold nanoflakes in electrochemical sensor for measuring bisphenol A. *RSC Adv.* 12 (52), 33825–33834. doi:10.1039/d2ra06300j

Pan, W., Zheng, Z., Wu, X., Gao, J., Liu, Y., Yuan, Q., et al. (2021). Facile synthesis of 2D/3D hierarchical NiCu bimetallic MOF for non-enzymatic glucose sensor. *Microchem. J.* 170, 106652. doi:10.1016/j.microc.2021.106652

Raju, C. V., Manohara Reddy, Y. V., Cho, C. H., Shin, H. H., Park, T. J., and Park, J. P. (2023). Highly sensitive electrochemical peptide-based biosensor for marine biotoxin detection using a bimetallic platinum and ruthenium nanoparticle-tethered metal-organic framework modified electrode. *Food Chem.* 428, 136811. doi:10.1016/j.foodchem.2023.136811

Shi, L., Zhu, X., Liu, T., Zhao, H., and Lan, M. (2016). Encapsulating Cu nanoparticles into metal-organic frameworks for nonenzymatic glucose sensing. *Sensors Actuators B Chem.* 227, 583–590. doi:10.1016/j.snb.2015.12.092

Shu, H., Lai, T., Yang, Z., Xiao, X., Chen, X., and Wang, Y. (2023). High sensitivity electrochemical detection of ultra-trace imidacloprid in fruits and vegetables using a Fe-rich FeCoNi-MOF. *Food Chem.* 408, 135221. doi:10.1016/j.foodchem.2022.135221

Song, S., Ma, X., Li, W., Zhang, B., Shao, B., Chang, X., et al. (2023). Novel stylophora coral-like furan-based Ni/Co bimetallic metal organic framework for high-performance capacitive storage and non-enzymatic glucose electrochemical sensing. *J. Alloys Compd.* 931, 167413. doi:10.1016/j.jallcom.2022.167413

Song, Y., Xu, M., Liu, X., Li, Z., Wang, C., Jia, Q., et al. (2021). A label-free enrofloxacin electrochemical aptasensor constructed by a semiconducting CoNi-based metal-organic framework (MOF). *Electrochimica Acta* 368, 137609. doi:10.1016/j.electacta.2020.137609

Sun, R., Lv, R., Li, Y., Du, T., Chen, L., Zhang, Y., et al. (2023). Simple and sensitive electrochemical detection of sunset yellow and Sudan I in food based on AuNPs/Zr-MOF-Graphene. *Food control.* 145, 109491. doi:10.1016/j.foodcont.2022.109491

Tang, J., Hu, T., Li, N., Zhu, Y., Li, J., Zheng, S., et al. (2022). Ag doped Co/Ni bimetallic organic framework for determination of luteolin. *Microchem. J.* 179, 107461. doi:10.1016/j.microc.2022.107461

Tang, J., Liu, Y., Hu, J., Zheng, S., Wang, X., Zhou, H., et al. (2020). Co-Based metal-organic framework nanopinnas composite doped with Ag nanoparticles: A sensitive electrochemical sensing platform for simultaneous determination of dopamine and acetaminophen. *Microchem. J.* 155, 104759. doi:10.1016/j.microc.2020.104759

Wang, H., Wang, X., Kong, R.-M., Xia, L., and Qu, F. (2021a). Metal-organic framework as a multi-component sensor for detection of Fe^{3+}, ascorbic acid and acid phosphatase. *Chin. Chem. Lett.* 32 (1), 198–202. doi:10.1016/j.cclet.2020.10.017

Wang, L., Hasanzadeh Kafshgari, M., and Meunier, M. J. F. M. (2020). Optical properties and applications of plasmonic-metal nanoparticles. *Adv. Funct. Mat.* 30 (51), 2005400. doi:10.1002/adfm.202005400

Wang, Q., Zhang, X., Chai, X., Wang, T., Cao, T., Li, Y., et al. (2021b). An electrochemical sensor for H_2O_2 based on Au nanoparticles embedded in UiO-66 metal-organic framework films. *ACS Appl. Nano Mater.* 4 (6), 6103–6110. doi:10.1021/acsanm.1c00915

Wang, Y., Dong, P., Huang, J., Xu, H., Lei, J., and Zhang, L. (2021c). Direct electrochemistry of silver nanoparticles-decorated metal-organic frameworks for telomerase activity sensing via allosteric activation of an aptamer hairpin. *Anal. Chim. Acta* 1184, 339036. doi:10.1016/j.aca.2021.339036

Wei, Y., Hui, Y., Lu, X., Liu, C., Zhang, Y., Fan, Y., et al. (2023). One-pot preparation of NiMn layered double hydroxide-MOF material for highly sensitive electrochemical sensing of glucose. *J. Electroanal. Chem.* 933, 117276. doi:10.1016/j.jelechem.2023.117276

Wu, C.-D., and Zhao, M. (2017). Incorporation of molecular catalysts in metal-organic frameworks for highly efficient heterogeneous catalysis. *Adv. Mater.* 29 (14), 1605446. doi:10.1002/adma.201605446

Xiao, L., Zheng, S., Yang, K., Duan, J., and Jiang, J. (2021). The construction of CoP nanoparticles coated with carbon layers derived from core-shell bimetallic MOF for electrochemical detection of dopamine. *Microchem. J.* 168, 106432. doi:10.1016/j.microc.2021.106432

Xu, J., Ma, J., Peng, Y., Cao, S., Zhang, S., and Pang, H. (2023). Applications of metal nanoparticles/metal-organic frameworks composites in sensing field. *Chin. Chem. Lett.* 34 (4), 107527. doi:10.1016/j.cclet.2022.05.041

Xu, L., Li, J., Zhang, J., Sun, J., Gan, T., and Liu, Y. (2020). A disposable molecularly imprinted electrochemical sensor for the ultra-trace detection of the organophosphorus insecticide phosalone employing monodisperse Pt-doped UiO-66 for signal amplification. *Analyst* 145 (9), 3245–3256. doi:10.1039/D0AN00278J

Xue, Z., Jia, L., Zhu, R.-R., Du, L., and Zhao, Q.-H. (2020). High-performance non-enzymatic glucose electrochemical sensor constructed by transition nickel modified Ni@Cu-MOF. *J. Electroanal. Chem.* 858, 113783. doi:10.1016/j.jelechem.2019.113783

Yang, Z., Zhong, Y., Zhou, X., Zhang, W., Yin, Y., Fang, W., et al. (2022). Metal-organic framework-based sensors for nitrite detection: A short review. *J. Food Meas. Charact.* 16 (2), 1572–1582. doi:10.1007/s11694-021-01270-5

Ye, T., Zhang, Z., Yuan, M., Cao, H., Yin, F., Wu, X., et al. (2020). An all-in-one aptasensor integrating enzyme powered three-dimensional DNA machine for antibiotic detection. *J. Agric. Food Chem.* 68 (9), 2826–2831. doi:10.1021/acs.jafc.9b08143

Yi, X., Zeng, W., Wang, C., Chen, Y., Zheng, L., Zhu, X., et al. (2022). A step-by-step multiple stimuli-responsive metal-phenolic network prodrug nanoparticles for chemotherapy. *Nano Res.* 15 (2), 1205–1212. doi:10.1007/s12274-021-3626-2

Zhang, L., Zhang, K., Wang, C., Liu, Y., Wu, X., Peng, Z., et al. (2021). Advances and prospects in metal-organic frameworks as key nexus for chemocatalytic hydrogen production. *Small* 17 (52), 2102201. doi:10.1002/smll.202102201

Zhang, W., Li, X., Ding, X., Hua, K., Sun, A., Hu, X., et al. (2023a). Progress and opportunities for metal-organic framework composites in electrochemical sensors. *RSC Adv.* 13 (16), 10800–10817. doi:10.1039/d3ra00966a

Zhang, W., Shi, W., Ji, W., Wu, H., Gu, Z., Wang, P., et al. (2020a). Microenvironment of MOF channel coordination with Pt NPs for selective hydrogenation of unsaturated aldehydes. *ACS Catal.* 10 (10), 5805–5813. doi:10.1021/acscatal.0c00682

Zhang, Y., Zhang, Z., Rong, S., Yu, H., Gao, H., Ding, P., et al. (2020b). Electrochemical immunoassay for the carcinoembryonic antigen based on Au NPs modified zeolitic imidazolate framework and ordered mesoporous carbon. *Microchim. Acta* 187 (5), 264. doi:10.1007/s00604-020-04235-5

Zhang, Z., Lin, X., Tang, S., Xie, H., and Huang, Q. (2023b). Self-supported system of MoO_2@Ni_2P heterostructures as an efficient electrocatalyst for hydrogen evolution reactions in alkaline media. *J. Colloid Interface Sci.* 630, 494–501. doi:10.1016/j.jcis.2022.10.041

Zhang, Z., Tang, S., Lin, X., Liu, C., Hu, S., and Huang, Q. (2022). N, P-doped multiphase transition metal sulfides are used for efficient electrocatalytic oxygen evolution reaction. *Appl. Surf. Sci.* 584, 152546. doi:10.1016/j.apsusc.2022.152546

Zhao, H., Du, X., Dong, H., Jin, D., Tang, F., Liu, Q., et al. (2021). Electrochemical immunosensor based on Au/Co-BDC/MoS_2 and DPCN/MoS2 for the detection of cardiac troponin I. *Biosens. Bioelectron.* 175, 112883. doi:10.1016/j.bios.2020.112883

Zhong, Y., Mao, Y., Shi, S., Wan, M., Ma, C., Wang, S., et al. (2019). Fabrication of magnetic Pd/MOF hollow nanospheres with double-shell structure: Toward highly efficient and recyclable nanocatalysts for hydrogenation reaction. *ACS Appl. Mater. Interfaces* 11 (35), 32251–32260. doi:10.1021/acsami.9b07864

Zhou, Y., Abazari, R., Chen, J., Tahir, M., Kumar, A., Ikreedeegh, R. R., et al. (2022). Bimetallic metal-organic frameworks and MOF-derived composites: Recent progress on electro- and photoelectrocatalytic applications. *Coord. Chem. Rev.* 451, 214264. doi:10.1016/j.ccr.2021.214264

frontiers | Frontiers in Bioengineering and Biotechnology

TYPE Original Research
PUBLISHED 03 November 2023
DOI 10.3389/fbioe.2023.1290413

OPEN ACCESS

EDITED BY
Qitong Huang,
Gannan Medical University, China

REVIEWED BY
Xing-Huo Wang,
Qingdao University, China
Meng Lyu,
Shenzhen People'Hospital, China

*CORRESPONDENCE
Hao Tang,
tangpku_zzuhao@zzu.edu.cn
Ruiqin Li,
lirqin@yeah.net
Hongtao Zhang,
zhtzzu@zzu.edu.cn

†These authors have contributed equally to this work

RECEIVED 07 September 2023
ACCEPTED 16 October 2023
PUBLISHED 03 November 2023

CITATION
Wang Y, Wang B, Xiao Y, Cai Q, Xing J, Tang H, Li R and Zhang H (2023), Baicalin-modified polyethylenimine for miR-34a efficient and safe delivery.
Front. Bioeng. Biotechnol. 11:1290413.
doi: 10.3389/fbioe.2023.1290413

Baicalin-modified polyethylenimine for miR-34a efficient and safe delivery

Yingying Wang[1,2†], Baiyan Wang[1†], Yangfan Xiao[2], Qingchun Cai[3], Junyue Xing[2], Hao Tang[2*], Ruiqin Li[4*] and Hongtao Zhang[5,6,7,8*]

[1]Medical College, Henan University of Chinese Medicine, Zhengzhou, Henan, China, [2]National Health Commission Key Laboratory of Cardiovascular Regenerative Medicine, Heart Center of Henan Provincial People's Hospital, Fuwai Central China Cardiovascular Hospital and Central China Branch of National Center for Cardiovascular Diseases, Central China Fuwai Hospital of Zhengzhou University, Zhengzhou, Henan, China, [3]Department of Clinical Lab, The Third Affiliated Hospital of Henan University of Chinese Medicine, Zhengzhou, China, [4]Academy of Chinese Medicine, Henan University of Chinese Medicine, Zhengzhou, Henan, China, [5]Blood Purification Center, The People's Hospital of Zhengzhou University, Zhengzhou, China, [6]Blood Purification Center, Henan Provincial People's Hospital, Zhengzhou, China, [7]Institute of Nephrology, Mathura, Henan, China, [8]Department of Nephrology Henan Provincial People's Hospital, Zhengzhou, China

The security and efficiency of gene delivery vectors are inseparable for the successful construction of a gene delivery vector. This work provides a practical method to construct a charge-regulated, hydrophobic-modified, and functionally modified polyethylenimine (PEI) with effective gene delivery and perfect transfection performance through a condensation reaction, named BA-PEI. The carrier was shown to possess a favorable compaction of miRNAs into positively charged nanoparticles with a hydrodynamic size of approximately 100 nm. Additionally, BA-PEI possesses perfect degradability, which benefits the release of miR-34a from the complexes. In A549 cells, the expression level of the miR-34a gene was checked by Western blotting, which reflects the transfection efficiency of BA-PEI/miR-34a. When miR-34a is delivered to the cell, the perfect anti-tumor ability of the BA-PEI/miR-34a complex was systematically evaluated with the suppressor tumor gene miR-34a system *in vitro* and *in vivo*. BA-PEI-mediated miR-34a gene transfection is more secure and effective than the commercial transfection reagent, thus providing a novel approach for miR-34a-based gene therapy.

KEYWORDS

baicalin, lung cancer, gene therapy, miR-34a, hydrophobic modification

1 Introduction

In the world, cancer, which accounts for one in six deaths, is one of the deadliest diseases (WHO, 2023). Due to the characteristic of lung cancer to metastasize easily, the death rate of lung cancer is the leading cause of mortality among all kinds of malignant tumors (IARC, 2020). Vaccination, initial diagnosis, and appropriate treatment are important measures to reduce cancer mortality. However, due to the variability and complexity of the tumor, these methods have a low success rate. Surgery and radiation therapy are used to treat orthotopic tumors, while anti-tumor agents, such as chemotherapy, hormonal therapies, and biotherapies, are preferred for metastatic tumors. With the increasing advancement of molecular biology and the understanding of unique tumor characteristics, chemotherapy drugs can induce apoptosis of normal cells and are toxic, so gene therapy is a promising targeted therapy for cancer.

Gene therapy involves the introduction of foreign nucleic acids, such as genes, gene fragments, oligonucleotides, miRNAs, or siRNAs, into target cells and regulating the synthesis of target genes, mRNAs, or foreign proteins (Xin et al., 2017; Ferrari et al., 2021; Hu et al., 2021; Wang et al., 2021; Paunovska et al., 2022). The most studied cancers include those of the liver, pancreas, breast, lung, colorectal, and prostate (Chen et al., 2019; Haffner et al., 2021; Khan et al., 2021; Yu et al., 2021; Hong and Xu, 2022). miR-34a causes cell cycle arrest, promotes cell senescence, and induces cell apoptosis and performs a function that prevents cell migration. In the occurrence and progression of tumors, the reason for tumor resistance to chemotherapeutic agents, which exert anti-tumor effects through p53, is that miR-34a is deactivated by the methylation of CpG islands (Kim and Kim, 2014; Qian et al., 2014). Studies indicate that the ectopic augmentation of miR-34a inhibits glioma cell proliferation and promotes G1/S phase cell cycle arrest. The success of cancer gene therapy depends not only on sound molecular strategies, including the construction of a factual genetic material specifically expressed in tumor cells, but also on a safe, highly effective, and controlled vector preparation (Raguram et al., 2022).

Viral vectors were the first vectors proposed for gene therapy. The properties and characteristics of viruses make them ideal vectors for delivering RNA and DNA to human cells, and a number of clinical trials have been carried out, resulting in the approval of some gene therapy drugs (Lundstrom, 2018). However, immunogenicity, limited genetic loads, cancer due to the insertion of a therapeutic payload near a gene that controls cell growth, and the risk of viral vector mass production have promoted the development and engineering of non-viral vectors supported by nanomedicine and facilitated the development and engineering of nanomedicine-supported non-viral vectors (Kaiser, 2020). Nowadays, several cationic polymers are being developed, due to their facile synthesis, low host immunogenicity, and perfect transfection performance, such as polyethylenimine (PEI) for gene delivery (Kim and Kim, 2014; Yamano et al., 2014), methacrylate-based cationic copolymer (Li et al., 2015), and poly (L-lysine) (Wang, 2009). For non-viral gene transfer, a 25 kDa branched PEI is the golden standard. However, its long-term toxicity and low biocompatibility due to excessive positive charge have become the key limitations to its clinical application.

Baicalin (BA), which can efficaciously inhibit cancer cell proliferation and induce its apoptosis, is the main component of *Scutellaria baicalensis* (SB) (Shou et al., 2017; Duan et al., 2019; Han et al., 2021). It was found that baicalin could activate SIRT1/AMPK signaling in A549 and H1299 cells, inhibiting their proliferation and migration. Moreover, baicalin, inducing cell cycle arrest and promoting cell apoptosis, chiefly exerts its anti-tumor activity in an Akt-dependent manner. Baicalin, as an effective component of traditional Chinese medicine Scutellaria, can be used as an effective anti-cancer drug. However, its effective components are delivered to the cells for further study. In this work, a BA-decorated PEI was synthesized to achieve positive charge density equilibrium. Then, miR-34a was selected as the therapeutic gene and BA-PEI was used as a carrier. In this system, miR-34a also cooperates with baicalin to exert an anti-tumor effect and enhance the curative effect. Moreover, baicalin can effectively bond with PEI to form a new complex, BA-PEI. The miR-34a genetic drug was integrally appraised by the inhibition of tumor proliferation and migration using A549 and tumor-bearing mice as models.

2 Methods

2.1 Hemolysis assay with the blood sample

In brief, the blood sample was collected in EDTA tubes to avoid clotting, and RBCs were extracted by centrifuging the blood at 1,500 rpm for 10 min. We removed the supernatant and re-suspend the erythrocytes in PBS to a density of 5.0 × 109 cells/mL. The suspension (100 μL) was incubated with a nanoparticle solution (900 μL) at 37°C for 30 min and centrifuged at 1,500 rpm for 10 min to obtain the supernatant. The absorbance of hemoglobin release was measured using the Varioskan™ LUX microplate reader (Thermo, United States) at 578 nm. Hemolysis was carried out based on the following formula:

$$Hemolysis\ (\%) = \frac{Sample\ OD578 - NC\ OD578}{PC\ OD578 - NC\ OD578} \times 100\%.$$

2.2 Cell apoptosis analysis

The cells were seeded and transfected as previously mentioned; then, Annexin V-FITC and PI were used to stain the treated cells, adhering to the instructions. The effect of apoptosis was evaluated by flow cytometry using a Canto II (BD, CA).

2.3 Cell colony experiment

Similarly, the cells were planted and transfected, as mentioned previously. 1 × 103 cells that had been cultured for approximately 7 days were redigested. The colonies were washed with 1 × PBS, fixed with cold 70% methanol, and stained with 0.5% crystal violet. Finally, we washed them twice with PBS and observed them using a fluorescence microscope, IX73 (OLYMPUS, Japan).

2.4 Wound healing assays

The A549 cells were seeded as described previously. Untreated cells were straightly scratched in the middle using a yellow pipette tip. Then, different nanoparticles were transferred and incubated in the corresponding wells. The FBS-free 1640 medium was utilized for 6 h and replaced by a complete 1640 medium. Meanwhile, the stationary view of the wound was measured by width and photographed via a microscope, IX73 (OLYMPUS, Japan).

2.5 Western blot assay

We planted and transfected the A549 cells, as previously mentioned. RIPA lysed the harvested cells to gather the total protein, and the protein concentration was measured using a BCA protein detection kit. The identical proteins were assayed using SDS-PAGE and transferred to the PVDF membrane in the running buffer and the transferring buffer, respectively. The membrane was treated with a 5% non-fat milk solution for 1 h to block background proteins at room temperature. The membrane

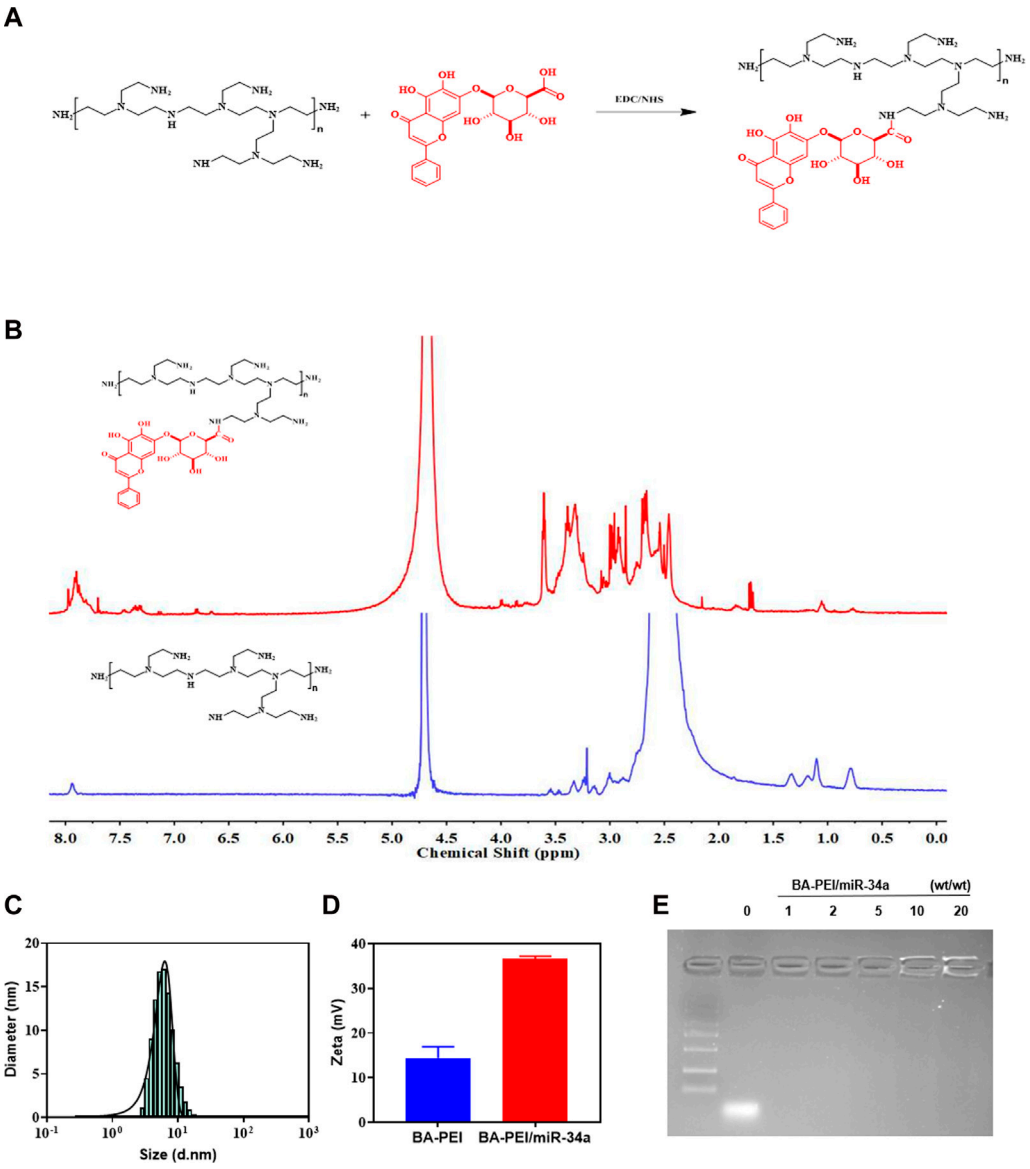

FIGURE 1
Synthesis of BA-PEI/miR-34a nanoparticles. **(A)** Synthetic route of BA-PEI. **(B)** ^{1}H NMR spectra of BA-PEI and PEI. **(C)** Hydrodynamic diameter of BA-PEI/miR-34a complexes. **(D)** Particle size and zeta potential of BA-PEI/miR-34a complexes. **(E)** Gel electrophoresis for BA-PEI/miR-34a at mass ratios of 0, 1, 2, 5, 10, and 20.

was incubated with primary antibodies at 4°C overnight and HRP-conjugated secondary antibodies at room temperature for 1 h, successively. The membrane was observed using the Tanon 4800 (Shanghai, China) using an ECL reagent and analyzed using ImageJ.

2.6 Establishment of the tumor-bearing model

The subcutaneous xenograft tumor-bearing model was established by BALB/c nude mice, which were acquired from Vital River Laboratory Animal Technology Co., Ltd. (Beijing, China). Furthermore, A549 cells were subcutaneously injected into the right side of the mice at a concentration of 1.0×10^{7} cells/mouse. The tumor volume was measured as length × (width) 2/2 and recorded along with the mice's body weight during the period. When the tumor volumes reached 50 mm^{3}, a different nanoparticle was injected into the tail vein every 3 days at a concentration of 0.5 mg/kg body weight.

2.7 Statistical analysis

All data were expressed as mean ± standard deviation, and unidirectional analysis of variance with GraphPad Prism 6 and *t*-tests were used to statistically test the differences between different experimental groups and control groups (ns, no significant; $^{*}p < 0.05$; $^{**}p < 0.01$).

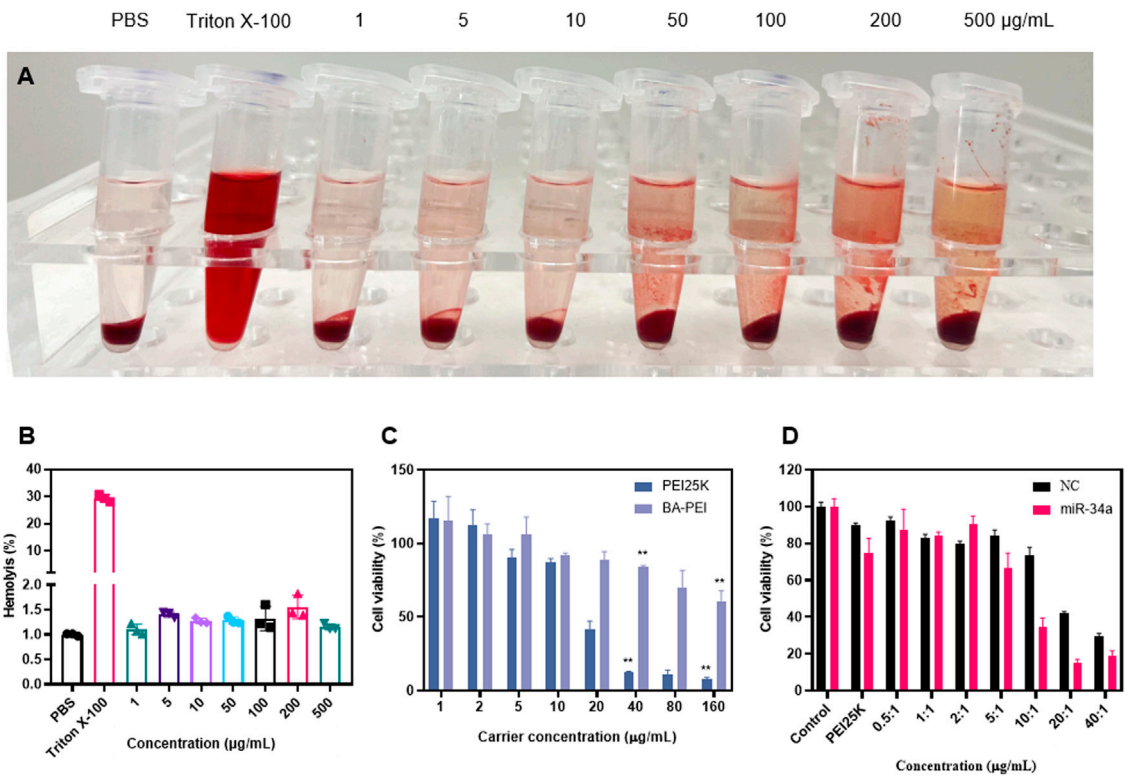

FIGURE 2
In vitro cytotoxicity of BA-PEI and BA-PEI/miR-34a. **(A)** Visual hemolysis assay and **(B)** quantitative hemolysis analysis for several BA-PEI concentrations and Triton X-100-treated mouse erythrocytes. **(C)** Cell viability (%) was conducted by CCK-8 assay for treated A549 cells by different BA-PEI concentrations and PEI. **(D)** Cell viability (%) was conducted by CCK-8 assay for treated A549 cells; the concentration of PEI is approximately 1.33 μg/mL. The concentrations are consistent with the mass ratio of carrier/miR-34a treated in A549 cells; *p <0.05; **p <0.01; ns, not significant.

3 Results and discussion

3.1 Synthesis and characterization of BA-PEI/miR-34a nanoparticles

BA-PEI was synthesized via a condensation reaction. For the sake of cutting down the PEI25K's cytotoxicity, we introduced the hydrophobic compound baicalin, which further enhances the cellular ingestion of PEI/miR-34a. In ^{1}H NMR, shown in Figure 1B, we can observe the generation of new peaks, indicating that BA has been successfully grafted onto PEI. Under the TEM, we distinctly caught sight of the BA-PEI/miR-34a genetic drug, which had a spherical morphology (Supplementary Figure S1) with a properly smaller particle size compared to BA-PEI measured by dynamic light scattering (DLS; Figure 1C). Furthermore, BA-PEI/miR-34a complexes were formed by electrostatic and hydrophobic interactions, which were characterized through an agarose gel retardation assay. This showed that BA-PEI and miR-34a could form consistently at a mass ratio of 5 (Figure 1E).

3.2 *In vitro* cytotoxicity of BA-PEI

In order to verify the safety of the material *in vivo*, a hemolysis experiment was used in the biological body, and the results showed that there was no hemolysis phenomenon and it could be safely injected into the tail vein (Figures 2A,B). In CCK-8, when BA-PEI ≤40 μg/mL, there was negligible cytotoxicity to A549 cells (Figure 2C). Compared with PEI25K, the carrier BA-PEI survival rate was higher with good biocompatibility. In order to better observe the transfection efficiency, miR-34a labeled with 5-carboxyfluorescein (FAM) was used for transfection with PEI25K as the control. We found that when the mass ratio is 10, the highest transfection efficiency of BA-PEI is achieved (Figure 2D and Supplementary Figure S2). In addition, in the experiment of living and dead cells, the activity of lipase in cells was detected by calcein-AM, and the living cells were stained with green fluorescence. PI (propyl iodide) detects the integrity of cell membranes and stains dead cells, showing red fluorescence. As shown in Supplementary Figure S3, the staining results showed that compared with PEI25K/miR-34a and the empty carrier BA-PEI, more dead cells were observed in the BA-PEI/miR-34a complex.

3.3 Anti-proliferation effect of BA-PEI/miR-34a nanoparticles

In order to clarify the anti-proliferation effect of BA-PEI/miR-34a nanoparticles, we conducted a cell colony experiment, as shown in Figures 3A,D. Compared with PEI25K/miR-34a and the empty carrier BA-PEI, the BA-PEI/miR-34a complex significantly inhibited the formation of cell colonies. In conclusion, due to the inhibitory

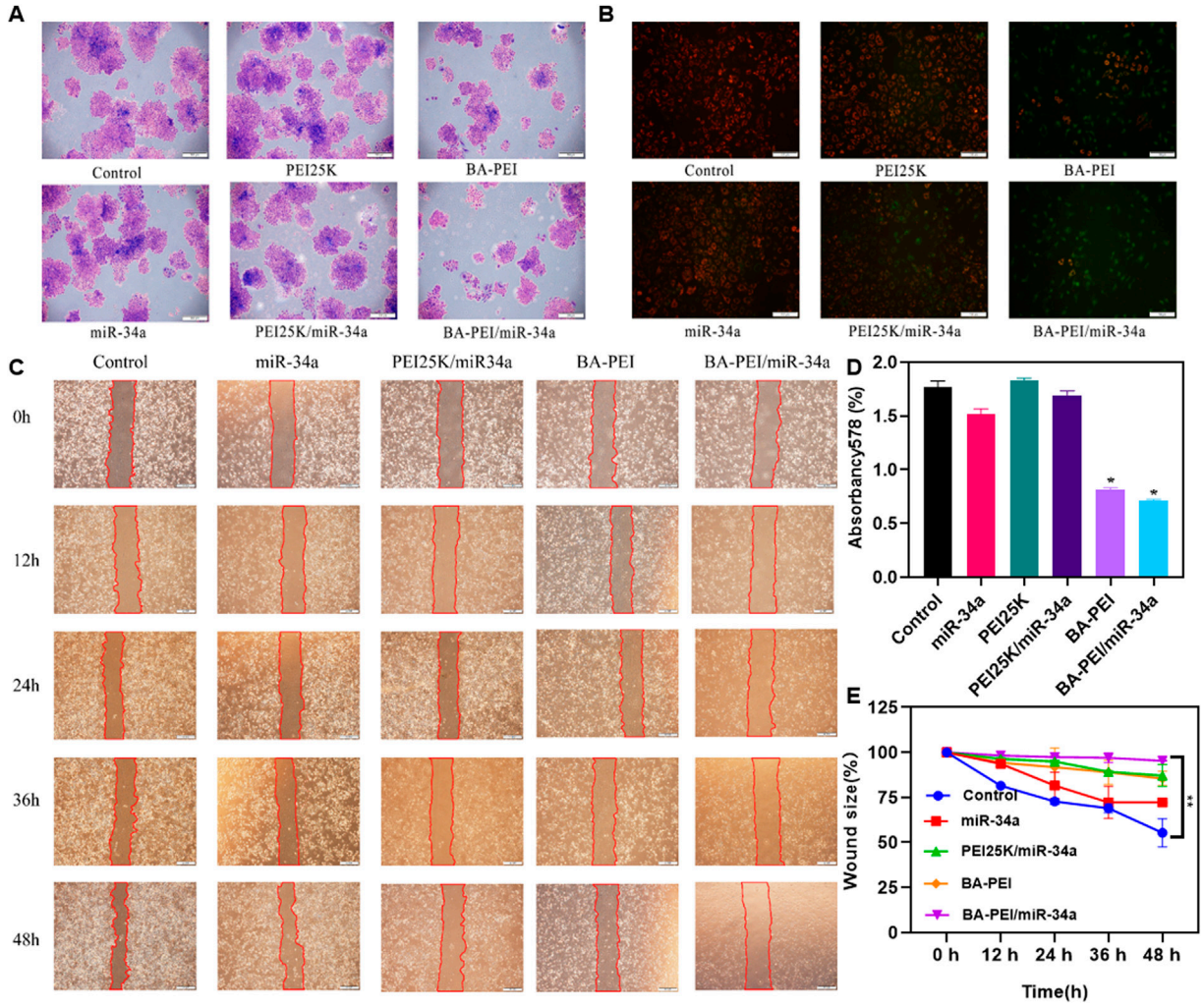

FIGURE 3
Anti-proliferation effect of BA-PEI/miR-34a nanoparticles. **(A)** One week of cell cloning results of A549 pre-treated with PEI, BA-PEI, miR-34a, PEI/miR-34a, and BA-PEI/miR-34a for 48 h. **(B)** JC-1 of A549 cells after treating with PEI, BA-PEI, miR-34a, PEI/miR-34a, and BA-PEI/miR-34a for 48 h. **(C)** Wound healing assay and **(D)** Quantitative analysis of A. **(E)** quantitative wound size in A549 cells transfected by carrier/miR-34a complexes at 0, 12, 24, 36, and 48 h. The data are shown as mean values ±SEM. *p <0.05; **p <0.01; ns, not significant. Scale bar = 200 μm.

effect of miR-34a on tumor cells, BA-PEI-mediated miR-34a transfection has a more effective inhibitory effect on the proliferation of tumor cells. The membrane-permeable JC-1 dye is crucial to monitoring mitochondrial health. In comparison with the control or BA-PEI-treated cells, BA-PEI/miR-34a can effectively achieve anti-tumor effects by inducing mitochondrial damage (Figure 3B). Meanwhile, we used a scratch test to observe the growth of tumor cells after BA-PEI/miR-34a intervention, and we found that the fusion speed of cells in the group of BA-PEI/miR-34a was significantly slower than that in the normal group, showing that BA-PEI/miR-34a could restrain A549 migration (Figures 3C,E).

3.4 BA-PEI/miR-34a induced apoptosis of tumor cell A549

In order to further investigate the tumor-killing effect of BA-PEI/miR-34a, we conducted the following research. Annexin V-FITC/PI staining, evaluated by flow cytometry, detected the apoptosis rate induced by BA-PEI/miR-34a. As shown in Figure 4A, the apoptosis rates of the empty vector BA-PEI and PEI25K/miR-34a were close to, but lower than that of BA-PEI/miR-34a, manifesting that both miR-34a and baicalin could effectively promote apoptosis and that baicalin and miR-34a acted on tumor cells together, showing the greatest advantage of their synergistic effect. Therefore, we detected the expression variation of proteins to further elucidate the apoptosis-induced pathway by BA-PEI/miR-34a. BA-PEI/miR-34a can significantly reduce the expression of pro-caspase-3 and accelerate the transformation of pro-caspase-3 to caspase-3, which has been considered to be a crucial medium in the caspase family-related apoptotic cascade (Yang et al., 2012). In addition, the alteration of pro-caspase-8 and pro-caspase-9 were decreased after BA-PEI/miR-34a transfection, indicating that caspase-8 and caspase-9 were activated by the cleavage of their precursors. Fundamentally, it has been established that caspase-8 is activated based on death receptor-dependent pathways and

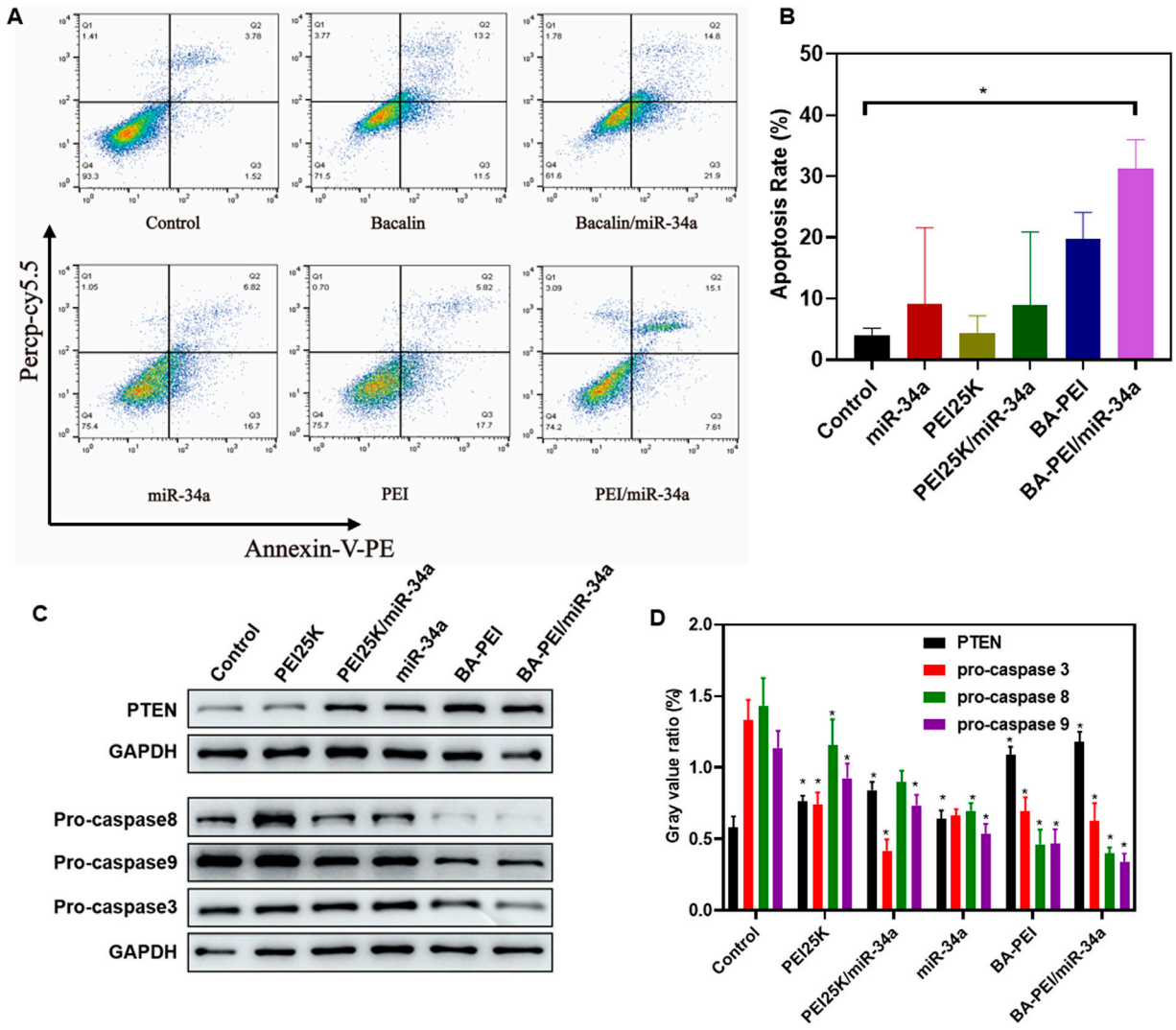

FIGURE 4
BA-PEI/miR-34a induced apoptosis of tumor cell A549. **(A)** Cell apoptosis analysis using flow cytometry, based on the control, miR-34a, PEI, BAPEI, PEI/miR-34a, and BA-PEI/miR-34a. **(B)** Quantitative analysis of A. **(C)** Western blots used to analyze the apoptotic protein (pro-caspase-3, -8, and -9 and PTEN), based on the control, miR-34a, PEI, BA-PEI, PEI/miR-34a, and BA-PEI/miR-34a. **(D)** Quantitative analysis of C. *p <0.05; **p <0.01; ns, not significant.

caspase-9 through mitochondrial pathways (Wang et al., 2018; Dong et al., 2019). Therefore, we conclude that BA-PEI/miR-34a may cure cancer through death receptor-dependent pathways and mitochondrial pathways and PTEN signaling pathways, which are well-studied tumor inhibition pathways (Jiang and Liu, 2009). PTEN signal transduction inhibits the origin and development of tumors through a variety of mechanisms, including promoting the death of cancer cells and inhibiting cancer cell propagation, migration, and invasion. The consequence was determined by Western blotting. In comparison with the control group, the cells treated with BA-PEI/miR-34a significantly improved the expression of PTEN, indicating that the upregulation of PTEN could inhibit the transfer of cancer cells. It was further confirmed that BA-PEI/miR-34a could regulate tumor suppressor genes to induce cell apoptosis.

3.5 *In vivo* anti-tumor efficacy of BA-PEI/miR-34a nanoparticles

In order to assess the inhibitory efficacy of BA-PEI/miR-34a complexes, we intravenously administered A549 cells in subcutaneous xenograft nude mice. The established subcutaneous xenograft model is demonstrated in Figure 5A. Moreover, the control group showed rapid tumor growth. When the average tumor volume in the control treated group reached 500 mm^3, all the mice were euthanized and photographed. As shown in Figures 5C,D, compared with the miR-34a group, mice treated with PEI/miR-34a and BA-PEI/miR-34a exhibited reduced tumor volumes, due to the accumulation of BA-PEI/miR-34a in the cancer regions. Additionally, to further assess the bio-toxicity of the complexes, the organs were harvested and stained with H&E after the treated mice were euthanized. The kidneys, lungs, spleens,

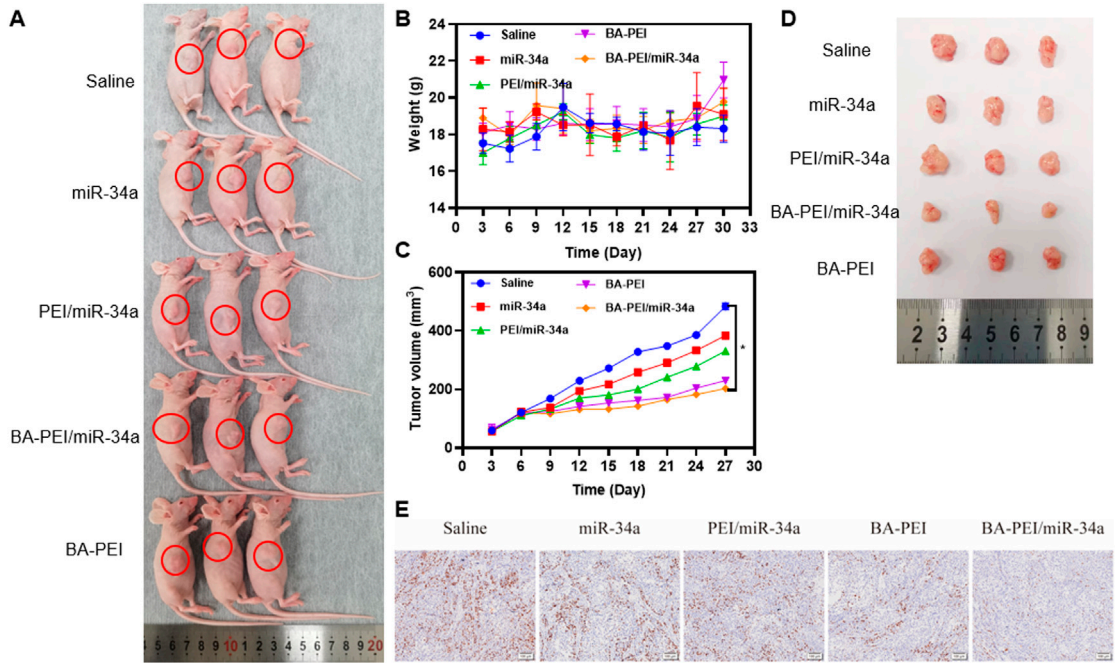

FIGURE 5
In vivo cytotoxicity of BA-PEI/miR-34a. **(A)** Subcutaneous A549 tumor-bearing mice model intravenously administrated with nanoparticles containing miR-34a. **(B)** Body weight of mice during the therapy. **(C), (D)** Tumor volume profiles administrated with saline miR-34a, PEI/miR-34a, BA-PEI/miR-34a, and BA-PEI, with a dose of 0.5 mg/kg every 3 days (n = 5). **(E)** Characteristic immunohistochemistry staining of Ki-67 of tumor organs from different complexes treating nude mice after their euthanization. *p <0.05; **p <0.01; ns, not significant. The scale bar is 100 μm.

hearts, and livers were stained with H&E. Also, there were no evident pathological alterations in any of the treated groups (Supplementary 2). Furthermore, we measured the body weight of the treated mice every 3 days, but no notable significance was observed in the different tumor-bearing mice (Figure 5B) because no system damage occurred after the intravenous injection of the carriers. These results certified that carrier-mediated transfection had relatively low bio-toxicity for the organs of nude mice, representing an attractive utilization of BA-PEI for clinical use. Furthermore, we performed Ki-67 IHC staining on the tumor sections to illustrate the anti-tumor response of different nanoparticles containing miR-34a. The naked miR-34a group showed an intact structure and dense cell arrangement, and the high positive and positive staining of Ki-67 in the tumor nuclei was observed (Figure 5D), indicating rapid tumor growth *in vivo*.

4 Conclusion

In conclusion, baicalin-modified PEI25K successfully constructed a traditional Chinese medicine composite BA-PEI vector to deliver miR-34a and achieve a synergic anti-tumor effect. Compared to PEI25K, BA-PEI showed a relatively high capacity for taking miR-34a into the cells and a low toxicity to them. Due to the triumphant expression of miR-34a in cells and animals and the cooperation with baicalin, BA-PEI/miR-34a significantly restrains their proliferation and migration, achieving the purpose of cancer therapy by inducing apoptosis and stalling the cell cycle in the S phase. Therefore, baicalin-modified PEI25K may be an efficient gene carrier for the therapy of cancer and other malignant diseases.

Data availability statement

The original contributions presented in the study are included in the article/Supplementary Material; further inquiries can be directed to the corresponding authors.

Ethics statement

The animal study was approved by the Institutional Ethics Review Committee of Zhengzhou University. The study was conducted in accordance with the local legislation and institutional requirements.

Author contributions

YW: conceptualization, data curation, formal analysis, software, supervision, and writing–original draft. BW: conceptualization, data curation, resources, supervision, and writing–original draft. YX: data curation, methodology, and writing–original draft. QC: data curation, supervision, and writing–original draft. JX: formal analysis, investigation, and writing–original draft. HT: data curation, funding acquisition, investigation, and writing–original draft. RL: conceptualization, funding acquisition, methodology, resources, supervision, visualization, writing–original draft, and writing–review and editing. HZ: data curation, methodology, writing–original draft, and writing–review and editing.

Funding

The authors declare that financial support was received for the research, authorship, and/or publication of this article. This work was supported by the special research project of TCM in Henan Province (2019ZY 2007) and the Henan Science and Technology Department (Project Number 221111310800).

Conflict of interest

The authors declare that the research was conducted in the absence of any commercial or financial relationships that could be construed as a potential conflict of interest.

Publisher's note

All claims expressed in this article are solely those of the authors and do not necessarily represent those of their affiliated organizations, or those of the publisher, the editors, and the reviewers. Any product that may be evaluated in this article, or claim that may be made by its manufacturer, is not guaranteed or endorsed by the publisher.

Supplementary material

The Supplementary Material for this article can be found online at: https://www.frontiersin.org/articles/10.3389/fbioe.2023.1290413/full#supplementary-material

References

Chen, J., Gingold, J. A., and Su, X. (2019). Immunomodulatory TGF-β signaling in hepatocellular carcinoma. *Trends Mol. Med.* 25 (11), 1010–1023. doi:10.1016/j.molmed.2019.06.007

Dong, M., Chen, J., Zhang, J., Liang, X., and Yang, J. (2019). A chemoenzymatically synthesized cholesterol-g-poly(amine-co-ester)-mediated p53 gene delivery for achieving antitumor efficacy in prostate cancer . *Int. J. Nanomedicine* 14, 1149–1161. doi:10.2147/ijn.s191905

Duan, X., Guo, G., Pei, X., Wang, X., Li, L., Xiong, Y., et al. (2019). Baicalin inhibits cell viability, migration and invasion in breast cancer by regulating miR-338-3p and MORC4 . *Onco Targets Ther.* 12, 11183–11193. doi:10.2147/ott.s217101

Ferrari, G., Thrasher, A. J., and Aiuti, A. (2021). Gene therapy using haematopoietic stem and progenitor cells. *Nat. Rev. Genet.* 22 (4), 216–234. doi:10.1038/s41576-020-00298-5

Haffner, M. C., Zwart, W., Roudier, M. P., True, L. D., Nelson, W. G., Epstein, J. I., et al. (2021). Genomic and phenotypic heterogeneity in prostate cancer. *Nat. Rev. Urol.* 18 (2), 79–92. doi:10.1038/s41585-020-00400-w

Han, S., Wang, W., Wang, S., Yang, T., Zhang, G., Wang, D., et al. (2021). Tumor microenvironment remodeling and tumor therapy based on M2-like tumor associated macrophage-targeting nano-complexes. *Theranostics* 11 (6), 2892–2916. doi:10.7150/thno.50928

Hong, R., and Xu, B. (2022). Breast cancer: an up-to-date review and future perspectives. *Cancer Commun. (Lond)* 42 (10), 913–936. doi:10.1002/cac2.12358

Hu, J., Cao, J., Topatana, W., Juengpanich, S., Li, S., Zhang, B., et al. (2021). Targeting mutant p53 for cancer therapy: direct and indirect strategies. *J. Hematol. Oncol.* 14 (1), 157. doi:10.1186/s13045-021-01169-0

IARC (2020). Today cancer[EB/OL]. Avaliable at: https://gco.iarc.fr/today/home.

Jiang, B. H., and Liu, L. Z. (2009). PI3K/PTEN signaling in angiogenesis and tumorigenesis. *Adv. Cancer Res.* 102, 19–65. doi:10.1016/S0065-230X(09)02002-8

Kaiser, J. (2020). How safe is a popular gene therapy vector? *Science* 367 (6474), 131. doi:10.1126/science.367.6474.131

Khan, P., Siddiqui, J. A., Lakshmanan, I., Ganti, A. K., Salgia, R., Jain, M., et al. (2021). RNA-based therapies: a cog in the wheel of lung cancer defense. *Mol. Cancer* 20 (1), 54. doi:10.1186/s12943-021-01338-2

Kim, H., and Kim, W. J. (2014). Photothermally controlled gene delivery by reduced graphene oxide–polyethylenimine nanocomposite. *Small* 10 (1), 117–126. doi:10.1002/smll.201202636

Li, Y., Xu, B., Bai, T., and Liu, W. (2015). Co-delivery of doxorubicin and tumor-suppressing p53 gene using a POSS-based star-shaped polymer for cancer therapy. *Biomaterials* 55, 12–23. doi:10.1016/j.biomaterials.2015.03.034

Lundstrom, K. (2018). Viral vectors in gene therapy. *Diseases* 6 (2), 42. doi:10.3390/diseases6020042

Paunovska, K., Loughrey, D., and Dahlman, J. E. (2022). Drug delivery systems for RNA therapeutics. *Nat. Rev. Genet.* 23 (5), 265–280. doi:10.1038/s41576-021-00439-4

Qian, X., Long, L., Shi, Z., Liu, C., Qiu, M., Sheng, J., et al. (2014). Star-branched amphiphilic PLA-b-PDMAEMA copolymers for co-delivery of miR-21 inhibitor and doxorubicin to treat glioma. *Biomaterials* 35 (7), 2322–2335. doi:10.1016/j.biomaterials.2013.11.039

Raguram, A., Banskota, S., and Liu, D. R. (2022). Therapeutic in vivo delivery of gene editing agents. *Cell.* 185 (15), 2806–2827. doi:10.1016/j.cell.2022.03.045

Shou, X., Wang, B., Zhou, R., Wang, L., Ren, A., Xin, S., et al. (2017). Baicalin suppresses hypoxia-reoxygenation-induced arterial endothelial cell apoptosis via suppressing pkcδ/p53 signaling. *Med. Sci. Monit.* 23, 6057–6063. doi:10.12659/msm.907989

Wang, S., Sun, F., Huang, H., Chen, K., Li, Q. J., Zhang, L., et al. (2021). The landscape of cell and gene therapies for solid tumors. *Cancer Cell.* 39 (1), 7–8. doi:10.1016/j.ccell.2020.12.005

Wang, X. (2009). Structure, mechanism and engineering of plant natural product glycosyltransferases. *FEBS Lett.* 583 (20), 3303–3309. doi:10.1016/j.febslet.2009.09.042

Wang, Y. S., Li, H., Li, Y., Zhu, H., and Jin, Y. H. (2018). Identification of natural compounds targeting Annexin A2 with an anti-cancer effect. *Protein Cell.* 9 (6), 568–579. doi:10.1007/s13238-018-0513-z

WHO (2023). cancer[EB/OL]. Avaliable at: https://www.who.int/health-topics/cancer#tab=tab_1.

Xin, Y., Huang, M., Guo, W. W., Huang, Q., Zhang, L. z., and Jiang, G. (2017). Nano-based delivery of RNAi in cancer therapy. *Mol. Cancer* 16 (1), 134. doi:10.1186/s12943-017-0683-y

Yamano, S., Dai, J., Hanatani, S., Haku, K., Yamanaka, T., Ishioka, M., et al. (2014). Long-term efficient gene delivery using polyethylenimine with modified Tat peptide. *Biomaterials* 35 (5), 1705–1715. doi:10.1016/j.biomaterials.2013.11.012

Yang, T. J., Haimovitz-Friedman, A., and Verheij, M. (2012). Anticancer therapy and apoptosis imaging. *Exp. Oncol.* 34 (3), 269–276.

Yu, J., Chai, P., Xie, M., Ge, S., Ruan, J., Fan, X., et al. (2021). Histone lactylation drives oncogenesis by facilitating m6A reader protein YTHDF2 expression in ocular melanoma. *Genome Biol.* 22 (1), 85. doi:10.1186/s13059-021-02308-z

frontiers | Frontiers in Bioengineering and Biotechnology

TYPE Original Research
PUBLISHED 16 January 2024
DOI 10.3389/fbioe.2024.1355004

OPEN ACCESS

EDITED BY
Qitong Huang,
Gannan Medical University, China

REVIEWED BY
Zhijin Fan,
Sun Yat-sen University, China
Ming Hu,
Nanjing Tech University, China

*CORRESPONDENCE
Zhijun Zhang,
zjzhang@zstu.edu.cn
Guixian Hu,
hugx_shiny@163.com

†These authors have contributed equally to this work

RECEIVED 13 December 2023
ACCEPTED 03 January 2024
PUBLISHED 16 January 2024

CITATION
Li X, Zhu W, Zhou Y, Wang N, Gao X, Sun S, Cao M, Zhang Z and Hu G (2024), Near-infrared light-heatable platinum nanozyme for synergistic bacterial inhibition.
Front. Bioeng. Biotechnol. 12:1355004.
doi: 10.3389/fbioe.2024.1355004

Near-infrared light-heatable platinum nanozyme for synergistic bacterial inhibition

Xue Li[1,2†], Weisheng Zhu[3†], Yuan Zhou[4,5], Nan Wang[3], Xiangfan Gao[3], Suling Sun[1], Mengting Cao[3], Zhijun Zhang[3,6*] and Guixian Hu[1*]

[1]Institute of Agro-product Safety and Nutrition, Zhejiang Academy of Agricultural Sciences, Hangzhou, China, [2]Key Laboratory of Information Traceability for Agricultural Products, Ministry of Agriculture and Rural Affairs of China, Hangzhou, Zhejiang, China, [3]Key Laboratory of Surface & Interface Science of Polymer Materials of Zhejiang Province, School of Chemistry and Chemical Engineering, Zhejiang Sci-Tech University, Hangzhou, China, [4]Department of Pharmacy, Taihe Hospital, Hubei University of Medicine, Shiyan, China, [5]College of Pharmacy, Hubei University of Traditional Chinese Medicine, Wuhan, China, [6]Shengzhou Innovation Research Institute of Zhejiang Sci-Tech University, Shengzhou, China

The development of non-antibiotic strategies for bacterial disinfection is of great clinical importance. Among recently developed different antimicrobial strategies, nanomaterial-mediated approaches, especially the photothermal way and reactive oxygen species (ROS)-generating method, show many significant advantages. Although promising, the clinical application of nanomaterials is still limited, owing to the potential biosafety issues. Further improvement of the antimicrobial activity to reduce the usage, and thus reduce the potential risk, is an important way to increase the clinical applicability of antibacterial nanomaterials. In this paper, an antimicrobial nanostructure with both an excellent photothermal effect and peroxidase-like activity was constructed to achieve efficient synergistic antimicrobial activity. The obtained nano-antimicrobial agent (ZIF-8@PDA@Pt) can not only efficiently catalyze the production of ROS from H_2O_2 to cause damage to bacteria but also convert the photon energy of near-infrared light into thermal energy to kill bacteria, and the two synergistic effects induced in a highly efficient antimicrobial activity. This study not only offers a new nanomaterial with efficient antibacterial activity but also proposes a new idea for constructing synergistic antibacterial properties.

KEYWORDS

nanozyme, metal–organic framework, photothermal effect, reactive oxygen species, bacterial inhibition

1 Introduction

Bacterial infection is a serious threat to global health, which is estimated to be the second leading cause of death worldwide, accounting for one in eight of all deaths in 2019 (Ikuta et al., 2022). Antibiotics, also known as antimicrobials, are the most commonly used treatment for bacterial infections. Antibiotics are a class of secondary metabolites with antipathogenic or other activities produced by microorganisms or higher plants and animals, which have shown high activity against bacterial infections. However, bacteria develop resistance to antibiotics over time, and the problem of bacterial resistance is growing due to the misuse of antibiotics. It is estimated that more than 1.2 million people—and potentially millions more—died globally a year as a direct result of antibiotic-

resistant bacterial infections, according to the most comprehensive estimate, to date, of the AMR) (Murray et al., 2022). Unfortunately, the rate of development of new antibiotics is much slower than the rate of emergence of bacterial resistance. In addition, the use of antibiotics for anti-infective therapy is prone to side effects such as liver damage and kidney injury. Thus, the development of novel antimicrobial strategies to reduce the use of antibiotics is of great clinical importance.

Many different new antimicrobial strategies have been reported in recent years (Sun et al., 2020; Niu et al., 2021a; Niu et al., 2021b; Du et al., 2021; Zhang et al., 2021; Li et al., 2022a; Li et al., 2022b; Fu et al., 2022; Guo et al., 2022; Wang et al., 2023; Wu et al., 2023). Among them, nanomaterial-mediated antimicrobial strategies show more significant advantages, including easy material synthesis, being less susceptible to bacterial resistance, and a high bacterial killing efficiency. In these strategies, nanomaterials usually play the role of mediators of energy or material conversion. Typically, nanomaterials can convert the energy of external physical stimuli into thermal energy that can directly damage the bacterial structure (Liu et al., 2022a; Hu et al., 2022). The photothermal antimicrobial strategy is such an energy conversion-based bacterial disinfection method, which is favored for its high killing efficiency and spatial and temporal controllability (Han et al., 2020). The photothermal effect is a property of materials that can harvest and transfer the photon energy from irradiated light to heat energy, which is promising for wide applications (Wang et al., 2019; Wu and Yeow, 2022; Zeng et al., 2022; Fan et al., 2023; Huang et al., 2023; Jiao et al., 2023; Yue et al., 2023; Zhao et al., 2023; Zhu et al., 2023). In the photothermal antimicrobial strategy, nanomaterials with photothermal conversion efficiency, such as graphene, Fe_3O_4, polydopamine (PDA), and gold nanostructures, can efficiently convert the photon energy of near-infrared light into thermal energy to achieve efficient killing of different types of bacteria (Niu et al., 2018; Wang et al., 2022). In addition, nanomaterials with enzyme-like activity can convert endogenous or exogenous chemicals into high-energy reactive oxygen species (ROS) to cause bacterial casualties (Chen et al., 2018; Liu et al., 2022b; Dorma Momo et al., 2022). For example, nanoenzymes such as graphene oxide and carbon dots can catalyze the production of ROS from highly expressed or exogenous H_2O_2 at the site of bacterial infection to cause the destruction of bacterial nucleic acids and proteins and thus lead to bacterial death. Nanomaterial-mediated antimicrobial strategies undoubtedly offer unlimited possibilities for replacing the use of antibiotics (Makabenta et al., 2021; Xie et al., 2023). Nevertheless, the clinical application of nanomaterials is still very limited at present as the biosafety issues of their clinical application are yet to be fully evaluated. Further improvement of antimicrobial activity to reduce the usage, and thus reduce the potential risk, is an important way to increase the clinical applicability of antibacterial nanomaterials.

In this paper, an antimicrobial nanostructure with both the photothermal effect and peroxidase-like activity was constructed to combine the photothermal antimicrobial and free radical antimicrobial strategies to achieve efficient synergistic antimicrobial activity (Scheme 1). ZIF-8, a frequently used metal–organic framework (MOF) in biomedical research, was chosen as the nanocarrier. A PDA layer with an excellent photothermal effect was encapsulated on the surface of ZIF-8 by *in situ* polymerization, and then, platinum nanoparticles (PtNPs) with peroxidase-like activity were allowed to grow on the PDA layer. The obtained nano-antimicrobial agent (ZIF-8@PDA@Pt) can not only efficiently catalyze the production of ROS from H_2O_2 to cause damage to bacteria but also convert photon energy of the near-infrared light into thermal energy to kill bacteria, and the two synergistic effects induced in a highly efficient antimicrobial activity.

2 Materials and methods

2.1 Synthesis of ZIF-8@PDA@Pt

ZIF-8 was synthesized through a specific coordination reaction between zinc ions and 2-methylimidazole. In a typical experiment, 1.069 g $Zn(NO_3)_2{\cdot}6H_2O$ was dissolved in 15 mL of DMF-MeOH mixture (v/v = 4:1) as solution **1**, 1.161 g of 2-methylimidazole was dissolved in 10 mL of DMF-MeOH (v/v = 4:1) as solution **2**; then, solution **1** was added to solution **2** and kept stirring vigorously overnight. Subsequently, the milky product was collected by centrifugation at 14,000 rpm for 10 min, rinsed with methanol and ultrapure water two times, and then dried at 80°C overnight to obtain ZIF-8 for subsequent experiments.

ZIF-8@PDA was attained by a self-polymerization reaction of dopamine. A measure of 20 mg ZIF-8 we prepared was dissolved in the Tris-HCl buffer solution (pH 8.5, 50 mM) with the assistance of sonicating for 2 min; then, 10 mg dopamine was added to the above solution, and the mixture was violently stirred for 90 min. Thereafter, the obtained black mixture was collected by centrifugation at 14,000 rpm for 10 min, washed with water three times, and eventually concentrated to 2 mL for later use.

Subsequently, ZIF-8@PDA@Pt was gained by an *in situ* reduction method using ZIF-8@PDA as a precursor. A measure of 2 mL of ZIF-8@PDA we prepared previously was added to 7,740 μL ultrapure water and sonicated for 2 min; then, 260 μL of H_2PtCl_4 (19.2 mM) was added and sonicated for 5 min; in a rapid subsequence, 500 μL of the refresh $NaBH_4$ solution (1 M) was added to the above solution under drastic magnetic stirring for 1 h. Finally, the mixture was collected by centrifugation at 14,000 rpm for 10 min and ultimately washed with ultrapure water three times to obtain ZIF-8@PDA@Pt.

2.2 Measurement of peroxidase-mimic activity

The peroxidase-mimic activity of ZIF-8@PDA@Pt was measured by a classical chromogenic reaction using TMB as the substrate. In brief, 5 μL TMB (80 mM), 50 mL H_2O_2 (10 mM), and 50 μL ZIF-8@PDA@Pt (0.2 mg mL^{-1}) were added to the phosphate buffer solution (pH 5.0, 20 mM) with a total volume of 0.5 mL, respectively. Subsequently, the mixture was incubated for 5 min, and the absorbance at 652 nm was recorded simultaneously by an ultraviolet-visible spectrum. o-Phenylenediamine (OPD) was employed as a chromogenic substrate to further evaluate the peroxidase-mimic activity of ZIF-8@PDA@Pt. Typically, 5 μL OPD (50 mM), 50 mL H_2O_2 (10 mM), and 50 μL ZIF-8@PDA@

Pt (0.2 mg mL^{-1}) were added to the phosphate buffer solution (pH 5.0, 20 mM) with a total volume of 0.5 mL, respectively. Subsequently, the mixture was incubated for 5 min, and the absorbance at 425 nm was recorded simultaneously by an ultraviolet-visible spectrum.

2.3 Catalytic kinetic assay

The kinetic assay of the peroxidase-mimic activity of ZIF-8@PDA@Pt was conducted by changing the concentration of H_2O_2 or TMB. The reaction was performed under an optimized condition (pH 5.0, 37°C). Typically, 2 μL TMB (80 mM), H_2O_2 with different concentrations, and 20 μL ZIF-8@PDA@Pt (0.2 mg mL^{-1}) were added to a phosphate buffer solution (pH 5.0, 20 mM) with a total volume of 0.2 mL; then, the absorbance at 652 nm was recorded in time at a time scanning window. The real-time velocity of the reaction was converted by the Beer–Lambert Law, A = εbC, where b is the path length (1 cm) and ε is the molar absorption coefficient of oxidized TMB (39,000 M^{-1} cm^{-1}). Corresponding parameters of kinetics were calculated according to the Michaelis–Menten equation and Lineweaver–Burk plot:

$$V_0 = V_{max}\frac{[S]}{[S] + K_m},$$

$$\frac{1}{V_0} = \frac{K_m}{V_{max}}\frac{1}{[S]} + \frac{1}{V_{max}},$$

where V_0 is the initial reaction rate and [S] is the concentration of the substrate (H_2O_2 or TMB).

2.4 Detection of ROS generation

Terephthalic acid (TA) was used as a fluorescent probe to validate the generation of •OH. Typically, TA (0.5 mM), H_2O_2 (2 mM), and ZIF-8@PDA@Pt (0.1 mg mL^{-1}) were first mixed into PBS (pH = 5.0, 20 mM) and incubated in dark for 2 h, and then were taken for fluorescent spectra characterization. In addition, 1,3-diphenylisobenzofuran (DPBF) and 9,10-anthracenediyl-bis(methylene)-dimalonic acid (ABDA) were used as probes to assay $O_2^{\bullet-}$ and $^1O_2$, respectively. Specifically, DPBF (1 mM), H_2O_2 (2 mM), and ZIF-8@PDA@Pt (0.1 mg mL^{-1}) were incubated together in PBS (pH = 5.0, 20 mM) for 5 min; meanwhile, the absorbance at 421 nm was recorded every 30 s. ABDA (0.05 mM), H_2O_2 (2 mM), and ZIF-8@PDA@Pt (0.1 mg mL^{-1}) were incubated together in PBS (pH = 5.0, 20 mM) for a while and then were taken to measure the change of absorbance using UV spectra.

2.5 Determination of the photothermal property

The photothermal property of ZIF-8@PDA@Pt was determined using an 808-nm laser, and the real-time temperature was observed with a thermal imaging camera. In brief, ZIF-8@PDA@Pt aqueous dispersion with different concentrations (0, 20, 40, 60, 80, 100, and 120 ug mL^{-1}) was radiated under 808 nm (1.0 W cm^{-1}) for 5 min. Concurrently, the temperature of the ZIF-8@PDA@Pt aqueous dispersion was recorded every 30 s. Thereafter, the heating–cooling curves were obtained to calculate the photothermal conversion efficiency in accordance with below equations:

$$\eta = \frac{hS\,(T_{max} - T_{surr}) - Q_0}{I\,(1 - 10^{-A_{808}})}, \quad (1)$$

$$\tau_s = \frac{m_d C_d}{hS}, \quad (2)$$

$$Q_0 = hS\,(T_{max,water} - T_{surr}), \quad (3)$$

where η is the photothermal conversion efficiency. The value of τ_s was obtained by linearly fitting the plot of the cooling time t versus the term -Lnθ, hS was obtained from Eq. 2, m_d is the mass of the solution (0.2 g), C_d is the heat capacity of water (4.2 J g^{-1}°C^{-1}), Q_0 was obtained from Eq. 3, T_{max} is the equilibrium temperature (61.5°C), $T_{max,\ water}$ is the maximum temperature of water (29.1°C), and T_{surr} is the surrounding ambient temperature (28.3°C). I is the incident light power (0.8 W cm^{-2}), and A_{808} is the absorbance of the ZIF-8@PDA@Pt aqueous dispersion (120 μg mL^{-1}) at 808 nm (0.17).

2.6 Antibacterial activity test

Staphylococcus aureus and *Escherichia coli* were selected as Gram-positive and Gram-negative model strains to estimate the antibacterial activity of ZIF-8@PDA@Pt, respectively. Mono colonies of *S. aureus* and *E. coli* on a solid agar plate were first transferred to 2 mL of the lysogeny broth (LB) medium and shaken at 37°C for 12 h at 150 rpm. Four different groups were set in this typical procedure, containing I: Control, II: H_2O_2, III: ZIF-8@PDA@Pt + H_2O_2, and IV ZIF-8@PDA@Pt + H_2O_2 + NIR. In addition, 0.3 was selected as the initial optical density of bacteria at $OD_{600\ nm}$. In addition, the final concentration of H_2O_2 and ZIF-8@PDA@Pt in the incubation system was 2 mM and 100 μg mL^{-1}, respectively. All groups were incubated at 37°C for 20 min. Thereafter, the bacterial suspensions were moved to the solid medium by the spread plate method and cultured at 37°C for another for 12 h. Finally, all experimental groups were taken for imaging and counting. Each assay was performed in triplicates.

2.7 Live/dead bacterial staining

Bacterial suspensions treated with the different experimental conditions were first centrifuged for 5 min (4,000 rpm), followed by washing two times using 0.85% NaCl solutions. Afterward, the above bacterial suspensions were stained with SYTO 9 and propidium iodide and then observed with a fluorescent microscope.

2.8 Cell viability assay

HSF cells were performed for the biocompatibility assay of ZIF-8@PDA@Pt. At first, the HSF cells were cultured in a 96-well plate (8,000 cells per well) at 37°C for 24 h; then, ZIF-8@PDA@Pt with

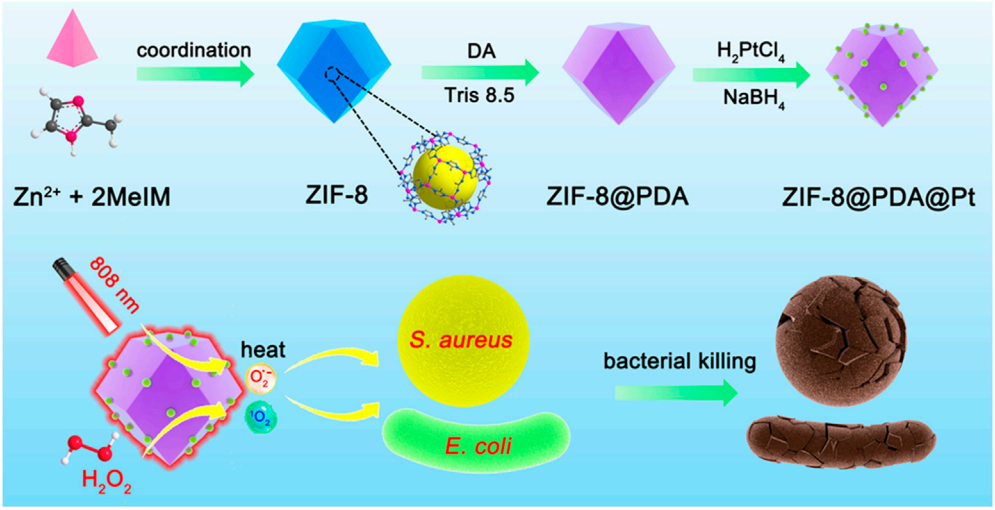

SCHEME 1
Schematic illustration of the synthesis of ZIF-8@PDA@Pt and the principle of bacterial killing.

different concentrations (0, 25, 50, 100, 150, and 200 μg mL^{-1}) were added to the above medium and incubated for another 24 h at 37°C. Thereafter, 10 μL of the MTT solution was added to every well. After 4 h, the medium was extracted and 150 μL of DMSO was added to every well. The cell viability was assayed using a microplate reader.

3 Results and discussion

3.1 Synthesis and characterization of ZIF-8@PDA@Pt

ZIF-8@PDA@Pt was prepared through *in situ* reduction of H_2PtCl_4 in the presence of a specific precursor obtained by modifying a layer of polydopamine on the surface of ZIF-8. To begin with, ZIF-8 was conducted by a specific coordination reaction between zinc ions and 2-methylimidazole. Afterward, a layer of PDA was modified on ZIF-8, relying on the self-polymerization reaction of dopamine under a weak alkaline environment to obtain ZIF@PDA. Eventually, Pt NPs were localized on ZIF@PDA by *in situ* reduction to obtain the nanozyme ZIF-8@PDA@Pt. TEM and SEM were primarily employed to characterize the morphology during the formation of ZIF-8@PDA@Pt (Figures 1A, B); it is clearly to be observed that ZIF-8 possesses the regular rhombic dodecahedral morphology while a thin layer at the edge of ZIF-8 was noticed after modifying polydopamine, verifying the formation of ZIF-8@PDA. In addition, it can be seen that ultra-small Pt NPs were distributed on ZIF-8@PDA. In addition, energy-dispersive X-ray spectrometry (EDX) mapping was recruited to characterize the elemental distribution of ZIF-8@PDA@Pt nanozyme (Figure 1C). The results presented the homogeneous distributions of elements C, N, O, Zn, and Pt in ZIF-8@PDA@Pt, demonstrating the successful loading of Pt NPs onto the ZIF-8@PDA platform. Meanwhile, ZIF-8@PDA@Pt exhibits a size of approximately 650 nm, according to the dynamic light scattering analysis (Figure 1D).

Additionally, in order to explore the chemical structure and composition, we executed X-ray diffraction (XRD), X-ray photoelectron spectroscopy (XPS), and UV-vis spectra. As illustrated in Figure 1E, the pattern of ZIF-8 exhibits several typical characteristic peaks at around 7.46°, 10.52°,12.87°, and 18.27°, ascribing to (001), (002), (112), and (222) crystal faces, respectively, which conforms its regular crystal structure. Of note, the main diffraction peaks of ZIF-8 remained after modifying PDA and loading Pt NPs. In particular, the XRD diffraction of ZIF-8@PDA@Pt presents an unmistakable peak at 39.5° in line with the (111) facet of the Pt crystal (JCPDS No. 04-0802), which further confirmed the successful preparation of ZIF-8@PDA@Pt. The UV-vis spectra were also measured and are presented in Figure 1F. It can be noted that two typical peaks at approximately 234 and 300 nm in ZIF-8 and ZIF-8@PDA assigned to the π-π^* transition of the conjugated system from the imidazole structure and n-π^* transition of polydopamine, respectively. Nonetheless, the peak at approximately 300 nm is not well-preserved in ZIF-8@PDA@Pt, which may be caused within the loading of Pt NPs. In addition, XPS was performed to characterize the element constitution of ZIF-8@PDA@Pt (Supplementary Figure S1). The element contents of C, N, O, Zn, and Pt are 53.08%, 9.55%, 25.03%, 10.72%, and 1.62%, respectively. More precisely, in the high-resolution spectrum of Pt 4f, the peaks located at 71.0, 72.2, 74.2, and 75.5 eV are ascribed to Pt^0 4f 7/2, Pt^{4+} 4f 7/2, Pt^0 4f 5/2, and Pt^{4+} 4f 5/2 binding energies, respectively, which are analogous to the majority of Pt NPs. Likewise, several typical peaks at approximately 284.5, 286.2, and 288.3 eV can be identified from the high-resolution C1s spectrum, which are assigned to C-C, C-N/C-O, and C=C groups, respectively. It can be observed that three peaks are located at 398.2, 399.3, and 400.7 eV from the N 1s spectrum, corresponding to pyridinic N, pyrrolic N, and graphitic N, respectively. Comparably, the curve-fitted O1s spectrum exhibits two peaks 531.3 and 533.1 eV, attributing to C-O and C-OH groups, respectively. In addition, the high-resolution Zn 2p spectra of ZIF-8@PDA@Pt present two peaks

10.3389/fbioe.2024.1355004

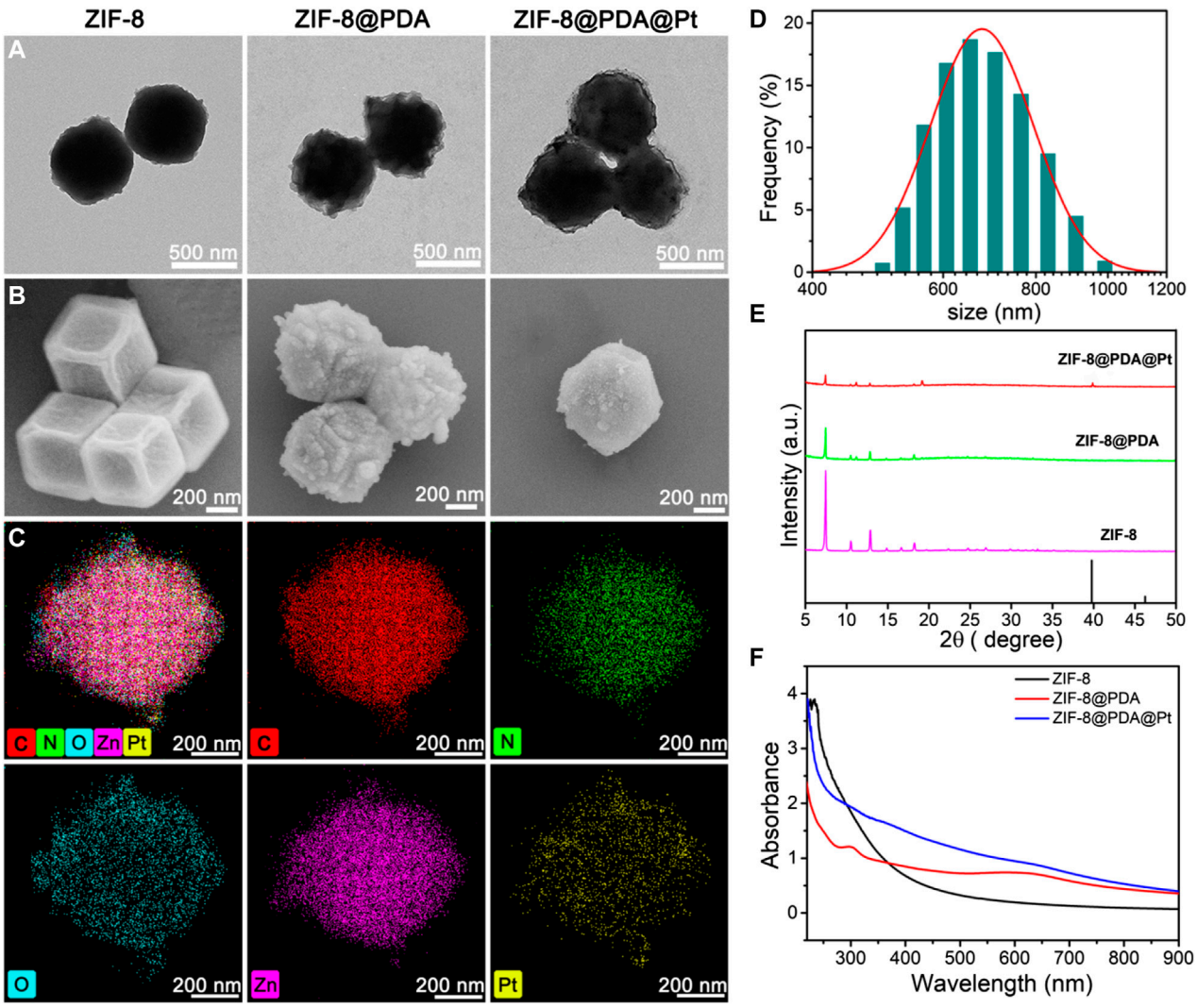

FIGURE 1
TEM **(A)** and SEM **(B)** images of the nanostructures, and the elemental mapping **(C)** and size distribution **(D)** of ZIF-8@PDA@Pt. XRD patterns **(E)** and UV-vis spectra **(F)** of these nanoparticles.

placed at 1022.3 and 1045.3 eV belonging to Zn 2p 1/2 and Zn 2p 2/3 of zinc oxide, respectively. In combination with the above results, it is believed that ZIF-8@PDA@Pt was successfully prepared.

3.2 Catalytic performance of ZIF-8@PDA@Pt

After successful synthesis of the ZIF-8@PDA@Pt nanoparticles, we then investigated its peroxidase (POD)-like activity using 3,3′,5,5′-tetramethylbenzidine (TMB) as the chromogenic substrate and H_2O_2 as the catalysis substrate. As shown in Figure 2A, without ZIF-8@PDA@Pt, H_2O_2 cannot cause any color change in the TMB solution. However, in the presence of ZIF-8@PDA@Pt and H_2O_2, the color of the TMB solution significantly changed to dark blue (Figures 2A–2iv), indicating the strong POD-like activity of ZIF-8@PDA@Pt. In this catalytic system, ZIF-8@PDA@Pt may catalyze H_2O_2 to produce ROS, which can oxidize TMB to generate blue color. Notably, without H_2O_2, the nanozyme ZIF-8@PDA@Pt can also cause an obvious change in the color of the TMB solution (Figures 2A–2iii), demonstrating that the nanozyme also possesses oxidase-like activity. The enzyme-like activity of ZIF-8@PDA@Pt was also demonstrated from the absorbance change of the TMB solution (Figure 2B). To further evaluate the enzymatic activities of the nanozyme ZIF-8@PDA@Pt, the catalytic dynamics was investigated. We carried out a steady-state kinetic study to obtain the rate constants by varying the concentration of TMB with a constant concentration of H_2O_2 or *vice versa*. The Michaelis constant (K_m) and maximum reaction rate (V_{max}) were calculated from the fitted Michaelis–Menten curves and Lineweaver–Burk double reciprocal plots (Figures 2C–F). As a comparison, the obtained K_m and V_{max} of ZIF-8@PDA@Pt and other catalysts including the natural enzyme HRP and Fe_3O_4 nanozymes are listed in Supplementary Table S1. K_m indicates the enzyme affinity toward substrates, and V_{max} defines the maximal catalytic capacity of an enzyme under specified conditions. Generally, a smaller K_m demonstrates higher affinity,

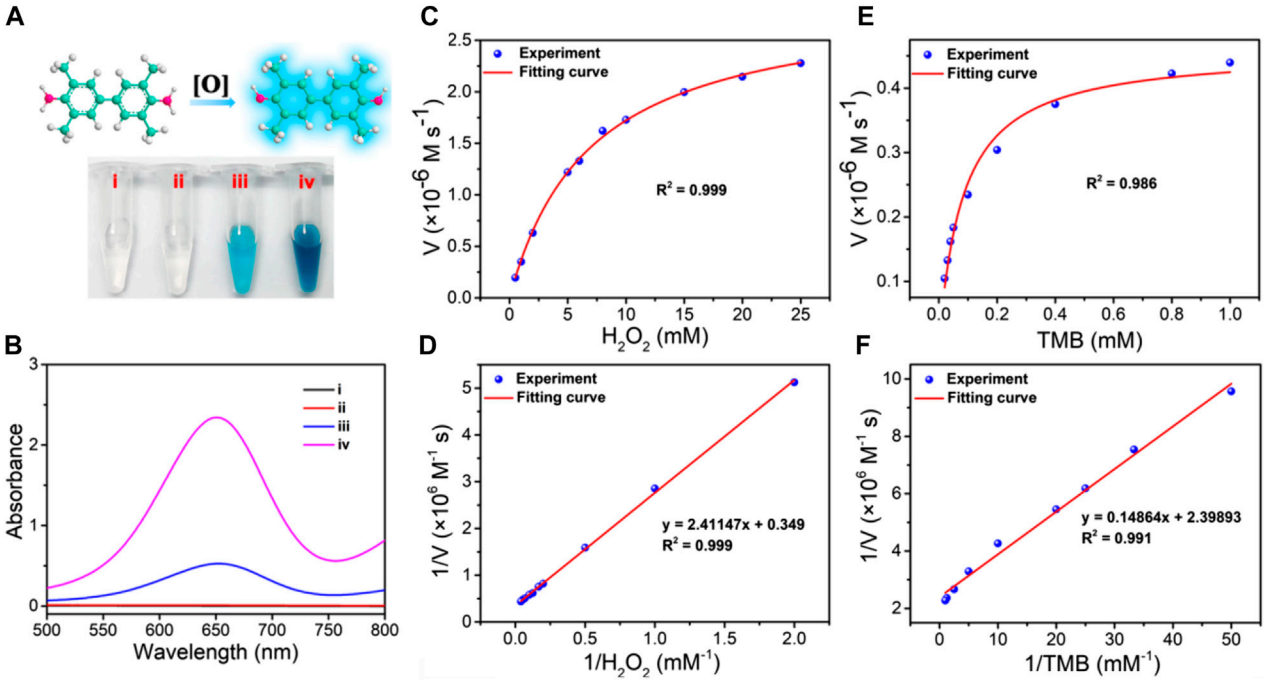

FIGURE 2
(A) Images and **(B)** UV-vis absorption spectra of the TMB solution under different conditions (i: TMB, ii: TMB + H_2O_2, iii: ZIF-8@PDA@Pt + TMB, and iv: ZIF-8@PDA@Pt + TMB + H_2O_2). **(C)** Michaelis–Menten curve under 0.8 mM TMB and various concentrations of H_2O_2. **(D)** Lineweaver–Burk plot for H_2O_2. **(E)** Michaelis–Menten curve under 1 mM H_2O_2 with various concentrations of TMB. **(F)** Lineweaver–Burk plot for TMB.

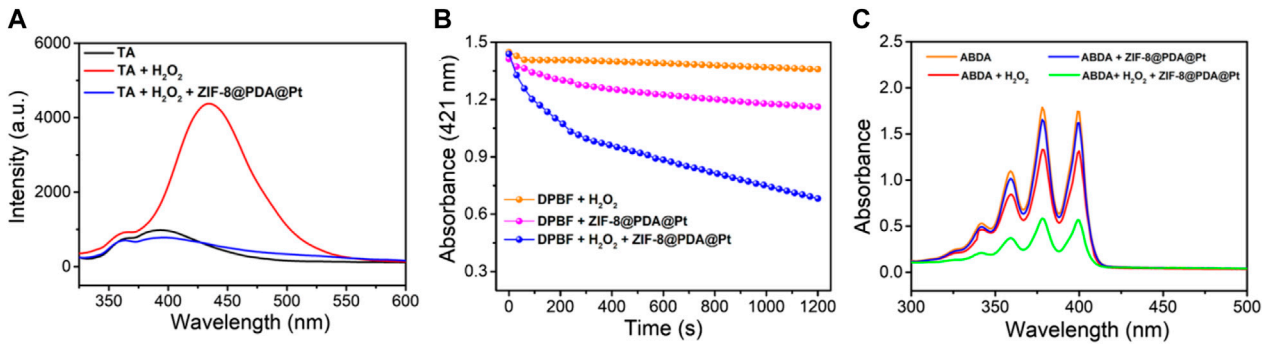

FIGURE 3
The spectral signals measured by using different ROS probes, TA **(A)**, DPBF **(B)** and ABDA **(C)**.

while the higher V_{max} refers to the better catalytic capability. These results indicated that the obtained nanozyme ZIF-8@PDA@Pt shows better catalytic performance than the classical POD nanozyme Fe_3O_4, and some parameters are even significantly better than natural enzymes. For example, K_m of ZIF-8@PDA@Pt was 0.062 mM for TMB, which is much lower than that of HRP and Fe_3O_4, indicating that ZIF-8@PDA@Pt has the highest enzyme affinity toward TMB. Moreover, ZIF-8@PDA@Pt also shows the highest V_{max} values. These results demonstrated that the obtained ZIF-8@PDA@Pt possesses excellent POD-like activity, also implying the strong ROS generation ability of the ZIF-8@PDA@Pt–H_2O_2 system.

To further verify the ability of ZIF-8@PDA@Pt to catalyze the production of different free radicals from H_2O_2, terephthalic acid (TA), 1,3-diphenylisobenzofuran (DPBF), and 9,10-anthracenediyl-bis(methylene)-dimalonic acid (ABDA) were chose as the indicators for the sensing of hydroxyl radical (•OH), $O_2^{\bullet-}$ (superoxide anion), and singlet oxygen ($^1O_2$), respectively. TA is a non-fluorescent molecule that can be oxidized by •OH to generated blue fluorescence. DPBF is a fluorescent molecule which possesses a specific reactivity toward $^1O_2$ and $O_2^{\bullet-}$, forming an endoperoxide that can decompose to give 1,2-dibenzoylbenzene. This decomposition of DPBF by $^1O_2$ and $O_2^{\bullet-}$ can be measured by the decrease in the absorbance intensity of DPBF at 412 nm. ABDA is a

10.3389/fbioe.2024.1355004

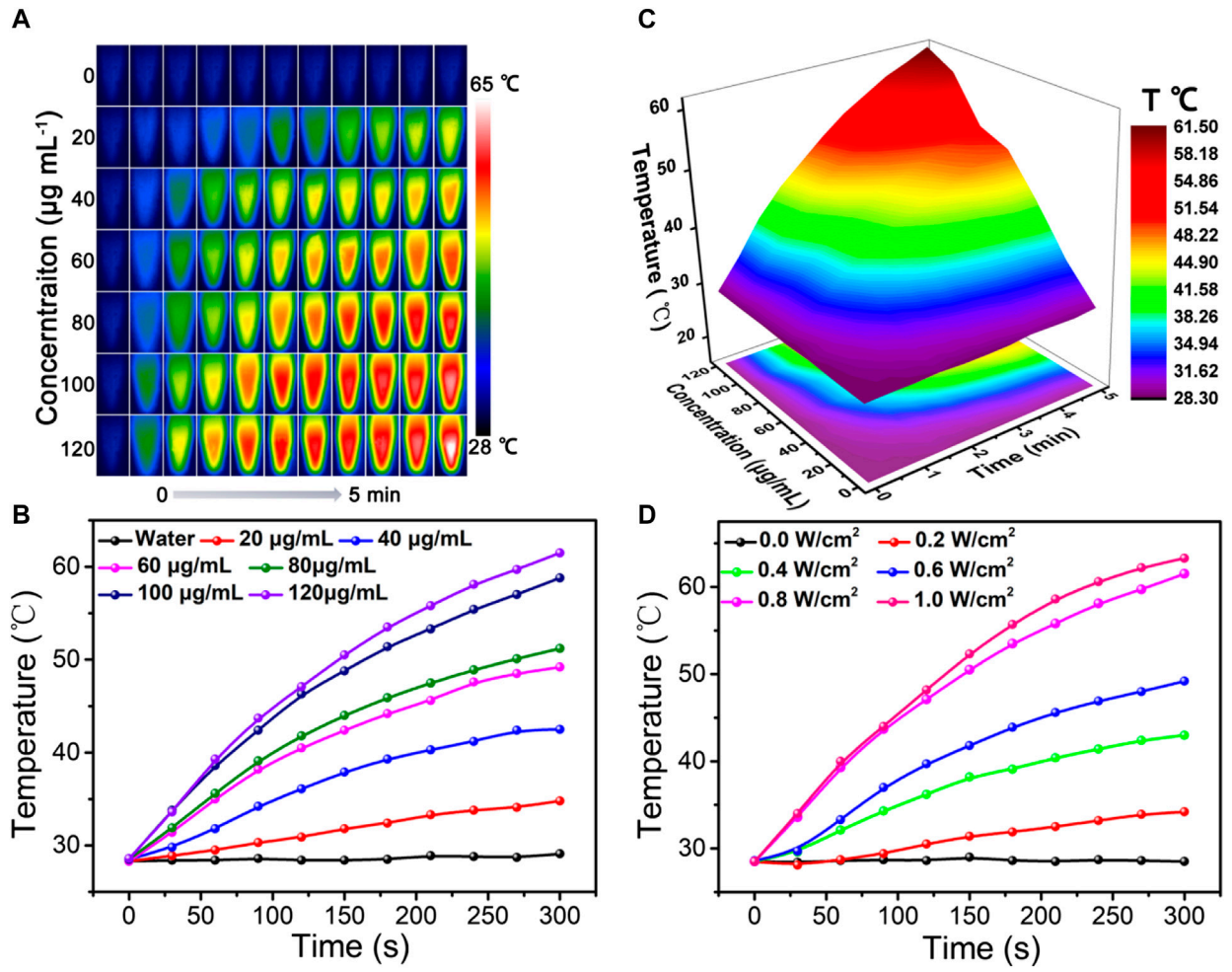

FIGURE 4
Thermal imaging **(A)**, temperature variation curve **(B)**, and corresponding 3D surface graph **(C)** of ZIF-8@PDA@Pt with different concentrations under laser irradiation (0.8 W) over time. **(D)** Temperature variation curve of the ZIF-8@PDA@Pt solution under different laser intensities over time (808 nm, 120 μg mL^{-1}).

highly selective probe for singlet oxygen $^1O_2$, which can be oxidized with the decrease in the absorbance intensity. As shown in Figure 3, in the solution with the probes and H_2O_2, the presence of ZIF-8@PDA@P can induce significant sensing signals of •OH, $O_2^{\bullet-}$, and $^1O_2$. These results strongly demonstrated that ZIF-8@PDA@Pt can catalyze the production of different free radical species from H_2O_2, which is very important for bacterial disinfection.

3.3 Photothermal effect of ZIF-8@PDA@Pt

As illustrated in the UV-vis spectra of Figure 1F, ZIF-8@PDA@Pt presents broad and intense adsorption from the ultraviolet to NIR region, manifesting ZIF-8@PDA@Pt possesses considerable photothermal conversion potential. So as to validate the supposition, the photothermal property of ZIF-8@PDA@Pt was primarily investigated, where the aqueous dispersions of ZIF-8@PDA@Pt with different concentrations were irradiated under an 808-nm NIR laser. Simultaneously, the real-time temperatures were recorded by a thermal imaging camera. It can be observed from Figures 4A–C that the temperature of the aqueous solution lifted promptly with the augment of the concentration of ZIF-8@PDA@Pt and the prolongation of irradiation time. Indeed, the constant arising trend of the curve implied that ZIF-8@PDA@Pt exhibits supreme photostability under the irradiation of the NIR laser. It can also be visually discovered from the quantitative data that the temperature of the ZIF-8@PDA@Pt solution (120 μg mL^{-1}) elevated rapidly from 28.5°C to 61.5°C within 5 min of irradiation, while the temperature of water only raised by 0.8°C under the same conditions. Such a result elucidated ZIF-8@PDA@Pt can serve as a remarkable photothermal agent. Hence, we further calculated the photothermal conversion efficiency of ZIF-8@PDA@Pt in line with a method reported previously (Supplementary Figure S2), where it can be up to 65.4% to our surprise, and this excellent property just met the experimental results we obtained as well, where the real-time temperature of the NIR-irradiated ZIF-8@PDA@Pt aqueous solution can reach up to 61.5°C in a short time.

In addition, it was found that ZIF-8@PDA@Pt presented a laser power-dependent behavior. As shown in Figure 4D, the temperature of solutions at the same time nodes increased gradually along with

10.3389/fbioe.2024.1355004

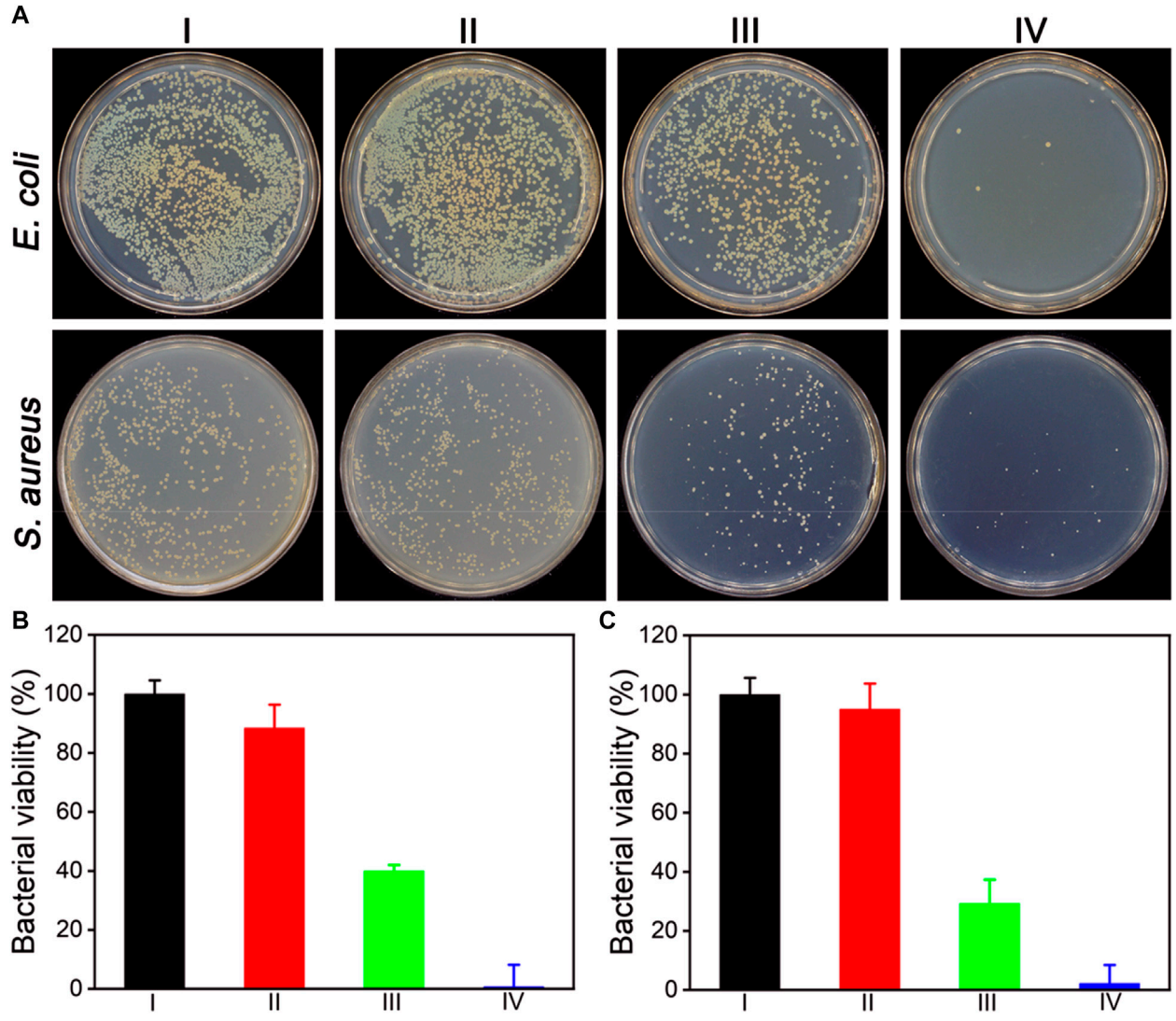

FIGURE 5
(A) Photographs of the colonies of *E. coli* and *S. aureus* treated under different conditions. alculated bacterial viabilities of C*E. coli* **(B)** and *S. aureus* **(C)** in **(A)**. I: Control, II: H_2O_2 (2 mM), III: ZIF-8@PDA@Pt + H_2O_2, and IV: ZIF-8@PDA@Pt + H_2O_2 + NIR. (H_2O_2 2 mM, ZIF-8@PDA@Pt 100 μg mL^{-1}, NIR 808 nm 0.8 W 5 min).

the increase in laser power, denoting the laser power to be imperative to the photothermal conversion ability of ZIF-8@PDA@Pt. Afterward, the thermal stability of ZIF-8@PDA@Pt was estimated by photothermal performance cycle monitoring within four laser cycles. It can be noted from Supplementary Figure S3 that there were no unmistakable temperature fluctuations in the four photothermal cycles, demonstrating ZIF-8@PDA@Pt endows considerable photothermal stability. All above results certified that ZIF-8@PDA@Pt possessed excellent photothermal properties, which can support its application for sterilization.

3.4 Synergistic antibacterial effect of ZIF-8@PDA@Pt

Inspired by the superior enzymatic activity and photothermal property of ZIF-8@PDA@Pt, the *in vitro* synergistic antibacterial effect of ZIF-8@PDA@Pt against Gram-negative bacteria (*E. coli*) and Gram-positive bacteria (*S. aureus*) was assessed by the plate counting method. As shown in Figure 5, H_2O_2 (2 mM) alone cannot induce significant influence on the bacterial viability. However, in the presence of ZIF-8@PDA@Pt, the viabilities of both *E. coli* and *S. aureus* decreased to below 40%. The ROS generated form H_2O_2 under the catalysis of ZIF-8@PDA@Pt would be responsible for this sharp decrease in the bacterial viability. Moreover, as expected, NIR irradiation greatly promoted the antibacterial efficiency of the ZIF-8@PDA@Pt/H_2O_2 system, in which the bacterial viabilities decreased to below 3%. The viability of the treated bacteria was also investigated by a live/dead staining kit, which contains two dyes, SYTO 9 and propidium iodide (PI). SYTO 9 is a membrane-permeable dye that can give a green fluorescence to indicate the live cells due to the binding with bacterial nucleic acid. PI is also a nucleic acid-binding dye used to give a red

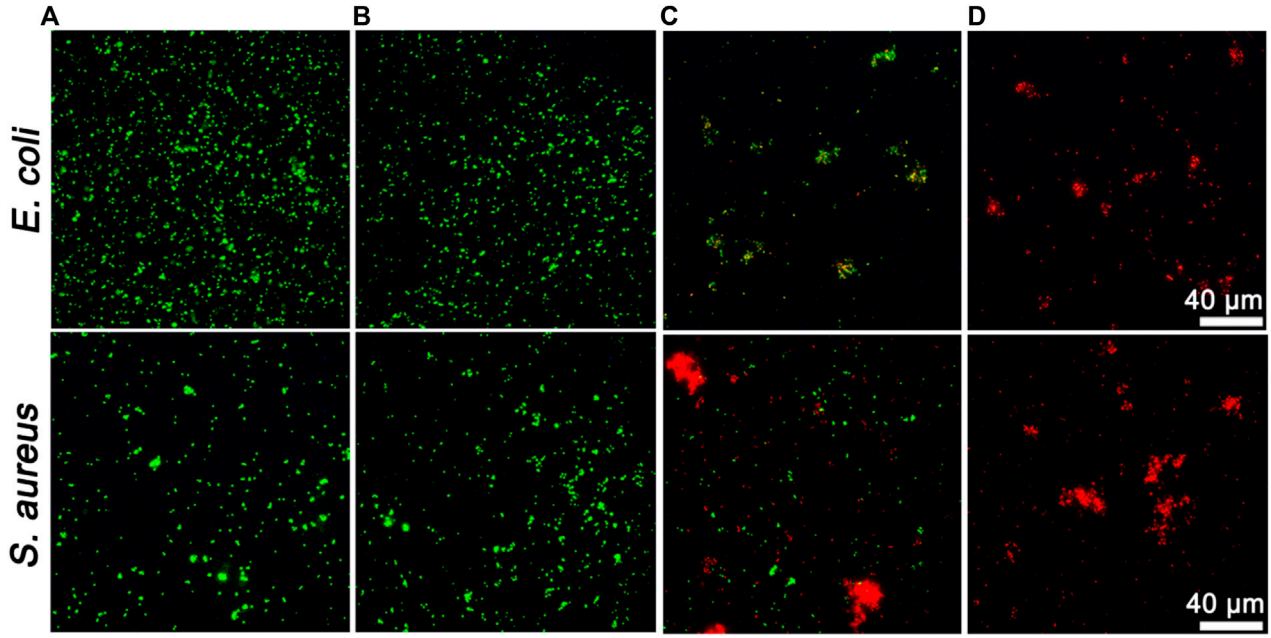

FIGURE 6
Fluorescent images of live/dead staining of bacteria upon different treatments. **(A)**: Control, **(B)**: H_2O_2 (2 mM), **(C)**: ZIF-8@PDA@Pt + H_2O_2, and **(D)**: ZIF-8@PDA@Pt + H_2O_2 + NIR. (H_2O_2 2 mM, ZIF-8@PDA@Pt 100 μg mL^{-1}, NIR 808 nm 0.8 W 5 min).

fluorescence, which can only penetrate the damaged membrane of dead bacteria. As shown in Figure 6, upon treating with ZIF-8@PDA@Pt and H_2O_2, significant amount of dead bacteria was found in the fluorescence images, and almost all of the bacteria were killed when the ZIF-8@PDA@Pt/H_2O_2 system was irradiated with the NIR light. This phenomenon was the same as that found in the plate counting experiments. These results clearly demonstrated the high synergistic antimicrobial activity of the nanozyme ZIF-8@PDA@Pt in the presence of H_2O_2 and NIR light irradiation. Notably, the nanozyme also has good biocompatibility; in the MTT assay, over 90% of the HSF cells remain alive when in the incubation with 250 μg mL^{-1} of ZIF-8@PDA@Pt.

4 Conclusion

In conclusion, a platinum nanozyme ZIF-8@PDA@Pt with high peroxidase-like activity was successfully synthesized. The catalytic activity is much higher than the classical nanozyme Fe_3O_4, and some parameters are even better than the natural enzyme HRP. The obtained nanozyme ZIF-8@PDA@Pt can efficiently promote the generation of different ROS from H_2O_2. Moreover, ZIF-8@PDA@Pt can harvest the photon energy from the NIR light to heating the solution. The combined excellent photothermal effect and peroxidase-like activity resulted in high synergistic antimicrobial activity of the nanozyme ZIF-8@PDA@Pt in the presence of H_2O_2 and NIR light irradiation. The developed nano-antibacterial strategy is highly promising for wide applications, for example, wound infection treatment, antibacterial coatings for medical materials, preservation and protection of agricultural products, etc.

Data availability statement

The original contributions presented in the study are included in the article/Supplementary Material; further inquiries can be directed to the corresponding authors.

Author contributions

XL: methodology, writing–review and editing, investigation, and writing–original draft. WZ: writing–review and editing, investigation, methodology, and writing–original draft. YZ: investigation, methodology, and writing–review and editing. NW: investigation, methodology, and writing–review and editing. XG: investigation, methodology, and writing–original draft. SS: methodology and writing–review and editing. MC: investigation and writing–review and editing. ZZ: methodology, conceptualization, funding acquisition, supervision, writing–original draft, and writing–review and editing. GH: methodology, funding acquisition, supervision, and writing–review and editing.

Funding

The author(s) declare that financial support was received for the research, authorship, and/or publication of this article. This research received financial support from the National Natural Science Foundation of China (NSFC) (No. 22007083), China Agriculture Research System (CARS-29), and the Fundamental Research Funds of the Shengzhou Innovation Research Institute of Zhejiang Sci-Tech University (No. SYY 2023B000004). The Program of Agricultural Product Quality Safety Risk Assessment (GJFP20210501).

Conflict of interest

The authors declare that the research was conducted in the absence of any commercial or financial relationships that could be construed as a potential conflict of interest.

Publisher's note

All claims expressed in this article are solely those of the authors and do not necessarily represent those of their affiliated organizations, or those of the publisher, the editors, and the reviewers. Any product that may be evaluated in this article, or claim that may be made by its manufacturer, is not guaranteed or endorsed by the publisher.

Supplementary material

The Supplementary Material for this article can be found online at: https://www.frontiersin.org/articles/10.3389/fbioe.2024.1355004/full#supplementary-material

References

Chen, Z., Wang, Z., Ren, J., and Qu, X. (2018). Enzyme mimicry for combating bacteria and biofilms. *Accounts Chem. Res.* 51, 789–799. doi:10.1021/acs.accounts.8b00011

Dorma Momo, C., Zhou, Y., Li, L., Zhu, W., Wang, L., Liu, X., et al. (2022). A metal–organic framework nanocomposite with oxidation and near-infrared light cascade response for bacterial photothermal inactivation. *Front. Chem.* 10, 1044931. doi:10.3389/fchem.2022.1044931

Du, Q., Wu, X., Bi, W., Xing, B., and Yeow, E. K. L. (2021). Increasing antibiotic activity by rapid bioorthogonal conjugation of drug to resistant bacteria using an upconverted light-activated photocatalyst. *J. Mater. Chem. B* 9, 3136–3142. doi:10.1039/d0tb02568b

Fan, C., Zhao, J., Tang, Y., and Lin, Y. (2023). Using near-infrared I/II light to regulate the performance of nanozymes. *J. Analysis Test.* 7, 272–284. doi:10.1007/s41664-023-00257-z

Fu, B., Liu, Q., Liu, M., Chen, X., Lin, H., Zheng, Z., et al. (2022). Carbon dots enhanced gelatin/chitosan bio-nanocomposite packaging film for perishable foods. *Chin. Chem. Lett.* 33, 4577–4582. doi:10.1016/j.cclet.2022.03.048

Guo, C., Zhang, J., Feng, X., Du, Z., Jiang, Y., Shi, Y., et al. (2022). Polyhexamethylene biguanide chemically modified cotton with desirable hemostatic, inflammation-reducing, intrinsic antibacterial property for infected wound healing. *Chin. Chem. Lett.* 33, 2975–2981. doi:10.1016/j.cclet.2021.12.086

Han, Q., Lau, J. W., Do, T. C., Zhang, Z., and Xing, B. (2020). Near-infrared light brightens bacterial disinfection: recent progress and perspectives. *ACS Appl. Bio Mater.* 4, 3937–3961. doi:10.1021/acsabm.0c01341

Hu, H., Kang, X., Shan, Z., Yang, X., Bing, W., Wu, L., et al. (2022). A DNase-mimetic artificial enzyme for the eradication of drug-resistant bacterial biofilm infections. *Nanoscale* 14, 2676–2685. doi:10.1039/d1nr07629a

Huang, Q., Zhu, W., Gao, X., Liu, X., Zhang, Z., and Xing, B. (2023). Nanoparticles-mediated ion channels manipulation: from their membrane interactions to bioapplications. *Adv. Drug Deliv. Rev.* 195, 114763. doi:10.1016/j.addr.2023.114763

Ikuta, K. S., Swetschinski, L. R., Robles Aguilar, G., Sharara, F., Mestrovic, T., Gray, A. P., et al. (2022). Global mortality associated with 33 bacterial pathogens in 2019: a systematic analysis for the Global Burden of Disease Study 2019. *Lancet* 400, 2221–2248. doi:10.1016/s0140-6736(22)02185-7

Jiao, L., Li, Q., Li, C., Gu, J., Liu, X., He, S., et al. (2023). Orthogonal light-triggered multiple effects based on photochromic nanoparticles for DNA cleavage and beyond. *J. Mater. Chem. B* 11, 2367–2376. doi:10.1039/d2tb02638d

Li, L., Zhou, Y., Li, P., Xu, Q., Li, K., Hu, H., et al. (2022b). Peptide hydrogel based sponge patch for wound infection treatment. *Front. Bioeng. Biotechnol.* 10, 1066306. doi:10.3389/fbioe.2022.1066306

Li, Y., Zheng, H., Liang, Y., Xuan, M., Liu, G., and Xie, H. (2022a). Hyaluronic acid-methacrylic anhydride/polyhexamethylene biguanide hybrid hydrogel with antibacterial and proangiogenic functions for diabetic wound repair. *Chin. Chem. Lett.* 33, 5030–5034. doi:10.1016/j.cclet.2022.03.116

Liu, J., Liu, X., Yang, L., Cai, A., Zhou, X., Zhou, C., et al. (2022a). A highly sensitive electrochemical cytosensor based on a triple signal amplification strategy using both nanozyme and DNAzyme. *J. Mater. Chem. B* 10, 700–706. doi:10.1039/d1tb02545g

Liu, S., Xu, J., Xing, Y., Yan, T., Yu, S., Sun, H., et al. (2022b). Nanozymes as efficient tools for catalytic therapeutics. *VIEW* 3, 20200147. doi:10.1002/viw.20200147

Makabenta, J. M. V., Nabawy, A., Li, C.-H., Schmidt-Malan, S., Patel, R., and Rotello, V. M. (2021). Nanomaterial-based therapeutics for antibiotic-resistant bacterial infections. *Nat. Rev. Microbiol.* 19, 23–36. doi:10.1038/s41579-020-0420-1

Murray, C. J. L., Ikuta, K. S., Sharara, F., Swetschinski, L., Robles Aguilar, G., Gray, A., et al. (2022). Global burden of bacterial antimicrobial resistance in 2019: a systematic analysis. *Lancet* 399, 629–655. doi:10.1016/s0140-6736(21)02724-0

Niu, J., Sun, Y., Wang, F., Zhao, C., Ren, J., and Qu, X. (2018). Photomodulated nanozyme used for a gram-selective antimicrobial. *Chem. Mater.* 30, 7027–7033. doi:10.1021/acs.chemmater.8b02365

Niu, J., Wang, L., Cui, T., Wang, Z., Zhao, C., Ren, J., et al. (2021a). Antibody mimics as bio-orthogonal catalysts for highly selective bacterial recognition and antimicrobial therapy. *ACS Nano* 15, 15841–15849. doi:10.1021/acsnano.1c03387

Niu, J., Zhao, C., Liu, C., Ren, J., and Qu, X. (2021b). Bio-inspired bimetallic enzyme mimics as bio-orthogonal catalysts for enhanced bacterial capture and inhibition. *Chem. Mater.* 33, 8052–8058. doi:10.1021/acs.chemmater.1c02469

Sun, Y., Zhao, C., Niu, J., Ren, J., and Qu, X. (2020). Colorimetric band-aids for point-of-care sensing and treating bacterial infection. *ACS Central Sci.* 6, 207–212. doi:10.1021/acscentsci.9b01104

Wang, W., Li, P., Huang, Q., Zhu, Q., He, S., Bing, W., et al. (2023). Functionalized antibacterial peptide with DNA cleavage activity for enhanced bacterial disinfection. *Colloids Surfaces B Biointerfaces* 228, 113412. doi:10.1016/j.colsurfb.2023.113412

Wang, Y., Zhang, C., Zhang, H., Feng, L., and Liu, L. (2022). A hybrid nano-assembly with synergistically promoting photothermal and catalytic radical activity for antibacterial therapy. *Chin. Chem. Lett.* 33, 4605–4609. doi:10.1016/j.cclet.2022.03.076

Wang, Z., Zhen, X., Upputuri, P. K., Jiang, Y., Lau, J., Pramanik, M., et al. (2019). Redox-activatable and acid-enhanced nanotheranostics for second near-infrared photoacoustic tomography and combined photothermal tumor therapy. *ACS Nano* 13, 5816–5825. doi:10.1021/acsnano.9b01411

Wu, T., Fu, Y., Guo, S., Shi, Y., Zhang, Y., Fan, Z., et al. (2023). Self-assembly multifunctional DNA tetrahedron for efficient elimination of antibiotic-resistant bacteria. *Aggregate*, e402. doi:10.1002/agt2.402

Wu, X., and Yeow, E. K. L. (2022). Exploiting the upconversion luminescence, Lewis acid catalytic and photothermal properties of lanthanide-based nanomaterials for chemical and polymerization reactions. *Phys. Chem. Chem. Phys.* 24, 11455–11470. doi:10.1039/d2cp00560c

Xie, M., Gao, M., Yun, Y., Malmsten, M., Rotello, V. M., Zboril, R., et al. (2023). Antibacterial nanomaterials: mechanisms, impacts on antimicrobial resistance and design principles. *Angew. Chem. Int. Ed.* 62, e202217345. doi:10.1002/anie.202217345

Yue, Y., Xu, Z., Ma, K., Huo, F., Qin, X., Zhang, K., et al. (2023). HSA shrinkage optimizes the photostability of embedded dyes fundamentally to amplify their efficiency as photothermal materials. *Chin. Chem. Lett.*, 109223. doi:10.1016/j.cclet.2023.109223

Zeng, X., Shan, C., Sun, M., Ding, D., and Rong, S. (2022). Graphene enhanced α-MnO2 for photothermal catalytic decomposition of carcinogen formaldehyde. *Chin. Chem. Lett.* 33, 4771–4775. doi:10.1016/j.cclet.2021.12.085

Zhang, C., He, W., Liu, C., Jiao, D., and Liu, Z. (2021). Cutting-edge advancements of nanomaterials for medi-translatable noninvasive theranostic modalities. *VIEW* 2, 20200144. doi:10.1002/viw.20200144

Zhao, J., Yu, D., Chen, J., Lin, S., Tang, Y., Fan, C., et al. (2023). Deciphering the high-carbonization-temperature triggered enzymatic activity of wool-derived N, S-co-doped carbon nanosheets. *Chin. Chem. Lett.* 35, 109080. doi:10.1016/j.cclet.2023.109080

Zhu, Q., Li, P., Huang, Q., Ding, X., Wang, N., Yao, W., et al. (2023). Near-infrared light-activatable melanized paclitaxel nano–self-assemblies for synergistic anti-tumor therapy. *J. Analysis Test.* 7, 204–214. doi:10.1007/s41664-023-00262-2

frontiers | Frontiers in Bioengineering and Biotechnology

TYPE Original Research
PUBLISHED 19 January 2024
DOI 10.3389/fbioe.2023.1338257

OPEN ACCESS

EDITED BY
Qitong Huang,
Gannan Medical University, China

REVIEWED BY
Hang Hu,
Changzhou University, China
Xiaofeng Lin,
Gannan Medical University, China

*CORRESPONDENCE
Chen Wang,
wangch@nanoctr.cn
Yanlian Yang,
yangyl@nanoctr.cn

RECEIVED 14 November 2023
ACCEPTED 29 November 2023
PUBLISHED 19 January 2024

CITATION
Lv L, Fu Z, You Q, Xiao W, Wang H, Wang C and Yang Y (2024), Enhanced photodynamic therapy through multienzyme-like MOF for cancer treatment.
Front. Bioeng. Biotechnol. 11:1338257.
doi: 10.3389/fbioe.2023.1338257

Enhanced photodynamic therapy through multienzyme-like MOF for cancer treatment

Letian Lv[1,2], Zhao Fu[1], Qing You[1], Wei Xiao[1], Huayi Wang[1], Chen Wang[1,2]* and Yanlian Yang[1,2]*

[1]CAS Key Laboratory of Standardization and Measurement for Nanotechnology, CAS Key Laboratory of Biological Effects of Nanomaterials and Nanosafety, CAS Center for Excellence in Nanoscience, National Center for Nanoscience and Technology, Beijing, China, [2]University of Chinese Academy of Sciences, Beijing, China

Overcoming resistance to apoptosis is a major challenge in cancer therapy. Recent research has shown that manipulating mitochondria, the organelles critical for energy metabolism in tumor cells, can increase the effectiveness of photodynamic therapy and trigger apoptosis in tumor cells. However, there is currently insufficient research and effective methods to exploit mitochondrial damage to induce apoptosis in tumor cells and improve the effectiveness of photodynamic therapy. In this study, we present a novel nanomedicine delivery and therapeutic system called PyroFPSH, which utilizes a nanozymes-modified metal-organic framework as a carrier. PyroFPSH exhibits remarkable multienzyme-like activities, including glutathione peroxidase (GPx) and catalase (CAT) mimicry, allowing it to overcome apoptosis resistance, reduce endogenous glutathione levels, and continuously generate reactive oxygen species (ROS). In addition, PyroFPSH can serve as a carrier for the targeted delivery of sulfasalazine, a drug that can induce mitochondrial depolarization in tumor cells, thereby reducing oxygen consumption and energy supply in the mitochondria of tumor cells and weakening resistance to other synergistic treatment approaches. Our experimental results highlight the potential of PyroFPSH as a versatile nanoplatform in cancer treatment. This study expands the biomedical applications of nanomaterials as platforms and enables the integration of various novel therapeutic strategies to synergistically improve tumor therapy. It deepens our understanding of multienzyme-mimicking active nanocarriers and mitochondrial damage through photodynamic therapy. Future research can further explore the potential of PyroFPSH in clinical cancer treatment and improve its drug loading capacity, biocompatibility and targeting specificity. In summary, PyroFPSH represents a promising therapeutic approach that can provide new insights and possibilities for cancer treatment.

KEYWORDS

photodynamic therapy, MOF, nanozyme, multi-functional nanoplatform, combination therapy

1 Introduction

Tumor cells have inherent defense mechanisms that can resist apoptosis triggered by single photodynamic therapy. For example, dihydroorotate dehydrogenase (DHODH) in mitochondria can reduce the damage caused by reactive oxygen species to tumor cell mitochondria (Mao et al., 2021). The presence of multiple defense mechanisms in tumor

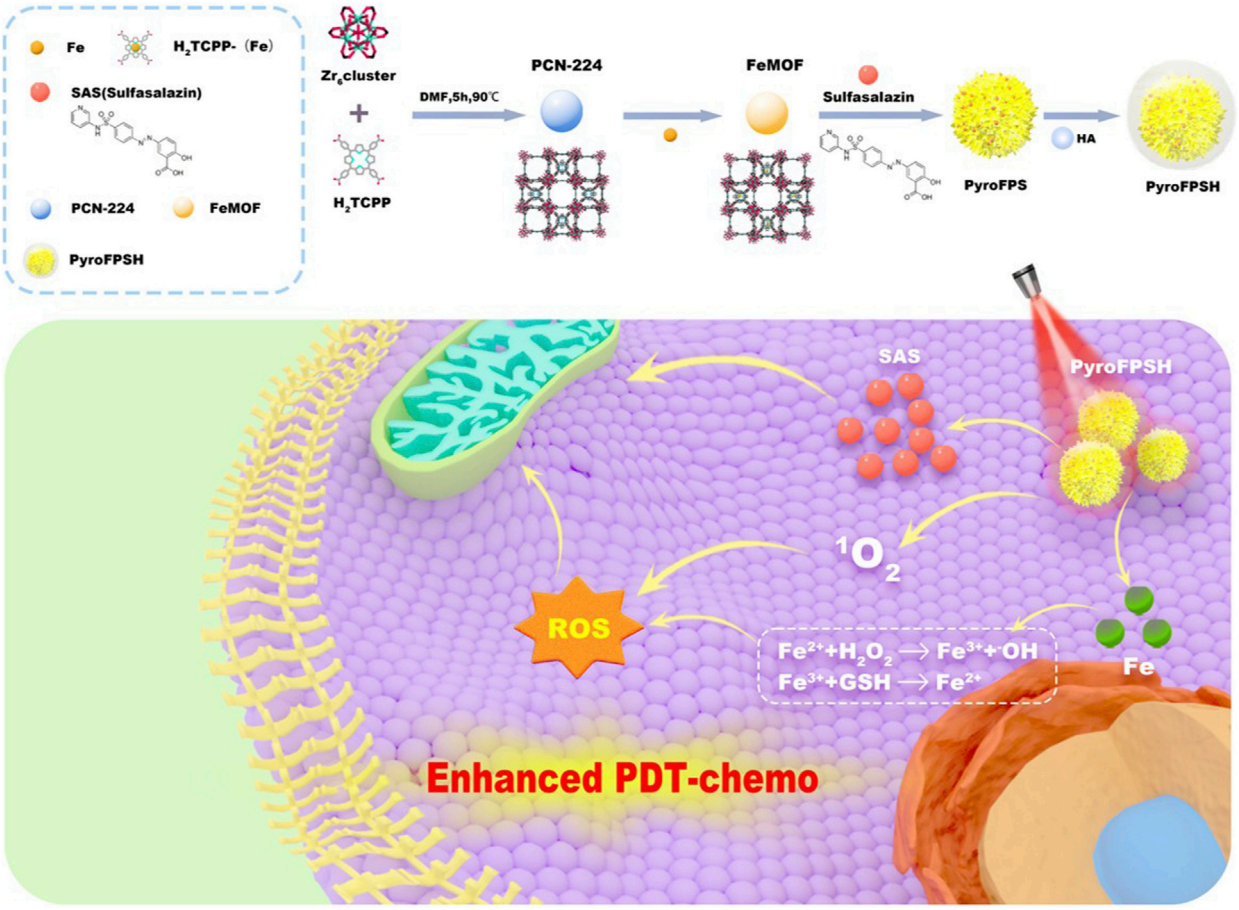

SCHEME 1
Schematic illustration of the synthesis process of PyroFPSH and its application in tumor treatment. PyroFPSH enhances the efficacy of photodynamic therapy through the combined treatment of nanozymes and small molecule drugs.

cells leads to incomplete killing of tumor cells with single treatment strategies, resulting in distant metastasis and tumor recurrence. These strategies can trigger sufficient cell damage through synergistic effects and prevent the recurrence and metastasis of tumors in the same treatment process (Shen et al., 2020; Ruan et al., 2021; Xu et al., 2021; Yang et al., 2023).

The level of cell apoptosis is closely related to levels of ROS arising from singlet oxygen produced by PDT or hydroxyl radicals generated by nanozymes and the corresponding resistance of mitochondria to ROS (Chen et al., 2020; Wan et al., 2020; Chen et al., 2021c; Chen et al., 2022). For nanozymes, several representative nanozymes like Fe_3O_4 particles could trigger the decomposition of endogenous H_2O_2 into highly reactive hydroxyl (•OH) radicals, invoking an intensive cytotoxic effect on the tumor cells. Building on this knowledge, we developed a strategy involving Fe with diverse nanozyme activities embedded in a photodynamic metal-organic framework PCN-224 to generate Fe@PCN-224 (FeMOF) (Wan et al., 2019; Shi et al., 2020; Chen et al., 2021b). This structure combined nanozyme activity and photodynamic effects as a platform for further modifications with HA and loading of the mitochondrial-targeting drug sulfasalazine (SAS) (Kang et al., 2019; Liu et al., 2021a; Xin et al., 2021). This led to HA@SAS@FeMOF (PyroFPSH) (Scheme 1), which was used to amplify ROS levels, particularly hydroxyl radicals and singlet oxygen, and inhibit malignant tumors. Given the significant reduction in ROS production due to hypoxia, we discovered that Fe embedded in PCN-224 can stimulate the generation of ROS and simultaneously release O_2 through a chemical kinetic process initiated by the Fenton reaction. Concurrently, the induction of mitochondrial polarization by SAS could further reduce O_2 consumption and energy production in tumor cell mitochondria. This mitochondrial polarization induced by SAS is thought to alleviate hypoxia, elevate ROS levels, and establish a window period during photodynamic therapy (Jiang et al., 2020; Zhang et al., 2023). Within this SAS-induced window period, severely weakened tumor cells are unable to combat ROS through O_2-generated energy, thereby minimizing resistance to the synergistic antitumor effects of different therapeutic strategies. Notably, in the presence of a 660 nm laser, PyroFPSH not only stimulates the production of various types of ROS through photodynamic therapy and nanozyme activity, but also enhances the SAS drug release process. In summary, nanozyme catalysis and mitochondrial polarization increase intracellular O_2 concentrations, thereby alleviating hypoxia. Together with the increase in ROS accumulation in tumors, this leads to the

activation of cell death, yielding impressive therapeutic effects in both *in vitro* and *in vivo* antitumor treatments.

Reactive oxygen species (ROS)-induced cell death has been used in various processes including apoptosis, ferroptosis, and pyroptosis (Zhou et al., 2018; Sun et al., 2021; Zhou et al., 2022). Photodynamic processes use a near-infrared laser that can penetrate tumor tissue. When this type of laser is introduced, it can enhance the catalytic activity and therapeutic effect of nanozymes. In particular, the catalytic activity of nanozymes can be enhanced by photodynamic therapy (PDT), whereby a light-augmented Fenton reaction enhances ROS generation under light illumination, significantly increasing the enzymatic activity and the corresponding reaction rate (Chen et al., 2020; Cui et al., 2021; Meng et al., 2021; Hu et al., 2022). Therefore, integrating PDT-enhanced enzymatic activity into a nanozyme can effectively suppress tumor growth and recurrence.

Metal-organic frameworks (MOF) represent a new type of nanomaterials characterized by excellent biocompatibility and a large surface area (Cui et al., 2023). Compared to traditional drug carriers, MOFs can deliver a higher drug dose. Current research in targeted cancer therapy focuses on the development of new materials based on MOFs. By capitalizing on the interaction between the tumor microenvironment (TME) and MOFs, we can develop TME-responsive MOFs to achieve effective TME-targeted cancer treatment. The excellent loading capacity of MOFs makes them effective carriers for photosensitizers, nanozymes, and drugs in tumor therapy.

In this study, we successfully constructed a drug delivery platform, FeMOF@HA, that combines nanozymes with photodynamic therapy (PDT) and chemotherapy (CDT) for synergistic tumor treatment. FeMOF@HA can also deliver the small molecule drug SAS, which regulates mitochondria, reduces tumor cell tolerance to combination therapy, induces tumor cell apoptosis, and accelerates cancer treatment. This study opens a new perspective on nanozyme and photodynamic therapy (PDT) combination treatment based on significant organelle damage in tumor cells, potentially paving the way for new approaches to cancer treatment and innovative strategies for combination cancer therapy.

2 Experimental section

2.1 Materials and instrumentation

Hydrogen peroxide (H_2O_2, 30 wt%) was obtained from Beijing Chemical Reagent Research Institute (Beijing, China). The catalase (3,500 units mg-1 protein from cow liver) was acquired from Beyotime Biotechnology (Shanghai, China). 2,2,6,6-Tetramethylpiperidine (TEMP, 99% pure) was provided by Alfa Aesar. 5,5-Dimethyl-1-pyrroline N-oxide (DMPO, 98% pure) was acquired from Innochem (Beijing, China). TMB (99% pure), 1,3-diphenylisobenzofuran (DPBF, 97% pure), 9,10-anthracenediyl-bis (methylene)dimalonic acid (ABDA, 98% pure) and Tris-HCl (pH 7.4) were obtained from Solarbio. Tetrakis (4-carboxyphenyl) porphyrin (TCPP), hyaluronic acid (HA) (MW, 7.9 kDa), N,N-dimethylformamide (DMF), benzoic acid, zirconium chloride octahydrate ($ZrOCl_2{\cdot}8H_2O$, 99.99%), and 5,5′-Dithiobis (2-nitrobenzoic acid) (DTNB) were purchased from Aladdin Reagent Co., Ltd. (Shanghai, China). $[Ru(dpp)_3]Cl_2$ (RDPP), glutathione (GSH), 3,3′,5,5′- tetramethylbenzidine (TMB), methylene blue (MB), 2,7-dichlorodihydrofluorescein diacetate (DCFH-DA), and $FeCl_3{\cdot}6H_2O$ were purchased from Sigma-Aldrich. Fetal bovine serum (FBS) and high glucose Dulbecco's modified Eagle medium (RPMI 1640) were purchased from Gibco Life Technologies. Calcein-AM and propidium iodide (PI) kit, 4′,6-diamidino-2-phenylindole (DAPI), 2,7-dichlorofluorescein diacetate (DCFH-DA), assay kit and JC-1 staining kit were purchased from Beyotime Biotechnology (Shanghai, China).

Topography and elemental mapping images were acquired using Ht-7700 transmission electron microscopy (Hitachi, Japan) and high-resolution TEM (HRTEM) (Tecnai G2 F20, United States), respectively. ICP measurement was performed using the Thermo Scientific iCAP 6,300. The ESR measurements were performed at ambient temperature in a Bruker EMX EPR spectrometer (Billerica, MA). The surface modification was identified by FT-IR spectroscopy (Spectrum One, United States). Zeta potential measurement was performed using the Zetasizer instrument (Zetasizer Nano ZS, England). The chemical composition and crystal structure of the nanosheets were analyzed using XPS (ESCALAB 250Xi, England). UV–Vis spectra were recorded using a Lambda UV–Vis spectrophotometer (Perkin Elmer, United States). Dynamic light scattering (DLS) for particle size and zeta potential was determined using Zetasizer Nano ZS (Malvern, United Kingdom). The XRD patterns were tested on a TZY-XRD (Rigaku, Japan). The experiment of Barrett–Joyner–Halenda model from the adsorption branch of isotherms was performed using an automatic surface area and porosity analyzer (Micromeritics Instrument, United States). The laser of 660 nm was managed by a power-tunable infrared laser (Laserwave, China).

2.2 Fabrication of PCN-224 and Fe@PCN-224

PCN-224 were fabricated as reported. In a typical experiment, 100 mg H_2TCPP, 300 mg $ZrOCl_2{\cdot}8H_2O$, and 2.8 g benzoic acid were first dissolved in 100 mL DMF. Then, the solution was heated to 90°C for 5 h while stirring (300 rpm). Finally, the PCN- 224 were recovered by centrifugation and washing with DMF three times and stored in fresh DMF for further analysis.

As for Fe@PCN-224, typically, 30 mg of PCN-224 were dispersed in 10 mL DMF containing 40 mg of $FeCl_3$. The solution was stirred for 10 min at room temperature and then was heated at 120°C for 7 h with slow magnetic stirring. After the reaction, Fe@PCN-224 were collected by centrifugation and washing three times with DMF and stored in fresh DMF for further characterizations.

2.3 Preparation of PyroFPSH

A coprecipitation and stirring method was used to prepare the SAS@FeMOF loaded with arylsulfonamide pyridine. First, 10 mg of FeMOF was dispersed in 10 mL of an ethanol solution. Then, 10 mL of a DMSO solution containing dissolved SAS at a concentration of 1 mg/mL was added. The solution was then stirred overnight at room temperature, protected from light. Next, 5 mL of 1 mg/mL

FeMOF and SAS@FeMOF were mixed with 5 mL of hyaluronic acid (HA, Mw: 7.9 kDa) at 1 mg/mL and sonicated for 15 min. The obtained FeMOF@HA and PyroFPSH were collected and further purified by centrifugation. After stirring for 24 h, the nanoparticle was recovered by centrifugation at 1,200 rpm, where the modification of hyaluronic acid was characterized by FTIR. All supernatants were collected by centrifugation to measure the drug loading amount of SAS, and the absorbance value at 356 nm was detected by UV-Vis spectroscope to evaluate the loading capacity of SAS using the following formula:

Loading capacity = $(M_{SAS}-M_{uSAS})/M_{PyroFPSH}\times100\%$, where M_{SAS}, M_{uSAS}, and $M_{PyroFPSH}$ were the total mass of SAS unloaded SAS and PyroFPSH, respectively.

2.4 Enzyme-mimic catalysis

To test the peroxidase-like activity, a solution containing FeMOF@HA (100 μg/mL), TMB (0.5 mM) and H_2O_2 (0.5 mM) in acetate buffer (100 mM, pH 4.0) was incubated for 10 min, followed by absorption measurement at 652 nm.

To establish the correlation between GSH consumability and different concentrations of FeMOF@HA, a solution of 10 mM GSH and 20 μM DTNB was introduced into 1 mL of PBS solution. The solution was then centrifuged and the supernatant was subjected to UV-Vis spectroscopy for further examination.

2.5 Photodynamic activity test

The photodynamic activity was examined in the assay by DPBF or ABDA. For the former, 1 mL of DPBF solution (20 μg/mL) and 100 μL of FeMOF@HA dispersion (100 μg/mL) were mixed, followed by stirring in the dark for 2 h. A continuous semiconductor diode laser (660 nm) with a power density of 50 mW/cm^2 was then used as a light source for 5 min. Then, the samples were taken for UV-Vis measurements.

For the latter, 1 mL of ABDA solution (100 μg/mL) was mixed with 100 μL of FeMOF@HA (100 μg/mL). A continuous semiconductor diode laser (660 nm) with a power density of 50 mW/cm^2 was then used as a light source for 5 min. Then, the samples were taken for UV-Vis measurements.

2.6 •OH generation by FeMOF@HA

To evaluate the ability of FeMOF@HA to produce •OH, FeMOF@HA samples at different concentrations were mixed with DMPO. The mixture was then exposed to irradiation (660 nm, 100 mW/cm^2) for 5 min to assess the formation of •OH. The •OH formation served as an indicator of the nitrogen-trapping agent's efficacy.

2.7 GSH reduction–mediated $^1O_2$ generation of FeMOF@HA

Different concentrations of GSH (0 mM and 10 mM) were prepared and reacted with FeMOF@HA (100 μg/mL) under different pH conditions (pH 7.4 and pH 5.5). The production of $^1O_2$ was measured using ESR. For the reaction, 100 μL of H_2O_2 (10 mM), 600 μL of the reaction mixture, and 300 μL of PBS were mixed. The TEMP scavenger was added to capture $^1O_2$.

2.8 Cell viability assay

EMT-6 cells were planted in 96-well plates at a density of approximately 8×10^3 cells per well and incubated for 24 h, then incubated with different materials (FeMOF@HA, PyroFPSH, FeMOF@HA + Laser, PyroFPSH + Laser) for 24 h. After washing with PBS, the cells were irradiated with a 660 nm laser (50 mW/cm^2, 5 min). Cell viability was measured 24 h after laser irradiation. Cell viability was assessed using the crystal violet colorimetric assay. At the end of the incubation period, cells were washed with PBS and fixed CCK-8 to determine cell viability.

2.9 Detection of O_2 production

The O_2 generating ability of FeMOF@HA and PyroFPSH *in vitro* was evaluated using $[Ru(dpp)_3]Cl_2$. EMT-6 cells were incubated in a plate overnight. Then, 100 μL of $[Ru(dpp)_3]Cl_2$ (50 μM) PBS solution was added to the cells and incubated for another 4 h. Then, 0.6 mL of PBS solution containing 100 μg/mL FeMOF@HA and PyroFPSH was added to each well. The cells were then incubated for varying lengths of time, with or without a laser (660 nm, 50 mW/cm^2). Finally, the cells were observed using CLSM.

2.10 Intracellular ROS assay

EMT-6 cells (6×10^3 cells/well) were seeded in a 96-well plate and incubated for 12 h. The medium was replaced with complete RPMI 1640 medium containing different materials (FeMOF@HA, PyroFPSH, FeMOF@HA + Laser, PyroFPSH + Laser) at a dose of 100 μg/mL for 12 h. After washing with PBS, the cells were irradiated with a 660 nm laser (50 mW/cm^2, 5 min). The DCFH-DA was added following the standard protocol provided by the supplier. After 20 min of incubation, the cells were washed twice with PBS and the fluorescence images of the treated cells were captured under an inverted fluorescence microscope.

2.11 Establishment of orthotopic 4T1 tumor models

BALB/c mice (female, 6–8 weeks old) were obtained from Beijing Vital River Experimental Animal Technology Co. Ltd. All animal experiments were approved by the Institutional Animal Care and Use Committee of the Chinese Academy of Medical Sciences Institute of Tumors (NCNST21-2108-0610). All procedures were performed according to guidelines. To establish the tumor models, 2×10^6 EMT-6 cancer cells suspended in PBS were implanted subcutaneously into the right mammary fat pad of each mouse as primary tumors.

10.3389/fbioe.2023.1338257

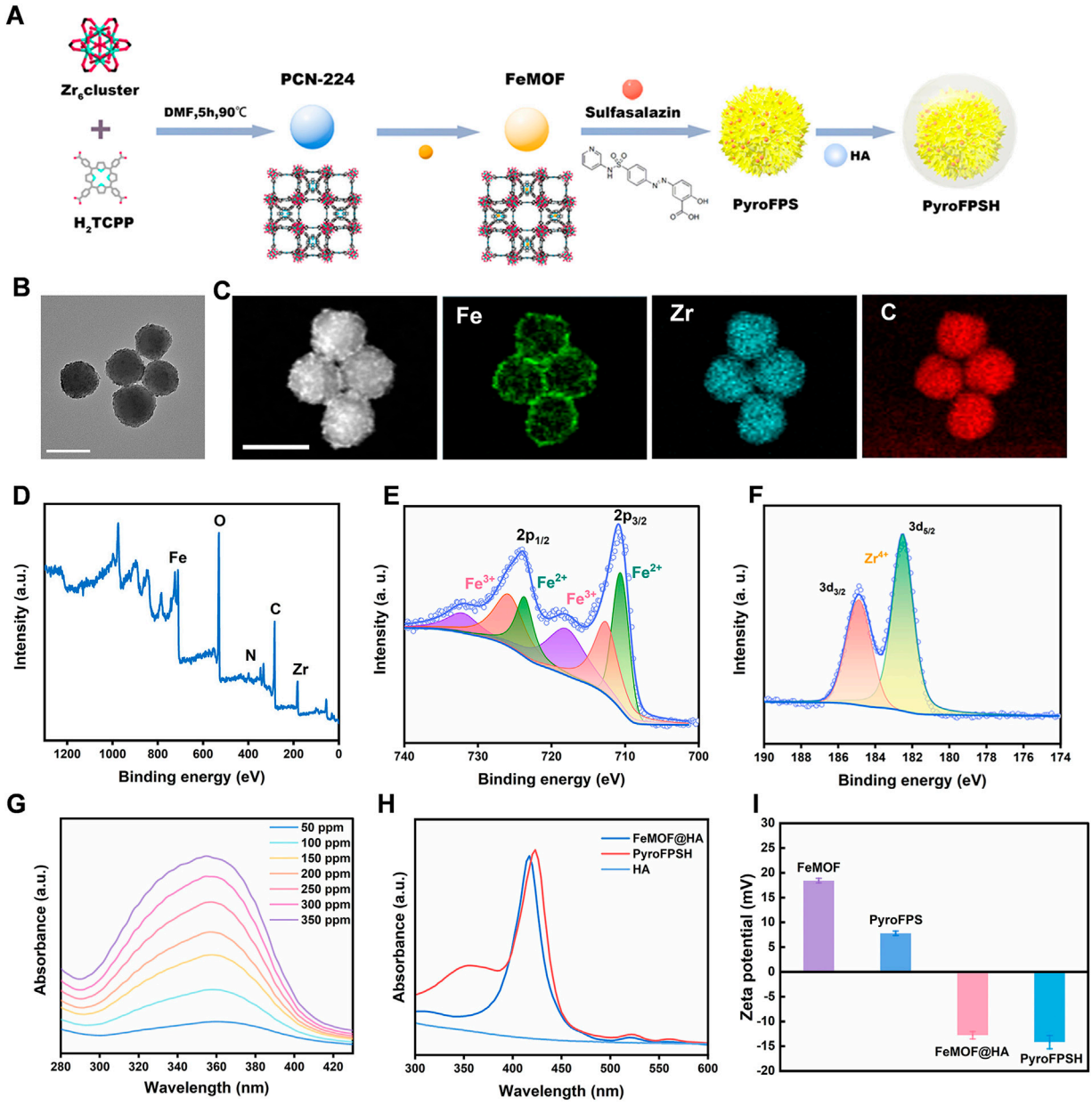

FIGURE 1
Synthesis and characterization of PyroFPSH. **(A)** The schematic of the synthetic preparation of FeMOF. **(B)** TEM image of FeMOF (scale bar: 100 nm). **(C)** HAADF-STEM image and elemental mapping of FeMOF (scale bar: 100 nm). **(D)** XPS spectrum of FeMOF. **(E)** High-resolution Fe 2p XPS spectrum of FeMOF. **(F)** High-resolution Zr 3d XPS spectrum of FeMOF. **(G)** UV-visible absorption spectra of sulfasalazine at different concentrations. **(H)** The UV-Vis absorption spectra of various samples including HA, FeMOF@HA, and PyroFPSH. **(I)** The zeta potential of different samples including FeMOF@HA, PyroFPS, FeMOF@HA, and PyroFPSH.

2.12 *In Vivo* therapeutic experiment

When the tumor size reached about 80 mm^3, the EMT-6 tumor-bearing BALB/c mice were randomly divided into eight groups (n = 5) and injected intratumorally with saline, FeMOF@HA, PyroFPSH (FeMOF@HA dose: 100 μg injected/mouse). After 12 h of injection, the mice were anesthetized with 2% (v/v) isoflurane and the tumors were irradiated with light (660 nm, 100 mW/cm^2, 5 min). Tumor sizes were measured daily with a caliper, with tumor volume equal to (width^2 × length)/2. The body weight of each group was monitored every 2 days. The mice were euthanized on day 14 and the excised tumors were photographed and weighed. Hematological and Histological Analysis.

Blood was collected from each mouse at day 14 and centrifuged at 2000 *g* for 15 min and the separated serum samples were tested for blood biochemical markers. The major organs (heart, liver, spleen, lung, and kidney) and the tumor were dissected and sectioned for TUNEL and H&E staining.

2.13 Statistical analyses

All results were presented as mean ± S.D. Means were indicated using the Student's t-test. Statistical significance was determined at a value of $^{*}p < 0.05$, $^{**}p < 0.01$, $^{***}p < 0.001$.

3 Results

3.1 Synthesis and characterization of the PyroFPSH

The synthesis of Fe@PCN-224 began with the preparation of PCN-224 using a well-established method (Figure 1A). Subsequently, Fe^{3+} was doped into the PCN-224 at 120°C for 8 h, resulting in the production of Fe@PCN-224 (Ding et al., 2020b). Once the reaction between Fe^{3+} and PCN-224 occurred, the resulting Fe@PCN-224, also known as FeMOF (Figure 1B), retained the same size and morphology as the original PCN-224 (Wang et al., 2021; Zhu et al., 2023). Additionally, STEM mapping images and energy dispersive spectroscopy (EDS) showed a uniform distribution of C, O, N, Zr, and Fe elements, confirming the successful synthesis of FeMOF (Supplementary Figure S1). The successful preparation of Fe@MOF was confirmed by energy dispersive X-ray spectrometer (EDS) analysis and the corresponding elemental mapping, which showed the coexistence of the elements Fe and Zr (Figure 1C). Further confirmation of the successful modification was obtained by XPS analysis performed to determine the chemical state of the Fe species in the Fe@MOF. The presence of Fe^{3+} was indicated by a peak at 711 eV in the Fe 2p core level spectrum (Figures 1D–F).

Sulfasalazine (SAS) is an FDA-approved small molecule drug. Research has shown that SAS can induce the accumulation of mitochondrial peroxides in tumor cells by weakening mitochondria's tolerance to reactive oxygen species (ROS). In this study, we developed a nanodrug delivery system, SAS@Fe@PCN-224 (PyroFPS), by co-incubating Fe@PCN-224 (FeMOF) with SAS. To improve the stability and dispersibility of SAS@FeMOF under physiological conditions, we further modified it with hyaluronic acid, resulting in HA-SAS@FeMOF (PyroFPSH) (Supplementary Figure S2). By comparing the observable differences in properties (like DLS and Zeta potential) of PyroFPSH with the original FeMOF before and after drug loading (Supplementary Figures S3–S5), we further confirm the successful HA coating and successful SAS loading (Figures 1G, H). When negatively charged sulfasalazine was loaded onto FeMOF, the surface potential changed from positive (18.6 mV) to negative (−12.4 mV). Compared to the positive potential of PyroFPS (8.28 mV), the potential of PyroFPSH decreases to −12.4 mV (Figure 1I), indicating that HA was successfully coated (Kim et al., 2019; Ding et al., 2020a).

3.2 Multienzyme activities of FeMOF@HA

Given the significant relationship between enzyme activity and anticancer properties, our investigation focused on whether FeMOF@HA has multienzyme-like activity (Chen et al., 2021a). The literature suggests that Fe ions, due to their peroxidase-like activity, can exploit the presence of H_2O_2 in tumor cells to generate significant hydroxyl radicals through the Fenton reaction. These radicals, in conjunction with the singlet oxygen generated during photodynamic therapy, cause oxidative damage to key intracellular organelles. To counteract this, tumor cells synthesize large amounts of GSH to compensate for oxidative damage and limit their susceptibility. Additionally, the Fe^{3+} generated from the H_2O_2 reaction interacts with the abundant intracellular GSH, attenuating the protective mechanism of tumor cells and augmenting the synergistic therapeutic effects of FeMOF@HA under diverse treatment regimens. Therefore, iron-based FeMOF@HA are an integral part of nanocatalytic therapy.

FeMOF@HA follow a definitive catalytic therapeutic mechanism. In the slightly alkaline tumor cell environment, Fe^{3+} in FeMOF@HA readily reacts with intracellular H_2O_2 to form O_2 and Fe^{2+}. The electrode redox potential for this reaction (Fe^{3+} to Fe^{2+} [$\varphi\theta(Fe^{3+}/Fe^{2+} = 0.77$ V)]) is significantly higher than that of H_2O_2 [$\varphi\theta(O_2/H_2O_2 = 0.68$ V)] and further substantiates the peroxidase-like (POD) activity of FeMOF@HA with the oxidation of tetramethylbenzidine (TMB) upon introduction of H_2O_2 (Figure 2A) (Li et al., 2019; Liang et al., 2021). This reaction yields a blue-green product with a peak absorption at 652 nm, confirming the peroxidase-like behavior of FeMOF@HA (Figures 2B, C). In summary, the multienzyme-like activity of FeMOF@HA allows it to neutralize ROS in tumor cells and enhance the efficacy of photodynamic therapy, resulting in improved antitumor treatment (Supplementary Figure S5).

Furthermore, FT-IR spectroscopy was used to analyze the incorporation of Fe^{3+}. The results showed that the asymmetric vibration absorption intensity of C=O and C-OH of both PCN-224 and Fe@MOF was significantly lower than that of H_2TCPP. This is attributed to the coordination between the Zr6 cluster and the carboxyl groups. Further evidence for Fe^{3+} coordination with porphyrin was provided by the symmetrical Fe-N stretching observed at approximately 1,000 cm^{-1} (Figure 2D). ICP-MS analysis revealed that the weight percentage of Fe in Fe@PCN-224 was 15%.

As illustrated in Figure 2E, the release of Fe ions remains minimal in the absence GSH, indicating the stable nature of FeMOF@HA. However, when FeMOF@HA is exposed to GSH, it triggers a sustained release of Fe ions (Liu et al., 2021b). FeMOF@HA not only mimics peroxidase and photosensitization activity, but also can deplete glutathione in tumor cells, thus amplifying ROS production and augmenting toxicity to tumor cells.

Tumor cells can often negate the effectiveness of ROS-based treatments by upregulating GSH expression. To investigate whether FeMOF@HA can counteract this mechanism, we used 5,5′-dinitrobenzoic acid (2-nitrobenzoic acid) dithioester (DTNB) to monitor GSH levels (Lin et al., 2018; Hu et al., 2019; Yi et al., 2021). DTNB serves as a reliable probe for the thiol group (-SH) in GSH and forms a compound with GSH that has a notable peak at 412 nm. Reduced absorption intensity would indicate GSH depletion. Consequently, FeMOF@HA was co-incubated with a 10 mM GSH solution, with the residual GSH being quantified at different incubation intervals using DTNB. The data in Figure 2F show that at a FeMOF@HA concentration of 100 μg/mL, the absorption peak at 412 nm disappears and only the DTNB absorption peak at 323 nm remains. This outcome supports the notion that FeMOF@HA

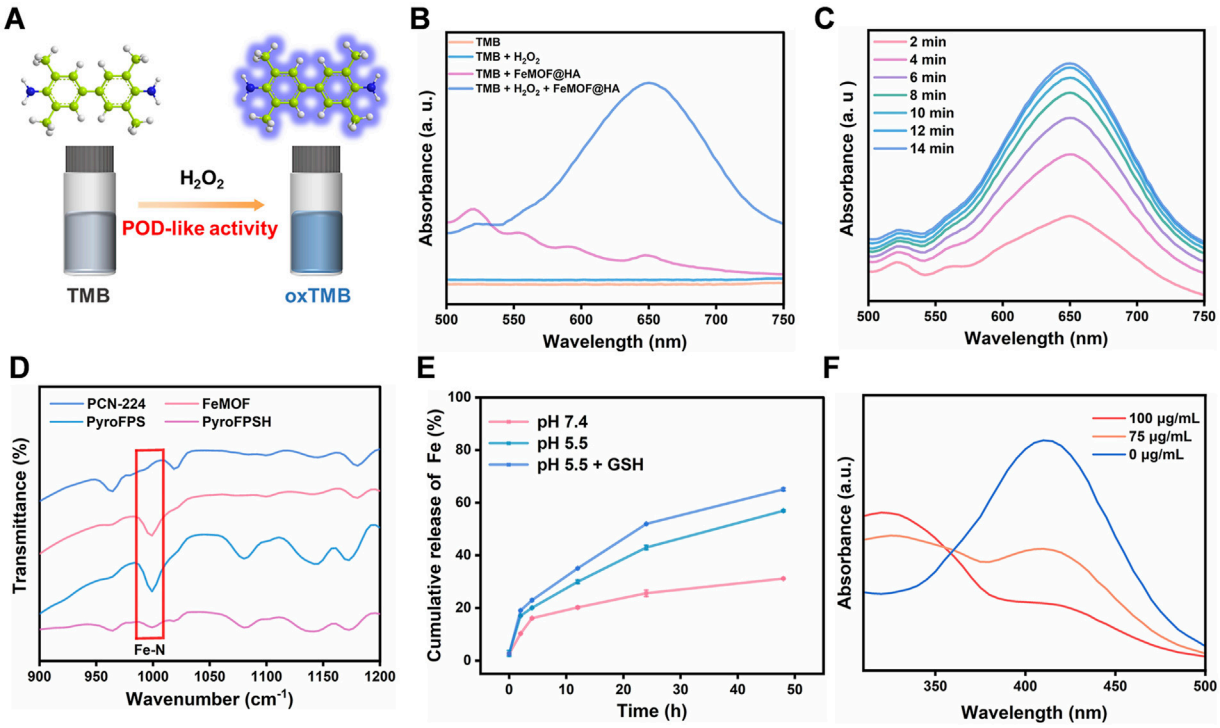

FIGURE 2
(A) The schematic diagram of the POD-like catalytic process of FeMOF@HA. **(B)** UV absorption spectra of the mixture of FeMOF@HA (100 μg/mL), TMB (0.5 mM), and H_2O_2 (0.5 mM). **(C)** Time-dependent changes in the absorption spectra of the mixture of FeMOF@HA (100 μg/mL), TMB (0.5 mM), and H_2O_2 (0.5 mM). **(D)** FT-IR spectroscopy of Fe-N. **(E)** The quantitative analysis of Fe release from FeMOF@HA (100 μg/mL), in different microenvironments (pH 7.4, pH 5.5, and pH 5.5 + GSH). Data represent the mean ± SD of 3 independent experiments. **(F)** UV–vis absorption spectra of DTNB (25 μg/mL) incubated with GSH (100 μM) plus FeMOF@HA.

consumes the ROS scavenger GSH and thereby maintains the ROS levels within cancer cells.

By exploiting their multienzyme-mimicking catalytic activity and GSH-depleting activity, FeMOF@HA could potentially enable efficacious nanocatalytic therapy. These unique properties position FeMOF@HA as a promising therapeutic approach with significant implications for future tumor treatment. Despite these encouraging findings, further research is required to verify the therapeutic efficacy and safety and to optimize the design of the drug delivery system.

3.3 Multienzyme activities of the FeMOF@HA

We began our study by using ROS indicators such as 1,3-diphenylisobenzofuran (DPBF) and 9,10-anthracene-bis (methylenemalonic acid) (ABDA) to evaluate the capacity of reactive oxygen species (ROS) generation under light exposure (Shi et al., 2020; Wang et al., 2020). Figure 3A illustrates that the generated ROS can undergo redox reactions with DPBF, as evidenced by a significant decrease in the UV-visible absorption peak at 411 nm. Notably, under 660 nm laser irradiation conditions of 100 mW/cm^2 and 50 mW/cm^2 for a duration of 5 min, the absorption intensity of FeMOF@HA rapidly decreased to 26% and 63% of the original value, respectively. This observation highlights the promising potential of FeMOF@HA for photodynamic therapy (PDT).

We first sought to evaluate the ability of FeMOF@HA to produce singlet oxygen, a key component for the effectiveness of photodynamic therapy. The FeMOF@HA were exposed to a laser power of 50 mW/cm^2 for 5 min, with generation of singlet oxygen leading to changes in ABDA UV absorption from 350–450 nm. Initial experiments without glutathione (GSH) showed minimal effects on photodynamic efficiency, with FeMOF@HA remaining largely unchanged under 5 min of 660 nm laser irradiation (50 mW/cm^2) and varying pH (Figures 3B, C). In summary, GSH concentration and pH had little influence on the photodynamic efficiency of FeMOF@HA. Subsequently, to further investigate how the photodynamic efficiency of FeMOF@HA is affected by high GSH concentrations, we simulated normal and tumor microenvironmental conditions. In contrast to normal conditions, the absorbance of FeMOF@HA decreased much faster under tumor conditions when exposed to the same 660 nm laser dose (Figures 3D, E). This enhanced absorption decrease signifies improved photodynamic efficiency specific to the tumor microenvironment. Overall, the increased photodynamic therapy activity can be attributed to FeMOF@HA in tumor environments (Figure 3F).

In addition, as shown in Figure 3G, the generation of •OH and $^1O_2$ was quantitatively evaluated using electron spin resonance (ESR) measurement, in which •OH was trapped by 5,5-dimethyl-1-pyrroline-N-oxide (DMPO) (Yang et al., 2020), and 2,2,6,6-tetramethylpiperidine (TEMP) was used to capture $^1O_2$ (Wu et al., 2022). As the concentration of FeMOF@HA nanoparticles increased,

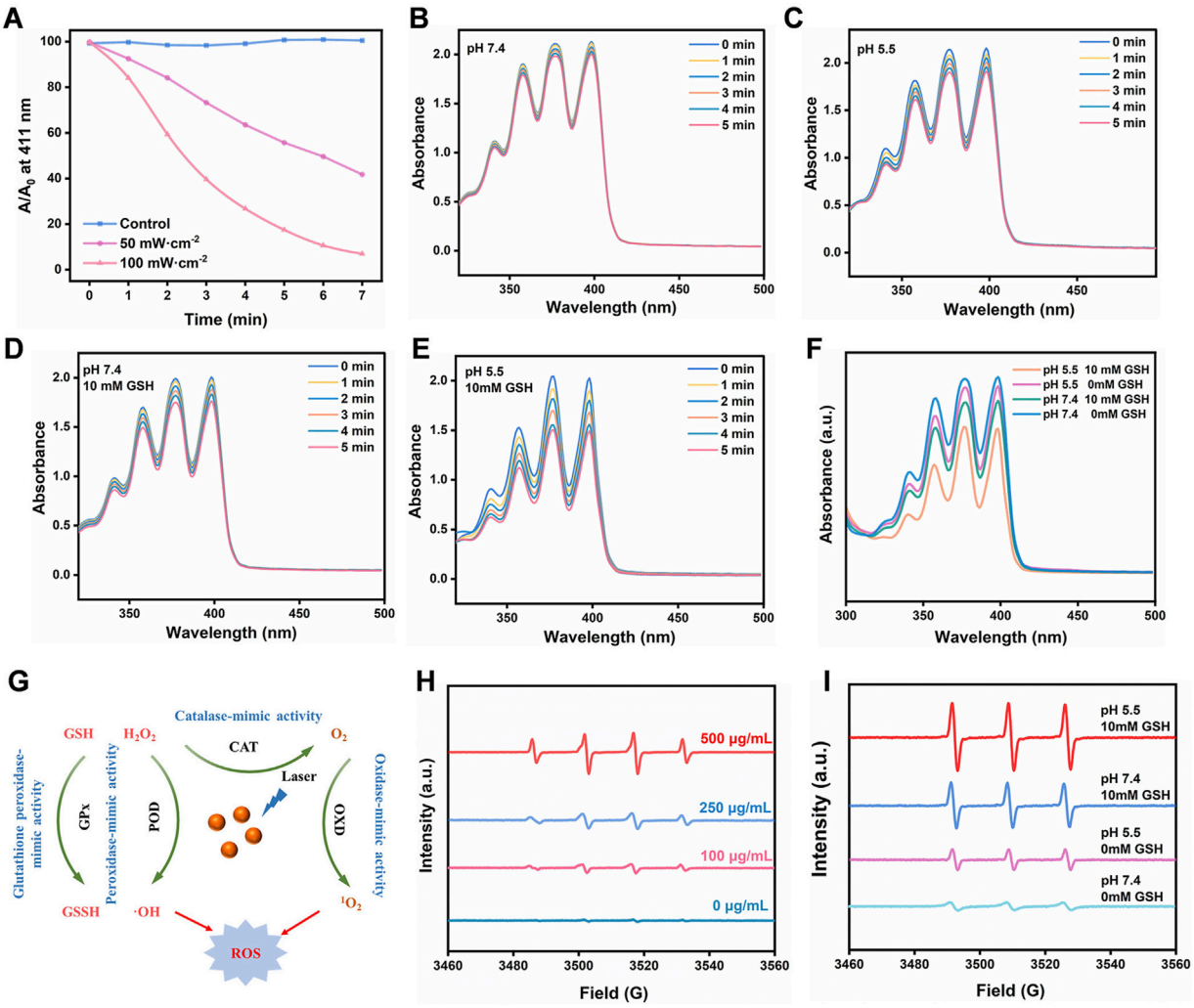

FIGURE 3
(A) Absorbance of DPBF solution (20 μg/mL) under 660 nm laser irradiation at different power levels. **(B–F)** Evaluation of the efficiency of singlet oxygen generation by FeMOF@HA under varying pH and GSH concentration conditions irradiated with a 660 nm laser at a power of 50 mW/cm^2, assessed by the photovoltaic changes in the signature peak absorbance (379 nm) of ABDA (100 μg/mL). **(G)** The overall multienzyme-like activity mechanism of FeMOF@HA. **(H)** The ESR spectra of ●OH in the presence of DMPO. **(I)** The ESR spectra of $^1O_2$ in the presence of TEMP.

the ESR signal steadily improved, and a stronger ESR signal of $^1O_2$ from FeMOF@HA was observed compared to other groups under 660 nm laser irradiation at pH 5.5 with 10 mM GSH (Figures 3H, I). These results suggest that the acidic conditions and high GSH concentrations in the tumor microenvironment could activate the fluorescence and PDT of the quenched FeMOF@HA, thereby minimizing the potential damage to normal cells by the photosensitizers.

In summary, our results clearly demonstrate that FeMOF@HA is able to effectively generate ROS, including ·OH and $^1O_2$, under light exposure, providing promising outcomes for photodynamic therapy.

3.4 Validation of the multienzyme-like activities

To evaluate the ability of FeMOF@HA and PyroFPSH to generate reactive oxygen species (ROS) in cells upon exposure to light, we used 2′,7′-dichlorodihydrofluorescein diacetate (DCFH-DA), a ROS probe that emits green fluorescence in the presence of ROS (Li et al., 2021; Wang et al., 2023). This feature was utilized in our investigations using confocal laser scanning microscopy (CLSM). As shown in Figure 4A, we made several interesting observations. Notably, groups treated with FeMOF@HA and PyroFPSH alone without laser exposure exhibited very weak fluorescence. However, when EMT-6 cells cultured with either FeMOF@HA or PyroFPSH were exposed to a 660 nm laser for 5 min, prominent green fluorescence was observed. This suggests that these nanoparticles produce only trace amounts of ROS without laser irradiation, but significantly enhance intracellular ROS levels upon irradiation. Therefore, under laser irradiation conditions, both FeMOF@HA and PyroFPSH show remarkable ROS-generating properties and potential for photodynamic therapy (PDT) applications.

Since SAS targets the mitochondria of tumor cells (Supplementary Figure S7), its mechanism of action involves

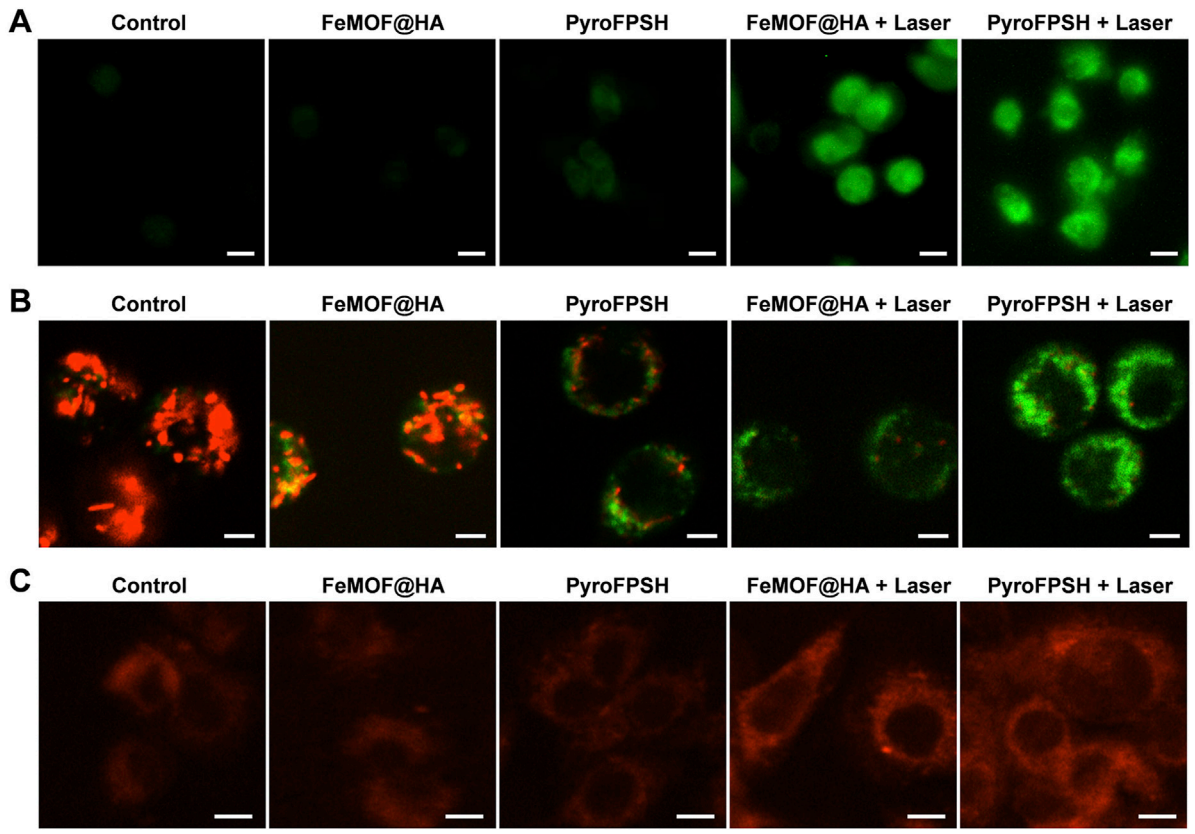

FIGURE 4
(A) CLSM images of EMT-6 cells stained with the ROS probe DCFH-DA under different treatments (scale bar: 20 μm). **(B)** JC-1 assay of EMT-6 tumor cells after coincubation with FeMOF@HA and PyroFPSH across different treatments (scale bar: 10 μm). **(C)** CLSM images of EMT-6 cells stained with O_2 probe RDPP under different treatments (scale bar: 10 μm).

reducing the resistance of tumor cells to ROS, thereby inducing mitochondrial polarization and tumor cell death (Bao et al., 2021). We hypothesized that the enhanced photodynamic effects of PyroFPSH and increased intracellular ROS levels are related to SAS-induced mitochondrial polarization. Our results showed that PyroFPSH induced the polarization of mitochondrial polarization more noticeably compared to FeMOF@HA under the same conditions, demonstrating the important role of SAS (Figure 4B).

We also investigated the catalysis of O_2 production by FeMOF@HA and PyroFPSH in EMT-6 cells using $[Ru(dpp)_3]Cl_2$ (RDPP) as an indicator (Hu et al., 2021). In tumor cells, the H_2O_2 concentration can be as high as 100 μM, which is significantly higher than in normal cells (below 20 nM). Therefore, an experiment using the O_2 probe RDPP was performed in live EMT-6 cells to confirm H_2O_2-triggered O_2 production. As shown in Figure 4C, the fluorescence intensity in the groups treated with FeMOF@HA and PyroFPSH is significantly lower than in the control group because the RDPP fluorescence can be quenched by O_2. When cells were treated with FeMOF@HA + Laser and PyroFPSH + Laser, the fluorescence intensity in the cells showed no significant change compared to the control group (Figure 4C). This clearly indicates that Fe^{3+} in FeMOF@HA and PyroFPSH catalyzes the production of O_2 within cells triggered by H_2O_2 and exhibits catalase-like enzyme activity. This not only overcomes the hypoxia of tumors but also facilitates the production of $^1O_2$ by PDT.

3.5 *In Vitro* therapeutic assessment at the cellular level

Considering the multienzyme-like activity and photodynamic therapy (PDT) effects of FeMOF@HA and PyroFPSH, we used Cell Counting Kit-8 (CCK-8) to examine the viability of EMT-6 cells under different treatment conditions (Figure 5A). First, we investigated the cytotoxicity of FeMOF@HA nanoparticles as a base carrier for EMT-6 cells. The results showed that FeMOF@HA had relatively low cytotoxicity. We then exposed EMT-6 tumor cells to different laser irradiation conditions (30 mW/cm^2 and 50 mW/cm^2) after treatment with 100 μg/mL FeMOF@HA. Cell viability decreased to 57.97% (660 nm, 30 mW/cm^2) and 42.63% (660 nm, 50 mW/cm^2), respectively (Figure 5B).

To assess the effect of SAS, we further examined its effects on cell viability (Figure 5C). EMT-6 cancer cells were coincubated with different concentrations of FeMOF@HA and PyroFPSH (0, 12.5, 25, 50, 75, and 100 μg/mL) for 48 h, followed by laser irradiation at 660 nm, 50 mW/cm^2 for 5 min. The activity of EMT-6 cells significantly decreased with increasing PyroFPSH concentration, suggesting that the addition of SAS can enhance the photodynamic therapy effect of PyroFPSH + Laser. The flow cytometry image (Figure 5D) showed varying degrees of apoptosis in the different treatment groups, which is consistent with the results of the CCK-8 cytotoxicity assay.

10.3389/fbioe.2023.1338257

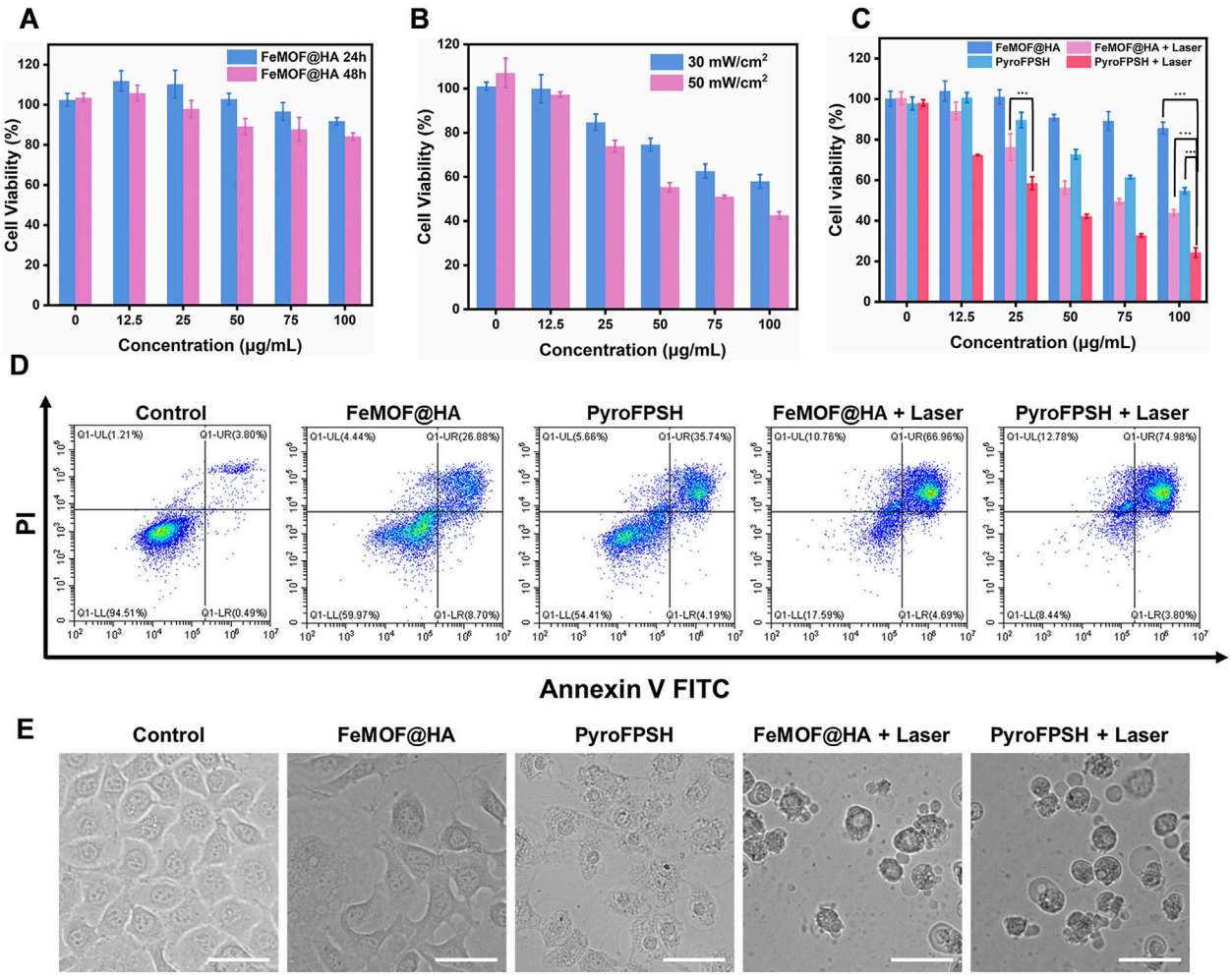

FIGURE 5
(A) Cell viability of EMT-6 cells incubated with FeMOF@HA for 24 h and 48 h at different concentrations. **(B)** Cell viability of EMT-6 cells coincubated with FeMOF@HA under 660 nm laser irradiation at power levels of 30 mW/cm^2 and 50 mW/cm^2. **(C)** Cell viability of EMT-6 cells was assessed 48 h post treatment with FeMOF@HA and PyroFPSH. The treatments were carried out with or without laser irradiation (660 nm, 50 mW/cm^2, 5 min). **(D)** Flow cytometry analysis of apoptosis of EMT-6 cells after different treatments. **(E)** Representative microscopy images (bright-field) of EMT-6 cancer cells after the different treatments. (Scale bar: 50 μm). Data are presented as the mean ± SD. Statistical analysis was performed using the Student's t-test (ns, nonsignificant. *$p < 0.05$, **$p < 0.01$, and ***$p < 0.001$).

Furthermore, the morphology of FeMOF@HA-treated cells showed no significant changes. However, treatment with FeMOF@HA + Laser, PyroFPSH, and PyroFPSH + Laser resulted in the appearance of obvious balloon-like membrane protrusions in EMT-6 cells (Figure 5E), which are characteristic features of cell death.

3.6 *In Vivo* antitumor effect

We monitored the biodistribution of various components of nanoparticles and observed effective accumulation of FeMOF@HA at the tumor site after intravenous injection, which exhibited strong fluorescence signals (Figure 6A). Additionally, Figure 6B showed that HA with a lower relative molecular weight increased the accumulation of nanoparticles at the tumor site while reducing the accumulation in the lung, indicating the tumor-targeting effect of HA *in vivo*.

Given the positive results obtained with FeMOF@HA and PyroFPSH in terms of catalytic, photodynamic, and cellular therapeutic effects, we evaluated their antitumor efficacy *in vivo*. A breast cancer model was established by subcutaneous injection of EMT-6 cells into female BALB/c mice at 3–4 weeks of age. The tumor-bearing mice were randomly divided into five groups (n = 5 per group): 1) control group; 2) FeMOF@HA group; 3) PyroFPSH group; 4) FeMOF@HA + Laser group; 5) PyroFPSH + Laser group (intravenous injection, 2 mg/kg). Each group received a tail vein injection and corresponding treatment every 12 h, with photodynamic therapy (660 nm, 100 mW/cm^2, 5 min) applied to the respective components on days 1, 3, and 5.

Figure 6C shows that mice treated with free FeMOF@HA, PyroFPSH, FeMOF@HA + Laser, and PyroFPSH + Laser exhibited tumor inhibition effects compared to the control group, with the PyroFPSH + Laser group demonstrating the strongest antitumor effects. The body weight and tumor volume of the

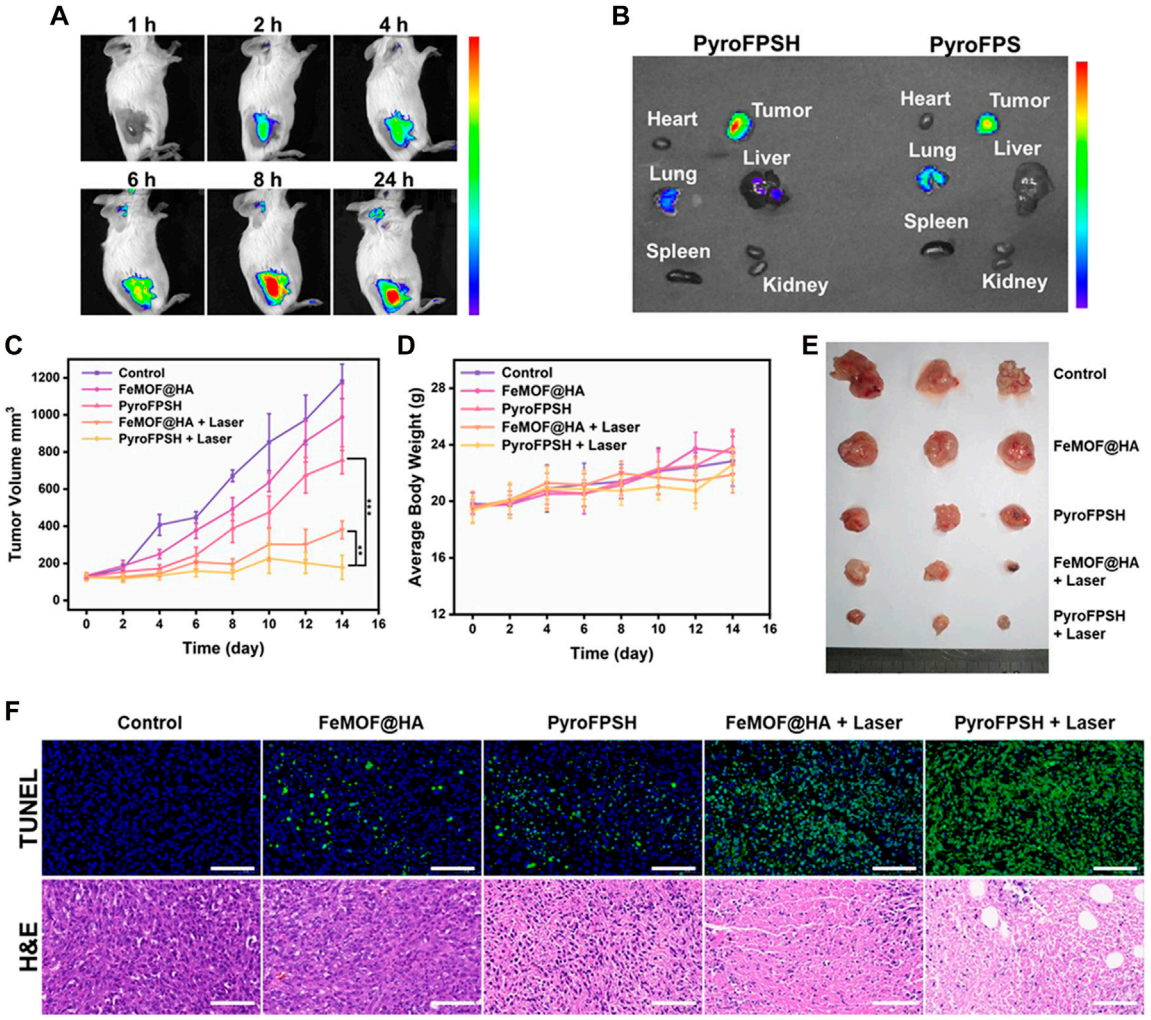

FIGURE 6
(A) FL imaging of EMT-6 tumor-bearing mice injected with PyroFPSH through the tail vein at different time points. **(B)** FL imaging of major organs and tumors 24 h post injection. **(C)** Schematic representation of the establishment and treatment of the EMT-6 tumor-bearing BALB/c mouse model. **(D)** Body weight of mice during 14 days of treatment. **(E)** Images of tumors after 14 days of treatment. **(F)** The representative H&E staining and TUNEL staining images of tumors with different treatments (scale bar: 50 μm). Data are presented as the mean ± SD. Statistical analysis was performed using one-way ANOVA.

mice were monitored every 2 days throughout the treatment period. Importantly, no significant changes in body weight were observed in any of the groups, indicating the high biosafety of the treatment (Figure 6D).

The final tumor volume and quality of excised tumors were consistent with the antitumor effects observed in different experimental groups (Figure 6E). To further investigate the therapeutic effects of the materials on tumor-bearing mice, tumor tissue sections from each group were stained with H&E and TUNEL, as shown in Figure 6F. In the five experimental groups, the rate of cell necrosis within the tumor tissue increased with increasing treatment intensity, indicating the therapeutic effects of the nano-drug delivery system. In addition, compared to the control group, the results of hematoxylin-eosin (H&E) staining of major organs (heart, liver, lungs, spleen, and kidneys) in mice (Supplementary Figure S8), as well as serum factor analysis, showed no significant pathological abnormalities or inflammatory lesions in the treatment group, confirming the excellent tissue compatibility of the materials (Supplementary Figure S9).

4 Conclusion

In conclusion, we developed PyroFPSH as a platform to synergize photodynamic therapy with multiple enzyme-mimicking activities for improved antitumor efficacy. The PyroFPSH integrate FeMOF@HA for enzyme-like activities, including peroxidase (POD), oxidase (OXD) to generate reactive oxygen species (ROS), and catalase (CAT) to counteract hypoxia. In addition, PyroFPSH contains SAS to induce mitochondrial dysfunction in tumor cells and reduce their metabolic activity and resistance to treatment. Mechanistically, SAS induces mitochondrial polarization in tumor cells through PyroFPSH, while photodynamic therapy simultaneously generates ROS. This

therapeutic window of mitochondrial polarization and elevated ROS results in potent cytotoxicity. Evaluations in an EMT-6 tumor model showed a significant inhibition of tumor growth. Overall, PyroFPSH can effectively induce tumor cell death by combining nanozyme activity with photodynamic and SAS combination therapy thereby presenting a promising new approach for cancer treatment.

Data availability statement

The original contributions presented in the study are included in the article/Supplementary Material, further inquiries can be directed to the corresponding authors.

Ethics statement

The animal study was approved by the Institutional Animal Care and Use Committee of the Chinese Academy of Medical Sciences Institute of Tumors (NCNST21-2108-0610). The study was conducted in accordance with the local legislation and institutional requirements.

Author contributions

LL: Conceptualization, Data curation, Formal Analysis, Investigation, Methodology, Software, Validation, Visualization, Writing–original draft. ZF: Conceptualization, Data curation, Formal Analysis, Investigation, Methodology, Validation, Writing–original draft. QY: Conceptualization, Formal Analysis, Methodology, Supervision, Validation, Writing–original draft. WX: Investigation, Software, Writing–original draft. HW: Formal Analysis, Resources, Writing–original draft. CW: Funding acquisition, Project administration, Supervision, Writing–review and editing. YY: Funding acquisition, Project administration, Supervision, Writing–review and editing.

Funding

The author(s) declare financial support was received for the research, authorship, and/or publication of this article. This work was supported by National Natural Science Foundation of China (Nos. 21721002, 32101130, and 31971295). Financial support from Strategic Priority Research Program of Chinese Academy of Sciences (XDB36000000) is also gratefully acknowledged.

Conflict of interest

The authors declare that the research was conducted in the absence of any commercial or financial relationships that could be construed as a potential conflict of interest.

Publisher's note

All claims expressed in this article are solely those of the authors and do not necessarily represent those of their affiliated organizations, or those of the publisher, the editors and the reviewers. Any product that may be evaluated in this article, or claim that may be made by its manufacturer, is not guaranteed or endorsed by the publisher.

Supplementary material

The Supplementary Material for this article can be found online at: https://www.frontiersin.org/articles/10.3389/fbioe.2023.1338257/full#supplementary-material

References

Bao, W., Liu, M., Meng, J., Liu, S., Wang, S., Jia, R., et al. (2021). MOFs-based nanoagent enables dual mitochondrial damage in synergistic antitumor therapy via oxidative stress and calcium overload. *Nat. Commun.* 12 (1), 6399. doi:10.1038/s41467-021-26655-4

Chen, G., Yang, Y., Xu, Q., Ling, M., Lin, H., Ma, W., et al. (2020). Self-amplification of tumor oxidative stress with degradable metallic complexes for synergistic cascade tumor therapy. *Nano Lett.* 20 (11), 8141–8150. doi:10.1021/acs.nanolett.0c03127

Chen, J., Wang, Y., Niu, H., Wang, Y., Wu, A., Shu, C., et al. (2021a). Metal–organic framework-based nanoagents for effective tumor therapy by dual dynamics-amplified oxidative stress. *ACS Appl. Mater. Interfaces* 13 (38), 45201–45213. doi:10.1021/acsami.1c11032

Chen, L., Huang, J., Li, X., Huang, M., Zeng, S., Zheng, J., et al. (2022). Progress of nanomaterials in photodynamic therapy against tumor. *Front. Bioeng. Biotechnol.* 10, 920162. doi:10.3389/fbioe.2022.920162

Chen, M., Yang, J., Zhou, L., Hu, X., Wang, C., Chai, K., et al. (2021b). Dual-responsive and ROS-augmented nanoplatform for chemo/photodynamic/chemodynamic combination therapy of triple negative breast cancer. *ACS Appl. Mater. Interfaces* 14 (1), 57–68. doi:10.1021/acsami.1c14135

Chen, X., Yin, X., Zhan, L., Zhang, J., Zhang, Y., Wu, Y., et al. (2021c). Organelle-specific anchored delivery system stretching a reversal of tumor hypoxia microenvironment to a combinational chemo-photothermal therapy. *Adv. Funct. Mater.* 32 (15). doi:10.1002/adfm.202108603

Cui, T., Zhang, Y., Qin, G., Wei, Y., Yang, J., Huang, Y., et al. (2023). A neutrophil mimicking metal-porphyrin-based nanodevice loaded with porcine pancreatic elastase for cancer therapy. *Nat. Commun.* 14 (1), 1974. doi:10.1038/s41467-023-37580-z

Cui, X., Du, K., Yuan, X., Xiao, W., Tao, Y., Xu, D., et al. (2021). A comparative study of the *in vitro* antitumor effect of mannose-doxorubicin conjugates with different linkers. *Drug Dev. Res.* 83, 646–658. doi:10.1002/ddr.21896

Ding, L., Lin, X., Lin, Z., Wu, Y., Liu, X., Liu, J., et al. (2020a). Cancer cell-targeted photosensitizer and therapeutic protein Co-delivery nanoplatform based on a metal–organic framework for enhanced synergistic photodynamic and protein therapy. *ACS Appl. Mater. Interfaces* 12 (33), 36906–36916. doi:10.1021/acsami.0c09657

Ding, Y., Xu, H., Xu, C., Tong, Z., Zhang, S., Bai, Y., et al. (2020b). A nanomedicine fabricated from gold nanoparticles-decorated metal–organic framework for cascade chemo/chemodynamic cancer therapy. *Adv. Sci.* 7 (17), 2001060. doi:10.1002/advs.202001060

Hu, C., Wang, J., Liu, S., Cai, L., Zhou, Y., Liu, X., et al. (2021). Urchin-shaped metal organic/hydrogen-bonded framework nanocomposite as a multifunctional nanoreactor for catalysis-enhanced synergetic therapy. *ACS Appl. Mater. Interfaces* 13 (4), 4825–4834. doi:10.1021/acsami.0c19584

Hu, H., Chen, J., Yang, H., Huang, X., Wu, H., Wu, Y., et al. (2019). Potentiating photodynamic therapy of ICG-loaded nanoparticles by depleting GSH with PEITC. *Nanoscale* 11 (13), 6384–6393. doi:10.1039/c9nr01306g

Hu, H., Liu, X., Hong, J., Ye, N., Xiao, C., Wang, J., et al. (2022). Mesoporous polydopamine-based multifunctional nanoparticles for enhanced cancer phototherapy. *J. Colloid Interface Sci.* 612, 246–260. doi:10.1016/j.jcis.2021.12.172

Jiang, Q., Wang, K., Zhang, X., Ouyang, B., Liu, H., Pang, Z., et al. (2020). Platelet membrane-camouflaged magnetic nanoparticles for ferroptosis-enhanced cancer immunotherapy. *Small* 16 (22), e2001704. doi:10.1002/smll.202001704

Kang, Y., Sun, W., Li, S., Li, M., Fan, J., Du, J., et al. (2019). Oligo hyaluronan-coated silica/hydroxyapatite degradable nanoparticles for targeted cancer treatment. *Adv. Sci.* 6 (13), 1900716. doi:10.1002/advs.201900716

Kim, K., Lee, S., Jin, E., Palanikumar, L., Lee, J. H., Kim, J. C., et al. (2019). MOF × biopolymer: collaborative combination of metal–organic framework and biopolymer for advanced anticancer therapy. *ACS Appl. Mater. Interfaces* 11 (31), 27512–27520. doi:10.1021/acsami.9b05736

Li, T., Hu, P., Li, J., Huang, P., Tong, W., and Gao, C. (2019). Enhanced peroxidase-like activity of Fe@PCN-224 nanoparticles and their applications for detection of H2O2and glucose. *Colloids Surfaces A Physicochem. Eng. Aspects* 577, 456–463. doi:10.1016/j.colsurfa.2019.06.012

Li, Z.-H., Chen, Y., Zeng, X., and Zhang, X.-Z. (2021). Ultra-small FePt/siRNA loaded mesoporous silica nanoplatform to deplete cysteine for enhanced ferroptosis in breast tumor therapy. *Nano Today* 38, 101150. doi:10.1016/j.nantod.2021.101150

Liang, X., Chen, M., Bhattarai, P., Hameed, S., Tang, Y., and Dai, Z. (2021). Complementing cancer photodynamic therapy with ferroptosis through iron oxide loaded porphyrin-grafted lipid nanoparticles. *ACS Nano* 15 (12), 20164–20180. doi:10.1021/acsnano.1c08108

Lin, L. S., Song, J., Song, L., Ke, K., Liu, Y., Zhou, Z., et al. (2018). Simultaneous fenton-like ion delivery and glutathione depletion by MnO2-based nanoagent to enhance chemodynamic therapy. *Angew. Chem. Int. Ed.* 57 (18), 4902–4906. doi:10.1002/anie.201712027

Liu, N., Zhang, J., Yin, M., Liu, H., Zhang, X., Li, J., et al. (2021a). Inhibition of xCT suppresses the efficacy of anti-PD-1/L1 melanoma treatment through exosomal PD-L1-induced macrophage M2 polarization. *Mol. Ther.* 29 (7), 2321–2334. doi:10.1016/j.ymthe.2021.03.013

Liu, Z., Hu, C., Liu, S., Cai, L., Zhou, Y., and Pang, M. (2021b). Facile synthesis of Fe–baicalein nanoparticles for photothermal/chemodynamic therapy with accelerated FeIII/FeII conversion. *J. Mater. Chem. B* 9 (15), 3295–3299. doi:10.1039/d1tb00200g

Mao, C., Liu, X., Zhang, Y., Lei, G., Yan, Y., Lee, H., et al. (2021). DHODH-mediated ferroptosis defence is a targetable vulnerability in cancer. *Nature* 593 (7860), 586–590. doi:10.1038/s41586-021-03539-7

Meng, X., Li, D., Chen, L., He, H., Wang, Q., Hong, C., et al. (2021). High-performance self-cascade pyrite nanozymes for apoptosis–ferroptosis synergistic tumor therapy. *ACS Nano* 15 (3), 5735–5751. doi:10.1021/acsnano.1c01248

Ruan, J., Liu, H., Chen, B., Wang, F., Wang, W., Zha, Z., et al. (2021). Interfacially engineered $Zn_xMn_{1-x}S$@polydopamine hollow nanospheres for glutathione depleting photothermally enhanced chemodynamic therapy. *ACS Nano* 15 (7), 11428–11440. doi:10.1021/acsnano.1c01077

Shen, J., Rees, T. W., Zhou, Z., Yang, S., Ji, L., and Chao, H. (2020). A mitochondria-targeting magnetothermogenic nanozyme for magnet-induced synergistic cancer therapy. *Biomaterials* 251, 120079. doi:10.1016/j.biomaterials.2020.120079

Shi, Z., Zhang, K., Zada, S., Zhang, C., Meng, X., Yang, Z., et al. (2020). Upconversion nanoparticle-induced multimode photodynamic therapy based on a metal–organic framework/titanium dioxide nanocomposite. *ACS Appl. Mater. Interfaces* 12 (11), 12600–12608. doi:10.1021/acsami.0c01467

Sun, X., He, G., Xiong, C., Wang, C., Lian, X., Hu, L., et al. (2021). One-pot fabrication of hollow porphyrinic MOF nanoparticles with ultrahigh drug loading toward controlled delivery and synergistic cancer therapy. *ACS Appl. Mater. Interfaces* 13 (3), 3679–3693. doi:10.1021/acsami.0c20617

Wan, S. S., Liu, M. D., Cheng, Q., Cheng, H., and Zhang, X. Z. (2020). A mitochondria-driven metabolic sensing nanosystem for oxygen availability and energy blockade of cancer. *Adv. Ther.* 3 (6). doi:10.1002/adtp.202000019

Wan, X., Zhong, H., Pan, W., Li, Y., Chen, Y., Li, N., et al. (2019). Programmed release of dihydroartemisinin for synergistic cancer therapy using a CaCO3 mineralized metal–organic framework. *Angew. Chem. Int. Ed.* 58 (40), 14134–14139. doi:10.1002/anie.201907388

Wang, B., Dai, Y., Kong, Y., Du, W., Ni, H., Zhao, H., et al. (2020). Tumor microenvironment-responsive Fe(III)–Porphyrin nanotheranostics for tumor imaging and targeted chemodynamic–photodynamic therapy. *ACS Appl. Mater. Interfaces* 12 (48), 53634–53645. doi:10.1021/acsami.0c14046

Wang, C., Yang, X., Qiu, H., Huang, K., Xu, Q., Zhou, B., et al. (2023). A co-delivery system based on chlorin e6-loaded ROS-sensitive polymeric prodrug with self-amplified drug release to enhance the efficacy of combination therapy for breast tumor cells. *Front. Bioeng. Biotechnol.* 11, 1168192. doi:10.3389/fbioe.2023.1168192

Wang, Z., Liu, B., Sun, Q., Feng, L., He, F., Yang, P., et al. (2021). Upconverted metal–organic framework janus architecture for near-infrared and ultrasound Co-enhanced high performance tumor therapy. *ACS Nano* 15 (7), 12342–12357. doi:10.1021/acsnano.1c04280

Wu, H., Wu, F., Zhou, T., Hu, Z., Wang, W., Liang, X., et al. (2022). Activatable autophagy inhibition-primed chemodynamic therapy via targeted sandwich-like two-dimensional nanosheets. *Chem. Eng. J.* 431, 133470. doi:10.1016/j.cej.2021.133470

Xin, H., Huang, Y., Tang, H., Chen, Y., Xia, H., Zhang, F., et al. (2021). Delivery of a system xc−inhibitor by a redox-responsive levodopa prodrug nanoassembly for combination ferrotherapy. *J. Mater. Chem. B* 9 (35), 7172–7181. doi:10.1039/d1tb00742d

Xu, R., Yang, J., Qian, Y., Deng, H., Wang, Z., Ma, S., et al. (2021). Ferroptosis/pyroptosis dual-inductive combinational anti-cancer therapy achieved by transferrin decorated nanoMOF. *Nanoscale Horizons* 6 (4), 348–356. doi:10.1039/d0nh00674b

Yang, B., Ding, L., Yao, H., Chen, Y., and Shi, J. (2020). A metal-organic framework (MOF) Fenton nanoagent-enabled nanocatalytic cancer therapy in synergy with autophagy inhibition. *Adv. Mater.* 32 (12), e1907152. doi:10.1002/adma.201907152

Yang, F., Yu, W., Yu, Q., Liu, X., Liu, C., Lu, C., et al. (2023). Mitochondria-targeted nanosystem with reactive oxygen species-controlled release of CO to enhance photodynamic therapy of PCN-224 by sensitizing ferroptosis. *Small* 19 (16), e2206124. doi:10.1002/smll.202206124

Yi, X., Zeng, W., Wang, C., Chen, Y., Zheng, L., Zhu, X., et al. (2021). A step-by-step multiple stimuli-responsive metal-phenolic network prodrug nanoparticles for chemotherapy. *Nano Res.* 15 (2), 1205–1212. doi:10.1007/s12274-021-3626-2

Zhang, L., Li, X., Yue, G., Guo, L., Hu, Y., Cui, Q., et al. (2023). Nanodrugs systems for therapy and diagnosis of esophageal cancer. *Front. Bioeng. Biotechnol.* 11, 1233476. doi:10.3389/fbioe.2023.1233476

Zhou, B., Zhang, J.-y., Liu, X.-s., Chen, H.-z., Ai, Y.-l., Cheng, K., et al. (2018). Tom20 senses iron-activated ROS signaling to promote melanoma cell pyroptosis. *Cell Res.* 28 (12), 1171–1185. doi:10.1038/s41422-018-0090-y

Zhou, M., Wen, L., Wang, C., Lei, Q., Li, Y., and Yi, X. (2022). Recent advances in stimuli-sensitive amphiphilic polymer-paclitaxel prodrugs. *Front. Bioeng. Biotechnol.* 10, 875034. doi:10.3389/fbioe.2022.875034

Zhu, L., Gui, T., Song, P., Li, W., Wang, J., Hu, C., et al. (2023). Metal–organic framework PCN-224 integrated with manganese dioxide, platinum nanoparticles, and glucose oxidase for enhanced cancer chemodynamic therapy. *ACS Appl. Nano Mater.* 6 (9), 7446–7455. doi:10.1021/acsanm.3c00610

frontiers | Frontiers in Bioengineering and Biotechnology

TYPE Original Research
PUBLISHED 13 February 2024
DOI 10.3389/fbioe.2024.1364975

OPEN ACCESS

EDITED BY
Qitong Huang,
Gannan Medical University, China

REVIEWED BY
Wenbo Wu,
Tianjin University, China
Shirong Hu,
Minnan Normal University, China

*CORRESPONDENCE
Xinyuan Zhu,
xyzhu@sjtu.edu.cn
Guolin Li,
liguolin@jmsu.edu.cn

RECEIVED 03 January 2024
ACCEPTED 30 January 2024
PUBLISHED 13 February 2024

CITATION
Zhang T, Li X, Wu L, Su Y, Yang J, Zhu X and Li G (2024), Enhanced cisplatin chemotherapy sensitivity by self-assembled nanoparticles with Olaparib.
Front. Bioeng. Biotechnol. 12:1364975.
doi: 10.3389/fbioe.2024.1364975

Enhanced cisplatin chemotherapy sensitivity by self-assembled nanoparticles with Olaparib

Tao Zhang[1], Xiao Li[2], Liang Wu[3], Yue Su[3], Jiapei Yang[3], Xinyuan Zhu[3]* and Guolin Li[1,4]*

[1]Key Laboratory of Microecology-immune Regulatory Network and Related Diseases, School of Basic Medicine, Jiamusi University, Jiamusi, China, [2]Department of Oral and Maxillofacial Surgery, The First Affiliated Hospital of Harbin Medical University, Harbin, China, [3]School of Chemistry and Chemical Engineering, State Key Laboratory of Metal Matrix Composites, Shanghai Jiao Tong University, Shanghai, China, [4]Department of Oral, Shanghai Eighth People's Hospital, Xuhui Branch of Shanghai Sixth People's Hospital, Shanghai, China

Cisplatin (CDDP) is widely used as one kind of chemotherapy drugs in cancer treatment. It functions by interacting with DNA, leading to the DNA damage and subsequent cellular apoptosis. However, the presence of intracellular PARP1 diminishes the anticancer efficacy of CDDP by repairing DNA strands. Olaparib (OLA), a PARP inhibitor, enhances the accumulation of DNA damage by inhibiting its repair. Therefore, the combination of these two drugs enhances the sensitivity of CDDP chemotherapy, leading to improved therapeutic outcomes. Nevertheless, both drugs suffer from poor water solubility and limited tumor targeting capabilities. To address this challenge, we proposed the self-assembly of two drugs, CDDP and OLA, through hydrogen bonding to form stable and uniform nanoparticles. Self-assembled nanoparticles efficiently target tumor cells and selectively release CDDP and OLA within the acidic tumor microenvironment, capitalizing on their respective mechanisms of action for improved anticancer therapy. *In vitro* studies demonstrated that the CDDP-OLA NPs are significantly more effective than CDDP/OLA mixture and CDDP at penetrating cancer cells and suppressing their growth. *In vivo* studies revealed that the nanoparticles specifically accumulated at the tumor site and enhanced the therapeutic efficacy without obvious adverse effects. This approach holds great potential for enhancing the drugs' water solubility, tumor targeting, bioavailability, and synergistic anticancer effects while minimizing its toxic side effects.

KEYWORDS

cisplatin, olaparib, enhanced chemotherapy sensitivity, self-assembly, nanoparticles

Abbreviations: BCA, bicinchoninic acid; CDDP, Cisplatin; CDDP-OLA NPs, Cisplatin-Olaparib nanoparticles; DLS, dynamic light scattering; DMEM, Dulbecco's Modified Eagle's Medium; DMSO, Dimethyl sulfoxide; DMSO-d6, Deuterium dimethylsulphoxide; EPR, enhanced permeability and retention; FT-IR, Fourier transform infrared; FBS, Fetal Bovine Serum; H&E, Hematoxylin and Eosin; LSCM, laser-scanning confocal microscopy; MD, molecular dynamics; MMP, mitochondrial membrane potential; MTT, 3-(4,5-dimethyl-2-thiazolyl)-2,5-diphenyl-2H-tetrazolium bromide; NMR, nuclear magnetic resonance; NPs, nanoparticles; OLA, Olaparib; PARP1, Poly (ADP-ribose) polymerase 1; PBS, Phosphate Buffered Saline; Pt, platinum; PME, particle-mesh Ewald; PVDF, polyvinylidene fluoride; RIPA, radioimmunoprecipitation assay; RDF, radial distribution function; TBST, Tris-buffered saline with Tween; TEM, transmission electron microscope; UV, ultraviolet; vdW, van der Waals; Vis, visible; XPS, X-ray photoelectron spectroscopy.

Introduction

Cancer stands as an imperative global health concern of unparalleled magnitude (Bray et al., 2018; Siegel et al., 2021). The primary treatment methods for cancer currently include surgery, radiation therapy, stem cell therapy (Chen et al., 2022) and chemotherapy. Cisplatin (CDDP) holds a prominent position for cancer therapy due to its extensive utilization (Wang and Lippard, 2005). It operates by engaging with purine bases on DNA, thereby inducing DNA damage, activating diverse signal pathways, and culminating in cellular apoptosis. Nonetheless, the existence of intracellular PARP1 (Poly (ADP-ribose) polymerase 1) plays a pivotal role in identifying and mending DNA strand breaks, consequently impeding the anticancer effectiveness of CDDP (Chaudhuri and Nussenzweig, 2017). Over the span of the preceding four decades, researchers have devoted their efforts to the development of numerous PARP1 inhibitors, among which Olaparib (OLA) stands out as a noteworthy drug (Farmer et al., 2005; Ledermann et al., 2014; Lord and Ashworth, 2017). As a PARP1 inhibitor, OLA augments the accumulation of DNA damage by impeding its repair. Based on the mechanism of action of drugs, OLA can enhance the anticancer sensitivity of CDDP. Therefore, the synergistic utilization of CDDP and OLA emerges as a promising and more effective treatment approach. This strategic alliance between CDDP and OLA holds great potential in improving cancer treatment efficacy (Prasad et al., 2017). However, prevailing combination therapies predominantly rely on a rudimentary physical blend of two chemotherapeutic drugs. The contrasting physical and chemical attributes of two drugs, coupled with their distinct pharmacokinetic profiles, posed a formidable challenge in maintaining an equitable distribution ratio within tumor tissue. Moreover, both CDDP and OLA exhibit limited water solubility and lack tumor targeting capabilities, further impeding the realization of optimal outcomes in combination therapy.

In recent years, the field of combined cancer therapy has witnessed widespread utilization of nanotechnology-based drug delivery systems, aiming to reduce drug toxicity and enhance drug bioavailability (Zhao et al., 2020; Yi et al., 2022; Jiang et al., 2023; Wang et al., 2023). These systems included liposomes (Liu et al., 2022), polymer nanoparticles, and hydrogels. For instance, Yuan et al. designed polyethylene glycol-modified nano-liposomes to facilitate the simultaneous delivery of docetaxel and resveratrol (Zhang et al., 2022). Wang and Li developed MPPD@IR825/DTX NPs, which utilized a pH-responsive charge-reversal mechanism to enable targeted delivery of docetaxel and a photosensitizer (IR825), enabling chemo-photothermal combination therapy (Wang et al., 2022). Li, Jin, and their research team created a nano-vaccine that responds to the tumor microenvironment. The vaccine was based on biodegradable hollow manganese dioxide and enabled synergistic cancer therapy (Wang et al., 2022). Additionally, Li and colleagues designed an injectable pH-responsive OE peptide hydrogel as a carrier material for the anticancer drugs gemcitabine and paclitaxel (Liu et al., 2022). These endeavors successfully addressed the issue of limited utilization of chemotherapeutic drugs caused by their poor water solubility. They also enhanced the tumor targeting abilities of drugs and mitigated toxic side effects on healthy organs. However, it is crucial to note that nano-scale drug delivery systems heavily relied on the use of exogenous carriers, which posed challenges in clinical applications. Limited drug loading efficiency and the complex metabolic, degradation, and excretion processes of these carriers within the body increased the potential risk of adverse reactions related to toxicity or the immune system.

To address these issues, the carrier-free strategy has been developed as a suitable choice. Carrier-free self-assembly strategy enhanced drug targeting to tumors, improved drug efficacy, mitigated the toxic side effects of chemotherapy drugs, and avoided the risks associated with carriers (Song et al., 2012; Huang et al., 2014; Zhang et al., 2015; Zhu et al., 2020). This strategy utilized intermolecular interactions for self-assembly into defined nanostructures (Zhang et al., 2017; Wu et al., 2018). Based on the chemical structures of CDDP and OLA, as well as the enhanced the CDDP chemotherapy sensitivity by OLA, we proposed the self-assembly of CDDP and OLA through hydrogen bonding to form stable and homogeneous nanoparticles (CDDP-OLA NPs). This nanosizing strategy improved the aqueous solubility of both drugs, eliminated the need for exogenous carriers and enabled targeted delivery to the tumor site through enhanced permeability and retention (EPR) effects. These enhancements resulted in improved properties that facilitated apoptosis in cancer cells while minimized harmful effects on normal cells. The acidic tumor microenvironment disrupted hydrogen bonding, leading to the liberation of free CDDP and OLA. CDDP, with its ability to induce DNA damage, initiated the apoptotic process, while OLA augmented the anticancer sensitivity of CDDP by inhibiting PARP activity, thereby reducing the repair of damaged DNA. Due to their mechanisms of action, it is highly plausible that the combination of these two drugs within nanoparticles can enhance efficacy against cancer, while minimize the toxic side effects associated with chemotherapy drugs (Scheme 1).

Experimental

Materials

All reagents used in this study were commercially available and did not undergo any additional purification. CDDP and OLA were obtained from Meilun Biotech (Dalian, China). Dimethyl sulfoxide (DMSO) was supplied by Sinopharm Chemical Reagent Co., Ltd. (Shanghai, China). Phosphate Buffered Saline (PBS), Dulbecco's Modified Eagle's Medium (DMEM), Fetal Bovine Serum (FBS), 0.25% pancreatin, and penicillin-streptomycin (100×) were acquired from Gibco (Grand Island, USA). 3-(4,5-dimethyl-2-thiazolyl)-2,5-diphenyl-2H-tetrazolium bromide (MTT), Annexin V-FITC/PI apoptosis detection kits, cell cycle test kits, and mitochondrial membrane potential (MMP) detection kits were obtained from Beyotime Biotechnology Co., LTD. (Shanghai, China). Hoechst live cell stain was acquired from Sigma Aldrich Co. (St Louis, MO, USA). All

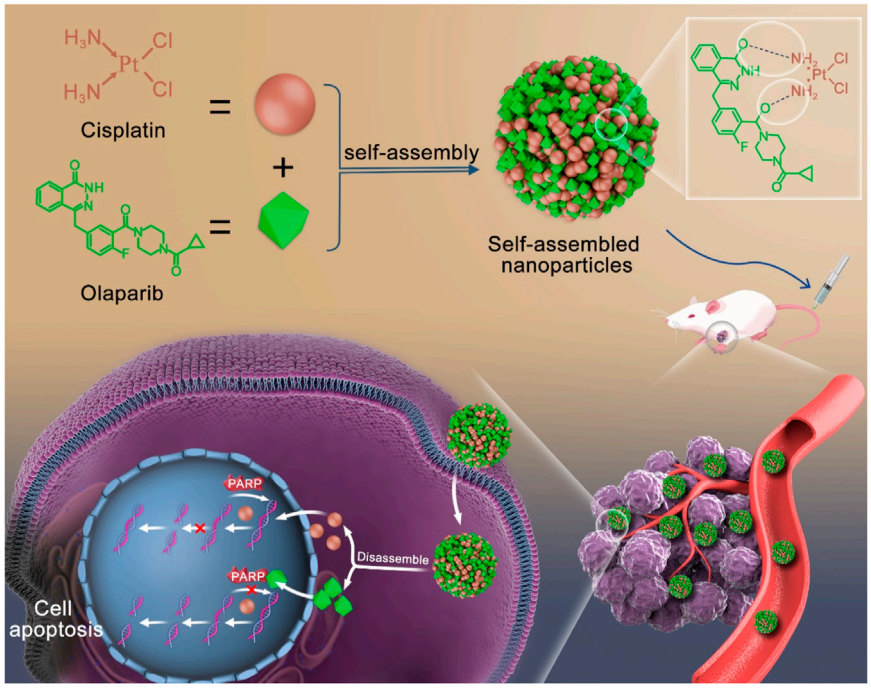

SCHEME 1
Schematic diagram of self-assembly route of CDDP-OLA nanoparticles and their synergistic mechanism.

antibodies used for Western blotting were purchased from Affinity Biosciences (Jiangsu, China), and the protein ladder was obtained from ThermoFisher Scientific (Waltham, MA, USA). Cell experiment consumables were sourced from Corning Incorporated (Corning, NY, USA).

Preparation of CDDP-OLA NPs

To fabricate CDDP-OLA NPs, CDDP (2.98 mg, 1 mmol) and OLA (4.34 mg, 1 mmol) were individually dissolved in 20 μL of DMSO. Subsequently, the solutions of CDDP and OLA were combined and added to 2 mL of ultrapure water under stirring, followed by an additional 10 min of stirring. To eliminate DMSO and unbound drug, we conducted the purification of CDDP-OLA NPs through ultrafiltration centrifugation. The ultrafiltration process employed a molecular weight cut-off of 500, and the centrifugation was carried out at 4°C for 10 min at 4,500 rpm.

Characterization of CDDP-OLA NPs

A total of 10 μL of freshly made CDDP-OLA NPs was dropped onto copper grids with a carbon film and left to stand for 10 min. A transmission electron microscope (Tecnai G2 Spirit Biotwin; FEI, Hillsboro, OR, USA) was utilized, with the voltage set at 120 kV, to image the dimensions and form of CDDP-OLA NPs. Dynamic light scattering (DLS; Zetasizer Nano ZS90, Malvern, England) was utilized at a temperature of 25°C to evaluate the size distribution of CDDP-OLA NPs in hydrodynamic fluid with 2 mL of the solution in disposable plastic cuvettes. The FT-IR spectra of CDDP-OLA NPs at 303, 333, 363, 393 and 423 K were determined using an FT-IR spectrometer (Nicolet 6700, ThermoFisher Scientific, Waltham, MA, USA). The scanning parameters were as follows: scan frequency range, 400–4,000 cm^{-1}; resolution, 4.0 cm^{-1}; and scan times, 32. A 400 MHz nuclear magnetic resonance (NMR) spectrometer (Avance III 400 MHz, Bruker, Germany) was used to measure the ^{1}H NMR spectra at various temperatures: 303, 333, 363, and 393 K. Deuterium dimethylsulphoxide (DMSO-d_6) was used to dissolve the samples. With an ultraviolet (UV)-visible (Vis) Spectrophotometer (UV-1800, Shimadzu, Japan), measurements in the UV-Vis spectrum were performed using cuvettes with a 1-cm light path. The platinum (Pt) atom was detected using an AXIS UltraDLD instrument (Kratos, Japan).

All-atom molecular dynamics (MD) simulation

MD simulation was conducted using the LAMMPS programming package (Wang et al., 2004) to investigate the self-assembly behavior of OLA and CDDP in an aqueous solution. The simulation employed a time step of 1 fs. The simulation systems were constructed using DFF (Plimpton, 1995), comprising 2,000 OLA molecules, 2,000 CDDP molecules, and 40,000 water molecules. The initial 5 ns simulation run was performed at a

temperature of 298.15 K and a pressure of 1 atm. Subsequently, the simulation was extended for an additional 10 ns, during which trajectory data were collected for analysis. The all-atom MD simulation utilized the TEAM force field, and the parameters for CDDP were adopted from previous publications (Yao et al., 1994; Cundari et al., 1996; Jin et al., 2015). The cross interactions between different atom types were modelled using Lorentz-Berthelot mixing rules. A tail correction was applied to limit the van der Waals (vdW) interactions within 1.2 nm, while long-range interactions within the all-atom force field were calculated using the particle-mesh Ewald (PME) method. Temperature was controlled using a Nosé–Hoover thermostat (Sebesta et al., 2016), and pressure was regulated using a barostat. VMD software was employed for visualizing the simulated boxes (Nosé, 1984). The structure of the aqueous solution was characterized using the radial distribution function (RDF) $g_{ab}(r_{ab})$, which represents the average distribution between two atoms with types a and b over the MD trajectory,

$$g_{ab}(r_{ab}) = \frac{\rho_{ab}(r_{ab})}{N_b/V}$$

where $N_b = \int_V \rho_{ab}(r)\mathrm{d}r$. RDF $g_{ab}(r_{ab})$ demonstrates the local correlations between two types of atoms with separation r_{ab}.

Cell culture

DMEM enhanced with 10% inactivated FBS, 1% 100 U/mL penicillin, and 100 μg/mL streptomycin was used to cultivate MDA-MB-231 cells at 37°C.

Cellular uptake of CDDP-OLA NPs

To gain insights into the cellular uptake of NPs, co-assembled Cy5.5 NPs were prepared. Briefly, Cy5.5-loaded CDDP-OLA NPs were generated by adding Cy5.5, dissolved in DMSO, to the NPs solution while stirring. *In vitro* uptake of the CDDP-OLA NPs was assessed using laser-scanning confocal microscopy (LSCM) and flow cytometry. MDA-MB-231 cells were seeded in 6-well plates at a density of 5×10^5 cells per well for flow cytometry experiments. The cells were then exposed to CDDP-OLA NPs for 0.5, 1, 2, 4, and 6 h. Following trypsin treatment and three washes with PBS, the uptake behavior of CDDP-OLA NPs was analyzed using a flow cytometer (LSRFortessa, BD, Franklin Lakes, NJ, USA). For LSCM investigations, MDA-MB-231 cells were seeded on glass coverslips placed in 6-well plates. Each well contained 3×10^5 cells. Subsequently, the cells were exposed to CDDP-OLA NPs for 0.5, 1, 2, 4, and 6 h. After three cold PBS rinses, the cells were fixed with 4% paraformaldehyde. Nuclei were stained with Hoechst for 5 min. Glass coverslips were mounted onto slides, and the uptake behavior of CDDP-OLA NPs was examined using a LSCM (TCS SP8 STED 3X, Leica, Germany).

Cytotoxicity of CDDP-OLA NPs

We evaluated *in vitro* cytotoxicity via MTT assays. A total of 1.5×10^4 MDA-MB-231 cells were seeded into each well using 96-well plates. Different doses (2, 4, 8, 16, 32, 64, and 128 μM) of CDDP, OLA, CDDP/OLA mixture, and CDDP-OLA NPs were applied to the cells for 48 h. Control cells were grown in DMEM. After 48 h, each well received 20 μL of a 5 mg/mL MTT solution in PBS. Followed a 4 h incubation in the dark at 37°C and removal of the supernatant, 150 μL of DMSO was added to each well to dissolve the formazan crystals. Followed 10 min of shaking, a BioTek Synergy H4 hybrid reader was used to measure the absorbance at 490 nm. The following equation was used to determine cell viability:

$$\textit{Cell survival} = \frac{OD_{490\,sample} - OD_{490\,blank}}{OD_{490\,control} - OD_{490\,blank}} \times 100$$

where $OD_{490\,sample}$, $OD_{490\,control}$, and $OD_{490\,blank}$ are the ultraviolet absorbance degrees at 490 nm with drugs, without drugs, and with DMEM alone.

Cell apoptosis

Cell apoptosis was analyzed via flow cytometry. Using a 6-well plate, 5×10^5 MDA-MB-231 cells were seeded into each well. After cell adhesion, cells were incubated with the same concentrations of CDDP, OLA, CDDP/OLA mixture, and CDDP-OLA NPs (CDDP 25 μM, OLA 25 μM) for 48 h. Cells were separated using pancreatin after 48 h, then washed three times with fresh PBS before added a binding buffer. The cell suspension was then stained with 10 μL PI and 5 μL Alexa Fluor FITC-coupled annexin-V. These processed cells were analyzed on the FITC and PI channels on a flow cytometer.

Mitochondrial membrane potential (MMP) measurement

Using the fluorescent probe JC-1, the MMP of the cells was determined. MDA-MB-231 cells were seeded in a 6-well plate (5×10^5 cells each well). After cell adhesion, cells were incubated with the same concentration of CDDP, OLA, CDDP/OLA mixture, and CDDP-OLA NPs (CDDP 25 μM, OLA 25 μM) for 48 h. Followed three rounds of rinsing with cold PBS, cells were treated with JC-1 (1.2×) for 20 min at 37°C. Afterwards, JC-1 dye buffer (1×) was used to rinse the cells twice to stain the mitochondria. Hoechst was used to stain cell nuclei for 5 min. The MMP was then assessed using a LSCM.

Cell cycle analysis

Using flow cytometry, cell cycle analysis was carried out. Briefly, 5×10^5 MDA-MB-231 cells were seeded into each well of a 6-well plate. After cell adhesion, all cells were incubated with same concentrations of CDDP, OLA, CDDP/OLA mixture, and CDDP-OLA NPs (CDDP 20 μM, OLA 20 μM) for 48 h. After 48 h detached cells were gathered and mixed with adherent cells digested via trypsinisation. Followed medium wash, the cells were pelleted, resuspended in 70% ethanol, and kept at 4°C for 1 h. Followed a centrifugation, the cells were washed three times with

PBS, resuspended in a PI dye solution, and then incubated for 30 min at 37°C without light. Cell cycle analysis was performed using a flow cytometer. Using doublet discrimination, the percentage of cells in each cell cycle phase was ascertained from 5×10^4 cells. FlowJo software was used to analyze the cell cycle position.

Western blot analysis

In 100 mm culture dishes, MDA-MB-231 cells were seeded at a density of 5×10^6 cells in 10 mL DMEM complete medium. After adhesion, cells were cultivated with same concentrations of CDDP, OLA, CDDP/OLA mixture, and CDDP-OLA NPs (CDDP 25 μM, OLA 25 μM) for 24 h. Cells were then washed three times with cool PBS and disrupted in radioimmunoprecipitation assay (RIPA) lysis buffer to extract cellular proteins. A bicinchoninic acid (BCA) protein assay kit was used to determine the amount of protein present in the extracts. Protein was run on an SDS-PAGE gel in equal proportions, transferred to 0.45 μm polyvinylidene fluoride (PVDF) membranes (Millipore, USA), and then blocked in 5% skim milk in Tris-buffered saline with Tween (TBST). Afterwards, mouse anti-human GAPDH, p53, and PARP1, and rabbit anti-human c-Caspase-3, Bax, and Bcl-2 antibodies were incubated with the membranes. GADPH was employed as a control for loading. A ChemiDocTM MP imaging system (Bio-Rad, Hercules, CA, USA) was used to visualize the protein bands.

Tumor models

Female Balb/c nude mice (6 weeks, Certificate No. 20221017Abbbbbbbb0105000315) were obtained from Ziyuan Experimental Animal Technology Co., LTD. (Hangzhou, China). In order to conduct an *in vivo* anticancer efficacy test, mice were given a hypodermic injection in the right flank containing 200 μL of a cell solution comprising 5×10^6 MDA-MB-231 cells. Experiments began when the tumors got to be approximately 100 mm^3 in size.

In vivo tumor targeting and biodistribution study

Two groups were randomly selected from mice with MDA-MB-231 tumors. Through the tail vein, mice were administered 200 μL of either Cy5.5-loaded CDDP-OLA NPs or Cy5.5 alone. Cy5.5 intrinsic fluorescence was measured at 0, 1, 4, 8, 12, and 24 h after injection using a Kodak multimode imaging system. Moreover, to assess the distribution of CDDP-OLA NPs *in vivo*, an injection of CDDP-OLA NPs solution (5 mg CDDP/kg, 7 mg OLA/kg) was given to MDA-MB-231 tumor-bearing mice through the tail vein at different time points. The heart, liver, spleen, lung, kidneys, and tumor were among the principal tissues dissected for fluorescence imaging.

Evaluation of antitumor effects

Twenty-five nude mice bearing MDA-MB-231 tumors were randomly assigned to one of five groups. Intravenous injections of PBS, CDDP, OLA, CDDP/OLA mixture, and CDDP-OLA NPs (CDDP 5 mg/kg, OLA 7 mg/kg) were administered to tumor-bearing animals once every 3 days for a total of 21 days. Before each drug delivery, the tumor weight and volume were calculated using a vernier caliper and platform scale. The following formula was used to determine the tumor volume:

$$Volume\ (mm^3) = \frac{1}{2} \times length\ (mm) \times width\ (mm^2)$$

Mice in all groups were sacrificed after 21 days, following the IACUC protocol. We removed, weighed, and photographed their organs, which included heart, liver, spleen, lung, kidneys, and tumors. Prior to being embedded in paraffin, the tumors and other tissues underwent further dissection and were then preserved in 4% polyoxymethylene. The tumors were then chopped into pieces for Hematoxylin and Eosin (H&E) staining, Ki67 labeling, and TUNEL assay. H&E staining was applied to sections of additional organs.

Statistical analysis

Data were collected from a minimum of three separate replicates. Individual data points were compared using the Student's t-test. $p < 0.05$ was considered statistically significant in each case.

Results and discussion

Preparation and characterizations of CDDP-OLA NPs

In our current study, we provided evidence for the self-assembly of the chemotherapeutic drugs CDDP and the PARP inhibitor OLA into NPs through a slow mixing process. Previous research (Humphrey et al., 1996; Liu et al., 2016; Zhang et al., 2016) led us to hypothesize that intermolecular interactions, such as hydrogen bonding, between the two molecules contribute to the formation of CDDP-OLA NPs. The size and shape of the resulting CDDP-OLA NPs were characterized via dynamic light scattering (DLS) and transmission electron microscopy (TEM). The hydrodynamic size of the NPs was approximately 60 nm, while the diameter observed under TEM imaging was around 50 nm. These size parameters, in conjunction with the enhanced permeability and retention effect, make the NPs favorable for accumulation at tumor sites, as depicted in Figures 1A, B. To further confirm the successful construction of CDDP-OLA NPs, the presence of platinum atoms was characterized using X-ray photoelectron spectroscopy (XPS) (Figure 1C).

To elucidate the mechanisms underlying the self-assembly of CDDP-OLA NPs and investigate the presence of intermolecular interactions between the two drug compounds, we employed various techniques. Firstly, we examined the existence of hydrogen bonding through ^{1}H NMR spectra and FTIR spectroscopy at different temperatures. Previous reports (Ma et al., 2016) have shown that breaking hydrogen bonds can significantly affect the movement of related protons. As the temperature increased from 303 K to 393 K, the hydrogen of the NH group in OLA gradually shifted to a lower

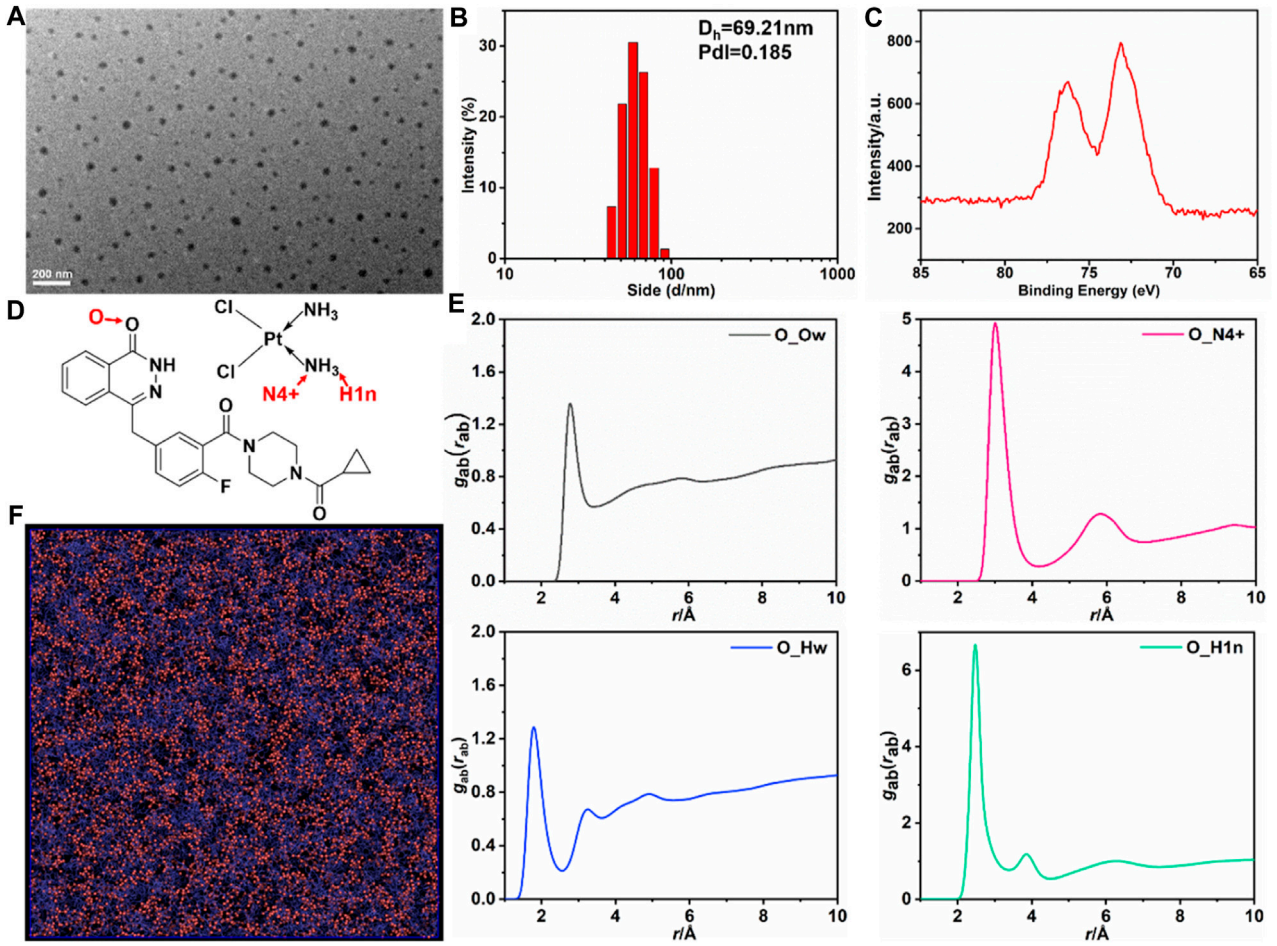

FIGURE 1
Characterizations of the CDDP-OLA NPs and All-atom MD simulation of CDDP and OLA in aqueous solution. **(A)** TEM image of CDDP-OLA NPs. Scale bar = 200 nm. **(B)** Hydrodynamic particle size of CDDP-OLA NPs in PBS. **(C)** XPS of detected NPs. **(D)** Atom type definitions in OLA and CDDP. **(E)** Radial distribution functions g_{ab} (r_{ab}), atom type O represents the carbonyl group in the OLA, type N4+ and H1n are the nitrogen and hydrogen in NH3 of CDDP, and Ow and Hw are the oxygen and hydrogen atoms of water molecules. **(F)** Snapshot of molecular configuration where OLA is purple, CDDP is red, and water molecules are not shown for clarity.

magnetic field (from 12.56 to 12.08 ppm), indicating the presence of hydrogen bonding (Supplementary Figures S1A–C). Furthermore, the FT-IR spectra demonstrated that the stretching vibration peak of the C=O bond shifted to a higher wavenumber indicating the involvement of the C=O bond in hydrogen bond formation (Supplementary Figures S2A–F). These results confirmed the interaction between CDDP and OLA through hydrogen bonding.

Molecular simulations to interrogate the self-assembly dynamics and mechanisms of CDDP-OLA NPs

To obtain a comprehensive understanding of CDDP and OLA self-assembly in aqueous solution, all-atom simulation was performed, with the simulation system containing 2,000 OLA, 2,000 CDDP, and 40,000 water molecules. A TEAM force field was adopted to describe the atomic interactions; the parameters of CDDP were entered based on previous publications (Yao et al., 1994; Cundari et al., 1996; Jin et al., 2015). The total 15 ns MD simulation was performed, and the last 10 ns trajectory was used for analysis. OLA interacted with CDDP to form aggregates in the aqueous solution. Atom type definitions in the OLA and CDDP are shown in Figure 1D. The RDF between OLA, CDDP, and water indicated that the self-assembly structure resulted from competition between intermolecular interactions among the three species. The carbonyl group in OLA strongly interacted with the NH3 group in CDDP, as illustrated by the high peaks in the RDF of the pairs O-N4+ and O-H1n pairs, located at 2.7 Å (O-H1n) and 3.0 Å (O-N4+), corresponding to the hydrogen bonding (Figure 1E). The association between the drugs and water was less favored and the peak in RDF fluctuated with average densities. The hydrogen bonding between OLA and CDDP was visualized in Figure 1F, clearly showing that CDDP binds closely with OLA.

Cellular uptake

To determine whether the CDDP-OLA NPs could be taken up by MDA-MB-231 cells, cellular uptake was investigated via LSCM

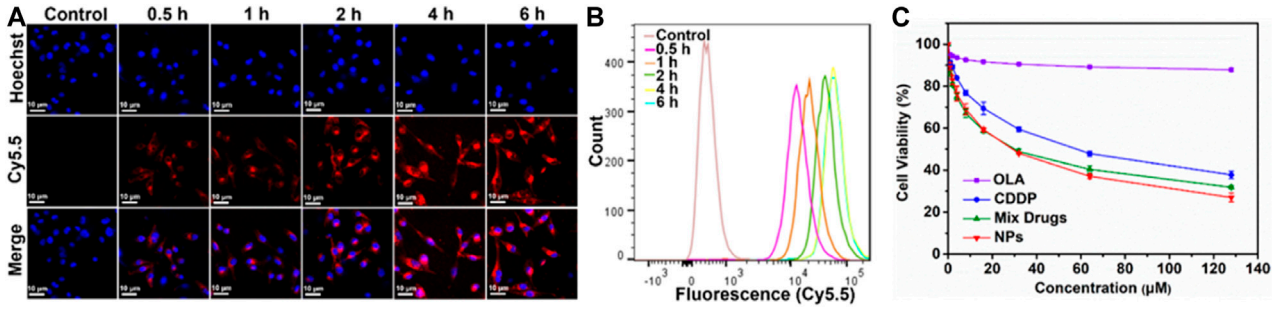

FIGURE 2
Effect of CDDP-OLA NPs on cancer cellular uptake, and cell proliferation *in vitro*. **(A)** Confocal images of MDA-MB-231 cells containing CDDP-OLA NPs at 0.5, 1, 2, 4, and 6 h. Blue represents the Hoechst nuclear stain and red represents Cy5.5. Scale bar = 10 μm. **(B)** Analysis of MDA-MB-231 cells using flow cytometry after they were exposed to CDDP-OLA NPs for 0.5, 1, 2, 4, and 6 h. **(C)** Viability of MDA-MB-231 cells cultured for 48 h with varying doses of CDDP, OLA, CDDP/OLA mixture, and CDDP-OLA NPs.

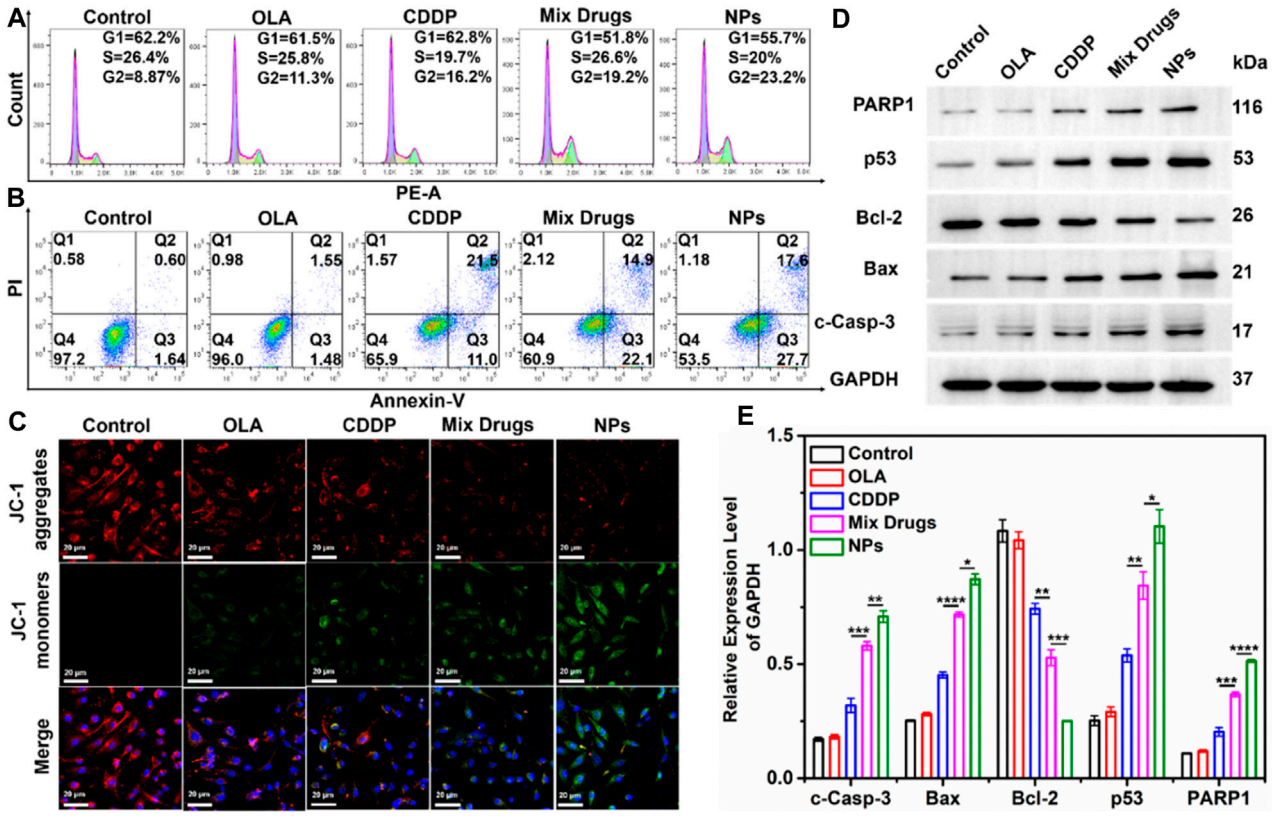

FIGURE 3
Effect of CDDP-OLA NPs on cancer cell cycle, cell apoptosis, mitochondrial membrane potential (ΔΨm), and cell apoptosis-related protein expression *in vitro*. **(A)** Cell cycle distribution of MDA-MB-231 cells treated with PBS, OLA, CDDP, CDDP/OLA mixture, and CDDP-OLA NPs. **(B)** Apoptosis of MDA-MB-231 cells stimulated by PBS, CDDP, OLA, CDDP/OLA mixture, and CDDP-OLA NPs. **(C)** Mitochondrial damage in MDA-MB-231 cells stimulated by PBS, CDDP, OLA, CDDP/OLA mixture, and CDDP-OLA NPs, as determined via LSCM. Hoechst-stained nuclei are shown in blue, red represents JC-1 aggregates, and green represents JC-1 monomers. Scale bar = 20 μm. **(D)** Expression and **(E)** relative protein levels of c-Caspase-3, Bax, Bcl-2, p53, and PARP in MDA-MB-231 cells treated with OLA, CDDP, CDDP/OLA mixture, and CDDP-OLA NPs (OLA 20 μM and CDDP 20 μM). $*p < 0.05$, $**p < 0.01$, $***p < 0.001$, $****p < 0.0001$ indicated significantly different between two groups.

and flow cytometry. Confocal imaging demonstrated that Cy5.5 fluorescence intensity in MDA-MB-231 cells steadily rose during the course of the incubation period (Figure 2A), which was consistent with our flow cytometry data (Figure 2B; Supplementary Figure S3). These results demonstrated that CDDP-OLA NPs could be effectively taken up by MDA-MB-231 cells.

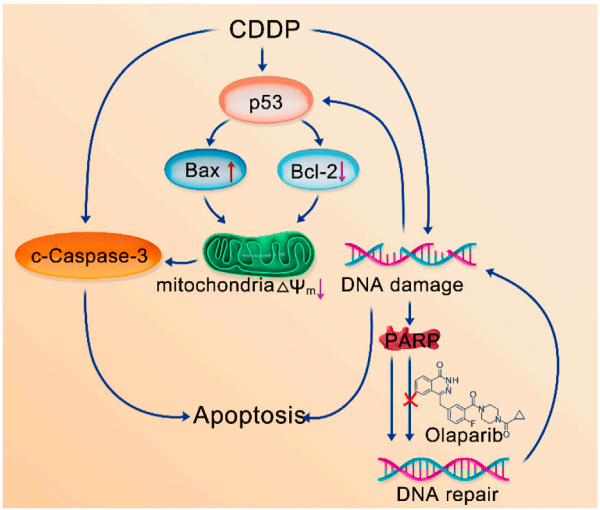

SCHEME 2
Mechanisms of the combination of CDDP and OLA-induced MDA-MB-231 cell apoptosis.

In vitro cytotoxicity

The *in vitro* cytotoxicity of different drug formulations was assessed using the MTT test. CDDP, OLA, CDDP/OLA mixture, and CDDP-OLA NPs were each applied to MDA-MB-231 cells in varying doses. The negative control cells that had not been treated. Followed a 48-h incubation period, both the CDDP/OLA mixture and the CDDP-OLA NPs exhibited higher cytotoxicity than the free CDDP with MDA-MB-231 cells, demonstrated that OLA effectively improves the oncological outcome of CDDP. As shown in Figure 2C and Supplementary Figure S4, the IC_{50} values of CDDP and the CDDP/OLA mixture in MDA-MB-231 cells were 55.14 and 30.08 μM, respectively. Meanwhile, the IC_{50} of CDDP-OLA NPs was 27.72 μM. It is important to note that the CDDP/OLA mixture showed inferior efficacy compared to the NPs due to the latter's higher cellular internalization capability and greater bioavailability (Lin et al., 2010).

Effects of CDDP-OLA NPs on the cell cycle

The cell cycle distributions of MDA-MB-231 cells incubated with CDDP, OLA, CDDP/OLA mixture, and CDDP-OLA NPs are shown in Figure 3A. All treatments induced an increase in the fraction of cells in G2 compared to the controls. Further, the cells exposed to CDDP-OLA NPs exhibited the highest proportion of G2 phase cells (23.2%) among all the groups. These results indicated that CDDP-OLA NPs could induce G2 phase arrest and subsequent apoptosis to a greater extent than CDDP, or CDDP/OLA mixture.

Apoptosis of cancer cells induced by CDDP-OLA NPs

We evaluated the capacity of CDDP-OLA NPs for inducing tumor cell apoptosis. We treated MDA-MB-231 cells with CDDP, OLA, CDDP/OLA mixture, or CDDP-OLA NPs for 48 h, then we double-stained the cells with FITC and PI. As shown in Figure 3B, the percentages of apoptotic MDA-MB-231 cells after treatment were 65.9, 60.9, and 53.5% with CDDP, CDDP/OLA mixture, and CDDP-OLA NPs treatment, respectively. This could have been due to the CDDP-OLA NPs being successfully internalized and retained in MDA-MB-231 cells, while the drugs that were free or mixed could leave cells with ease. Such elevated drug accumulation in tumor cells has been shown to cause greater apoptosis (Maeda et al., 2000). The aforementioned findings indicated that NPs have a greater capacity to induce apoptosis than a single agent or mixed drugs.

Analysis of mitochondrial damage and apoptosis mechanism

Mitochondrial damage in cancer cells was assessed using JC-1 dye, which built up in healthy mitochondria and released red fluorescence. This dye inversely dispersed into a monomeric state to produce green fluorescence in response to a drop in the mitochondrial membrane potential (ΔΨm). As seen in Figure 3C, after separated 48 h treatments with PBS, CDDP, and OLA, high red fluorescence and faint green fluorescence were observed, indicative of healthy mitochondria. In contrast, strong green fluorescence and modest red fluorescence were seen in the cells after treatment with the CDDP/OLA mixture and CDDP-OLA NPs, particularly in the latter group, suggested considerable damage to the mitochondria.

Mechanism of action of the CDDP-OLA NPs

While the CDDP-OLA NPs exhibited superior *in vitro* cytotoxicity compared to either free drug or the mixture of both, their mechanism of action remained unclear. We sought to obtain greater insight into the mechanism of CDDP-OLA NPs action using Western blot analysis. In this study, the expression of p53 protein was markedly elevated by CDDP-OLA NPs compared to the single drug and control treatment; the same trend was observed with the expression of Bax protein, but the opposite was observed with Bcl-2 protein. In addition, the expression levels of c-Caspase-3 and PARP1 proteins were increased in MDA-MB-231 cells exposed to CDDP-OLA NPs compared to the other four groups (Figures 3D, E). These results were repeated three times and can be seen in the Supplementary Material (Supplementary Figure S5).

In general, the caspase signaling pathway serves as a crucial apoptotic marker; the induction of apoptosis leads to caspase activation (Savitskaya and Onishchenko, 2015). PARP1 is the main substrate of caspase-3, being cleaved by it upon the initiation of apoptosis. As a result of this cleavage, PARP1 is no longer able to carry out its role in genome maintenance. DNA damage can activate the p53 signaling pathway (Polo and Jackson, 2011). Further, p53 proteins are linked to oxidative stress. Mitochondria play a pivotal role in the apoptotic cascade (Lin et al., 2018), and downstream proteins, including Bax and Bcl-2, can cause cancer cell apoptosis by destroying the mitochondria (Deus et al., 2015). Based on the aforementioned studies and our experimental proposed that CDDP-OLA NPs released CDDP and OLA after aggregated at the tumor site. CDDP could induce DNA damage in tumor cells and activated the caspase signaling pathway to trigger apoptosis. Additionally, it could activate the p53 signaling

10.3389/fbioe.2024.1364975

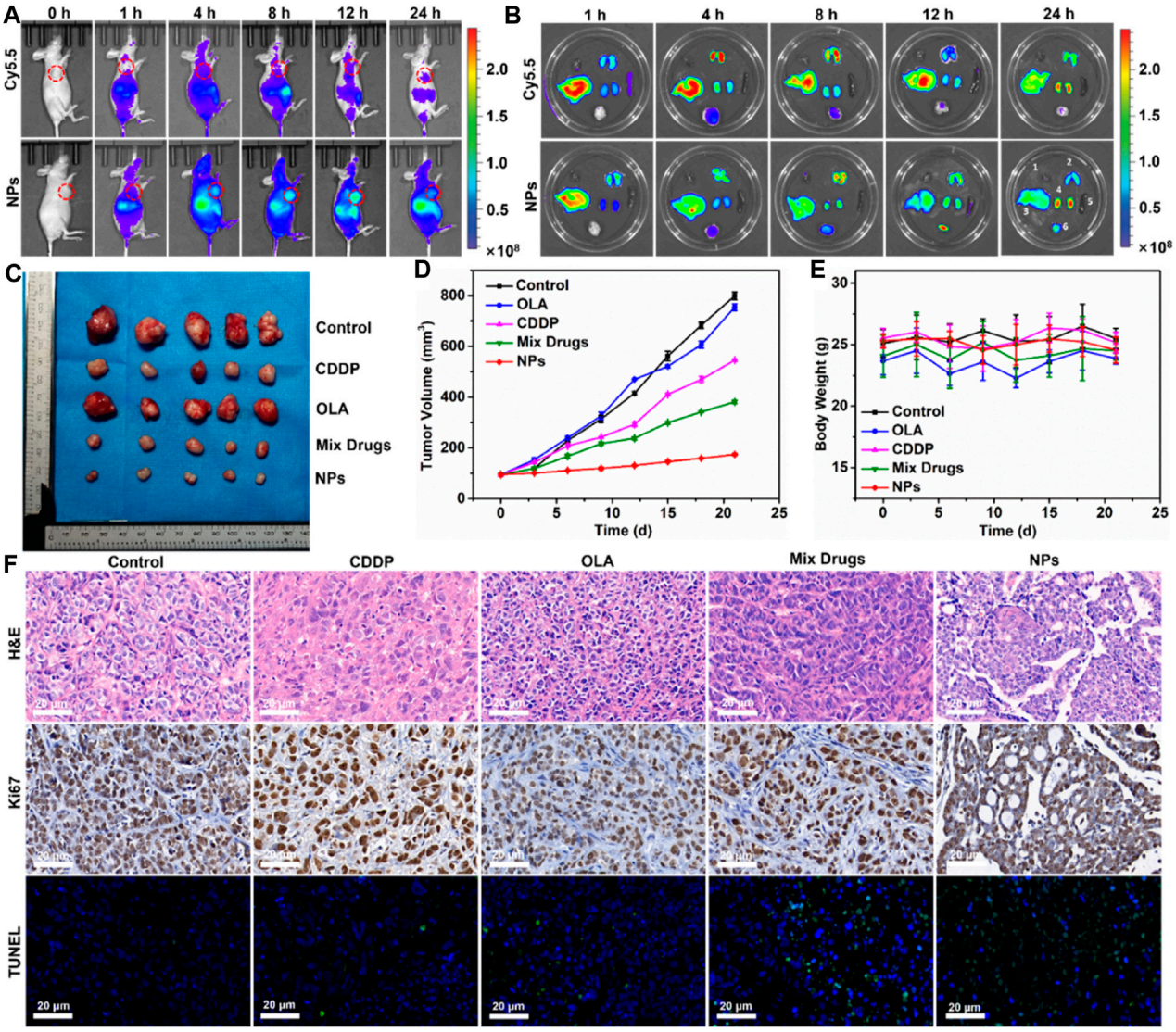

FIGURE 4
Antitumor efficacy of CDDP-OLA NPs in MDA-MB-231 tumor-bearing Balb-c/nude mice. **(A)** Free Cy5.5 and Cy5.5-loaded CDDP-OLA NPs imaging *in vivo*. **(B)** *In vivo* biodistribution of the two aforementioned formulations—1: heart; 2: lung; 3: liver; 4: kidneys; 5: spleen; and 6: tumor. **(C)** Tumor tissue after 21 days of therapy. **(D)** Treatment-related changes in tumor volume. **(E)** Treatment-related changes in animal weight. **(F)** H&E, Ki67, and TUNEL-stained slices of tumor tissue.

pathway, and the downstream mitochondria-related genes, Bax and Bcl-2, regulated by p53, could be up and downregulated, respectively. This leaded to a further decrease in the mitochondrial membrane potential (ΔΨm) and regulated caspase-dependent apoptosis. Meanwhile, OLA, as a PARP inhibitor, hinders DNA repair, which further amplified DNA damage, leading to the induction of apoptosis (Scheme 2).

Real-time optical imaging and biodistribution analysis

Based on the strong antitumor efficacy of CDDP-OLA NPs observed *in vitro*, we assessed their antitumor impact *in vivo*. First, the tumor-specific targeting capability of CDDP-OLA NPs was evaluated using *in vivo* imaging of nude mice carrying MDA-MB-231 tumors. At 1, 4, 8, 12, and 24 h after injection, free Cy5.5 and NPs loaded with Cy5.5 were examined. As illustrated in Figure 4A, the brightest fluorescence signal from tumors was observed at 4 h following the injection of free Cy5.5, after which the fluorescence intensity declined. Since free Cy5.5 is quickly degraded *in vivo*, at 12 h after injection, the fluorescent signal of free Cy5.5 in MDA-MB-231 tumor-bearing nude mice was nearly undetectable. Meanwhile, the fluorescence signals of Cy5.5-loaded CDDP-OLA NPs near the tumor site steadily increased over the first 12 h, which may be attributed to the EPR effect causing CDDP-OLA NPs to accumulate there. Biodistribution analysis in several organs consistently indicated that free Cy5.5 was completely cleared during the first 12 h post-injection, while CDDP-OLA NPs continued to accumulate at the tumor site (Figure 4B). These

data highlight the improved tumor-targeting capacity of CDDP-OLA NPs compared to the free small-molecule drugs.

In vivo antitumor efficacy

With the enhanced biodistribution and tumor accumulation of NPs confirmed, we proceeded to evaluate their antitumor efficacy *in vivo*. A tail vein intravenous infusion of PBS (control), CDDP, OLA, CDDP/OLA mixture, or CDDP-OLA NPs was administered to mice with MDA-MB-231 tumors. As shown in Figures 4C, D, the tumor diameters in mice given PBS injections increased from around 100 mm^3 to approximately 800 mm^3 through the course of therapy, with no tumor suppression observed. When mice were given CDDP or OLA alone, tumor volumes increased to approximately 550 mm^3 and 750 mm^3, respectively, proving that a single anticancer treatment only moderately limit tumor growth. Owing to the synergistic effects of CDDP and OLA in suppressing MDA-MB-231 cell growth, tumor volumes in the CDDP/OLA mixture group reached approximately 380 mm^3. Meanwhile, mice administered CDDP-OLA NPs experienced minor tumor growth to approximately 170 mm^3, proved the superior efficacy of this formulation. We attributed this effect to the enhanced biodistribution and effective tumor accumulation. There was no discernible difference in body weight among the mice with MDA-MB-231 tumors in the early part of the experimental period, but slight increases in weight were observed at the later stages (Figure 4E). This was attributed to the small doses of administered therapeutics.

The antitumor efficacy of CDDP-OLA NPs was further analyzed via H&E staining, Ki67, and TUNEL assays. H&E staining revealed an abundance of cancer cells in tumor tissue from control mice, without obvious signs of damage. In contrast, tumor tissue from groups treated with CDDP-OLA NPs contained a high level of cells devoid of nuclei. In addition, a considerable reduction in the number of brown (Ki67-positive) tumor cells was observed in CDDP-OLA NPs-treated mice as opposed to those who received the different formulas. TUNEL analysis indicated that CDDP-OLA NPs induced tumor cell apoptosis most potently (Figure 4F). Importantly, heart, liver, spleen, lung, and kidney tissue from NPs-treated mice exhibited no obvious injury (Supplementary Figure S6). Taken together, these results indicated that CDDP-OLA NPs exhibit promising antitumor efficacy and favorable tolerability.

In current work, we developed a novel kind of supramolecular self-delivery nanodrugs with OLA using non-covalent interactions for enhancing CDDP chemotherapy sensitivity. This nanodrug system was formulated by the hydrogen bonding interaction and hydrophobic interaction of OLA and CDDP, which avoids chemical modification of parent drugs or introduction of any non-clinically proven materials and thus facilitates their clinical translation. Both the computer simulations and experiments confirmed the feasibility of their self-assembly. These supramolecular nanodrugs exhibited a synergistic therapeutic effect by inhibiting the DNA repair and increased DNA damage accumulation and enhancing the sensitivity of CDDP chemotherapy. More importantly, *in vitro* and *in vivo* studies demonstrated that these nanodrugs improved pharmacokinetics, bioavailability and therapeutic efficacy while having considerably reduced side effects of free drugs.

Conclusion

The complementary mechanisms of CDDP and OLA synergistically enhance the sensitivity of CDDP chemotherapy, resulted in improved therapeutic outcomes. CDDP induced DNA damage for apoptosis, while OLA, a PARP1 inhibitor, inhibited DNA repair and increased DNA damage accumulation. The synergistic use of CDDP and OLA showed promise for more effective cancer treatment. By self-assembling CDDP and OLA into nanoparticles (CDDP-OLA NPs) through hydrogen bonding, with a uniform shape and size distribution, the CDDP-OLA NPs exhibited improved cell uptake, superior tumor selectivity, and pronounced therapeutic efficacy *in vitro* and *in vivo* compared to CDDP or CDDP/OLA mixture. We enhanced both chemotherapeutic agents' solubility and tumor targeting without the need for external carriers. This optimization improved bioavailability, maximized the anticancer effect while minimized the toxic side effects of chemotherapy. Importantly, the CDDP-OLA NPs were easily prepared without the requirement for sophisticated chemical changes. Considering these benefits, we believe that this strategy holds great potential as an anticancer therapy with a low risk of adverse effects.

Data availability statement

The original contributions presented in the study are included in the article/Supplementary Material, further inquiries can be directed to the corresponding authors.

Ethics statement

Ethical approval was not required for the studies on humans in accordance with the local legislation and institutional requirements because only commercially available established cell lines were used. The animal study was approved by the Institutional Animal Care and Use Committee (IACUC) of Shanghai Rat&Mouse Biotech. The study was conducted in accordance with the local legislation and institutional requirements.

Author contributions

TZ: Conceptualization, Data curation, Software, Writing–original draft, Writing–review and editing. XL: Data curation, Methodology, Software, Writing–review and editing. LW: Methodology, Software, Writing–review and editing. YS: Writing–review and editing. JY: Methodology, Writing–review and editing. XZ: Investigation, Project administration, Writing–review and editing. GL: Funding acquisition, Project administration, Writing–review and editing, Methodology.

Funding

The author(s) declare financial support was received for the research, authorship, and/or publication of this article. This work is supported by Natural Science Foundation of Shanghai (Grant number 19ZR1438300); Shanghai Eighth People's Hospital talent introduction start-up funds (Grant number 7201).

Conflict of interest

The authors declare that the research was conducted in the absence of any commercial or financial relationships that could be construed as a potential conflict of interest.

Publisher's note

All claims expressed in this article are solely those of the authors and do not necessarily represent those of their affiliated organizations, or those of the publisher, the editors and the reviewers. Any product that may be evaluated in this article, or claim that may be made by its manufacturer, is not guaranteed or endorsed by the publisher.

Supplementary material

The Supplementary Material for this article can be found online at: https://www.frontiersin.org/articles/10.3389/fbioe.2024.1364975/full#supplementary-material

References

Bray, F., Ferlay, J., Soerjomataram, I., Siegel, R. L., Torre, L. A., and Jemal, A. (2018). Global cancer statistics 2018: GLOBOCAN estimates of incidence and mortality worldwide for 36 cancers in 185 countries. *CA Cancer J. Clin.* 68 (6), 394–424. doi:10.3322/caac.21492

Chaudhuri, A. R., and Nussenzweig, A. (2017). The multifaceted roles of PARP1 in DNA repair and chromatin remodelling. *Nat. Rev. Mol. Cell. Biol.* 18 (10), 610–621. doi:10.1038/nrm.2017.53

Chen, J., Li, D., Li, H., Zhu, K., Shi, L., and Fu, X. (2022). Cell membrane-targeting NIR fluorescent probes with large Stokes shifts for ultralong-term transplanted neural stem cell tracking. *Front. Bioeng. Biotechnol.* 11, 1139668. doi:10.3389/fbioe.2023.1139668

Cundari, T. R., Fu, W., Moody, E. W., Slavin, L. L., Snyder, L. A., Sommerer, S. O., et al. (1996). Molecular mechanics force field for platinum coordination complexes. *J. Phys. Chem.* 100 (46), 18057–18064. doi:10.1021/jp961240x

Deus, C. M., Zehowski, C., Nordgren, K., Wallace, K. B., Skildum, A., and Oliveira, P. J. (2015). Stimulating basal mitochondrial respiration decreases doxorubicin apoptotic signaling in H9c2 cardiomyoblasts. *Toxicology* 334, 1–11. doi:10.1016/j.tox.2015.05.001

Farmer, H., McCabe, N., Lord, C. J., Tutt, A. N. J., Johnson, D. A., Richardson, T. B., et al. (2005). Targeting the DNA repair defect in BRCA mutant cells as a therapeutic strategy. *Nature* 434 (7035), 917–921. doi:10.1038/nature03445

Huang, P., Wang, D., Su, Y., Huang, W., Zhou, Y., Cui, D., et al. (2014). Combination of small molecule prodrug and nanodrug delivery: amphiphilic drug-drug conjugate for cancer therapy. *J. Am. Chem. Soc.* 136 (33), 11748–11756. doi:10.1021/ja505212y

Humphrey, H., Dalke, A., and Schulten, K. (1996). VMD: visual molecular dynamics. *J. Mol. Graph* 14 (1), 33–38. doi:10.1016/0263-7855(96)00018-5

Jiang, M., Liao, J., Liu, C., Liu, J., Chen, P., Zhou, J., et al. (2023). Metal-organic frameworks/metal nanoparticles as smart nanosensing interfaces for electrochemical sensors applications: a mini-review. *Front. Bioeng. Biotechnol.* 11, 1251713. doi:10.3389/fbioe.2023.1251713

Jin, Z., Yang, C., Cao, F., Li, F., Jing, Z., Chen, L., et al. (2015). Hierarchical atom type definitions and extensible all-atom force fields. *J. Comput. Chem.* 37 (7), 653–664. doi:10.1002/jcc.24244

Ledermann, J., Harter, P., Gourley, C., Friedlander, M., Vergote, I., Rustin, G., et al. (2014). Olaparib maintenance therapy in patients with platinum-sensitive relapsed serous ovarian cancer: a preplanned retrospective analysis of outcomes by BRCA status in a randomised phase 2 trial. *Lancet Oncol.* 15 (8), 852–861. doi:10.1016/S1470-2045(14)70228-1

Lin, I. H., Cheng, C. C., Yen, Y. C., and Chang, F. C. (2010). Synthesis and assembly behavior of heteronucleobase-functionalized poly(ε-caprolactone). *Macromolecules* 43 (3), 1245–1252. doi:10.1021/ma9026614

Lin, Y., Shen, Z., Song, X., Liu, X., and Yao, K. (2018). Comparative transcriptomic analysis reveals adriamycin-induced apoptosis via p53 signaling pathway in retinal pigment epithelial cells. *J. Zhejiang Univ. Sci. B* 19 (12), 895–909. doi:10.1631/jzus.B1800408

Liu, K., Xing, R., Zou, Q., Ma, G., Möhwald, H., and Yan, X. (2016). Simple peptide-tuned self-assembly of photosensitizers towards anticancer photodynamic therapy. *Angew. Chem. Int. Ed. Engl.* 55 (9), 3036–3039. doi:10.1002/anie.201509810

Liu, Y., Quan, X., Li, J., Huo, J., Li, X., Zhao, Z., et al. (2022). Liposomes embedded with PEGylated iron oxide nanoparticles enable ferroptosis and combination therapy in cancer. *Natl. Sci. Rev.* 10 (1), nwac167. doi:10.1093/nsr/nwac167

Liu, Y., Ran, Y., Ge, Y., Raza, F., Li, S., Zafar, H., et al. (2022). pH-Sensitive peptide hydrogels as a combination drug delivery system for cancer treatment. *Pharmaceutics* 14 (3), 652. doi:10.3390/pharmaceutics14030652

Lord, C. J., and Ashworth, A. (2017). PARP inhibitors: synthetic lethality in the clinic. *Science* 355 (6330), 1152–1158. doi:10.1126/science.aam7344

Ma, K., Xing, R., Jiao, T., Shen, G., Chen, C., Li, J., et al. (2016). Injectable self-assembled dipeptide-based nanocarriers for tumor delivery and effective *in vivo* photodynamic therapy. *ACS Appl. Mater Interfaces* 8 (45), 30759–30767. doi:10.1021/acsami.6b10754

Maeda, H., Wu, J., Sawa, T., Matsumura, Y., and Hori, K. (2000). Tumor vascular permeability and the EPR effect in macromolecular therapeutics: a review. *J. Control Release* 65 (1-2), 271–284. doi:10.1016/s0168-3659(99)00248-5

Nosé, S. (1984). A unified formulation of the constant temperature molecular dynamics methods. *J. Chem. Phys.* 81 (1), 511–519. doi:10.1063/1.447334

Plimpton, S. (1995). Fast parallel algorithms for short-range molecular dynamics. *J. Comput. Phys.* 117 (1), 1–19. doi:10.1006/JCPH.1995.1039

Polo, S. E., and Jackson, S. P. (2011). Dynamics of DNA damage response proteins at DNA breaks: a focus on protein modifications. *Genes. Dev.* 25 (5), 409–433. doi:10.1101/gad.2021311

Prasad, C. B., Prasad, S. B., Yadav, S. S., Pandey, L. K., Singh, S., Pradhan, S., et al. (2017). Olaparib modulates DNA repair efficiency, sensitizes cervical cancer cells to cisplatin and exhibits anti-metastatic property. *Sci. Rep.* 7 (1), 12876. doi:10.1038/s41598-017-13232-3

Savitskaya, M. A., and Onishchenko, G. E. (2015). Mechanisms of apoptosis. *Biochem. (Mosc)* 80 (11), 1393–1405. doi:10.1134/S0006297915110012

Sebesta, F., Sláma, V., Melcr, J., Futera, Z., and Burda, J. V. (2016). Estimation of transition-metal empirical parameters for molecular mechanical force fields. *J. Chem. Theory Comput.* 12 (8), 3681–3688. doi:10.1021/acs.jctc.6b00416

Siegel, R. L., Miller, K. D., Fuchs, H. E., and Jemal, A. (2021). Cancer statistics, 2021. *CA Cancer J. Clin.* 71 (1), 7–33. doi:10.3322/caac.21654

Song, J., Zhou, J., and Duan, H. (2012). Self-assembled plasmonic vesicles of SERS-encoded amphiphilic gold nanoparticles for cancer cell targeting and traceable intracellular drug delivery. *J. Am. Chem. Soc.* 134 (32), 13458–13469. doi:10.1021/ja305154a

Wang, C., Yang, X., Qiu, H., Huang, K., Xu, Q., Zhou, B., et al. (2023). A co-delivery system based on chlorin e6-loaded ROS-sensitive polymeric prodrug with self-amplified drug release to enhance the efficacy of combination therapy for breast tumor cells. *Front. Bioeng. Biotechnol.* 11, 1168192. doi:10.3389/fbioe.2023.1168192

Wang, D., and Lippard, S. J. (2005). Cellular processing of platinum anticancer drugs. *Nat. Rev. Drug Discov.* 4 (4), 307–320. doi:10.1038/nrd1691

Wang, J., Wolf, R. M., Caldwell, J. W., Kollman, P. A., and Case, D. A. (2004). Development and testing of a general amber force field. *J. Comput. Chem.* 25 (9), 1157–1174. doi:10.1002/jcc.20035

Wang, W., Chen, X., Li, J., Jin, Q., Jin, H. J., and Li, X. (2022). Hollow MnO2 nanoparticles loaded with functional genes as nanovaccines for synergistic cancer therapy. *ACS Appl. Nano Mat.* 5, 10537–10547. doi:10.1021/acsanm.2c01877

Wang, X., Gu, Y., Li, Q., Xu, Y., Shi, Y., Wang, Z., et al. (2022). Synergistic chemo-photothermal cancer therapy of pH-responsive polymeric nanoparticles loaded IR825 and DTX with charge-reversal property. *Colloids Surf. B Biointerfaces* 209 (Pt 2), 112164. doi:10.1016/j.colsurfb.2021.112164

Wu, C., Xu, L., Shi, L., Gao, X., Li, J., Zhu, X., et al. (2018). Supramolecularly self-assembled nano-twin drug for reversing multidrug resistance. *Biomater. Sci.* 6 (8), 2261–2269. doi:10.1039/c8bm00437d

Yao, S., Plastaras, J. P., and Marzilli, L. G. (1994). A molecular mechanics AMBER-type force field for modeling platinum complexes of guanine derivatives. *Inorg. Chem.* 33 (26), 6061–6077. doi:10.1021/ic00104a015

Yi, X., Zeng, W., Wang, C., Chen, Y., Zheng, L., Zhu, X., et al. (2022). A step-by-step multiple stimuli-responsive metal-phenolic network prodrug nanoparticles for chemotherapy. *Nano Res.* 15, 1205–1212. doi:10.1007/s12274-021-3626-2

Zhang, L., Lin, Z., Chen, Y., Gao, D., Wang, P., Lin, Y., et al. (2022). Co-delivery of Docetaxel and Resveratrol by liposomes synergistically boosts antitumor efficiency against prostate cancer. *Eur. J. Pharm. Sci.* 174, 106199. doi:10.1016/j.ejps.2022.106199

Zhang, R., Xing, R., Jiao, T., Ma, K., Chen, C., Ma, G., et al. (2016). Carrier-free, chemophotodynamic dual nanodrugs via self-assembly for synergistic antitumor therapy. *ACS Appl. Mater Interfaces* 8 (21), 13262–13269. doi:10.1021/acsami.6b02416

Zhang, T., Huang, P., Shi, L., Su, Y., Zhou, L., Zhu, X., et al. (2015). Self-assembled nanoparticles of amphiphilic twin drug from floxuridine and bendamustine for cancer therapy. *Mol. Pharm.* 12 (7), 2328–2336. doi:10.1021/acs.molpharmaceut.5b00005

Zhang, Z., Shi, L., Wu, C., Su, Y., Qian, J., Deng, H., et al. (2017). Construction of a supramolecular drug-drug delivery system for non-small-cell lung cancer therapy. *ACS Appl. Mater Interfaces* 9 (35), 29505–29514. doi:10.1021/acsami.7b07565

Zhao, M., Straten, D. v., Broekman, M. L. D., Préat, V., and Schiffelers, R. M. (2020). Nanocarrier-based drug combination therapy for glioblastoma. *Theranostics* 10 (3), 1355–1372. doi:10.7150/thno.38147

Zhu, L., Guo, Y., Qian, Q., Yan, D., Li, Y., Zhu, X., et al. (2020). Carrier-free delivery of precise drug-chemogene conjugates for synergistic treatment of drug-resistant cancer. *Angew. Chem. Int. Ed. Engl.* 59 (41), 17944–17950. doi:10.1002/anie.202006895

Frontiers in
Bioengineering and Biotechnology

Accelerates the development of therapies, devices, and technologies to improve our lives

A multidisciplinary journal that accelerates the development of biological therapies, devices, processes and technologies to improve our lives by bridging the gap between discoveries and their application.

Discover the latest Research Topics

See more →

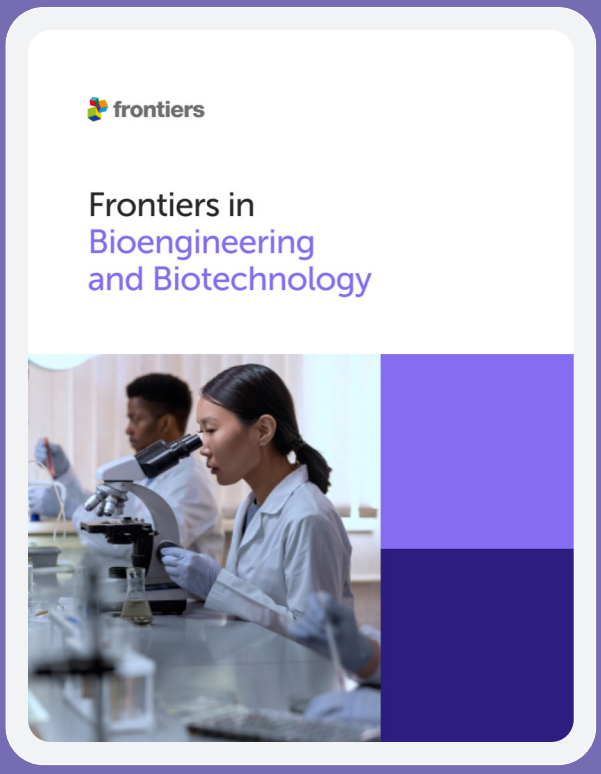

Frontiers

Avenue du Tribunal-Fédéral 34
1005 Lausanne, Switzerland
frontiersin.org

Contact us

+41 (0)21 510 17 00
frontiersin.org/about/contact